Distribution Agreement

In presenting this thesis or dissertation as a partial fulfillment of the requirements for an advanced degree from Emory University, I hereby grant to Emory University and its agents the non-exclusive license to archive, make accessible, and display my thesis or dissertation in whole or in part in all forms of media, now or hereafter known, including display on the world wide web. I understand that I may select some access restrictions as part of the online submission of this thesis or dissertation. I retain all ownership rights to the copyright of the thesis or dissertation. I also retain the right to use in future works (such as articles or books) all or part of this thesis or dissertation.

Signature:

_____	_____
Nicholas Alberto Arce	Date

Force-dependent von Willebrand factor activation and allosteric modulation by single-domain antibodies

By

Nicholas Alberto Arce
Doctor of Philosophy

Graduate Division of Biological and Biomedical Science
Molecular and Systems Pharmacology

_____
Renhao Li, Ph.D. Advisor

_____
Christopher B. Doering, Ph.D. Committee Member

_____
Nael A. McCarty, Ph.D. Committee Member

_____
Khalid Salaita, Ph.D. Committee Member

_____
Roy L. Sutliff, Ph.D. Committee Member

Accepted:

_____
Kimberly J. Arriola, Ph.D., MPH
Dean of the James T. Laney School of Graduate Studies

_____
Date

Force-dependent von Willebrand factor activation and allosteric modulation by single-domain antibodies

By

Nicholas Alberto Arce
B.S., Georgia Institute of Technology, 2017

Advisor: Renhao Li, Ph.D.

An abstract of a dissertation submitted to the Faculty of the James T. Laney School of Graduate Studies of Emory University in partial fulfillment of the requirements for the degree of Doctor of Philosophy in the Graduate Division of Biological and Biomedical Science, Molecular and Systems Pharmacology 2022

Abstract

Force-dependent von Willebrand factor activation and allosteric modulation by single-domain antibodies

By

Nicholas Alberto Arce

Over the course of several million years, animals have evolved to survive predation. The development of boney jaws and the ability to bite coincided with the ability to withstand and heal from an attack. While the flowing circulatory system of these animals was fundamental to transport oxygen and nutrients, the preservation of vessel integrity was also paramount. Hemostasis is the process of capturing platelets and activating coagulation factors to generate a clot.

Primary hemostasis is carried out by two distinct interactions. Disruption or elimination of either interaction in humans by deleterious mutations or pharmacological inhibition will lead to bleeding. Subendothelial collagen contains binding sites for the A3 domain of the plasma glycoprotein, von Willebrand factor (VWF). VWF is a soluble, multimeric protein that can span enormous lengths. Its polymeric properties enable it to undergo extensional elongation after VWF has been immobilized or when it undergoes a mixture of shear and rotational forces. VWF A3 can bind to exposed collagen to serve as a long tether to capture platelets. The VWF A1 domain is responsible for binding to platelet membrane receptor glycoprotein (GP)Ibα. The binding of VWF to platelets in this manner not only physically sequesters platelets near the site of injury, but also stimulates platelets to engage other receptors to form a stable basis for coagulation to occur. The interactions of collagen with VWF and then VWF with GPIbα are the interactions which define primary hemostasis.

The regulation of the GPIbα-VWF interaction has been the host of great debate over several decades. It postulated many years ago that force must be involved in the activation of VWF, as plasma VWF does not spontaneously bind to platelets. In this dissertation, I sought to elucidate the molecular mechanism that controls the force dependent activation of VWF. Using single-domain antibodies, I further probed VWF activation by modulating the functions of VWF both under flow and under static conditions. The research outlined in this dissertation demonstrates the importance of local autoinhibitory elements to the control of VWF activation and outlines an approach to target these elements to regulate VWF activity.

Force-dependent von Willebrand factor activation and allosteric modulation by single-domain antibodies

By

Nicholas Alberto Arce
B.S., Georgia Institute of Technology, 2017

Advisor: Renhao Li, Ph.D.

A dissertation submitted to the Faculty of the James T. Laney School of Graduate Studies of Emory University in partial fulfillment of the requirements for the degree of Doctor of Philosophy in the Graduate Division of Biological and Biomedical Science, Molecular and Systems Pharmacology 2022

Acknowledgements

I would first like to thank my family for supporting my career as a scientist and the uncertainties that come with this career choice. I would like to thank my girlfriend, Sara, for listening to me and standing by me when I need to dedicate time to the lab. I would also like to thank my friends for helping take my mind off of the science when needed. To my dog, Bash, who will never read this, for always reminding me of what truly matters in life.

Dr. Renhao Li has served as my mentor for the last four years. I am grateful for his input towards my project, his mentorship and guidance in both experimental design, writing, and navigating personal relationships. Many of our spirited debates have elucidated how passionate he is for conducting and communicating good science. I have certainly improved as a scientist, a mentee, and a mentor under him. To the members of my committee, Drs. Chris Doering, Nael McCarty, Khalid Salaita, and Roy Sutliff, I have to thank for helping to guide me and keep everything in perspective. It is hard to see the bigger picture when you are in the weeds. I would also like to thank Dr. Pete Lollar and Ernie Parker for their input and discussing experiments and analysis. I would also like to thank two major collaborators, Drs. X. Frank Zhang and Jonas Emsley, for their willingness to invest in my projects.

I must thank the members of the Renhao Li lab for teaching me and helping me with various experiments around the lab. The expertise of Drs. Yingchun Wang and Wenchun Chen have helped me troubleshoot many problems over the years. To my past and present fellow students, Ed, Sarah, and Emily, for being confidants and friends. To the technicians, Kayleigh and Moriah, and my mentee, Ally, for both helping me, teaching me, and allowing me to teach you. To the many other students on the floor and within my MSP cohort for their friendship and collaboration.

Table of Contents

List of Figures and Tables

List of Abbreviations

Hemophilia A (HA)
Coagulation factor VIII (fVIII)
Von Willebrand's Disease (VWD)
Von Willebrand factor (VWF)
Platelet-rich plasma (PRP)
Glycoprotein (GP)
Bernard-Soulier Syndrome (BSS)
Cysteine Knot (CK)
Trypsin inhibitor-like (TIL)
Von Willebrand factor type A/B/C/D/E domain (VWA/VWB/VWC/VWDD/VWE)
A disintegrin and metalloprotease with thrombospondin type motifs, member 13 (ADAMTS13)
N-terminal ligand-binding domain (LBD)
Thrombotic thrombocytopenic purpura (TTP)
Leucine-rich repeats (LRR)
Autoinhibitory module (AIM)
Extracellular matrix (ECM)
Mechanosensory domain (MSD)
Complementarity-determining region (CDR)
Fragment antigen-binding (Fab)
Fragment crystallizable (Fc)
Immunoglobulin (IgG)
Heavy-chain antibody (HCAb)
Tobacco etch virus (TEV)
Bio-layer interferometry (BLI)

Chapter 1

Introduction

1.1 Early history of von Willebrand factor

In 1924, a Finnish doctor by the name of Erik A. von Willebrand treated a young girl for incessant bleeding. Her family had a history of spontaneous bleeding, with several family members dying from catastrophic gastrointestinal bleeds. Despite normal platelet counts and normal procoagulant clotting time, family members would show prolonged bleeding times. Due to the inheritance of bleeding showing as a dominant trait, Dr. von Willebrand could rule out hemophilia A (HA), a recessive disorder characterized by a genetic deficiency of coagulation factor VIII (fVIII). Dr. Von Willebrand called the disorder hereditary pseudo-hemophilia (1). Patients presenting with this hereditary disease from then on were said to be diagnosed with von Willebrand's Disease (VWD).

It was many years until the missing plasma factor in VWD plasma was discovered. It was first realized that this plasma factor, now known as von Willebrand factor (VWF), is bound to fVIII. Dr. Theodore Zimmerman developed antibodies against purified fVIII and noticed that his antibody detection level varied in normal, VWD, and HA patients (2). Around the same time, researchers documented that platelet-rich plasma (PRP) from VWD patients responded differently than healthy PRP when exposed to ristocetin, an antibiotic that could induce profound thrombocytopenia, or low platelet count, in humans (3). A specific protein, then named fVIII-related antigen, was then identified and experiments demonstrated that reconstitution of VWD plasma with this factor would correct the response to ristocetin (4). Eventually, the adoption of 'von Willebrand factor' came about after identification of the protein not only in the plasma, but also in endothelial cells, megakaryocytes, and platelets (5-7). In 1985, four different labs independently cloned the entire cDNA of VWF (8-11). Dr. Evan Sadler carefully compiled the amino acid residues of VWF from his five cDNA clones and took note of several things (12).

First, he documented that VWF contains a signal peptide with a sequence similar to other known secreted proteins. Second, he noted that there were repetitive domains within VWF and named them A, B, C, D, and E respectively. He also commented on the existence of an integrin binding motif of RGDS in the one of the C domains and noted the cleavage site between two of the D domains had an identical sequence to several prodomain proteins that are cleaved following expression. This nomenclature was subsequently adopted and is used today, with the exception of the B domains, which are now known as C1 and C2. More specific domain boundaries were recently defined and assigned by Dr. Tim Springer (13). Functional tests of VWF revealed its involvement in contact between vessels and platelets, suggesting its importance to the initial events of blood coagulation (14). Other experiments also demonstrated that VWF must be immobilized onto the endothelial lining, which then allows platelets to be captured (15-17). Work from Drs. Evan Sadler, Zaverio Ruggeri, David Ginsburg, Tim Springer and others would further identify and isolate certain domains of VWF to be discussed below.

1.2 History of glycoprotein (GP)Ibα

In 1948, Drs. Jean Bernard and Jean Pierre Soulier described an inherited bleeding disorder in France (18). It was not until the 1970s until the receptor missing on the surface of platelets in Bernard-Soulier Syndrome (BSS) was identified. Around the same time as the initial laboratory investigations of VWF were being conducted, several labs were attempting to identify the protein content on the surface of platelets. Using both 1-dimensional and 2-dimensional gel electrophoresis, the major platelet receptors were being identified. Rather archaically, the size of each protein band on a gel was named according to its size, *i.e.,* the highest molecular weight would be glycoprotein I, the next II, and so on. Under reducing conditions, many of these bands would not be preserved indicating the usage of disulfide bonds to link subunits (19; 20). It was

identified by SDS-PAGE that patients with BSS were missing a major band. Similarly, patients with Glanzmann's thrombasthenia (weak platelets) were missing a different band (21). Using 2D reducing electrophoresis it was demonstrated that GPI was not a single protein, but two, and one of them was comprised of two subunits. GPIa is now known as integrin subunit α2. GPIb was shown to contain two subunits, named α and β which were linked by disulfide bonds (20). Using antibodies against GPIbα and immunoprecipitation of platelet lysates, it was further demonstrated that GPIX was associated with GPIb (22). Further approaches using milder detergents to solubilize the membrane revealed the presence of GPV in complex with GPIb and GPIX, which gives rise to the GPIb-IX-V complex that we know today (23). The previous citation suggested the organization of the complex with only one GPV and two GPIbα, two GPIbβ, and two GPIXs. It was later confirmed that the complex instead is formed by one GPIbα, two GPIbβ, one GPIX, and one GPV (24; 25) (Figure 1.1). The molecular pathogenesis of BSS was largely a mystery, as mutations in GPIbα, GPIbβ, and even GPIX nullified surface expression of the complex. Detailed work from my mentor, Dr. Renhao Li, identified that GPIbβ and GPIX are required for expression of GPIbα (26). Furthermore, a sequence in GPIbα is targeted for constant degradation by the proteasome, and GPIbβ and GPIX occlude this sequence from exposure to the proteasome (27). Any mutations in the transmembrane domains or juxtamembrane sequences that stop the assembly of the complex will therefore stop surface expression of the GPIbα subunit and render the platelets unable to bind to VWF.

Early studies of platelets mixed with preparations of bovine plasma 'revealed' bovine fibrinogen could agglutinate human platelets (28). Purification of fibrinogen (or VWF) from plasma will yield contamination with the other protein. BSS platelets exposed to this bovine fibrinogen did not agglutinate – and the lack of VWF binding to BSS platelets was confirmed

Figure 1.1

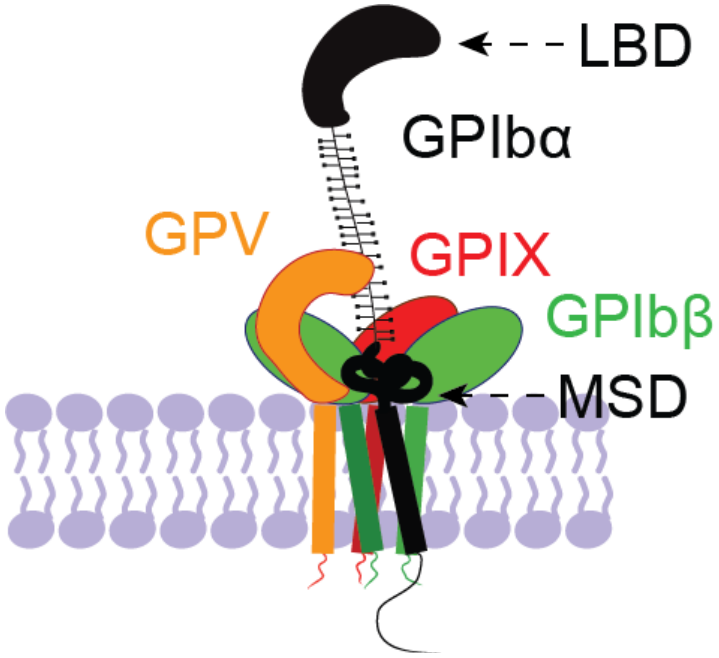

Figure 1.1 Subunit organization of the GPIb-IX-V complex. The GPIb-IX-V complex is comprised of transmembrane receptors GPIbα (black), GPIbβ (green), GPIX (red), and GPV (orange). There are two copies of GPIbβ per complex. The ligand binding domain (LBD) of GPIbα engages with VWF, thrombin, and other ligands. The mechanosensory domain (MSD) of GPIbα will unfold under force to initiate signaling of this complex. GPV is non-covalently associate with the complex.

after the discovery of the activating agent ristocetin (3; 29). Ristocetin is discussed in detail in Chapter 4. It was eventually identified that 1) VWF is responsible for binding to platelet GPIbα and 2) VWF must be immobilized or exposed to an activating agent in order to bind to platelets.

The intricate nature of the GPIb-IX-V complex made elucidation of its organization, expression, and functions incomplete until recently (30). Still, there is debate as to the relatively weak nature of GPIb-dependent platelet activation, the role of GPV in hemostasis (31), and how disruption (or stabilization) of GPIbβ can modulate GPIb signaling (32).

1.3 Structure and organization of VWF

VWF synthesis occurs, as for most extracellular proteins, in the endoplasmic reticulum. There, VWF is dimerized at intermonomer cysteines at the C-terminal cysteine knot (CK) of each respective monomer (33). The C-terminal dimers are further processed in the trans-golgi apparatus to form multimers, where intermonomer D'D3 assemblies form two additional disulfide bonds, giving rise to the concatemers of VWF (34). The D1 and D2 assemblies (also known as the VWF propeptide) that were used to assist in this process are proteolytically cleaved by furin, and the mature VWF is ready for temporary storage. The D1 and D2 assemblies are dissociated from the mature VWF upon exposure to the pH of blood (35). VWF is packaged in specialized organelles, primarily in Weibel Palade Bodies of endothelial cells, but also is packaged into the α-granules of platelets (36). In its mature form, VWF is organized from amino terminus to carboxy terminus D'D3-A1-A2-A3-D4-C1-C2-C3-C4-C5-C6-CK (37) (Figure 1.2).

The different domains of VWF each serve unique, and essential roles, as many mutations in various domains can lead to a variety of problems for maintaining hemostasis. The D'D3 assembly is comprised of a von Willebrand factor type D domain (VWDD), a trypsin inhibitor-like (TIL) domain, and a VWE domain. It serves not only as the basis for VWF multimerization,

Figure 1.2

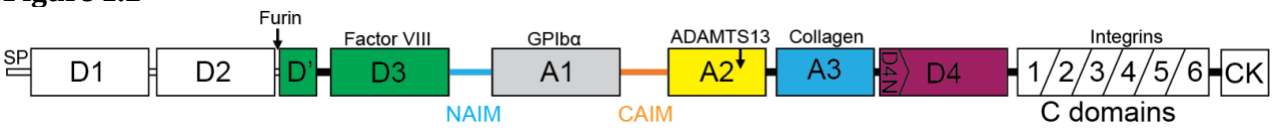

Figure 1.2 Overall organization of pre-pro-von Willebrand factor. The N-terminus of VWF contains a signal peptide for endoplasmic reticulum localization. The D1 and D2 assemblies help to mediate dimerization of VWF and are cleaved by furin. The D'D3 assembly forms head-head dimers with another monomer, as well as binds to fVIII in the plasma. The A1 domain mediates binding to GPIbα. The A2 domain can be cleaved by plasma ADAMTS13 to regulate VWF size. The A3 domain of VWF mediates attachment to collagen. The D4 domain helps to steer ADAMTS13 towards the A2 domain. The C-domains have no know function but can bind to integrins. The CK domain mediates multimerization of VWF.

but also acts as a chaperone and homing mechanism for fVIII. For every 50 VWF monomers, only one is occupied by fVIII, yet without VWF, the half-life of fVIII is reduced to a point where defects in coagulation are comparable to complete deficiency of fVIII (38; 39). It is no surprise that mutations in D'D3 that inhibit its interaction with fVIII give rise to a bleeding tendency and is classified as type 2N VWD (40). As VWF interacts with injured vessels, it will sequester fVIII to the site of injury. Thrombin will then activate and induce dissociation of fVIII from VWF to continue propagation of the coagulation cascade (41).

The A1 domain of VWF has been studied intensely as it is the domain in VWF which binds to platelets to mediate the initial steps of platelet capture. The A1 domain is first von Willebrand factor type A domain (VWA), sharing homology to other Rossman folds such as integrin I domains with alternating antiparallel alpha helices and beta strands (42). VWA domains are known for their roles in protein-protein interactions, and many contain metal ion dependent adhesion sites, although the A1 domain does not bind to any ions. A proteolytic and denatured fragment of full-length VWF starting from residue 1212 migrating at 48/52 kDa was found to bind to platelet GPIb (43). Further protease treatments and protein sequencing revealed a 39/34 kDa fragment (difference due to glycosylation) consisting of residues 1243 to 1481 contains the GPIb binding domain (44). Future experiments would demonstrate the intricacies of A1 binding to GPIb discussed below.

The A2 domain is a unique VWA fold in that it lacks a typical α4 helix and does not contain a long-range disulfide bond to hold the termini of the domain together. These two features enable the A2 domain to be completely unfolded under shear. A series of experiments from the Sadler Lab followed by confirmation in the Springer Lab demonstrated that the A2 domain unfolds under force by using optical tweezers to unfold full length VWF (45) or the

isolated A2 domain (46). This unique linearization allows for proteolytic regulation of VWF size by a disintegrin and metalloprotease with thrombospondin type motifs, member 13 (ADAMTS13) (47). ADAMTS13 will cleave the A2 domain only after A2 has been linearized, which serves as a useful shear-bolt mechanism to control VWF. This shear-based mechanism of control is discussed further below.

The A3 domain is a rather simple domain compared to its N-terminal neighbors. The A3 domain is the major collagen-binding domain of VWF (48). Interestingly, the A1 domain can also bind to collagen, but its contributions to hemostasis *in-vivo* are questionable (49). The collagen binding properties of A3 are not subject to the same level of regulation that the A1 and A2 are subject to, as VWF needs to be able to constantly survey vessels for exposed collagen to latch onto.

The D4 assembly is arguably the least studied of all the major domains. It shares homology to the other D assemblies but contains a so-called 'D4N' module that shares no homology to any known protein (37). The function of D4 is to steer the active site of ADAMTS13 towards the A2 domain, acting as a major binding partner of the protease (50). The shear-dependent nature of this interaction, and the specific mechanisms behind the recognition are currently under investigation in several labs. No structure of ADAMTS13 bound to D4 has been published to date.

The VWC domains 1 through 6 are oblong globules, highly reinforced with disulfide bonds to give VWF length but also make them resistant to proteolytic cleavage. There is no known function of the C domains, although C4 bears an RGD sequence, an integrin-binding site (13). This site can bind to integrin αIIbβ3 although its relevance and importance in thrombus formation are not completely agreed upon (51). The RGD found on fibrinogen is much more

important for platelets during clot formation (52; 53). Regardless, there is work to be done on the function of these domains.

The CK domain shares homology to TGF-β, containing many intradomain disulfide bonds as well as intermonomer disulfide bonds (33). The CK will dimerize any truncated forms of VWF as well, even those lacking the D'D3 assembly (54).

1.4 Von Willebrand's Disease

The functions of each domain of VWF serve important roles to regulate its adhesive properties. Within nearly all domains, mutations can be found that are deleterious to its function. Often the most impactful mutations are those which can nullify dimerization, or introduce aberrant cysteine residues, which can completely inhibit VWF secretion into the plasma. Other qualitative defects can modulate VWF's functions but can present with similar symptoms in the clinic. VWD is the most common bleeding disorder in humans, affecting roughly 1% of the population (40).

Type 1 VWD is the most common subtype of VWD, and simply indicates that the amount of VWF in the plasma is lower than normal (55). A homozygous slightly defective mutation that inhibits VWF secretion or folding may decrease VWF antigen levels. Type 1 mutations can be found in every domain of VWF. Type 1 can be difficult to diagnose, as blood groups as well as VWF clearance receptors or other factors outside of the VWF gene locus can affect VWF level (56).

Type 2 VWD is classified as a qualitative defect in VWF. Type 2 is complex and multifaceted, and is further subdivided into 2A, 2B, 2M, and 2N.

Type 2A is characterized by a near-complete loss of VWF multimerization. There are two main reasons why this loss of multimers may occur. The first reason for defective

multimerization are mutations in the D1-D2-D'D3 or CK domains that mediate multimerization (57). Furthermore, mutations in the A2 domain can constitutively expose A2 for cleavage by ADAMTS13 even under static conditions (57). There are even mutations in the A1 domain that may be classified as 2A, as misfolded A1 can greatly impact VWF multimerization (58). The molecular basis for A1 impacting multimerization is unknown but is likely due to incorrect formation of the long-range A1 disulfide bond, as mutations at residues C1272 or C1458 are classified as 2A.

Type 2B results from mutations in the A1 domain, or the autoinhibitory module (AIM) that surrounds A1, that increase the affinity of A1 for GPIbα (59). This increase in affinity paradoxically can result in bleeding, as the high molecular weight multimers of VWF are preferentially degraded in type 2B (60). Platelet-VWF complexes are more easily subjected to unfolding under low shear forces, aiding in ADAMTS13-mediated cleavage (61). Interestingly, all type 2B mutations found so far are in the A1 domain or AIM, and furthermore all seem to destabilize a region surrounding the disulfide bond that holds the A1 domain together. I discuss how 2B mutations could potentially also decrease the autoinhibition of VWF in later chapters.

Type 2B cannot be mentioned without discussing platelet-type (PT) VWD. Mutations within GPIbα can also increase the affinity of platelets for VWF (62). These mutations all cluster in the N-terminal ligand-binding domain (LBD) of GPIbα (63; 64). The clinical presentation is the same as 2B, yet treatment of PT VWD with DDAVP or desmopressin to increase VWF levels can be catastrophic. This treatment in PT VWD will only lead to further thrombus development, platelet activation, and platelet clearance (65). It is therefore important to confirm 2B VWD or PT VWD by genetic sequencing before treatment options can be considered.

Mutations that cause type 2M affect VWF-GPIbα interactions, or VWF-collagen interactions, resulting in severe defects of primary hemostasis. To this end, mutations in either A1 or A3 impact the binding of VWF to platelets or collagen (66). Type 2M VWF will circulate at normal levels and contain normal multimeric patterns. However, it will show little to no GPIb-binding activity or collagen binding activity.

Given the importance of VWF to fVIII half-life, it is no surprise that mutations in the D'D3 assembly can yield coagulation specific defects due to fast fVIII clearance and decreased concentrations in the blood. 2N clinically presents as hemophilia-like, but can be confirmed by fVIII and VWF antigen testing followed by fVIII:VWF binding assays (67).

Type 3 VWD is a rare condition where the circulating VWF concentration is, for all intents and purposes, zero. No Type 3 mutations have been found in the A2 or A3 domains but may be present in all other domains. There are usually homozygous defects in VWF assembly or secretion that prevent any VWF from entering the blood stream (68). Patients with type 3 will need replacement factor or plasma infusions to correct for the inability to control primary hemostasis.

1.5 Activation of VWF and the VWF-GPIbα interaction

VWF must adopt two distinct states in regard to its adhesive abilities. Each state is equally important, and spatiotemporal regulation of each state is what makes the function of VWF so unique. The first state, autoinhibited VWF, is that of a quiescent protein. Isolated blood that is gently manipulated or flowing through the blood stream does not spontaneously bind to platelets. The second state is activated VWF. This VWF is capable of binding to platelets with high affinity to mediate platelet capture at high shear stresses. This section will discuss these states,

and most importantly the transition between them. The regulation between these states is of paramount importance for the maintenance of hemostasis.

The length, or size of VWF, is the most important determinant of its hemostatic ability. The force that a polymer experiences under shear or elongational flows will differ depending on the length of the polymer (69). VWF multimers largely recapitulate the behavior of a polymer under flow (38; 70). VWF that is too long, such as in ADAMTS13-deficient blood, will be easier to activate under force. Typical forces that would not activate VWF may therefore cause unwanted platelet accumulation. Thrombotic thrombocytopenic purpura (TTP) occurs as a result of this ultra-large VWF, resulting in platelet-VWF complexes that can infarct small vessels in the brain, liver, lung, and kidney, resulting in organ failure, and even death (71). TTP survival rates were shockingly low before the introduction of plasma exchange, at around 10% (72). VWF that is too short will result in bleeding (see Type 2A VWD above). Multimers that contain only a few monomers will not be able to respond to force in order to unfold and expose the A1 domain. ADAMTS13 based regulation of VWF size through cleavage of A2 is arguably the most important physiological regulator of VWF activity from a global perspective. On a molecular basis, the binding of GPIbα to VWF is more complex, as discussed below.

The GPIbα LBD is comprised of seven leucine-rich repeats (LRR), flanked by an N-terminal cap that contains one disulfide bond and a C-terminal cap with disulfide knots. The LBD differs from a canonical LRR-containing protein with the presence of a loop structure, also known as the thumb or β-switch, that extends from the C-terminal cap (73). The VWF A1 domain is a globular Rossman fold where its conformation is stabilized by an intrachain disulfide bond between C1272 and C1458 (74). In the crystal structures of the LBD-A1 complex, binding of the A1 domain to the concave face of the LRR is mediated by long range electrostatic interactions of

two discontinuous regions on each protein (75; 76). The primary binding site is located between the central β3 strand of A1 and the β-strands in the LBD thumb region to form an extended β-sheet complex. Meanwhile, the secondary binding site is located between the first LRR of GPIbα and the α1β2, β3α2, and α3β4 loops toward the bottom of the A1 (Figure 1.3) (75; 76).

Type 2M mutations that inhibit or abolish platelet-VWF interactions can be found in the β-strand on A1 that interacts with GPIbα (40). All mutations that give rise to platelet-type (PT) VWD localize in the β-loop of the thumb region of GPIbα (63), whereas mutations that are classified as type 2B VWD localize near the hydrophobic base of the A1 body and the adjacent flanking regions, distal from the binding interface (37; 77). In either case, there is increased binding between platelets and VWF, leading to premature platelet activation, unfolding of the A2 domain, excessive cleavage of VWF, and increased clearance of VWF due to VWF-platelet complexes (60; 61). Thus, the formation of the LBD-A1 complex is tightly regulated to properly carry out hemostasis *in-vivo*.

Under normal physiological flow conditions, VWF multimers in the plasma exhibit essentially no affinity for platelets. This low affinity is consistent with reports of VWF or many A1 domain-containing recombinant fragments having binding affinities for the GPIbα LBD around 1-30 μM (78-81), as the physiological plasma concentration of VWF is around 60 nM (82), thus receptor occupancy (VWF binding) is negligible at this low concentration. Only upon activation can multimeric VWF efficiently bind the LBD of GPIbα. High shear force is a critical factor in regulating the GPIbα-VWF interaction. After immobilization to the vessel wall and above a critical shear force under flow, VWF becomes elongated due to the polymeric shape of VWF. Subsequently, the A1 domain therein becomes exposed and ready to bind platelet bound GPIbα

Figure 1.3

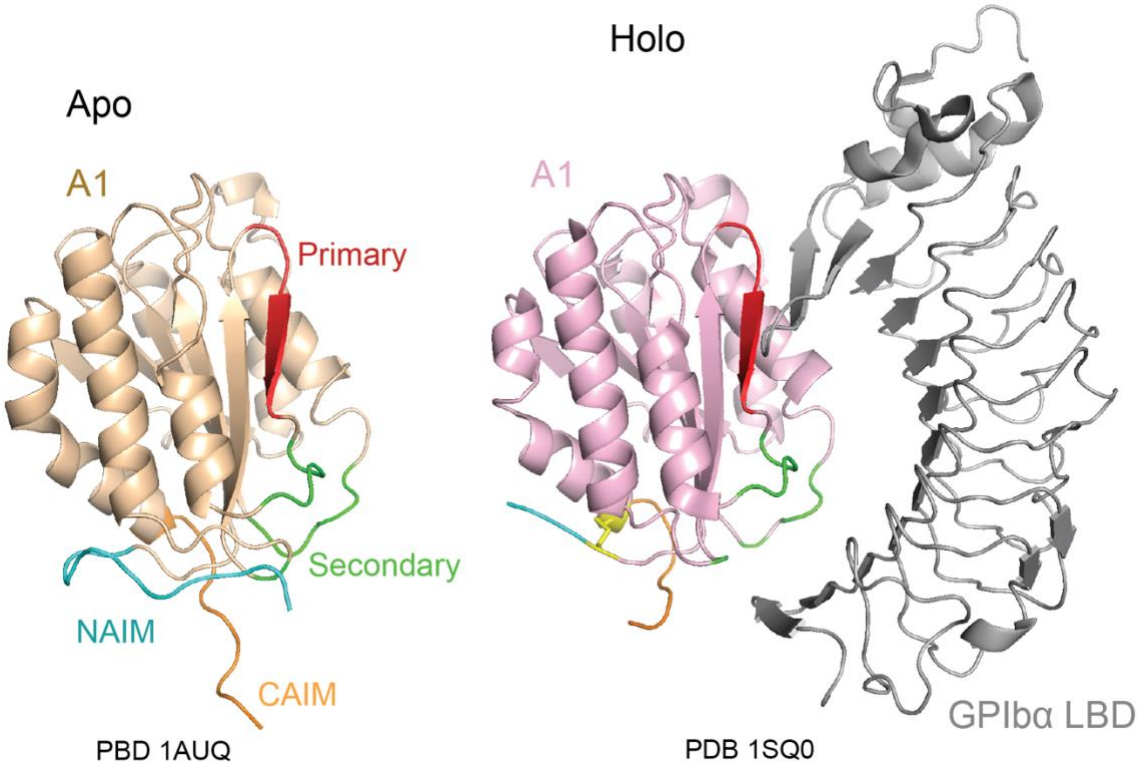

Figure 1.3. Crystal structures of A1 and A1 bound to GPIbα. The A1 domain shown to the left was crystallized alone (74). Not all residues in the crystallized protein are visible in the electron density. The primary binding site β strand is labelled in red, the secondary binding site loops are labelled in green. The NAIM is displayed in cyan, while the CAIM is displayed in orange. The AIM and some of the secondary binding loops adopt a different conformation when bound to the LBD on the right (83). The β-switch forms and extended β-sheet from the primary binding site (red), while residues on the lower section of the LBD interact with the flexible loops (green) in the secondary binding site.

(37; 84). The molecular mechanism of A1 exposure has been a point of contention over the last several decades.

The interaction between GPIbα and VWF is dominated by a fast off rate without sustained shear force to keep A1 exposed. Typical sensorgrams in surface plasmon resonance assays of immobilized LBD binding to A1 are characterized by immediate equilibrium, typical of fast dissociating complexes (85). Pathological mutations in either A1 or LBD decrease the dissociation rate of this interaction, as seen by prolonged platelet pause times on VWD type 2B mutant A1 (86; 87). In either case, the exposure of A1 can likely increase the on rate, as supported by the increased affinity of truncated A1 (1261-1472) compared to longer 1238-1472 and 1238-1493 fragments (88; 89). In this scenario, truncation may simulate shear dependent exposure of A1, allowing for GPIbα to interact at nanomolar concentrations. Once exposed A1 binds the LBD, the drag force exerted on the arrested platelet under flow creates a pulling force on this bond, and above 10 pN of force, the interaction switches between a typical slip bond to a catch bond (90). Upon the application of force, a slip bond will weaken, in contrast to a catch bond that strengthens to a certain degree of increasing force. The switch to a catch bond may be critical for VWF to be able to capture platelets long enough to unfold the GPIbα mechanosensory domain, leading to platelet activation (91-93).

The molecular basis underlying the LBD-A1 catch bond may occur due to conformational changes in either the LBD and/or A1. For the LBD, stretching of LRRs under force may push the concave domain closer to A1, allowing for a larger binding interface (94; 95). Interestingly, no crystal structures have revealed a direct contact between the middle LRRs and A1, but substitutions in the middle LRRs greatly diminish the GPIbα-VWF interaction under shear (94; 95). At the same time, A1 may adopt a high-affinity conformational state under force, although this has yet been

shown experimentally. The only bond over which force would directly be applied to through A1 would be across the disulfide bond. It has been shown that the inclusion of ristocetin can shift the slip-to-catch behavior into low force regimes and increase the force resistance of this interaction (90). Furthermore, PT and type 2B VWD mutations also push the slip-to-catch transition into low force regimes, as well as stabilize this interaction state, a molecular explanation for the increased off rate (96).

How the elevated shear induces VWF activation remains incompletely understood. A recent demonstration of shear-dependent VWF activation and binding of GPIbα uncovered that flow-induced elongation of VWF multimer precedes its activation (97). In other words, VWF can elongate while remaining inactive. Only above a certain force threshold does VWF truly activate, likely due to disruption of local elements around A1 that unfold under such force (97). Other recent studies, described in this dissertation, suggest that such mechano-sensitive local elements likely contain adjacent domains and/or regions flanking the A1 domain. Tensile force induces the dissociation of the elements from A1 and exposes A1 for platelet binding. However, the structure of these autoinhibitory elements and single-residue level details of activation remain elusive.

A number of factors have been reported to induce VWF binding to the LBD of GPIbα in the absence of elevated shear. Earlier mutagenesis studies sought to delineate binding regions for GPIbα and modulators such as ristocetin and botrocetin. These studies suggested that the acidic flanking regions of the A1 domain (*i.e.* residues outside the 1272-1458 disulfide bond), as well as residues just within the confines of the disulfide bond, play an inhibitory role in GPIbα binding (98). The flanking regions are rich with prolines, charged residues, and contain 4 O-linked glycosylation sites per flanking region (99). Primarily thought as intrinsically disordered sequences, they have been implicated to modulate VWF binding to GPIbα. Mutagenesis studies in

full-length VWF constructs reported that deletion of the N-terminal flanking region enabled VWF-GPIbα association and decreased multimer formation. Deletion of either N- or C-terminal flanking regions proximal to the 1272-1458 (Fig. 1.4) disulfide in combination with an arginine to alanine substitution at the base of the A1 domain (residue 1308) resulted in enhanced binding of recombinant human VWF to platelets (100). This marked increase in binding was further enhanced by ristocetin (100). Furthermore, deletion of residues 1238-1260 from a recombinant A1 fragment created a highly active A1 (1261-1472) (75; 88; 90; 101). In the absence of shear stress this fragment could bind the LBD, and inclusion of a 1238-1260 peptide could inhibit binding to platelets under flow (101). These reports and other evidence (102) suggest that flanking residues proximal to the 1272-1458 disulfide bond form specific interactions with the A1 domain to regulate VWF binding to platelets and subsequent platelet activation in the bloodstream. Interestingly, insertion of a highly glycosylated sequence into the N-terminal flanking region, but not the C-terminal flanking region, resulted in a full-length variant that displays all hallmarks of a type 2B variant (103).

The N-terminal flanking region has been implicated in both the regulation of the LBD-A1 interaction, as well as bond kinetics. Further investigation in an A1-A2-A3 construct showed similar effects as isolated A1, where a protein beginning at E1260 could support platelet adhesion on a collagen substrate, but the same protein starting at Q1238 showed markedly decreased platelet adhesion (104). The importance of the N-terminal flanking region also lies in bond kinetics. The investigation into the unbinding force between GPIbα and A1 using 1238-1471 versus 1261-1471 showed differences in catch-bond behavior, where deletion of the N-terminal linker abolished flex-bond behavior instead of shifting the interaction to only slip bond behavior (105). Interestingly, collagen-bound A1 appears to enhance affinity for GPIbα and prolong bond lifetimes (106).

Figure 1.4

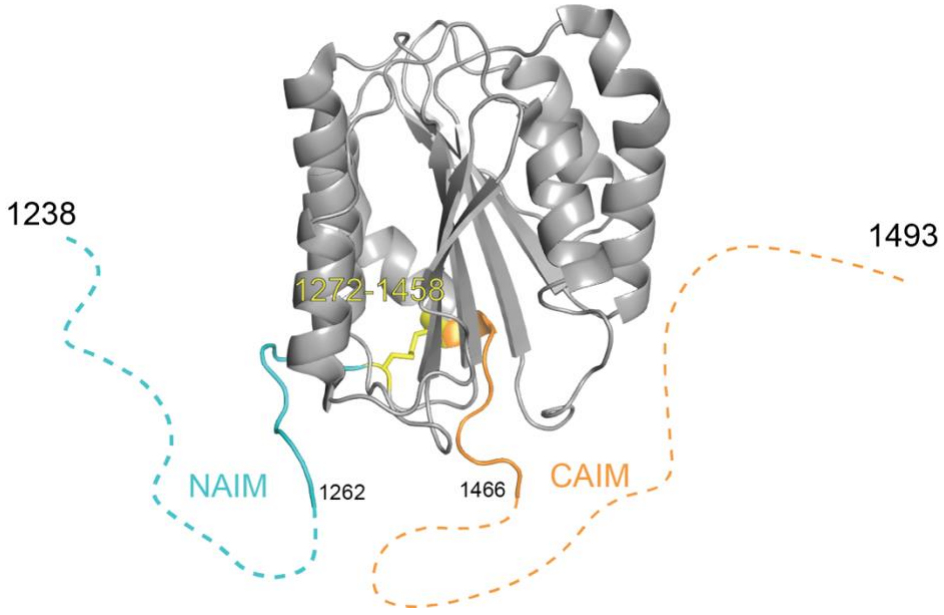

Figure 1.4. Layout of AIM-A1 with unresolved residues. Structure of AIM-A1 found in PDB 7A6O. The A1 domain (grey) is delimited by a disulfide bond (yellow) between residues 1272 and 1458. The NAIM residues (cyan) from 1238-1261 are unresolved. CAIM residues (orange) from 1467 to 1493 are unresolved.

Although much evidence has been shown that the N-terminal linker serves an inhibitory function, specific residues responsible for the inhibition remain largely unclear. An investigation into the negatively charged aspartic acid of 1261 revealed its importance in inhibitory function (102). Charge reversal of this residue yielded an A1 species that greatly decreased platelet translocation due to reversal of A1 inhibitory function and enhanced platelet capture. Furthermore, it is apparent that the entire linker sequence is important for its inhibitory function, as gradual truncation of this linker decreased platelet adhesion, again representative of increased ability to bind GPIbα and capture platelets (102).

A recent study of the dynamics of flanking regions of the A1 domain by hydrogen-deuterium exchange mass spectrometry suggests that both N- and C-terminal flanking regions may cooperatively form a structured autoinhibitory module (AIM) that masks the A1 domain, especially the secondary binding site therein, and thereby impedes its interaction with GPIbα (88). Consistently, while a recombinant A1 fragment containing residues 1238-1493 exhibits a poor binding affinity for GPIbα, removal of either N-terminal (1238-1270) or C-terminal (1462-1493) regions yield proteins capable of binding GPIbα with apparent K_D in the tens of nanomolar range (78-80; 88; 89). Furthermore, it is worth noting that all type 2B VWD mutations identified to-date localize within the A1 domain and in both flanking regions (37; 88). Exogenous factors, such as botrocetin, a snake toxin, and ristocetin, a bacterial glycopeptide (107), can induce spontaneous GPIbα-VWF interaction, although through different mechanisms. Botrocetin forms a ternary complex with LBD and A1, thus facilitating their interactions (108). In fact, botrocetin binds to many species' platelets and VWF, indicating its evolution as a broad-spectrum activator of GPIb. In comparison, ristocetin appears to bind a sequence in the C-terminal and possibly also N-terminal flanking region and induces the exposure of A1 for GPIbα binding (88; 107). Ristocetin shows

much variation in binding to the VWF from different organisms. Ristocetin shows no effect on mouse plasma, and also shows reduced activity towards ancestral sequence reconstructed VWF proteins that bear changes in the residues from 1459 to 1475 (109). There is also genetic evidence from naturally occurring substitutions in human genes to support that ristocetin binds to this region. VWF that contains the D1472H or P1467S polymorphisms, despite their VWF and platelet function remaining normal, show low ristocetin based VWF activation (110; 111).

Following these studies, it has remained contested whether the flanking residues regulate binding through specific interactions with A1 or through steric hinderance, and how O-linked glycosylation sites on VWF play into the picture. Changes in glycosylation, particularly variation in ABO(H) blood groups, have been linked to variable levels and activities of plasma VWF (112; 113). Desialylated plasma derived VWF can bind platelets without agonist to induce spontaneous platelet aggregation and this response is dependent on the A1-GPIbα interaction (114). Recently, a group has posited that the O-linked glycans on VWF sterically hinder GPIbα binding rather than maintaining or contributing to a more specific structural role (85). However, steric hindrance as a mechanism does not fully encompass previous observations of enhanced sensitivity to ristocetin in targeted mutations of glycosylation sites (107; 115; 116). Furthermore, we recently demonstrated that removal of the sialic acid moieties on the terminal ends of these O-glycans in the AIM can activate A1 (117). Therefore, studies investigating the presence of inherent structural elements between flanking residues and the A1 domain remain imperative for a thorough understanding of the mechanisms guiding complex formation between A1 and GPIbα.

In addition to flanking regions, neighboring domains of A1 have been implicated in regulation of its interaction with GPIbα. VWF constructs lacking the D'D3 assembly can cause platelet agglutination at low concentrations of ristocetin, similar to multimeric VWF bearing type

2B mutations. Furthermore, the monoclonal antibody 1C1E7, which targets a region around residue Lys968 in D'D3, could induce platelet aggregation (118). Conversely, antibodies targeting the residues 1222-1235 in the E3 module of D3 were able to inhibit both ristocetin- and shear-induced platelet aggregation (119). Further investigation demonstrated that deletion of D'D3 or disruption of its presumed interaction with A1 leads to an increased affinity of VWF to GPIbα and presentation of a TTP-like phenotype *in-vivo* (103; 120). These studies suggest that the D'D3 assembly partly regulates A1 exposure. A2 may bind A1 and inhibit its activity in thrombus formation (121; 122). A recent study pointed to a potential role of the vicinal 1669-1670 disulfide bond on A2 as recombinant A2 without the disulfide, but not one with, can bind A1 and inhibit its interaction with the platelet (123). It has also been suggested that this disulfide can act as a brake for the initial denaturation of the A2 domain under force (46).

The interaction between GPIbα and VWF is essential for the rolling of platelets along the injured vessel wall, where the extracellular matrix (ECM) and collagen become exposed to circulating blood (15; 124; 125). The immobilization of VWF through its A3 domain and capture of platelets brings them in close proximity to the ECM. Thus, through the GPIbα-VWF interaction, platelets gain ample time to interact with the ECM and become activated at the injury site, which also involve GPVI activation via collagen binding and integrin αIIbβ3 activation (124-126).
The GPIb-IX-V complex has been considered as a major shear-sensor on the platelet surface (124). How GPIb-IX-V senses shear force and transduces mechanical information into intracellular signals remained unsettled, until the identification of a juxtamembrane shear sensor in GPIbα, called the mechanosensory domain (MSD) (91). VWF binding to platelets under physiological shear generates a pulling force on GPIbα and induces unfolding of the MSD

therein, which sets off GPIb-IX-V-mediated signaling into the platelet (92). An overview of VWF activation, platelet adhesion, and thrombosis is shown in Figure 1.5.

1.6 Single-domain antibodies

The discovery and subsequent methods to produce antibodies to specific targets was a quantum leap forward for science. The ability to immunoprecipitate, identify, and purify the protein antigens of antibodies have led to countless discoveries and Nobel Prizes. Antibodies are comprised of an antigen recognition domain, or the Fab (Fragment antigen binding) and a Fc section (Fragment crystallizable). Together, a dimeric Fc with heavy chains forms a disulfide linked tetramer with two light chains to form an immunoglobulin (IgG). In humans, as with most other mammals, the pairing of a heavy chain to a light chain generates considerable diversity, as 6 complementarity determining regions (CDRs) contribute to antigen recognition and binding. In 1993, a study using sera from camels was fractionated using traditional antibody binding resins coupled with protein A or G to purify their IgG (127). The camel sera contained an extra heavy chain-based band, of around 100 kDa, along with a band of around 150 kDa which is expected for normal IgG. The authors further investigated this heavy-chain only antibody and confirmed that this type of antibody was generated in response to viral infection. The authors were able to identify that there were three distinct VH families by sequencing. The IgG1 subclass was comprised of a traditional, four chain IgG. The IgG2 and IgG3 families contained two heavy-chain only proteins, connected by either a short (IgG3) or a long (IgG2) hinge region, before converging into an Fc. The authors noted that these heavy chain antibodies (HCAb) had slight differences in sequence where the light chain would normally interact with the heavy chain, suggesting that these antibodies are indeed soluble and functional. These camel derived HCAbs were found to occur in animals in the *Camelidae* family such as llamas and vicuña. Remarkably,

Figure 1.5

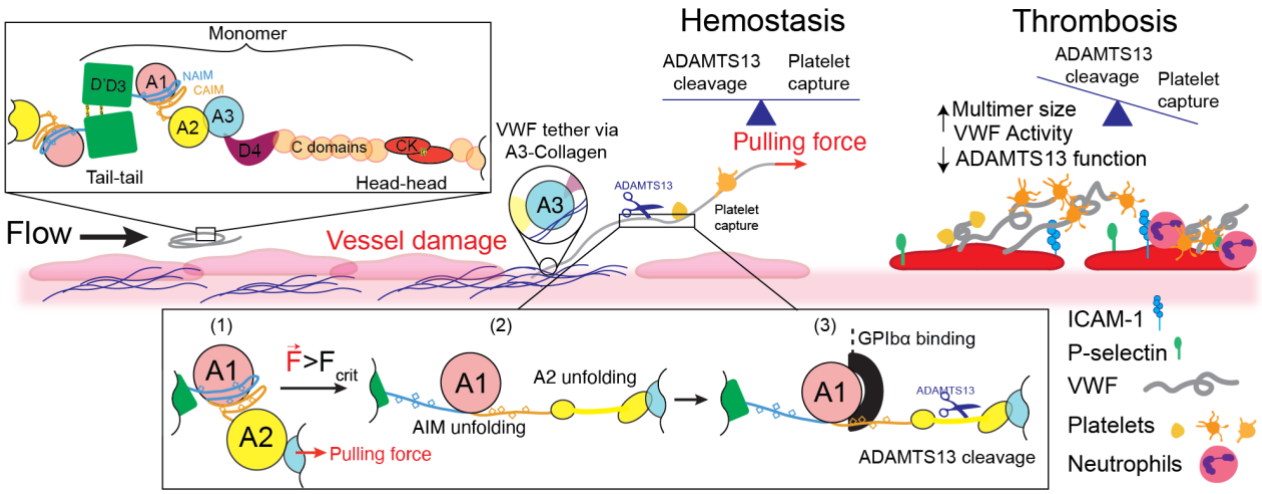

Figure 1.5 Molecular activation of VWF and the balance between thrombosis and hemostasis. A schematic of the domain structure of VWF is shown in the left box. Upon endothelial disruption due to injury, sub endothelial collagen will become exposed, facilitating the localization of VWF to the site via its A3 domain. VWF will begin to unravel under the force of the flowing blood, which causes two conformational changes to occur. This process starts as (1) is VWF still bound together by potential intra and interdomain interactions. A pulling force along the spine of the VWF will lead to (2) where there are local unfolding events in the AIM as well as the A2 domain. In (3), the consequences of these unfolding events can be seen as now GPIbα can recognize the A1 domain, and ADAMTS13 can bind and cleave the A2 domain. In hemostasis, the balance between platelet capture and VWF cleavage is maintained. Thrombosis can be cause due to VWF, such as in TTP, or VWF may instigate further thrombosis in inflammatory diseases. In these states, ultra-large VWF can be secreted, which can lead to immune cell recruitment and activation, which further inflames endothelial cells, which in turn will express more adhesive receptors and secrete more VWF.

antibodies resembling the *Camelidae* HCAbs can be found in nurse sharks and are a result of convergent evolution (128).

The antigen recognizing sequence of a HCAb is referred to as a VHH domain, and an isolated VHH separate from the Fc is called a single-domain antibody or nanobody. I will use VHH and nanobody interchangeably in this dissertation. Nanobodies have particularly favorable biochemical properties compared to VH-VL paired fragments, scFvs (Single-chain variable fragments), or Fabs given their small size, high stability, and ease of production (Figure 1.6).

A nanobody is of a typical immunoglobulin V domain fold with nine β-strands and three antigen-binding hypervariable, CDR loops. To compensate for the missing VL for antigen surface binding, nanobodies possess considerably longer CDR loops, specifically CDR3 can contain over 20 residues. In fact, the third CDR loop will often contain its own secondary structure and can even form inter-loop disulfide bonds with CDRs 1 or 2. The oblong nature of the VHH lends it to binding into pockets, such as in the active site of an enzyme, whereas antibodies tend to bind to more planar, flat surfaces or can bury a peptide (129). There are exceptions to these features as discussed in Chapter 4. Nanobodies are remarkably stable, often resisting unfolding at 2 M urea and certain nanobodies can survive temperatures up to 95°C (130). Nanobodies can also be selected for their resistance to pH induced unfolding and lack of proteolysis by pepsin or trypsin due to their high stability (131).

Production of nanobodies can be performed in microorganisms, typically in the periplasmic space as the reducing nature of bacterial cytoplasm will not form the necessary disulfide bonds that stabilize the nanobody. Intrabodies, or nanobodies that can be expressed in the cytosol without a disulfide bond have been produced to target intracellular proteins (132). The development of bacterial strains that express thiol isomerases and folding chaperones have

Figure 1.6

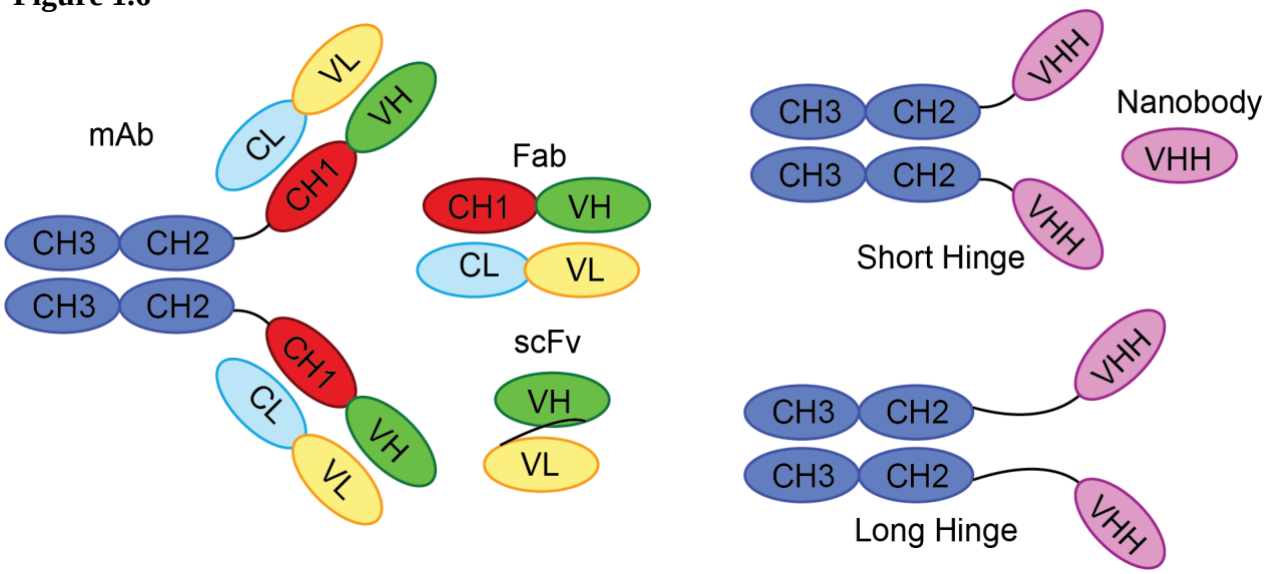

Figure 1.6. The structure of immunoglobulins found in *Camelidae.* Typical tetrameric IgG (mAb) is shown on the left, with constant heavy (CH) or constant light (CL) assembling to present the variable regions (VL or VH). Truncations of the Fc (CH3 with CH2) will yield a Fab, while production of an scFv involves production of the VH and VL fused together with a linker. HCAbs are found with two different linkers, and production of the VHH domain alone will yield a small antigen recognizing nanobody.

been used to produce nanobodies in the cytoplasm of bacteria (133). Indeed, my own experience has shown that production of a monomeric form of caplacizumab in the periplasm may yield 2 milligrams per liter of culture, whereas cytoplasmic production can yield 50+ milligrams per liter. Fermentation and optimization of culture nutrients, expression time, temperature, and induction conditions can yield grams per liter. Mammalian or yeast based secreted expression of nanobodies also is feasible depending on the application. Nanobody fusion proteins may also be useful for certain applications, such as fusion to albumins or carrier proteins. The production of nanobodies fused to an IgG-Fc will enhance their half-life due to FcRn receptor recycling, as well as bring the molecule above the renal filtration limit. Nanobodies are rapidly cleared from systemic circulation by the kidneys as they are quite small, and I have observed half-lives on the order of minutes for regular nanobodies after intravenous administration into mice.

Nanobody genes are easily extracted from peripheral blood mononuclear cells, with production bleeds of 50 mL from alpacas yielding roughly a million VHH genes. Generation of VHH only genes is difficult, as the sequence of traditional VH genes will contaminate the preparation. Luckily, the hinge regions differ greatly between VHH and VH families, and VHH only can be isolated using specific primers (134). A nested PCR approach can be used but can result in library bias and reduction of diversity (135). Isolation of antigen specific binders can be achieved using display technologies, such as on the surface of filamentous phages (136) or yeast. The laboratories led by Drs. Jan Steyaert, Brian Kobilka, and Andrew Kruse have pioneered methods to develop nanobodies against fragile, unstable, and membrane proteins using yeast display (135; 137; 138). Yeast display of antibody fragments was first proven feasible by Dr. Dane Wittrup, who used the yeast mating receptor A-agglutinin, Aga1p and Aga2p, to ‘display’ scFvs on the surface of yeast (139; 140). Aga1p is a surface anchored protein that forms multiple

disulfide bonds with the secreted portion of Aga2p. Fusing an scFv, or any other protein, to the Aga2p subunit will allow for the protein to be displayed on the yeast. Yeast display may be particularly advantageous over phage display as yeast do not display poorly folded proteins. Furthermore, yeast display uses fluorescence-activated cell sorting to generate quantitative sorting protocols to isolate high affinity binders. Furthermore, the desired antigen does not need to be immobilized to an immunotube or ELISA plate, which may denature or unfold certain proteins. Yeast will display around 4 to 5 thousand copies of Aga2p, which also aids in isolation of binders due to avidity effects. Other methods have been developed to display proteins, such as using a directly surface-anchored protein with an extremely long linker (138). Diversification of naïve libraries can be achieved using error prone PCR or building a library using NNK/NNS codons to completely randomize amino acids in CDR loops as desired (139). Recently, a method was developed such that yeast will replicate nanobody-bearing plasmids using a particularly inaccurate polymerase, such that affinity maturation is done in yeast, instead of extracting genes and subjecting them to PCR (141).

Nanobodies are currently used in the clinic and countless others are in clinical trials to treat a variety of indications (142). Ablynx, since acquired by Sanofi, developed a dimeric nanobody targeting VWF to treat TTP, which has seen some success, but also is often cost-prohibitive despite the production method from fermented bacteria (143). The method of action and structure of this nanobody, caplacizumab, in complex with VWF is a subject of Chapter 2. Nanobodies are largely non-immunogenic, although methods to humanize certain framework residues are usually employed (144). Their fast clearance is also advantageous in imaging applications for diagnostic purposes, as excess nanobody will be quickly eliminated through the urine (145). Owing to their favorable biochemical properties and expiration of crucial patents in

the next few years, nanobodies, fusion proteins, nanobody-drug conjugates, and CAR-T cells bearing nanobodies will generated to treat a variety of diseases. It is unlikely they will displace monoclonal antibodies, but likely will contribute to the fast-growing biologics treatment modality.

1.7 Outstanding questions

The lack of clarity surrounding the VWF activation mechanism is a large motivator for the following studies. Disparities in the types of VWF fragments used and technologies used to interrogate them have led to perhaps more confusion than clarity. It is known that deletion of certain sections around A1, especially residues upstream of this domain, can lead to VWF activation (104; 146). However, the 'N-terminal linker' hypothesis does not explain why ristocetin can activate VWF, as ristocetin binds to the 'C-terminal linker' (147). Furthermore, ristocetin largely mimics shear-dependent VWF activation, further confounding why only deletion of parts of the N-terminal linker can activate A1 (147). Therefore, we needed to take a systematic approach to understand the impact of the entire sections from 1238 to 1268 and 1461 to 1493. We sought to determine a universal molecular mechanism that can explain how VWF is autoinhibited in flowing blood but can quickly capture platelets when necessary.

These studies seek to explain both VWF autoinhibition, as well as force-dependent activation. Previous studies have been unable to demonstrate precisely where in VWF a conformational change occurs to activate it. We can suspect that the N- and C-terminal linkers, which we call the AIM, play a crucial role based on results from previous studies (88). However, we needed to demonstrate that the AIM unfolds under force, that the force is physiologically relevant, and that deletion of the AIM (either NAIM, CAIM, or a mixture of both) can mimic force-dependent activation. We also sought to tie in genetic evidence that the AIM is crucial to

VWF autoinhibition. Thus, we explore the impact of gain-of-function, type 2B VWD mutations on the AIM. We also interrogate VWF activity in the presence of certain modulators that we suspect bind to the AIM. In later chapters we specifically generate novel modulators to the AIM using nanobody discovery. We selectively isolated nanobodies that bound to either the NAIM or CAIM and investigated their function.

Approaching the question of force-dependent VWF activation from several orthogonal approaches allows us to stand firmly behind our results when in agreement with each other. Through the use of fundamental biochemical measurements, crystallography, single-molecule force spectroscopy and platelet activation assays we probe the function of the AIM from macroscopic to microscopic levels. In these studies, we aim to demonstrate the importance of a reductionist approach to understanding protein structure and function, as well as the utility of developing novel binders to further interrogate how VWF works.

Chapter 2

Activation of von Willebrand factor via mechanical unfolding of its discontinuous autoinhibitory module

This research was published in *Nature Communications*.

Nicholas A. Arce, Wenpeng Cao, Alexander K. Brown, Emily R. Legan, Moriah S. Wilson, Emma-Ruoqi Xu, Michael C. Berndt, Jonas Emsley, X. Frank Zhang and Renhao Li

Nature Communications, 12, Article number: 2360 (2021)

N.A.A., E.R.L., and M.S.W. cloned and generated VWF fragments; N.A.A. performed BLI experiments, produced, and ran experiments with VHH81 and 6G1; W.C. performed single-molecule experiments; N.A.A. and E.R.L. ran platelet aggregometry experiments; A.K.B., E.X., and J.E. crystallized and refined structures; M.C.B. provided critical reagents; X.F.Z. and R.L. designed the research; N.A.A., W.C., X.F.Z., J.E., and R.L. analyzed the results; N.A.A., W.C., J.E., X.F.Z., and R.L. prepared the figures; N.A.A. and R.L. wrote the paper; all authors edited the paper.

2.1 Abstract

Von Willebrand factor (VWF) activates in response to shear flow to initiate hemostasis, while aberrant activation could lead to thrombosis. Above a critical shear force, the A1 domain of VWF becomes activated and captures platelets via the GPIb-IX complex. Here we show that the shear-responsive element controlling VWF activation resides in the discontinuous autoinhibitory module (AIM) flanking A1. Application of tensile force in a single-molecule setting induces cooperative unfolding of the AIM to expose A1. The AIM-unfolding force is lowered by truncating either N- or C-terminal AIM region, type 2B VWD mutations, or binding of a ristocetin-mimicking monoclonal antibody, all of which could activate A1. Furthermore, the AIM is mechanically stabilized by the nanobody that comprises caplacizumab, the only FDA-approved anti-thrombotic drug to-date that targets VWF. Thus, the AIM is a mechano-regulator of VWF activity. Its conformational dynamics may define the extent of VWF autoinhibition and subsequent activation under force.

2.2 Introduction

Virchow's Triad describes the interplay between three broad categories of factors — blood, vessel, and flow — that contribute to thrombosis. Von Willebrand factor (VWF), a large, concatenated plasma glycoprotein (37), is a canonical embodiment of such interplay. It is primarily secreted from endothelial cells lining the blood vessel, and it critically mediates hemostasis, thrombosis and thromboinflammation by sensing and responding to changes in blood shear flow (148-150). Under low shear conditions, plasma VWF is autoinhibited and does not bind glycoprotein (GP)Ibα, the major subunit of the platelet GPIb-IX complex. However, when VWF is either exposed to elevated shear or immobilized under flow, it experiences tension and subsequently exposes its A1 domain for binding to GPIbα and the platelet (84; 97; 151). The binding transmits a signal into the platelet that leads to platelet aggregation and clearance (15; 92; 152; 153). Pathological binding of VWF to platelets in circulation could lead to microthrombosis, thrombotic thrombocytopenia, and sometimes organ failure (40; 154). Understanding the mechano-activation mechanism of VWF is key to elucidate the pathophysiology of thrombotic diseases and to develop safe anti-thrombotic therapeutics.

It has been documented for more than 30 years that under several conditions independent of flow change, VWF can overcome its autoinhibition and bind to GPIbα with high affinity. These conditions are present in some disease states, the most notable of which is type 2B von Willebrand's disease (VWD). All reported type 2B mutations are located in the A1 domain or the flanking regions around A1 (77), suggesting that autoinhibitory elements are localized around A1. This is consistent with recent observations that global extension of VWF multimer under flow occurs before a local, tension-dependent activation of the A1 domain for GPIbα binding (97). In addition, well-known activating agents, such as glycopeptide ristocetin and snake

venom protein botrocetin, can also induce VWF binding to GPIbα in the absence of shear (155; 156). Ristocetin, but not botrocetin, mimics shear-dependent activation of VWF (147). Although ristocetin is widely used in research and diagnostic tests, and the ristocetin-binding site in VWF has been mapped to include a proline-rich sequence following A1 (88; 110), its mechanism of activation is not fully clear.

Crystal structures of individual domains of VWF show that the D'D3 assembly extends to residue 1237 and that the A2 domain starts at residue 1494 (157; 158). The A1 domain is encompassed by the 1272-1458 disulfide bond and flanked by stretches of sequences (residues 1238-1271, 1459-1493) that are O-glycosylated. Truncating these flanking regions around the disulfide bond has yielded A1 fragments with disparate affinities for GPIbα. Their roles in modulating A1 binding have been speculated over the years, albeit without definitive evidence (78; 79; 88; 89; 100; 102; 104). Except for a few residues close to the disulfide bond, these flanking sequences are not resolved in crystal structures of the A1 domain (74; 75; 159). Our recent characterization of A1 fragments with differential affinities for GPIbα suggests that both N- and C-terminal flanking sequences cooperatively provide hydrogen-deuterium exchange protection on many residues in A1, particularly the β3α2 loop as a part of the GPIbα-binding site, and thus may constitute an autoinhibitory module (AIM) (88; 89).

Here, we report that the discontinuous AIM does resist tensile force, and cooperatively unfolds above a certain threshold of force to expose A1. We provide additional evidence that links disruption of the AIM with an increase of the A1 affinity for GPIbα under pathologically relevant conditions. Finally, the AIM could be targeted effectively by a recently developed anti-thrombotic agent.

2.3 Methods

Materials. Ristocetin was purchased from MP Biomedicals. Most recombinant VWF fragments and type 2B mutants were expressed from baby hamster kidney cells as described (88; 89). Plasma-derived VWF was reconstituted in phosphate buffered saline (PBS) from outdated lyophilized Humate-P (CSL-Behring). Monoclonal antibodies 6G1, CR1, and 11A8 have been described(88; 160). ARC1172(161) was synthesized by Integrated DNA Technologies. Mammalian cells were maintained in DMEM/F12 culture media (ThermoFisher), with 10% Foundation-B fetal bovine serum (Gemini Bio-Products, Sacramento, CA), and 1% penicillin/streptomycin (ThermoFisher). Bovine serum albumin, fraction V was purchased from Fisher Scientific. Tobacco etch virus (TEV) protease was produced with plasmid pD2087 in BL21pRIL cells and purified as described (162). Human GPIb-IX complex was purified from outdated and deidentified leuko-reduced apheresis-derived platelets as described(163).

Construction of Expi293F-BirA cells. The gene encoding *E. coli* biotin ligase BirA was subcloned from vector pBIG5b (91) using the EcoRI and XbaI sites and ligated into pcDNA3.1-Zeo(+) vector (Invitrogen). The resulting plasmid was transfected into Expi293F cells using Lipofectamine 3000 (ThermoFisher). Single clones were selected using 400 μg/mL zeocin (ThermoFisher). For biotinylation, Expi293F-BirA cells were transfected to express proteins bearing a BioTag (LNDIFEAQKIEWH) sequence in 10 μM biotin.

Recombinant VWF and BioSpy-VWF fragments. For recombinant VWF fragment 1268-1493 (A1-CAIM), the encoding DNA fragment was amplified from the expression vector encoding 1238-1493-10His using primers IgK-1268F and 1268XbaStopR (all the primers are listed in

Supplementary Table 1), and subcloned into the pcDNA3.1-Hygro(+) vector (Invitrogen) as a XbaI-NheI fragment. The resulting vector was subsequently transfected into Expi293F cells for stable protein expression and purification as described using a GE Healthcare Ni Sepharose excel column followed by size exclusion chromatography on a GE Healthcare HiLoad 16/600 Superdex 200 pg column (88; 89).

To clone BioSpy-VWF constructs, a decahistidine (10His) and SpyTag (AHIVMVDAYKPTK)(164) sequence was appended to the C-terminus of VWF fragments using primers 1493F and 1493RSpyStop. Each gene fragment was ligated into the pBIG4a vector using SpeI and XhoI sites such that a consensus Kozak sequence, α1-antitrypsin signal sequence, and a BioTag was appended to the N-terminus(165). The expression cassette was subsequently subcloned into pcDNA3.1-Hygro as a NheI-XhoI fragment. Type 2B constructs were generated by site-directed mutagenesis using primers EL003/EL004 for R1341Q and EL007/EL008 for H1268D. All DNA sequences were verified by sequencing.

Each pcDNA-BioSpy-VWF vector was transfected into adherent Expi293F-BirA cells using Lipofectamine 3000. Single clones were selected using 250 µg/mL hygromycin B (ThermoFisher). Stably expressing clones were adapted to SFM4-CHO UT (GE Healthcare) or FreeStyle F17 Expression media (ThermoFisher), supplemented with 8 mM L-Glutamine or 2x GlutaMAX (ThermoFisher) in 125-mL flasks (Thomson Instruments) or 50-mL spinning culture vessels (Corning). Cells were passed into a 250-mL flask or 500-mL spinning flask at 200,000-400,000 cells/mL and cultured for 7-10 days. Protein was purified from the media as previously described(89). When needed, cell-free biotinylation was performed using the BirA500 kit from Avidity LLC (Aurora, CO). Excess biotin was removed by size-exclusion chromatography on a HiLoad 16/600 Superdex 200 pg column (GE). Subsequent fractions were tested for

biotinylation by Western blot using Streptavidin IR-Dye680 (Licor) (1:2000), verified using anti-His-tag antibody 4E3D10H2/E3 (ThermoFisher) (1:2000) followed by secondary antibody IRDye 800CW Goat anti-Mouse IgG (Licor) (1:5000) and analyzed for purity by Coomassie stain. Purified protein was stored at -80°C before use.

Recombinant ligand-binding domain (LBD) of GPIbα. The gene fragment encoding human GPIbα residues His1-Arg290 was amplified from a GPIbα vector(166) using primers GPIba_Biotag and GPIba290_2xFLAGstop to append a BioTag and a 2xFLAG tag to N- and C-termini, respectively. This fragment was ligated into a modified pcDNA3.1-Hygro vector, which contains a signal sequence followed by a 10His tag and the TEV protease cleavage sequence at the N-terminus, as a BamHI-XhoI fragment. Stably expressing clones were generated in *Expi*293F-BirA cells. The protein was purified using the same method as for VWF fragments.

Construction and production of VHH81 nanobody. The sequence of VHH81 was obtained from international patent WO2011/067160 (clone PMP12A2h1) and its encoding DNA fragment was synthesized by Integrated DNA Technologies. For crystallization experiments, primers pD14_VHH81F and pD14_VHH81R were used to amplify a gene fragment encoding VHH81 with C-terminal hexahistidine (VHH81-6His), cloned into a modified pDEST14 vector(164), and produced in the cytoplasm of SHuffle T7 Express cells. To induce expression in both cases, 0.4 mM IPTG was added to bacteria culture at OD_{600} of 0.9 at 30°C. After 4-5 hours, cells were centrifuged at 8,000 g for 20 min at room temperature and lysed with BugBuster with benzonase (Novagen/Sigma-Aldrich) according to manufacturer's directions. The lysate was centrifuged at 17,000 g and supernatant filtered by a Steriflip unit (Millipore). VHH81-6His was purified by

Ni-affinity chromatography and gel filtration chromatography in PBS. Purified protein was flash-frozen in liquid nitrogen and stored at -80°C until use.

To express Flag-VHH81 for BLI experiments, the gene fragment encoding VHH81 with an N-terminal FLAG tag, a C-terminal TEV protease cleavage sequence, and a 6His tag was cloned into the pET22b+ plasmid and expressed in SHuffle T7 Express cells (New England Biolabs). To purify Flag-VHH81 from the periplasm, cell pellets were resuspended in 30 mM Tris-HCl, 20% sucrose, pH 8.0, at 80 ml per gram wet weight. EDTA was added dropwise to 1 mM. Cells were incubated on ice for 10 min with gentle agitation. The cell suspension was centrifuged at 8,000 g for 20 min at 4°C, and pellet resuspended in the same volume of ice-cold 5 mM $MgSO_4$. The cell suspension was incubated on ice for 10 min with gentle agitation. The suspension was centrifuged as before, and the protein in the supernatant was purified by Ni-affinity chromatography. Cleavage of the 6His tag by recombinant TEV protease (1 mg nanobody/125 μg protease) was performed overnight at 4°C in PBS with 10% glycerol. The mixture was applied to a His-Trap column and the flow through containing Flag-VHH81 collected and analyzed via western blot and ELISA. The lack of the 6His tag in purified Flag-VHH81 was verified via immunoblot with anti-His antibody 4E3D10H2/E3 at 1:2000 dilution or ELISA (Supplementary Fig. 2.13).

Blood preparation. Human fresh whole blood was obtained from healthy donors via venipuncture into Vacutainer 3.2% sodium citrate tubes (BD). Written informed consent was obtained from participants before their inclusion in studies, and all procedures using donor-derived human blood and platelets were approved by the Institutional Review Board at Emory University.

Platelet Aggregometry. Platelet-rich plasma and washed platelets were prepared from citrated whole blood as described (167). For platelet aggregometry, washed platelets were resuspended in modified Tyrode's buffer (134 mM NaCl, 2.9 mM KCl, 0.34 mM Na_2HPO_4, 12 mM $NaHCO_3$, 20 mM HEPES, 1 mM $MgCl_2$) with 5 mM D-glucose. Platelets were recalcified with 5 mM $CaCl_2$ and was normalized to 150,000/μL at 240 uL per cuvette. Recombinant AIM-A1 fragments were centrifuged at 100,000 g for 30 min at 4°C, and the protein concentration was measured on a Nano-Drop (ThermoFisher) using the protein's extinction coefficient(89). After stable baseline was established, AIM-A1 fragments were added to the platelet suspension. In tests of VHH81 inhibition, VHH81 was mixed with AIM-A1 fragments, and then added to the platelet suspension. Alternatively, VHH81 was added to the PRP in the cuvette, followed 30 seconds later by the addition of 1.5 mg/mL ristocetin. In all cases, platelet samples before experiments were monitored for premature aggregation and activity verified at various time points by observing full aggregation after adding 60 nM AIM-A1 and 1.5 mg/mL ristocetin. Platelet aggregation was recorded in AGGRO/LINK software (Chrono-log, Havertown, PA), exported, and normalized to initial optical densities of 100 manually. Extent of aggregation was measured as the optical density at 600 seconds.

Bio-Layer Interferometry (BLI). BLI experiments were performed on an Octet QK^e instrument (ForteBio) using black non-binding plates (Greiner Bio-One, Monroe, NC) and manufacturer-supplied Data Acquisition software v11.1.1.19. Plate temperature was set to 23°C and plate shaking to 1,000 rpm. Streptavidin sensors (for biotinylated LBD) or Ni-NTA sensors (for AIM-A1 fragments) were equilibrated in the kinetics buffer (KB, ForteBio) for at least 10 min prior to

initiation of experiment. All proteins were diluted in sample diluent (ForteBio) to minimize non-specific interactions. Equilibrated sensors were loaded with 15 µg/mL biotinylated LBD for 300 seconds, followed by a 120-second baseline. Sensors were then dipped into AIM-A1-containing wells for 300 seconds of association, followed by dissociation in KB for 300 seconds. To regenerate the sensors, the sensors were regenerated by 4 cycles of 5-s wash in 2 M NaCl, followed by 5 seconds in KB. Consistent LBD regeneration was evidenced by a return to baseline accumulation after the initial loading step at 0 nm. A reference sensor was included in all measurements whereby LBD was loaded to the sensor, but VWF fragments were absent in wells. For binding to Flag-VHH81, VWF fragments were loaded to Ni-NTA sensors at a set threshold of 3 nm. Sensors were regenerated in 5-s cycles of 10 mM glycine, pH 1.6 and neutralized in KB. Sensors were reloaded with 10 mM $NiCl_2$ for 60 seconds. Baseline subtraction of the loaded reference sensors was applied to all runs. Heterogenous ligand, global curve fitting was performed on binding experiments using the Data Analysis HT software v11.1.1.39 (ForteBio). In this scheme, both high- and low-affinity A1 could bind to immobilized LBD,

$$A' + B \rightleftarrows A'B$$

$$A + B \rightleftarrows AB$$

where A' is the higher affinity A1. In this model, interconversion of AB to A'B was not accounted for as the binding was performed in the absence of force. Similarly, VHH81 binding is dependent on the structure of a discontinuous binding epitope spanning the NAIM and A1, where A1 could sample both states. Data was exported to Prism and the steady state plots were fit to hyperbolic binding curve. Each set of experiments were repeated at least twice.

Single-Molecule Force Spectroscopy. Single-molecule force measurement was performed largely as described(168). Briefly, the biotinylated VWF fragment (*e.g.* BioTag-1238-1493-10His-SpyTag) was immobilized on a streptavidin bead held by a fixed micropipette. SpyCatcher protein with a C-terminal Cys residue(164), a kind gift from Dr. Mark Howarth, was coupled to a biotin-DNA handle of 802 bp, and then coupled to streptavidin beads of 2.0-μm diameter (Spherotech, Lake Forest, IL). For pulling experiments, the SpyCatcher-DNA handle bead, trapped and controlled by the optical tweezer, was brought to interact with the VWF fragment bead. The force measurement was performed at force-ramp mode with varying pulling speeds (50, 100, 200, 400, and 500 nm/s) in Tris-buffered saline (20 mM Tris, 150 mM NaCl, pH 7.5). The force-extension data were fitted to the worm-like chain (WLC) model,

$$\frac{F(x)\cdot L_p}{k_B T} = \frac{1}{4}\left(1-\frac{x}{L_c}\right)^{-2} - \frac{1}{4} + \frac{x}{L_c}, \quad [1]$$

where $F(x)$ is the applied force on the polymer, x is the end-to-end distance, L_c is the contour length, and L_p is the persistence length of the polymer. Unfolding extension is defined as the increase in end-to-end distance between the point of unfolding and the point at which the force at unfolding is re-established. In order to find the most probable extension at various forces, the force-extension data was first binned by force. Next, the extension data within each bin were plotted as histograms to identify the peak extension (Supplementary Fig. 2.3A). Unfolding was also analyzed according to the Bell-Evans model, a theory first developed to describe the influence of an external force on the rate of molecular complex dissociation(169; 170) and has been applied later to study protein unfolding(46; 168). In this model, a pulling force, *f*, distorts the intramolecular potential of a protein complex, leading to a lower activation energy and an increase in the unfolding rate $k_u(f)$ as follows:

$$k_u(f) = 1/t_u(f) = k_u^0 \exp\left(\frac{f\gamma_u}{k_B T}\right) \quad [2]$$

where k_u^0 is the unfolding rate constant in the absence of a pulling force, γ_u the barrier position, T the absolute temperature, and k_B the Boltzmann constant. For a constant loading rate R_f, the probability for the unfolding of the complex as a function of the pulling force f is given by

$$p(f) = k_u^0 \exp\left(\frac{f\gamma_u}{k_B T}\right)\exp\left\{\frac{k_u^0 k_B T}{\gamma_u R_f}\left[1-\exp\left(\frac{f\gamma_u}{k_B T}\right)\right]\right\} \quad [3]$$

with the most probable unfolding force f^*

$$f^* = \frac{k_B T}{\gamma_u}\ln\left(\frac{\gamma_u}{k_u^0 k_B T}\right) + \frac{k_B T}{\gamma_u}\ln(R_f) \quad [4]$$

Bell-Evans model parameters k_u^0 and γ_u were determined by fitting equation [4] to the plot of f^* versus $\ln(R_f)$.

Enzyme-linked immunosorbent assay (ELISA). VWF and recombinant AIM-A1 fragments (6 μg/mL in PBS) were coated to high-binding half-area 96 well plates (Corning). VHH81 binding to immobilized VWF and AIM-A1 fragments was detected with HRP-conjugated anti-VHH monoclonal antibody 96A3F5 (Genscript) (1:1000). Purified GPIb-IX complex was coated to the plate using 0.1% Triton X-100, 20 mM $NaHCO_3$, pH 9.6. Fixed platelets, prepared from human washed platelets followed by two rounds of washing in 4% paraformaldehyde, were coated to the plate using 1% poly-l-lysine (Sigma) in PBS. Bound AIM-A1 fragments were detected with HRP-conjugated anti-HisTag antibody 4E3D10H2/E3 (1:2000). Monoclonal antibody binding to AIM-A1 fragments was detected using HRP-conjugated anti-mouse secondary antibody sc2005 (Santa Cruz Biotechnology) (1:2000). In all cases, plates were washed 3 times with HEPES

buffered saline with 0.1% Tween-20 on a BioTek ELx405 plate washer. After binding and washing, 1-Step Ultra-TMB substrate (ThermoFisher) was added to each well, quenched with 2 M H_2SO_4. Absorbance was measured at 450 nm. Empty wells were used to subtract baseline absorbance.

Construction of TEV-1238-1481. Primers MW002 and MW003 were used to amplify the gene fragment and cloned into the aforementioned modified pcDNA3.1-Hygro vector using BamHI and XhoI sites. The N-terminus of the secreted protein starts with ERHHHHHHHHHHENLYFQGS, followed by VWF residues 1238-1481. Stably transfected Expi293F cells were adapted to SFM4CHO-UT media, following the procedure described above. The target protein was purified by Ni-affinity chromatography and gel filtration as described above for VWF fragments. It was digested with recombinant TEV protease, at a w/w ratio of 11/1, in PBS containing 0.3 mM freshly prepared glutathione and 3 mM oxidized glutathione overnight at 4°C. The digestion mixture was centrifuged at 4,000 g at 4°C and applied onto a His-Trap column, and the flow through was further purified on a HiLoad 16/600 Superdex 200 pg column. Fractions containing the tag-less AIM-A1 fragment were pooled, concentrated, and mixed with VHH81-6His at a molar ratio of 1/1.5 for 20 minutes before the AIM-A1/VHH81 complex was separated from unbound VHH81 by gel filtration chromatography (Supplementary Fig. 2.16D). Purified complex was flash-frozen in liquid nitrogen and stored at -80°C until use.

Crystallization, data collection and structural determination. The AIM-A1/VHH81 complex was concentrated to ~15 mg/ml for crystallization trials using commercial sparse matrix screens (JCSG+, Morpheus, MemGold, Proplex) from Hampton Research (Aliso Viejo, CA) and

Molecular Dimensions (Sheffield, UK) in sitting-drop crystallization plates at 10°C. Single crystals grew from conditions of 3.2 M ammonium sulphate, 0.08 M sodium citrate, pH 5.2 (MemGold, H2). Crystals were harvested and 20% glycerol added as a cryo-protectant, then flash-frozen in liquid nitrogen for data collection on beamline I04 and Diamond Light Source. Diffraction data were collected from multiple crystals and processed with xia2 and CCP4 suite to 2.1-Å resolution. The structure was then solved using molecular replacement (Phaser) with the A1 domain crystal structure (1AUQ [10.2210/pdb1AUQ/pdb]) and a nanobody homology model without CDR loops as the templates(74; 171). Buccaneer was used to build the initial model followed by manual model building using COOT and refinement with REFMAC. There is evidence of anisotropy in the diffraction data. No TLS refinement was performed. Crystallographic statistics are listed in Supplementary Table 2. The coordinates of the complex structure have been deposited at the Protein Databank (ID: 7A6O [10.2210/pdb7A6O/pdb]). Structures were visualized using PyMOL.

Parallel-plate flow chamber assay. Parallel-plate flow chamber experiments were performed using a Maastricht Instruments flow chamber (H:50μm, W:5mm, L:60mm). Citrated human whole blood was perfused at room temperature using a Harvard Apparatus Pump 11 Elite. Coverslips were imaged under a Nikon Ti-Eclipse microscope equipped with a 20x Plan Fluor objective lens. Coverslips (22x60 mm) were coated with 200 µg/mL bovine type I collagen (Chrono-log) in 5% glucose, pH 2.7 overnight at 37°C, and blocked with 1% BSA in PBS for 1 hour. After blood was mixed with 2 µg/mL DIOC-6 (Invitrogen) for 10 minutes to label platelets and recalcified with 5 mM $CaCl_2$, 1 µM ARC1172, 880 nM or 2.64 µM VHH81-6His, or 880 nM VHH81-6His and 15 µg/mL 11A8 was added and mixed for 10 min before perfusion. After the

coverslip was assembled into the flow chamber, it was washed with modified Tyrode's buffer with 5 mM glucose for 1 min. Blood was perfused for 4 minutes at each shear rate. The chamber was subsequently washed with modified Tyrode's buffer for 2 min at the same shear rate and immediately imaged in the FITC filter (excitation 480nm/30nm, barrier 535nm/45nm). On average 20 fluorescent images were collected, with collagen deposited on slides often visible in bright-field images. Area covered by adhered platelets was calculated using FIJI, thresholding for each image using the greyscale LUT. Experiments at various shear rates were performed using blood from 2 to 3 donors with similar results observed throughout.

Statistical Analysis. Data are shown as mean ± standard deviation, with number of replicates indicated in relevant figure legends. Where applicable, one or two-way ANOVA with Tukey's multiple comparison correction was performed to analyze platelet coverage as indicated in the figure legends. For BLI experiments, all binding interactions were fit to a heterogeneous ligand binding model in the Data Analysis HT software from ForteBio. Steady state analysis was performed in Prism by fitting concentration-response curves to a hyperbola. Relevant fitting parameters for force spectroscopy are described above.

2.4 Results

The autoinhibitory module unfolds under tensile force, as a single unit

To detect and determine mechanical properties of the AIM under force, a recombinant AIM-A1 protein (containing VWF residues 1238-1493) with an N-terminal biotin and a C-terminal SpyTag sequence(164) was affixed to a SpyCatcher-biotin DNA handle, and trapped between two streptavidin-coated beads in an optical trap (Fig. 2.1A,B, Supplementary Fig. 2.1). The trapped construct was exposed to repeated cycles of extension and retraction. The AIM-A1 construct consistently showed an abrupt extension around 10-20 pN (Fig. 2.1C, Supplementary Fig. 2.2). This extension event could not be attributed to unfolding of the A1 domain, which would have required rupture of its encompassing 1272-1458 disulfide bond and a rupture force greater than 100 pN(172; 173). Fitting extension traces of AIM-A1 to the worm-like chain (WLC) model(174) yields a contour length of 26.6±0.5 nm, suggesting that the underlying unfolding event involves approximately 67 residues, which is remarkably close to the length of both flanking sequences in the AIM-A1 construct (N-terminal 34, C-terminal 32) (Fig. 2.1D, Supplementary Fig. 2.3; Table 2.1). Replacing the DNA handle with a polyethylene glycol handle produced similar magnitudes of unfolding forces and extensions, indicating that, contrary to a recent report(175), the DNA handle did not bind the A1 domain in this study and interfere with unfolding (Supplementary Fig. 2.4).

While about 80-90% of force pulling cycles produced a single large extension event, a small percentage produced either one (5-15%) or two (~5%) smaller, separate extension events (Fig. 2.1F, Supplementary Fig. 2.2). Truncated “AIM-less” constructs, A1-CAIM (containing VWF residues 1268-1493) or NAIM-A1 (1238-1461), showed only one small extension event with contour lengths of 13.1±0.9 and 12.9±1.0 nm, respectively (Fig. 2.1D,F, Supplementary

Figure 2.1

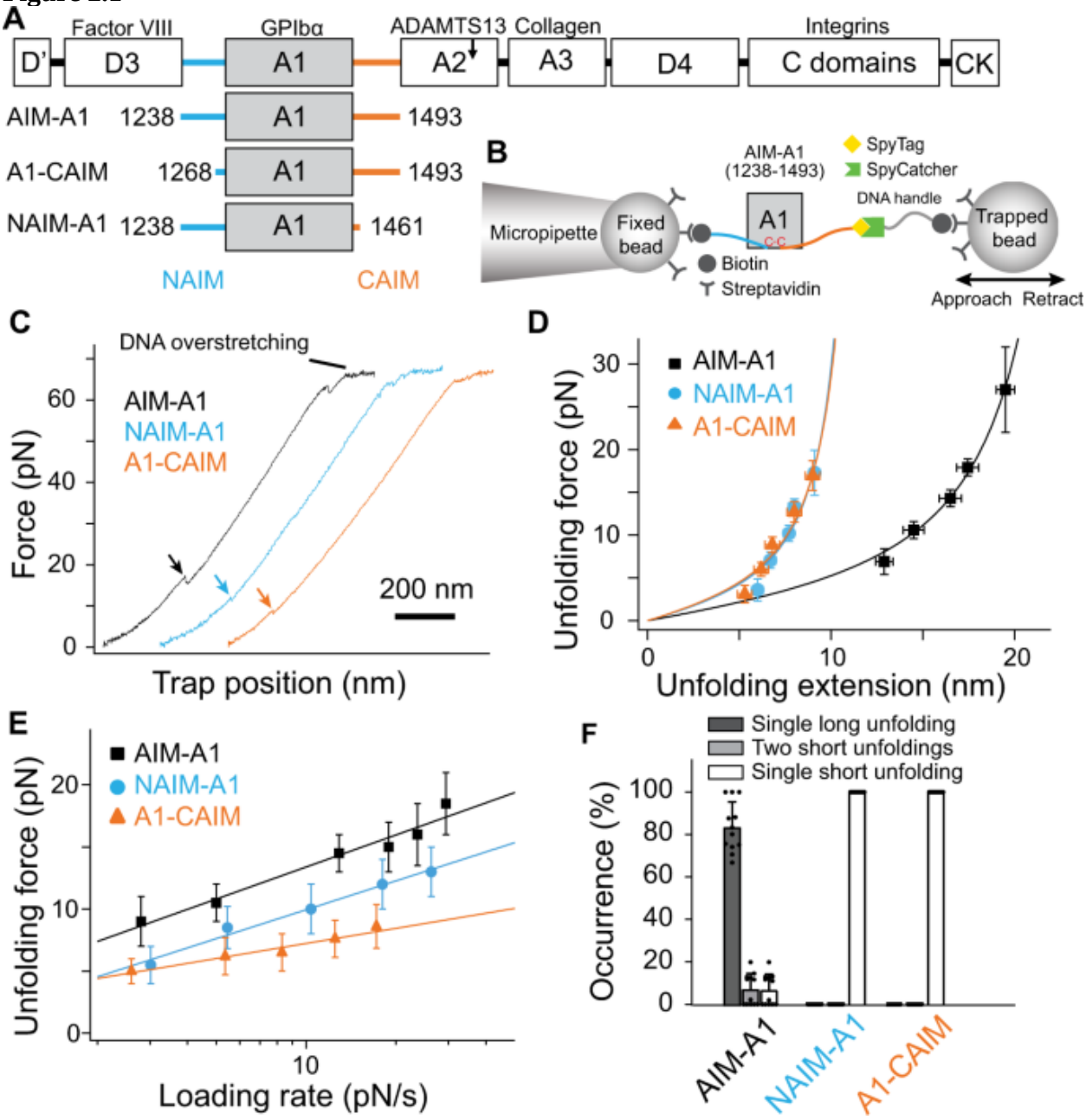

Figure 2.1 Cooperative unfolding of the discontinuous AIM.

(A) Schematic of a VWF monomer, marked above with binding sites of related proteins, is aligned with various AIM-A1 fragments. NAIM and CAIM are colored cyan and orange, respectively. (B) Schematic of single-molecule optical tweezer apparatus in this study. The 1272-1458 disulfide bond is marked red in the A1 domain. (C) Representative force-extension traces

of AIM-A1 (black), NAIM-A1 (cyan), and A1-CAIM (orange). The extension event in each trace is marked by an arrowhead. (D) Plots of unfolding force versus unfolding extension for noted AIM-A1 fragments and fits to the worm-like chain model. Force data are presented as mean values ± standard deviation, and extension data are presented as the peak of the Gaussian fit ± the full width at half maximum (FWHM) of Gaussian fit divided by the square root of counts. The data was obtained from n=52, 80, and 75 biologically independent single-molecule tethers for AIM-A1, NAIM-A1 and A1-CAIM, respectively. (E) Plots of unfolding force versus loading rate for noted AIM-A1 fragments and fits to the Bell-Evans model. Unfolding force data are presented as the center of the tallest bin of the histogram ± one-half of the bin width. The data was obtained from n=52, 80, and 75 biologically independent single-molecule tethers for AIM-A1, NAIM-A1 and A1-CAIM, respectively. (F) Average occurrence of a single long unfolding event (black bar), two short unfolding events (gray bar), and a single short unfolding event (white bar) during repeated cycles of extension and retraction. The constructs were pulled at 200 nm/s after relaxation under 1 pN for 1 second. Error bars represent standard deviation. N=12, 17, and 19 biologically independent single-molecule tethers for AIM-A1, NAIM-A1 and A1-CAIM, respectively. Source data for (D-F) are provided in 3 worksheets of the Source Data file.

Table 2.1

Single-molecule force spectroscopy parameters associated with unfolding events of various constructs and additives.

Construct/Additive	Contour length L_C (nm)[a]	Persistence length L_p (nm)[a]	Unstressed unfolding rate k_u^0 (s^{-1})[b]	Barrier position γ_u (nm)[b]
AIM-A1	26.6 ± 0.5	0.60 ± 0.05	0.074 ± 0.021	1.10 ± 0.10
A1-CAIM	13.1 ± 0.9	0.72 ± 0.17	0.093 ± 0.033	2.34 ± 0.29
NAIM-A1	12.9 ± 1.0	0.78 ± 0.22	0.154 ± 0.024	1.22 ± 0.09
AIM-A1 H1268D	17.7 ± 0.9	0.67 ± 0.11	0.288 ± 0.052	0.84 ± 0.12
AIM-A1 R1341Q	14.5 ± 0.3	1.32 ± 0.09	0.27 ± 0.12	1.15 ± 0.29
AIM-A1 with 6G1	14.6 ± 1.0	0.76 ± 0.19	0.10 ± 0.05	1.48 ± 0.28
A1-CAIM with 6G1	13.0 ± 0.6	1.08 ± 0.15	0.096 ± 0.008	3.38 ± 0.08
NAIM-A1 with 6G1	14.2 ± 1.4	0.95 ± 0.37	0.247 ± 0.069	1.17 ± 0.18
AIM-A1 with CR1	27.9 ± 2.2	0.37 ± 0.07	0.133 ± 0.030	0.94 ± 0.10
AIM-A1 with VHH81	25.3 ± 0.8	0.56 ± 0.07	0.0061 ± 0.0032	1.47 ± 0.14

[a] Contour length and persistence length are fitted worm-like chain model parameters.

Uncertainties are the standard error of the fits.

[b] Unstressed unfolding rate and barrier position are fitted Bell-Evans model parameters.

Uncertainties are the standard error of the fits.

Fig. 2.3; Table 2.1). As small extension events in pulling A1-CAIM or NAIM-A1 closely resemble those small extension events in AIM-A1, each small extension should correspond to the unfolding of either NAIM or CAIM. More importantly, the large extension event in most AIM-A1 pulling traces should correspond to concurrent unfolding of both NAIM and CAIM. In other words, the NAIM and CAIM cooperatively form a single structural unit that unfolds together. Not surprisingly, as shown in fits to the Bell-Evans model(169; 170), both NAIM-A1 and A1-CAIM exhibited lowered unfolding forces compared to AIM-A1 at all loading rates (Fig. 2.1E). Moreover, the NAIM unfolding force is higher than the CAIM unfolding force, in agreement with previous reports of the influence of NAIM residues on both GPIbα-A1 bond kinetics and platelet accumulation(105; 146; 176). Nonetheless, both NAIM and CAIM contribute to the force resistance of AIM-A1.

It is noteworthy that refolding events were observed in only 9.6% of relaxation traces of AIM-A1. In cases where refolding was not apparent, AIM unfolding still occurred in subsequent pulls, indicating that refolding of AIM did happen when the molecule was relaxed at the present minimum hold force of 0.5 or 1 pN (Supplementary Fig. 2.5). The frequency of apparent refolding event decreased to 4.5% in NAIM-A1 and 3.1% in A1-CAIM, suggesting that refolding was more difficult or slower in these constructs. Overall, these results suggest that, similar to refolding of the A2 domain(46), AIM refolding is a relatively slow process and requires relaxation at low force for an extended time, most likely seconds. The AIM is likely metastable and has low folding free energy.

The importance of both NAIM and CAIM in shielding A1 from the ligand-binding domain (LBD) of GPIbα (residues 1-290) is made apparent by bulk binding measurements with AIM-less proteins. The AIM-A1 protein, at up to 1 μM concentration, showed little binding

towards immobilized LBD, which is consistent with an apparent K_D of 32 μM previously reported for a glycosylated 1238-1471 fragment(85). In comparison, either AIM-less protein showed markedly higher apparent affinity for the LBD, indicating that removal of either half of the AIM exposes A1 (Fig. 2.2A-D, Supplementary Fig. 2.6). Binding sensorgrams were best fit to a two-phase association and dissociation, suggesting that A1 binding to LBD is likely more complex, with A1 adopting high- and low-affinity states(81; 177). Partial truncation of both NAIM and CAIM (tAIM-A1, containing VWF residues 1261-1472) also yielded an active A1 fragment with a similar apparent affinity as AIM-less proteins(88) (Supplementary Fig. 2.6). Furthermore, at 60 nM, the normal physiological concentration of plasma VWF, both A1-CAIM and NAIM-A1, but not AIM-A1, induced significant aggregation of washed platelets, the kinetics of which exceeded aggregation induced by 60 nM AIM-A1 with 1.5 mg/ml ristocetin (Fig. 2.2E-H). The aggregation was inhibited by the addition of EDTA, suggesting that these A1 proteins triggered GPIb-IX signaling and activated integrin αIIbβ3 binding to fibrinogen(178) (Fig. 2.2F). Interestingly, at higher concentrations, AIM-A1 could also induce aggregation, albeit at lower and slower responses than AIM-less proteins (Fig. 2.2E,H). Overall, these results demonstrate that the AIM constitutes a specific, cooperative shielding mechanism that is mechanically removable. Truncation of either part of the AIM, simulating mechanical separation of the AIM from A1, similarly exposes A1 for GPIbα binding and subsequent platelet aggregation.

Type 2B VWD mutations destabilize or disrupt the AIM

To test if type 2B VWD mutations alter mechanical properties of the AIM, two mutant AIM-A1 proteins bearing representative mutations (H1268D and R1341Q) were generated and

Figure 2.2

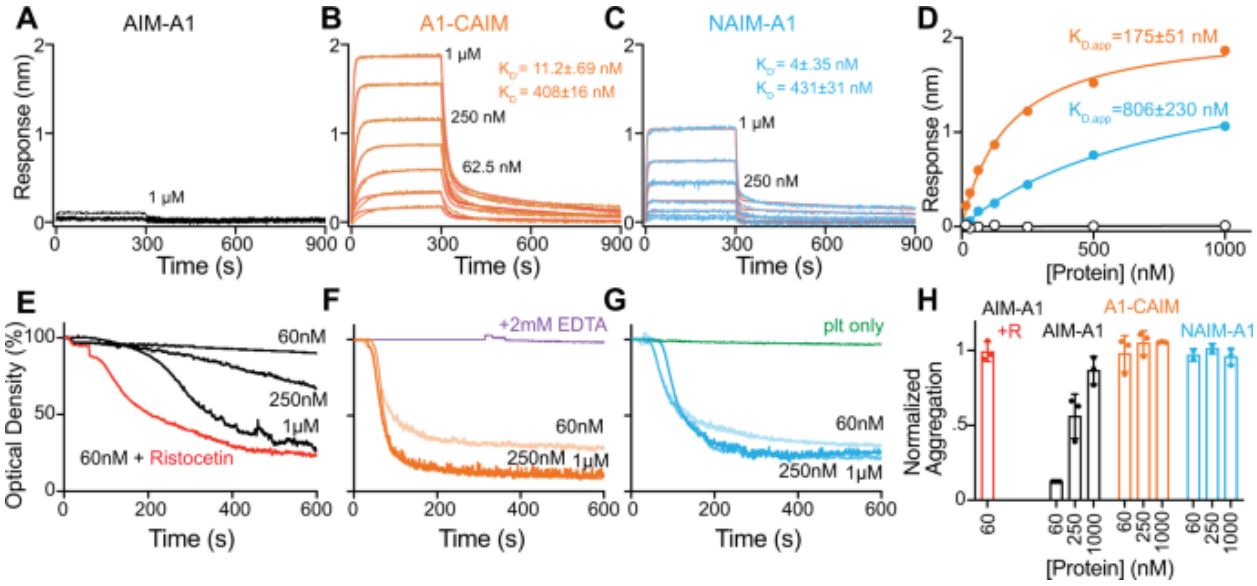

Figure 2.2 Truncation of either NAIM or CAIM activates A1.

(A-C) Sensorgrams of VWF fragments binding to immobilized GPIbα-LBD. VWF fragments were serially diluted from 1 μM to 15.6 nM. Curves were fitted to a heterogenous-ligand binding model that accommodates two affinity states of A1. $K_{D'}$ is the equilibrium dissociation constant of A1 binding to LBD with a higher affinity, while K_D is that with a lower affinity. Error is the standard deviation of the fitted rate constant. Fitting traces are in red, residuals are reported in Supplementary Fig. 2.6C. (D) Steady state analysis of binding interactions between VWF fragments and GPIbα. Values from binding data shown in (A-C) are plotted and fit to a hyperbola. Apparent K_D is reported as mean ± 95% confidence interval. (E-G) Representative washed platelet aggregation traces of (E) AIM-A1, (F) A1-CAIM and (G) NAIM-A1. 60 nM AIM-A1 + 1.5 mg/mL ristocetin is shown as a red trace in (E). Addition of 2 mM EDTA before addition of VWF fragment A1-CAIM is shown as a purple trace in (F). Platelet only control is shown as a green trace in (G). (H) Extent of platelet aggregation at 600 s normalized to AIM-A1 at 60 nM with 1.5 mg/mL ristocetin. Data are means ± standard deviation, n=3 per condition. Source data are provided in a worksheet of the Source Data file.

characterized (Supplementary Fig. 2.7A). Patients with these mutations present with bleeding, thrombocytopenia and a loss of high molecular-weight VWF(77; 179). Previously published crystal structures of A1 indicate a hydrogen bond between H1268 and D1305(159), but no apparent interactions involving the side chain of R1341. As expected, both H1268D and R1341Q showed increased affinities towards the LBD than wild-type AIM-A1, although their affinities are weaker than those of AIM-less proteins (Fig. 2.3A, Supplementary Fig. 2.7B-E). Like AIM-less proteins, both mutants were able to spontaneously aggregate washed platelets at 60 nM (Fig. 2.3B). In single-molecule force measurements, H1268D showed a significant reduction in unfolding force at all loading rates compared to wild-type, with a large reduction in unfolding extension; R1341Q showed a single, short extension in the majority of traces (~90%) and one long extension event in the others (~10%), indicating the disruption of the cooperative AIM therein (Fig. 2.3C,D, Supplementary Fig. 2.2; Table 2.1). In most traces, the short extension had a low unfolding force, suggesting that it is due to unfolding of the CAIM and that the NAIM is disrupted in this mutant (Fig. 2.3D,E, Supplementary Fig. 2.3). Overall, these results indicate that H1268D and R1341Q activate A1 by destabilizing or disrupting the AIM, and suggest that other type 2B VWD mutations could activate A1 in a similar manner.

Disruption of the AIM-A1 interface by 6G1, a ristocetin-mimicking antibody

Since ristocetin tends to flocculate proteins(180) and may cause technical issues in single-molecule force measurements (Supplementary Fig. 2.4B), monoclonal antibody 6G1 was utilized in its place. 6G1 binds residues 1463-1472, a linear epitope in the CAIM, which overlaps with the ristocetin-binding sequence(88; 160) (Supplementary Fig. 2.8). In platelet-rich plasma (PRP), 6G1 could hinder ristocetin-induced platelet aggregation, owing to its competition with

Figure 2.3

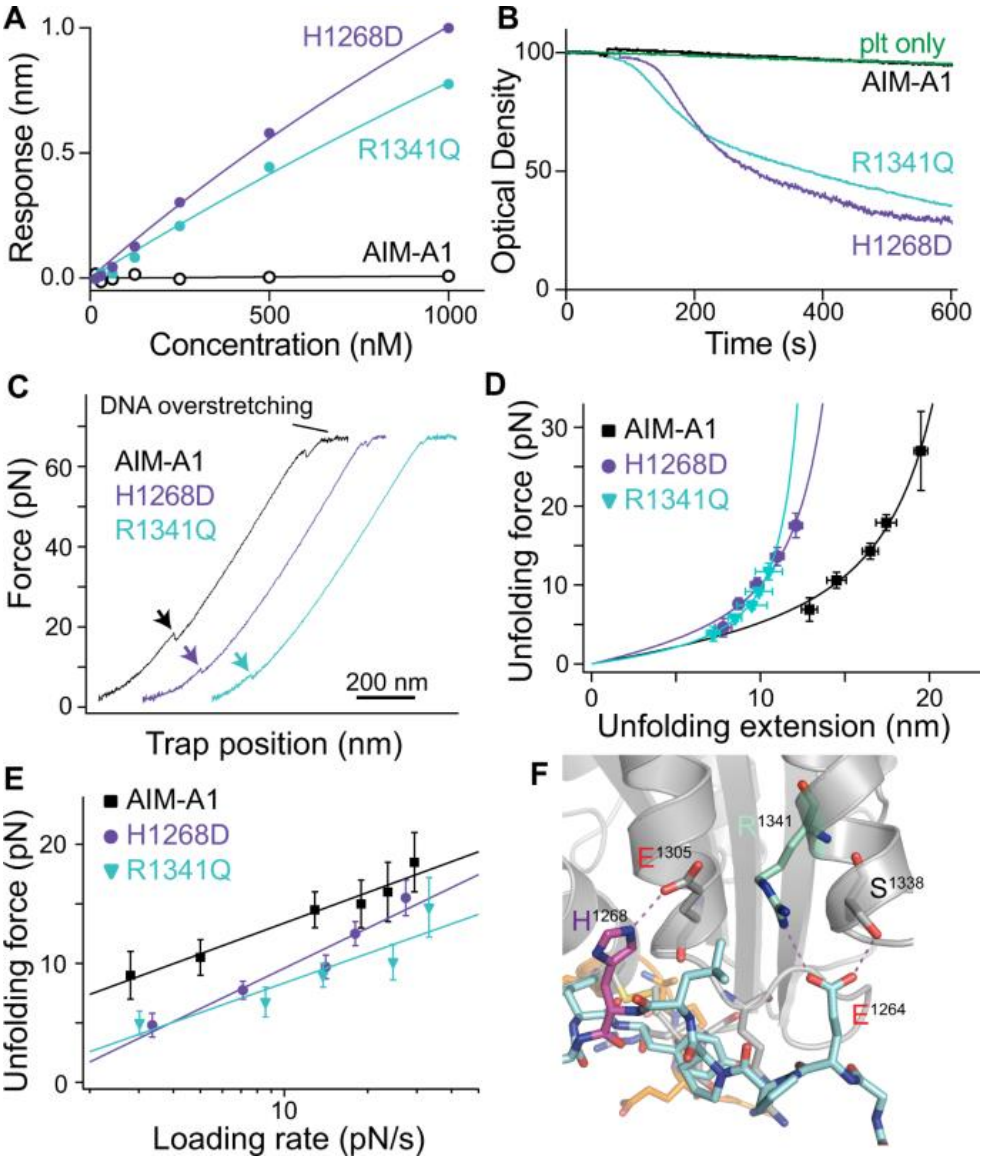

Figure 2.3 Type 2B VWD mutations alter AIM unfolding and A1 activity.

(A) Steady state analysis of WT AIM-A1, H1268D and R1341Q to immobilized GPIbα. Protein was serially diluted from 1 μM to 15.6 nM and fit to a hyperbola. (B) Washed platelet aggregation responses to 60 nM H1268D (purple), R1341Q (aquamarine), or WT (black). Resting washed platelets are shown in green. (C) Representative force-extension traces of H1268D (purple), R1341Q (aquamarine), and WT AIM-A1 (black). The extension event in each trace is marked by an arrowhead. (D) Superimposed plots of unfolding force versus unfolding

extension data and their fits to the worm-like chain model. Force data are presented as mean values ± standard deviation, and extension data are presented as the peak of the Gaussian fit ± the FWHM of Gaussian fit divided by the square root of counts. The data was obtained from n=52, 37, and 42 biologically independent single-molecule tethers for AIM-A1, H1268D, and R1341Q, respectively. (E) Regression of most probable unfolding forces fits to the Bell-Evans model. Unfolding force data are presented as the center of the tallest bin of the histogram ± one-half of the bin width. The data was obtained from n=52, 37, and 42 biologically independent single-molecule tethers for AIM-A1, H1268D, and R1341Q, respectively. Source data for (D-E) are provided in 2 worksheets of the Source Data file. (F) Structure of AIM-A1/VHH81 with highlighted interactions between H1268 (purple) to E1305 and R1341 (aquamarine) to E1264.

ristocetin binding (160) (Supplementary Fig. 2.9A). Although 6G1 was unable to induce full platelet aggregation with plasma VWF, it dose-dependently induced aggregation of washed platelets incubated with 60 nM AIM-A1 (Fig. 4A, Supplementary Fig. 2.9B,C). The extent of platelet aggregation induced by 6G1 was significantly greater than that by anti-His-tag antibody at the same concentration, confirming that the effects of 6G1 on platelets were due to more than its divalent structure. Upon addition of 6G1 to the optical trap, most pulling traces of AIM-A1 showed a single smaller extension event with a lower unfolding force (Supplementary Fig. 2.2, Fig. 2.4B, C). Unfolding force of AIM-A1 with 6G1 is similar to that of NAIM-A1 with 6G1 but not A1-CAIM with 6G1, suggesting that 6G1 treatment disrupts folding of CAIM and/or its cooperativity with NAIM (Fig. 2.4D). In contrast to 6G1, a conformation-dependent monoclonal antibody CR1 that binds A1 and inhibits ristocetin-induced platelet aggregation (160) did not alter the mechanical property of the AIM (Supplementary Fig. 2.3, 2.10). Overall, these results indicate that the AIM can be disrupted by displacement of the CAIM through binding to 6G1. Since the 6G1 epitope overlaps significantly with the ristocetin-binding site (88), ristocetin may activate A1 by disrupting the AIM in a similar manner.

VHH81 binds to the NAIM and impedes AIM-A1-induced platelet aggregation

As both type 2B mutations and the antibody 6G1 activate A1 binding to GPIbα by destabilizing the AIM, we tested next if an exogenous factor can stabilize the AIM and inhibit A1 binding. Caplacizumab (ALX-0081) was recently approved by the FDA to treat thrombotic thrombocytopenic purpura (TTP), a disease characterized by presence of active ultra-large VWF multimers due to insufficient ADAMTS13 activity(181). Caplacizumab binds to VWF and blocks its interaction with platelet GPIbα(182), but its mode of inhibition has not been

Figure 2.4

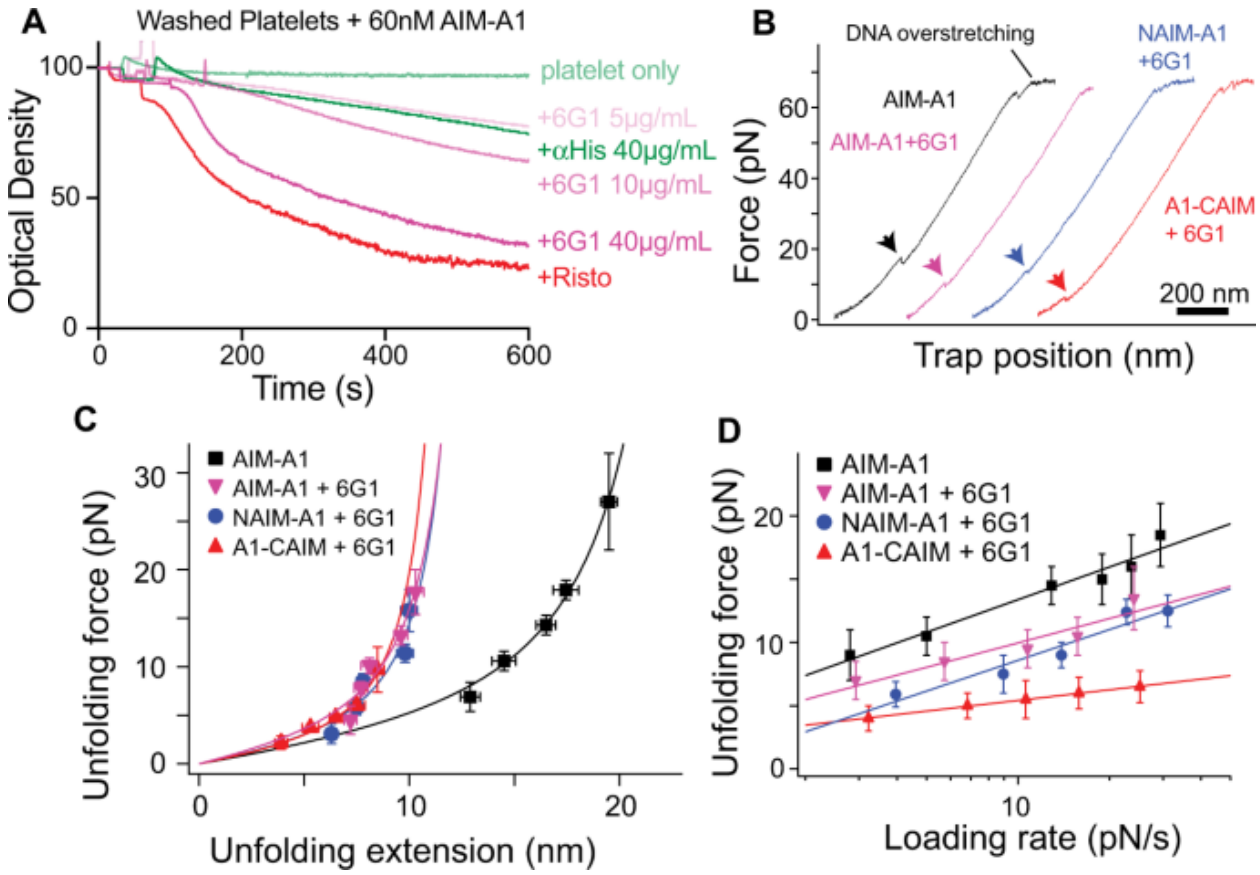

Figure 2.4 Disruption of AIM cooperativity by 6G1 activates A1.

(A) Washed platelet aggregation in response to 1.5 mg/mL ristocetin (red), various concentrations of Mab 6G1 (pink) or anti-His-tag Mab (dark green) with 60 nM AIM-A1. Resting washed platelets are shown in light green. It should be noted the relative molarity for activation of 60 nM AIM-A1 is considerably lower for 6G1 compared to ristocetin, approximately 300 nM and 730 μM respectively. (B) Representative force-extension traces of AIM-A1 alone (black) and AIM-A1 (pink), NAIM-A1 (blue), and A1-CAIM (red) in the presence of 30 μg/mL 6G1. The extension event in each trace is marked by an arrowhead. (C) Superimposed plots of unfolding force versus unfolding extension data and their fits to the worm-like chain model. Force data are presented as mean values ± standard deviation, and extension data are presented as the peak of the Gaussian fit ± the FWHM of Gaussian fit divided

by the square root of counts. The data was obtained from n=52, 58, 42, and 51 biologically independent single-molecule tethers for AIM-A1, AIM-A1 + 6G1, NAIM-A1 + 6G1, A1-CAIM + 6G1, respectively. (D) Regression of most probable unfolding forces fit to the Bell-Evans model. Unfolding force data are presented as the center of the tallest bin of the histogram ± one-half of the bin width. The data was obtained from n=52, 58, 42, and 51 biologically independent single-molecule tethers for AIM-A1, AIM-A1 + 6G1, NAIM-A1 + 6G1, A1-CAIM + 6G1, respectively. Source data for (C, D) are provided in 2 worksheets of the Source Data file.

elucidated. Caplacizumab is composed of two copies of the nanobody PMP12A2h1 (designated as VHH81 in this paper) linked by a tri-alanine sequence(182). In this study, monomeric recombinant VHH81 was produced in bacteria and it bound purified VWF and plasma-derived VWF with ~20-nM affinity (Supplementary Fig. 2.11). Consistent with previous reports (182; 183), VHH81 dose-dependently inhibited ristocetin-induced binding of AIM-A1 to platelet GPIb-IX and platelet aggregation (Supplementary Fig. 2.12).

Through binding of various truncated AIM-A1 proteins with a FLAG-tagged VHH81, the binding epitope of VHH81 was mapped to include VWF residues 1261-1267 as VHH81 bound with high affinity to tAIM-A1 (containing VWF residues 1261-1472) and other NAIM-containing proteins, but not A1-CAIM (Fig. 2.5A-C, Supplementary Fig. 2.13, 2.14). Consistently, VHH81 could impede aggregation of washed platelets induced by aforementioned AIM-A1 proteins except A1-CAIM (Fig. 2.5D-F, Supplementary Fig. 2.15).

To further characterize the interaction of VHH81 with AIM-A1, the crystal structure of a complex of VHH81 with a VWF fragment 1238-1481 was determined to 2.1-Å resolution (Fig. 2.6, Supplementary Fig. 2.16; Supplementary Table 2.1; Supplementary Video 2.1). In the structure, many residues, including residues 1262-1267 and some in the A1 domain, are in direct contact with all three complementarity-determining region (CDR) loops of VHH81 (Fig. 2.6A). For instance, VWF residue R1274 forms a salt bridge to the side chain of E105 in CDR3, and residues 1262-1267 pack around Y32 in CDR1. Some CAIM residues also make contact with VHH81, such as the side chain of E1463 with backbone amides of R103 and A104 in CDR3. Also pertinent to this study is the hydrogen bond between side chains of E1264 and R1341, which has not been observed in any previous structures of A1 (Fig. 2.3F). Moreover, comparison of the AIM-A1/VHH81 complex structure to previously reported A1 structures, especially the

Figure 2.5

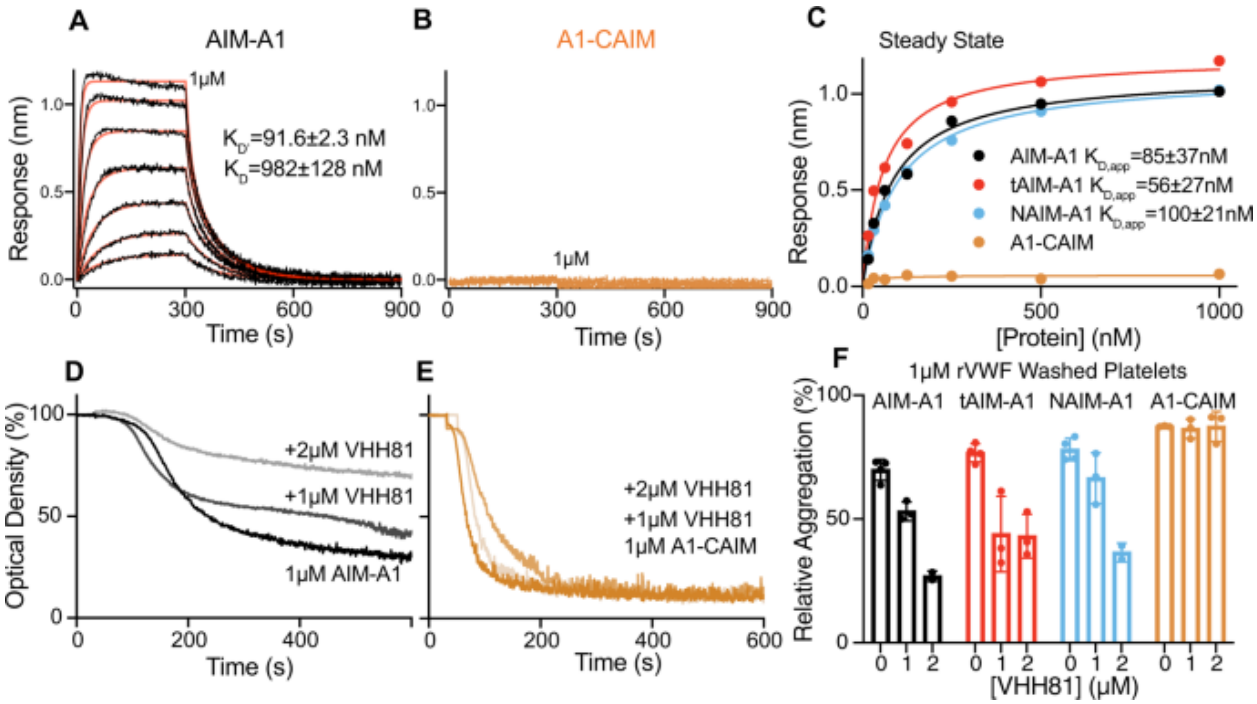

Figure 2.5 VHH81 binds to the NAIM to inhibit the A1-GPIbα interaction.

Sensorgrams of immobilized AIM-A1 (A) or A1-CAIM (B) binding to serial dilutions of VHH81 from 1 μM to 15.6 nM. Global curve fits are displayed in red over binding traces. Fitted equilibrium dissociation constants are shown as global fitted value ± standard deviation of the fit. No observable binding response was detected for A1-CAIM. (C) Steady state binding curves of VWF constructs to VHH81. Binding data shown in A,B and Supplementary Figure 14 are plotted and fit to a hyperbola. tAIM-A1 comprises residues 1261-1472. Washed platelet aggregation responses to AIM-A1 (D) and A1-CAIM (E) pre-incubated with 0, 1 or 2 μM VHH81. (F) Comparison of relative inhibition of washed platelet aggregation using various concentration of VHH81. In all cases 1 μM VWF fragments were used. Data are means ± standard deviation, n=3 per condition. Source data are provided in a worksheet of the Source Data file.

A1/LBD complex structure(76), reveals that the largest difference in VWF conformation lies in the α1β2 loop, as well as NAIM and CAIM residues, such that these residues appear to move away from the α1β2 loop upon binding of the LBD (Fig. 2.6B). In the AIM-A1/VHH81 complex, with residues 1463-1466 in position close to the α1β2 loop as shown in Figure 2.6C, the unresolved residues beyond 1466 (*i.e.* residues 1467-1481) would clearly interfere with LBD binding to A1.

VHH81 increases the mechanical stability of the AIM and is a shear-reversible antagonist of VWF

To characterize the effect of VHH81 on the AIM under tension, single-molecule force measurement was performed to monitor AIM unfolding in the presence of 1 μg/mL VHH81. VHH81 binding increased significantly the unfolding force for AIM-A1 at all loading rates and did not alter its contour length (Fig. 2.7A-C, Supplementary Fig. 2.3; Table 2.1). The energy difference between the transition states could be calculated as $\Delta G_{12} = k_B T \cdot \ln(k_1/k_2)$, where k_B is the Boltzmann constant, T is the absolute temperature, and k_1 and k_2 are the unstressed unfolding rate constants of two A1 variants used for comparison, respectively. Using this equation and the unstressed unfolding rates from Table 2.1, the activation energy difference between AIM-A1 with and without VHH81 is estimated to be 2.5 $k_B T$. Such enhanced unfolding activation energy may keep A1 masked under forces or shear stresses that would normally activate VWF. At the same time, such protection should be of a finite nature, since the VHH81-elevated force threshold could conceivably be still overcome by an even larger force, resulting in activation of VWF.

Figure 2.6

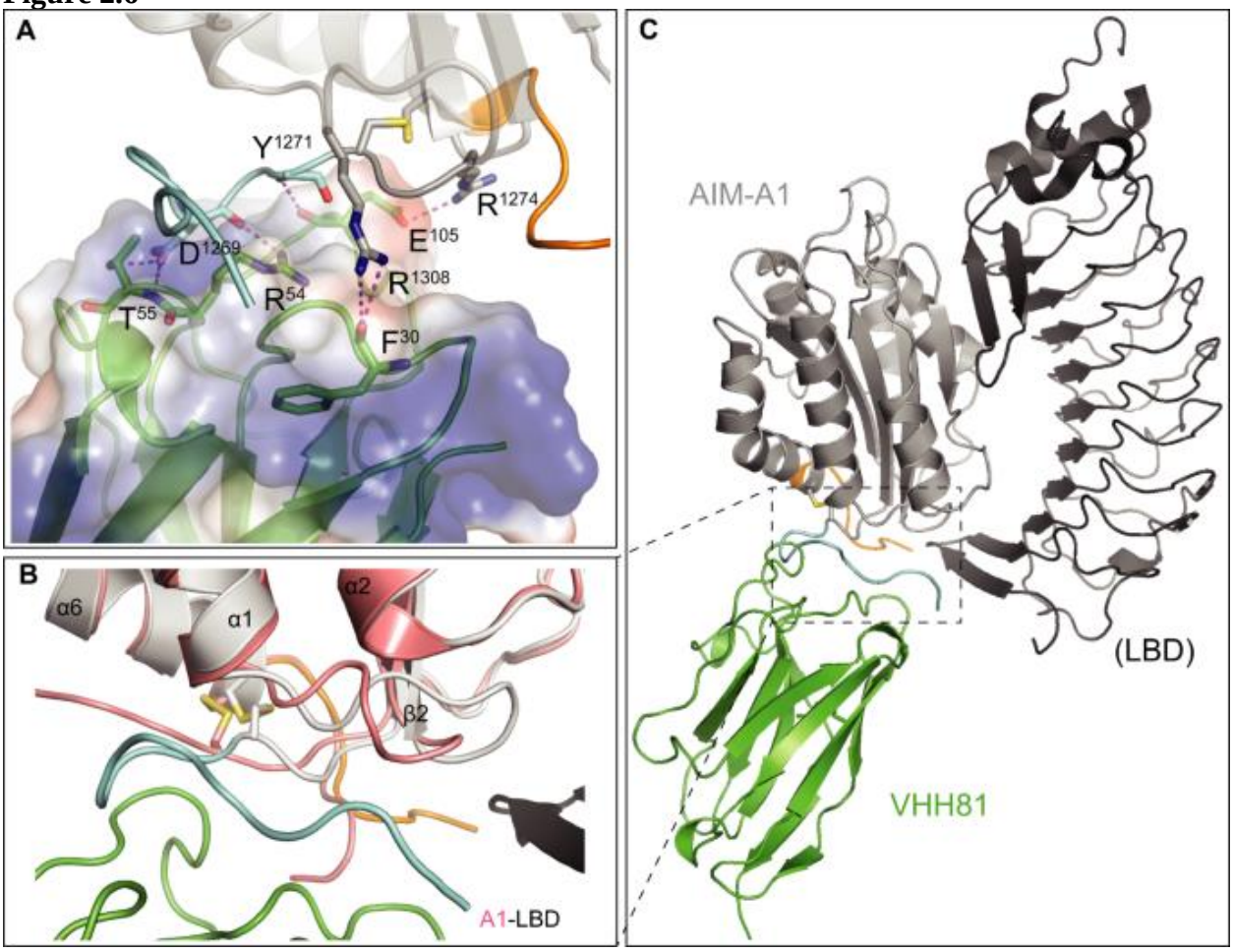

Figure 2.6 Crystal structure of the AIM-A1/VHH81 complex.

(A) Co-crystal of VHH81 with AIM-A1 (Protein data bank (PDB) ID: 7A6O [doi]). The nanobody is shown in green overlaid with electrostatic surface potential. AIM-A1 is shown in grey with NAIM in cyan and CAIM in orange. Specific contacts of VHH81 to VWF are labelled. For instance, VWF residue R1308 forms a hydrogen bond with the backbone carbonyl of F30 in CDR1, both backbone and side chain of D1269 make contacts with R54 and T55 in CDR2, residue R1274 forms a salt bridge to the side chain of E105, and the amide of Y1271 forms a hydrogen bond with the carbonyl of E105 in CDR3. (B) Conformational difference around the AIM between binding of VHH81 and GPIbα. Structures of the AIM-A1/VHH81 complex and the A1/LBD complex (PDB: 1SQ0 [10.2210/pdb1SQ0/pdb]) are superimposed by the shared A1

domain. Note that the α1β2 loop in A1 (colored salmon) in complex with LBD (black) is rotated upwards compared to the same loop in AIM-A1 (grey) in complex with VHH81 (green). In addition, resolved NAIM (cyan) and CAIM (orange) residues in AIM-A1 take on different conformations from those in A1. Some of them would be in steric hinderance with N-terminal residues in the LBD. (C) Overview of the two superimposed complexes. For clarity, the A1 domain in the A1/LBD complex is not shown. The dashed box outlines the interface area as highlighted in (B). Note that unresolved residues in the NAIM and CAIM would occupy the space surrounding the secondary GPIbα-binding site in the A1 domain.

Figure 2.7

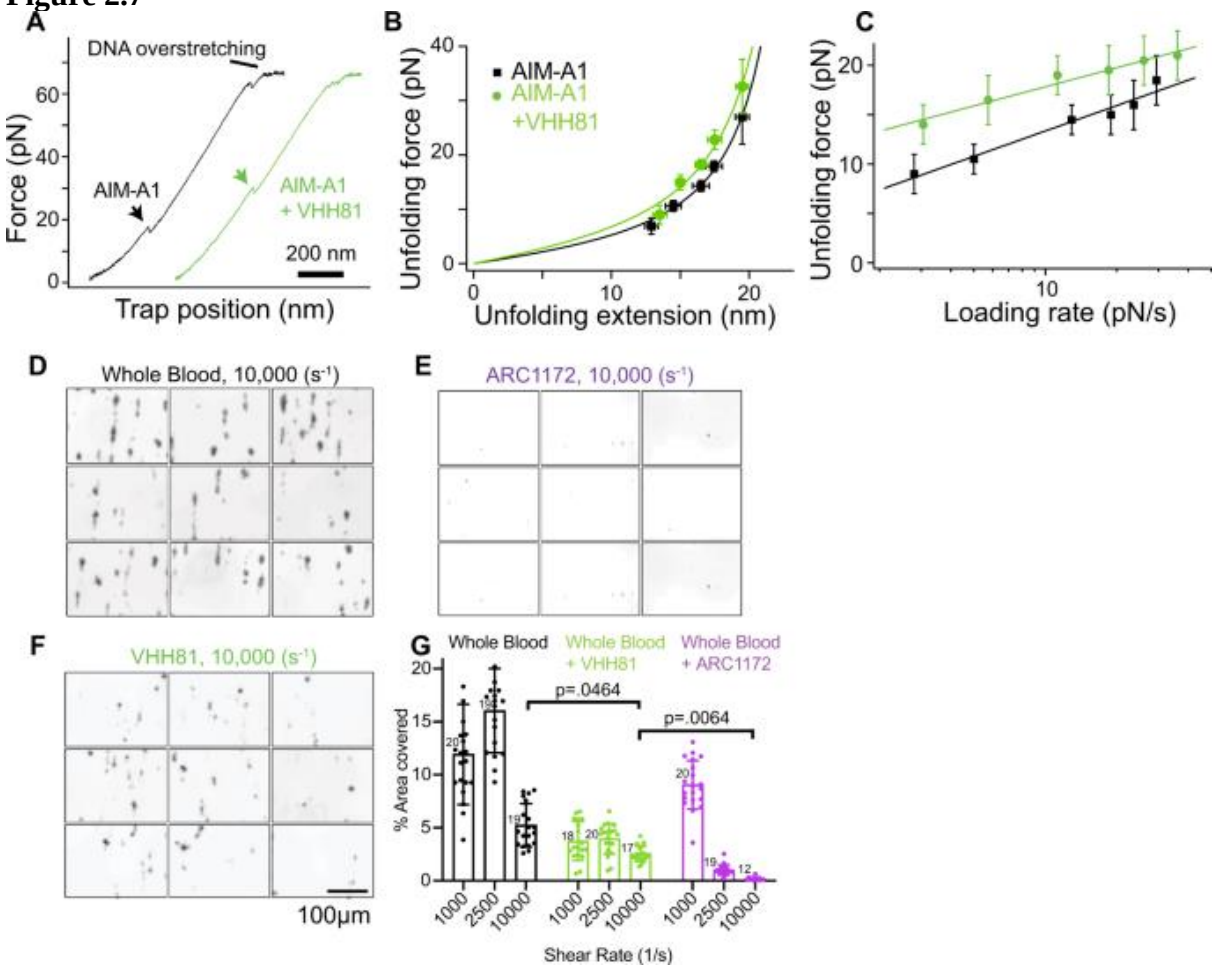

Figure 2.7. VHH81 acts as a shear reversible antagonist of A1-GPIbα by increasing the unfolding force of the AIM.

(A) Representative force-extension traces of AIM-A1 unfolding with 1 ug/mL VHH81 (green) and without (black). The extension event in each trace is marked by an arrowhead. (B) Superimposed plots of unfolding force versus unfolding extension data and their fits to the worm-like chain model. Force data are presented as mean values ± standard deviation, and extension data are presented as the peak of the Gaussian fit ± the FWHM of Gaussian fit divided by the square root of counts. The data was obtained from n=52 and 54 biologically independent single-molecule tethers for AIM-A1 and AIM-A1 + VHH81, respectively. (C) Regression of most probable unfolding forces fit to the Bell-Evans model. Unfolding force data are presented

as the center of the tallest bin of the histogram ± one-half of the bin width. The data was obtained from n=52 and 54 biologically independent single-molecule tethers for AIM-A1 and AIM-A1 + VHH81, respectively. (D-F) Comparison of perfused whole blood platelet adhesion to collagen at 10,000/s shear rate. No inhibitors (D), ARC1172 (1 μM, E), or VHH81 (14 μg/mL, F) was mixed with recalcified blood before perfusion. Scale bar is 100 μm. (G) Comparison between platelet coverage was analyzed with a 2-way ANOVA with mixed effects with Tukey's multiple comparison correction. P-values after multiple comparison correction are displayed for relevant groups. Data are means ± standard deviation with n=number of fields analyzed per condition. Interaction $F(4,155)=42.12$, shear rate $F(2,155)=67.17$, treatment $F(2,155)=169.6$. Source data for (B, C, G) are provided in 3 worksheets in the Source Data file.

Platelet adhesion, activation and aggregation over the collagen surface in a parallel-plate flow chamber has been extensively used to simulate blood clotting for hemostatic purposes(17). At high shear rates, plasma VWF immobilized to the collagen surface becomes essential in mediating platelet adhesion(17). Consistent with previous studies(182), infusing VHH81 with whole blood over the collagen surface significantly inhibited platelet adhesion at various shear rates (Fig. 2.7D-G, Supplementary Fig. 2.17, 2.18). Importantly, the inhibition by VHH81 was not complete, particularly at a shear rate of 10,000/s in which platelet adhesion is exclusively dependent on VWF(184; 185). In contrast, DNA aptamer ARC1172 or antibody 11A8, which directly blocks the VWF-GPIbα binding interface on A1 and LBD domains, respectively(88; 161), could completely abolish VWF-mediated platelet adhesion at high shear rates (Fig. 2.7G, Supplementary Fig. 2.17, 2.18). Since the 880-nM concentration of VHH81 used in this assay is much higher than its K_D for VWF, and much higher than that used *in-vivo* by typical dosing regimens(181; 183), VHH81 was likely bound to nearly all the A1 domain in plasma VWF (*i.e.* about 60 nM). This suggests that the incomplete inhibition by VHH81 is not due to incomplete binding to VWF. Thus, these results suggest that VHH81 inhibits the VWF-GPIbα interaction by a mechanism that protects the AIM from forces that would normally activate VWF.

2.5 Discussion

Coupling structural, functional and single-molecule analysis, we have provided the first evidence for a cooperative mechanical modulation of A1 binding by both halves of the discontinuous AIM. Deletion of either half of the AIM, introduction of a type 2B VWD mutation at the AIM/A1 interface, or addition of a ristocetin-mimicking antibody that binds to CAIM residues results in significantly decreased mechanical stability of the AIM and drastically

increased activity of A1. These results suggest that widely documented factors of VWF activation, such as shear force, type 2B VWD mutations, and ristocetin, may share a common molecular mechanism — by destabilizing or disrupting the AIM and its shielding of the A1 domain (Fig. 2.8, Supplementary Video 2.2).

Numerous studies have reported that residues flanking the A1 domain could affect A1 binding to GPIbα and VWF activity(100; 104; 105). A plethora of recombinant A1 fragments with variable lengths and glycosylation patterns displayed a wide range of affinities for GPIbα, spanning tens of micromolar to tens of nanomolar(75; 78; 80; 100; 186; 187). However, there has not been a coherent model to account for all the reported observations. For instance, it was postulated that a N-terminal flanking sequence, residues 1238-1260, interacts with and shields A1(146). But this model could account for neither the sensitivity of residue 1472 polymorphism to ristocetin nor type 2B mutations in the C-terminal flanking region(110). It was also postulated that residues immediately outside the 1272-1458 disulfide bond modulate A1 activity through their hydrogen bonding with A1(96). While this model could potentially explain activation by force or some type 2B mutations, it could not explain why the recombinant 1261-1472 fragment binds platelets with high affinity and readily induces platelet aggregation(88). Neither could it explain the type 2B-like activating effect by distal mutations such as T1255A(115; 116). Recently a model was proposed for a discontinuous AIM that consists of both N- and C-terminal flanking residues around A1(88). This AIM model was supported by the reduced hydrogen-deuterium exchange rates in both halves of the AIM, as well as enhanced protection at the GPIbα-binding site in A1(88). The cooperativity between NAIM and CAIM was postulated but lacked direct evidence. Relatedly, doubt was raised about the AIM as a distinct structural entity, as it was suggested that the flanking regions simply sterically occlude GPIbα binding(85). In

Figure 2.8

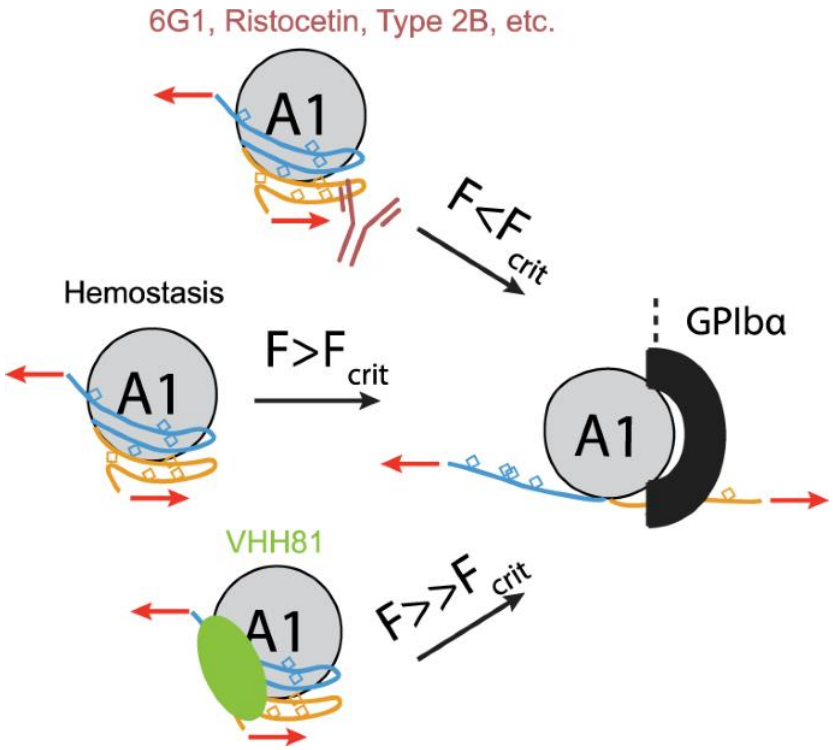

Figure 2.8. Molecular model of force induced VWF A1 domain activation via dissolution of the AIM.

During hemostasis, only above a critical force (F_{crit}), will the AIM unfold to expose the A1 domain for GPIbα binding. VWF bearing type 2B mutations, binding to ristocetin, or Mab 6G1 lowers the critical unfolding force of the AIM, allowing GPIbα to bind under lower tensile forces. VWF bound to VHH81 is able to withstand forces that would normally activate A1 and increases the critical unfolding force of the AIM.

this study, we demonstrated that the AIM constitutes a single structural unit as it unfolds under tensile force mostly in a single extension event instead of separate unfolding events of NAIM and CAIM (Fig. 2.1F). Importantly, the contour length increase of 26.6 nm (Fig. 2.1, Table 2.1) corresponds to about 67 residues present in unstructured regions after the unfolding event, which most likely include both NAIM and CAIM. The unfolding force of the AIM is greater than the individual unfolding forces of NAIM and CAIM, providing additional evidence supporting the cooperativity of NAIM and CAIM. Moreover, type 2B mutations or addition of the ristocetin-like antibody also disrupted cooperative unfolding of the AIM, resulting in significantly lowered unfolding force and shortened contour length.

Responses of full-length VWF and its fragments to mechanical force have been studied using optical or magnetic tweezers as well as atomic force microscopy. Several mechano-responsive elements therein have been identified, including the D4 assembly and the A2 domain(45; 46; 188-190). It is noteworthy that the unfolding force of the AIM is 15-20 pN, which is similar to that of the A2 domain. A recent study estimated the local tensile force necessary to activate A1 in full-length multimeric VWF as 21 pN(97), which is in line with the unfolding forces of the AIM. The D'D3 assembly and A2 domain have been suggested to modulate A1 binding to GPIbα(118; 121; 123; 191). Considering the proximity of these domains to AIM and A1, it is not unreasonable to speculate they may also affect the mechanical stability of the AIM through their interactions. The details of such modulation await future investigation.

Our results have provided several insights on the structural basis for the cooperativity of the AIM. In the AIM-A1/VHH81 complex structure (Fig. 2.6), in which the AIM is stabilized, residues 1238-1261 and 1265-1481 are not resolved. They do not appear to assume a stable structure. Considering the large contour length of the AIM as well as the reduced hydrogen-

deuterium exchange rates in some residues therein(88; 89), a likely scenario is that these residues are partially folded, but they interact specifically with each other to form a cohesive module. Certain mutations, such as at residues D1261 and T1255(102; 115; 116), may conceivably disrupt these interactions, destabilize the AIM, and produce type 2B-like effects. On the other hand, although no direct contacts are observed between NAIM and CAIM residues that are resolved in the complex structure, many of them form hydrogen bonds and salt bridges with residues in the A1 domain, sometimes through a water molecule. Thus, in addition to NAIM and CAIM residues, those in the A1 domain may also contribute to the cooperativity in the AIM. It is not a coincidence that all of type 2B VWD mutations reported to-date are located at or near the AIM-A1 interface and should disrupt the elaborate interaction network thereof. In particular, our AIM-A1/VHH81 complex structure shows an interaction between residues 1264 and 1341 that has not been observed before (Fig. 2.3F). It is unknown if this interaction is present in AIM-A1 without VHH81 but could explain the activating effect of type 2B mutations at R1341. It may also provide structural evidence for the increase in force resistance of the AIM when bound to VHH81. Similarly, the AIM-A1 interface as observed in the complex structure illustrates the effects of many type 2B mutations such as P1337L and those of residues 1305, 1306, 1308 and 1309 at the base of the α1 helix or α1β2 loop could certainly disrupt the interactions between NAIM and A1. The exact residues responsible for cooperativity between NAIM and CAIM are subjects of future study and may yield new synthetic VWD mutations.

The interaction of platelet GPIbα with VWF through their respective LBD and A1 domains is critical to thrombus formation in many thrombotic diseases. It has been a target in the development of anti-thrombotic therapeutics for the last few decades(192). Many competitive inhibitors that directly block the binding site in either LBD or A1, including monoclonal

antibodies, conformationally constrained peptides, DNA aptamers, and snake venom derivatives, have been reported(193-198). Since the GPIbα-VWF interaction is essential to primary hemostasis, as genetic deletion of either protein would result in a severe bleeding disorder(149; 199), pharmacological inhibition of the interaction may lead to side effects of severe bleeding. Caplacizumab is the first and to-date the only inhibitor of the GPIbα-VWF interaction that has been approved by the FDA(143; 181). TTP patients treated with caplacizumab showed a small risk of a bleeding event, mostly limited to epistaxis or gingival bleeding. The severity of these events was low and almost entirely resolved without intervention(143; 181). In this study, we show that VHH81 differs from all the previously reported inhibitors of the GPIbα-VWF interaction. It does not directly interfere with the GPIbα-binding site in A1 but rather binds to primarily NAIM residues. VHH81 stabilizes the AIM-A1 interface, as exemplified by the interaction between residues 1341 and 1264, and increases the unfolding force threshold for the AIM. In other words, binding of VHH81 raises the shear threshold of VWF mechanoactivation (Fig. 2.8). These results could explain why at very high shear rates VHH81 could not completely abolish VWF-mediated platelet adhesion, whereas traditional antagonists such as ARC1172 could and thus would render VWF completely incapable of platelet capture at high shear rates as required for normal hemostasis (Fig. 2.7F). This critical difference may help explain the lack of major bleeding risk with caplacizumab. While inhibiting the GPIbα-VWF interaction always presents a risk of bleeding, our results suggest that the approach of targeting the AIM may be more productive with less impact on hemostasis than that of direct antagonism of the A1 domain.

As VWF is critical to primary hemostasis and also a number of thrombotic diseases, its level, size, and binding activity are tightly regulated. In this study we have provided evidence supporting a model of the discontinuous AIM as the mechanism of VWF mechanoactivation.

This model may also be applicable to other scenarios of VWF activation, including type 2B VWD and ristocetin-induced platelet aggregation. While the AIM can be destabilized or disrupted for an increase in VWF activity, it could also be stabilized with anti-thrombotic consequences. These observations suggest that modulation of the AIM, mechanically or thermodynamically, may be a common mechanism for regulation of VWF function. Furthermore, to the best of our knowledge, VHH81 is the first reported case by which a drug modulates the function of its target via mechanically linked allostery. As an increasing number of mechanosensors and mechanoreceptors are being identified and linked to a variety of diseases, the example of VHH81 suggests they could be likewise targeted for mechanical modulation and therapeutic purposes.

2.6 Acknowledgements

This work was supported in part by NIH research grants (HL082808, HL143794, and HL152348), NIH training grants (GM008602 and GM008367), a studentship grant from the British Heart Foundation (FS/18/70/33893) awarded to JE/AB, and an infrastructure grant from Hemophilia of Georgia Center for Bleeding & Clotting Disorders of Emory. NAA was supported in part by AHA grant 20PRE34990025 and NIH fellowship HL154656. ERL was supported in part by NIH fellowship HL149357. The authors would like to thank Diamond Light Source for beamtime (proposal MX19880), and the staff of beamlines I04 for assistance.

2.7 Supplemental Information

Digital assets, supplemental movies, and source data associated with this publication can be located at:

https://doi.org/10.1038/s41467-021-22634-x

Supplemental Tables

Supplementary Table 2.1. Data collection and refinement statistics of solved crystal structure of a recombinant VWF fragment (residues 1238-1481) in complex with VHH81.

Space group	P 4_32_12
Cell dimensions	
a, b, c (Å)	65.2, 65.2, 233.3
α, β, γ (°)	90, 90, 90
X-ray Source	DLS I04
Wavelength (Å)	0.9795Å
Data Range (Å)	62.8 – 2.1
Reflections unique	19344
R_{merge} [a]	0.048 (0.850)
I / σI	15.1 (1.7)
Completeness (%)	92.4 (70.9)
Multiplicity	5.2 (4.9)
Refinement	
Resolution (Å)	62.8 – 2.1
R_{work} [b] / R_{free} [c]	0.191/0.251 (0.36/0.64)
Half-set correlation CC(1/2)	0.999 (0.645)
Atoms	
Nonhydrogen protein atoms	2626
Solvent	160
Ion (SO_4)	5
B-factors average (Å^2)	54.0
R.M.S.D	
Bond Lengths (Å)	0.0097
Bond angles (°)	1.727
Validation	
MolProbity Score	2.16 (70th percentile[d])
Clashscore, all atoms	5.88 (97th percentile[d])
Ramachandran Plot	
Most favoured	317 (96.35%)
Allowed	8 (2.43%)
Outliers	4 (1.22%)

[a] *R*merge = ∑hkl∑j |Ihkl,j - Ihkl|/∑hkl∑jIhkl,j, where Ihkl is the average of symmetry-related observations of a unique reflection. In brackets on the right are values from the outer, high resolution shell of the diffraction data.
[b] *R*work = ∑hkl ||*F*obs(hkl)|-|*F*calc(hkl)||/∑hkl|*F*obs(hkl)|.
[c] *R*free= The cross-validation *R* factor for 5% of reflections against which the model was not refined.
[d]100th percentile is the best among structures of comparable resolution.

Supplementary Table 2.2. Primers used in this study

Primer Name	5’ Sequence 3’
IgK-1268F	GCTAGCATGGAGACAGACACACTCCTGCTATGGGTGCTGC TGCTCTGGGTTCCAGGTTCCACTGGTAAGCACGATTTCTAC TGCAGCAGG
1268XbaStopR	TCTAGATCAATGATGATGATGATGATGATGATGATGATG
1493F	CTAGATACTAGTCAGGAGCCGGGA
1493RSpyStop	TAGCCTCTCGAGTCACTTAGTCGGCTTATATGCATCGACC ATAACGATATGGGCATGATGATGATGATGATGATGATGAT GATG
EL007	CGGAACCGCCGTTGGACGATTTCTACTGC
EL008	GCAGTAGAAATCGTCCAACGGCGGTTCCG
EL003	GCGACCGTCAGAGCTGCAGCGCATTGCCAGCCAG
EL004	GGCTGGCAATGCGCTGCAGCTCTGACGG
GPIba_Biotag	AGCTGGATCCGGCCTGAACGACATCTTCGAGGCTCA GAAAATCGAATGGCACGAACACCCCATCTGTGAGGTCTCC
GPIba290_2xFLAGstop	CTGACTCGAGTCATTTGTCATCATCATCCTTATAGTCTTTG TCATCATCATCCTTATAGTCACGCACCTTATCGCCCTCAGT
pD14_VHH81F	GCATCTCGAGTCAGTGGTGGTGATGATGATGGGATGACAC AGTTACC
pD14_VHH81R	GCAGCATATGGAGGTTCAACTTGTGGAGAG
MW002	AATCAGGATCCCAGGAGCCGGGAGGCCTG
MW003	TAAGACTCGAGTTACCCCGGGCCCACAGTGAC

Supplemental Figures

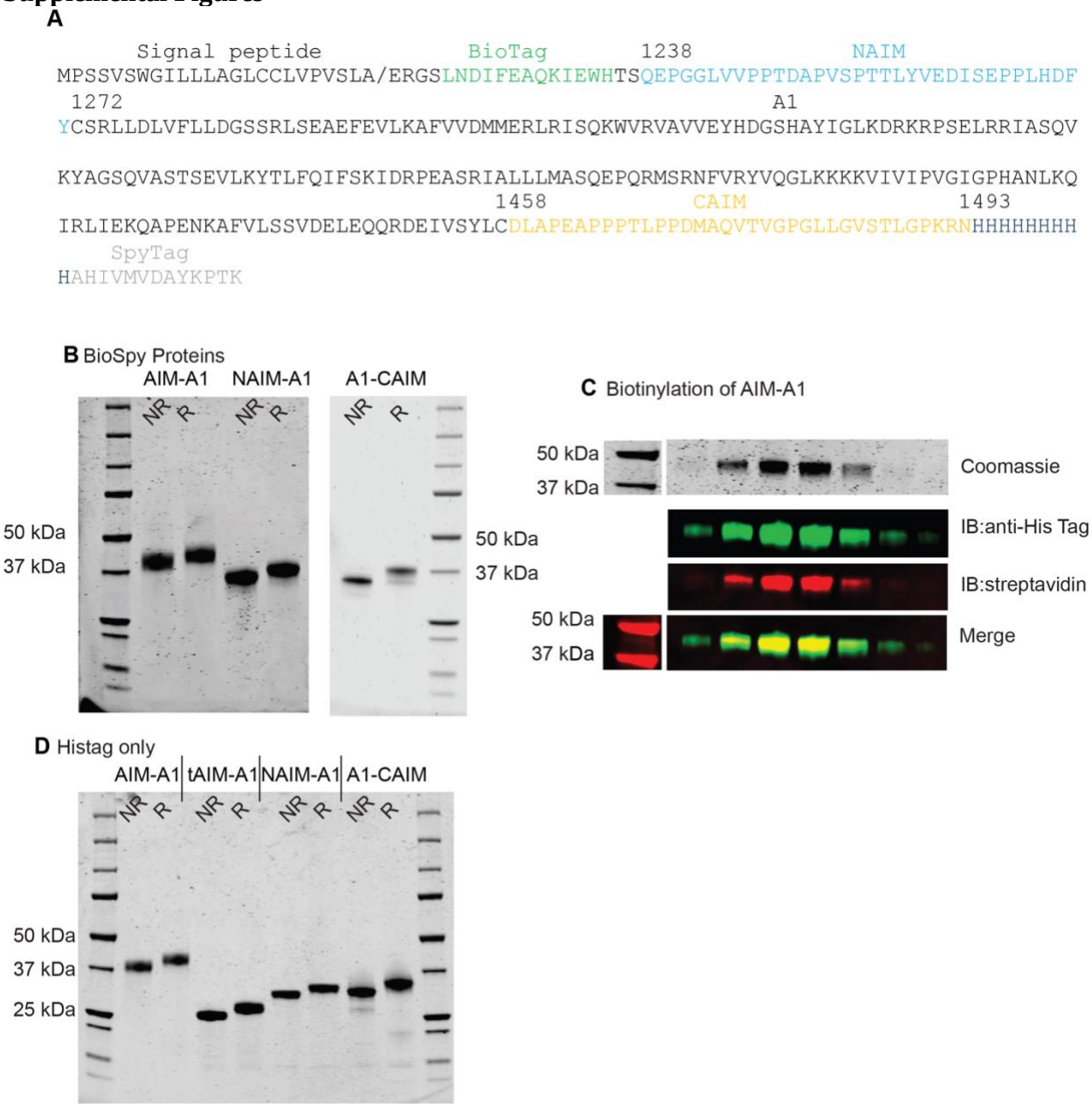

Supplementary Figure 2.1. Sequence of Biospy AIM-A1 and expression of rVWF Biospy fragments, rVWF-His Fragments, and GPIbα LBD.

(A) Sequence of Biospy 1238-1493 with corresponding labels for NAIM (cyan), A1 (black), CAIM (orange), Biotag (green), and SpyTag (grey). (B) Coomassie stained gels of Biospy proteins used for single-molecule experiments. The first lane corresponds to the molecular weight markers, with 50 kDa and 37 kDa labelled. These gels are the result after 4 successful

protein purification run. (C) Representative size exclusion fractions of Biospy 1238-1493 (AIM-A1) stained with Coomassie blue (top), blotted for anti-His tag (middle), and streptavidin (bottom). Merged images results in a yellow color, indicating that the protein bands are reactive to both streptavidin and anti-His tag antibody. These gels are the result after 2 successful protein purification run following ~3 runs to optimize preparation conditions. (D) Coomassie stained gels of rVWF fragments bearing only a poly-histidine tag on the C-terminus used for binding experiments and platelet aggregation. The gel shows the purity of various proteins that are prepared from 3-5 successful protein purification runs.

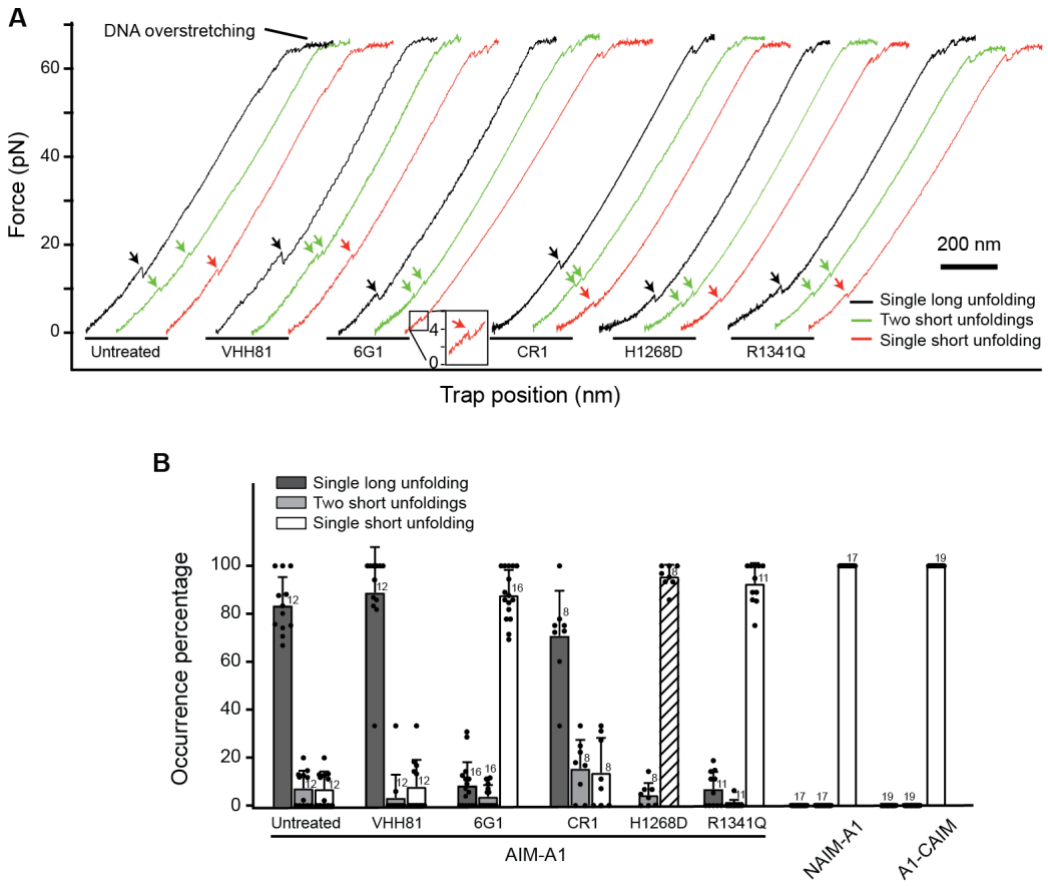

Supplementary Figure 2.2. Force-extension traces and unfolding extension grouping for all constructs tested.

(A) Representative force-extension traces (generated by pulling at 200 nm/s) of AIM-A1 alone, and treated with VHH81, CR1 or 6G1. Force extension traces of the type 2B VWD mutants are also included. The extension event(s) in each trace is marked by an arrowhead. Single unfolding events are represented by black traces, with two short unfolding traces in green and one short unfolding in red. Inset: a zoom-in view of a low force unfolding event. (B) Percentage of three unfolding types for different constructs pulled at 200 nm/s after relaxation under 1 pN for 1 second. The AIM-A1 construct unfolds as a singlet unfolding the majority of the time, while NAIM-A1 and A1-CAIM have lower force singlet unfolding. In some instances, two lower force unfolding events can occur, corresponding to NAIM and CAIM unfolding separately. *Mutation

H1268D resulted in a shortened AIM unfolding extension. As a result, we were not able to distinguish single-short and single-long unfolding signals. All single unfolding events are represented by the stripe-patterned bar. Error bars represent standard deviation. The data was obtained from n=12, 12, 16, 8, 8, 11, 17 and 19 biologically independent single-molecule tethers for untreated, VHH81, 6G1, CR1, H1268D, R1341Q, NAIM-A1, and A1-CAIM, respectively.

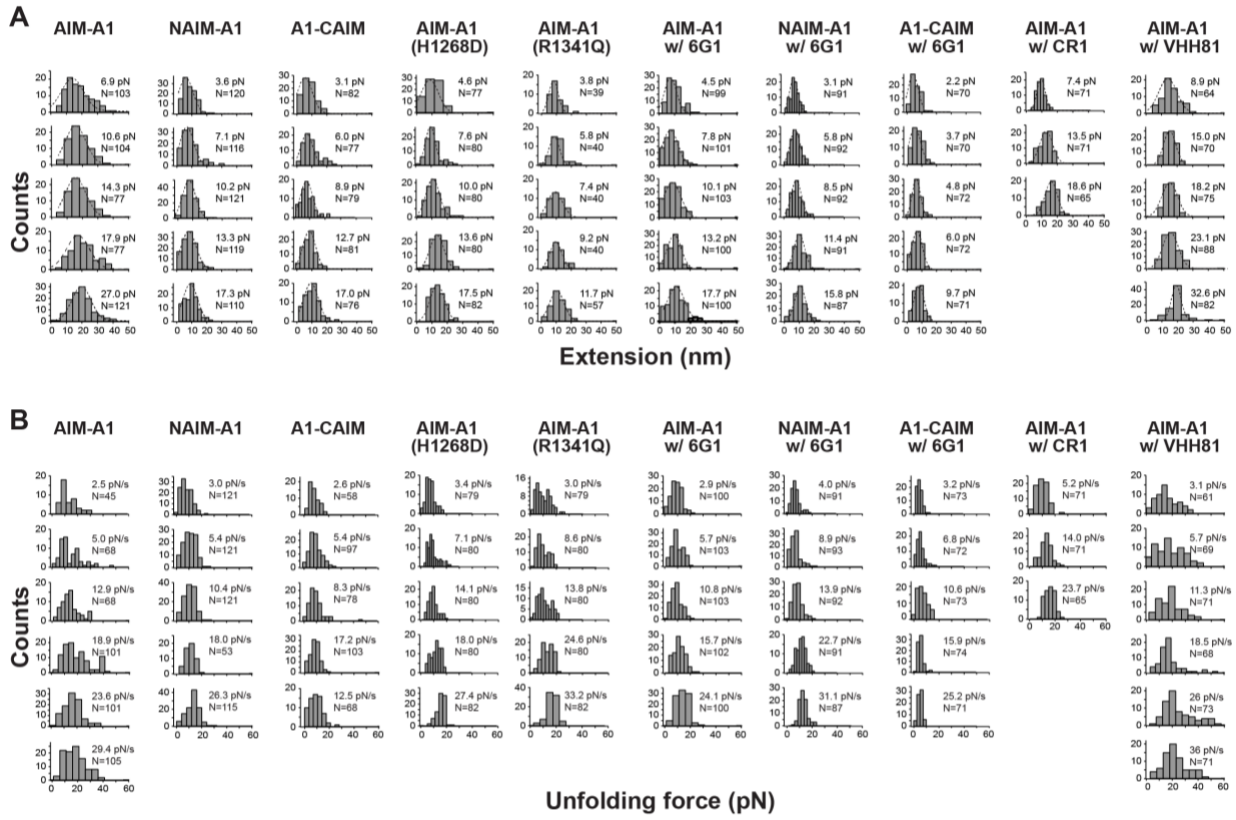

Supplementary Figure 2.3. Histograms of AIM unfolding in various fragments and additives.

(A) Unfolding extension histograms at various forces. A Gaussian fit is overlaid as a dashed line on each histogram. (B) Unfolding force histograms at various loading rates.

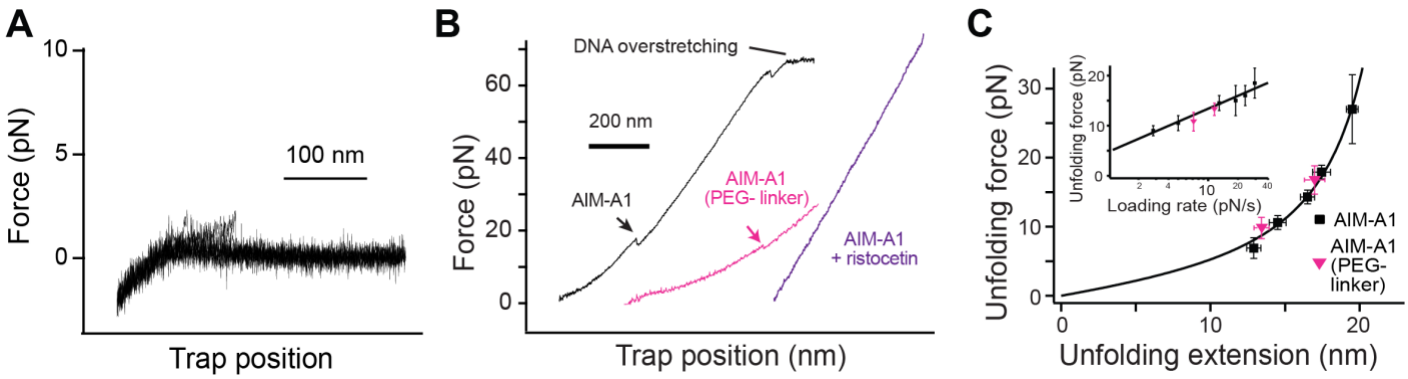

Supplementary Figure 2.4. The DNA handle does not interfere with AIM unfolding.

(A) Overlay of eight representative consecutive retraction traces of a DNA handle-coupled bead interacting with an AIM-A1 coupled bead. To address a potential concern that DNA may bind A1 through electrostatic interactions, AIM-A1 was immobilized on one bead and the DNA handle alone (no SpyCatcher) on another bead, no specific binding forces were observed between AIM-A1 and DNA, as non-specific forces between two beads are typically below 2 pN. (B) Typical force-trap position curves generated by pulling (200 nm/s) AIM-A1 using DNA handle method (black) and using PEG-linker (magenta), and AIM-A1 using DNA handle in the presence of 1 mg/ml ristocetin (purple). (C) Relationship between unfolding force and extension for unfolding events in AIM-A1 using DNA handle method (black) and using PEG-linker (magenta). Force data are presented as mean values ± standard deviation., and extension data are presented as the peak of the Gaussian fit ± the FWHM of Gaussian fit divided by the square root of counts. The data are fitted to a worm-like chain model (solid lines). Inset: the relationship between the most probable unfolding forces plotted against loading rate. Unfolding force data are presented as the center of the tallest bin of the histogram. Error bars are one-half of the bin width for unfolding force. The solid lines are fits to the Bell-Evans model. Note that although there was no overstretching signal in PEG-linked beads, similar magnitudes of AIM unfolding forces and

extensions were observed. The data was obtained from n=52 and 16 biologically independent single-molecule tethers for AIM-A1 and PEG, respectively.

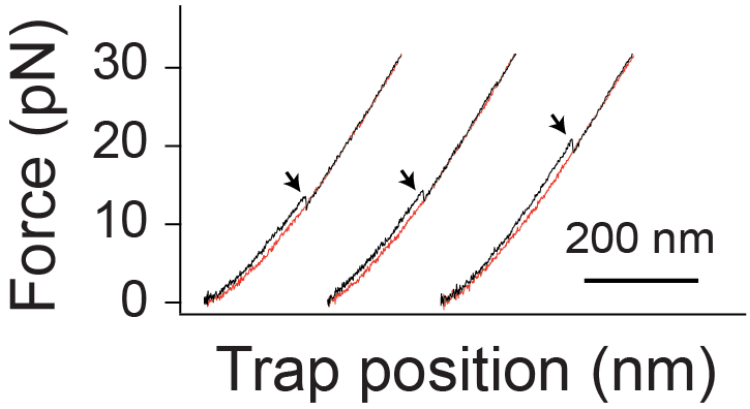

Supplementary Figure 2.5. Representative unfolding-refolding traces (generated by pulling at 200 nm/s) of AIM-A1.

Pulling and relaxation traces are shown in black and red, respectively. Arrows indicate unfolding (black) events.

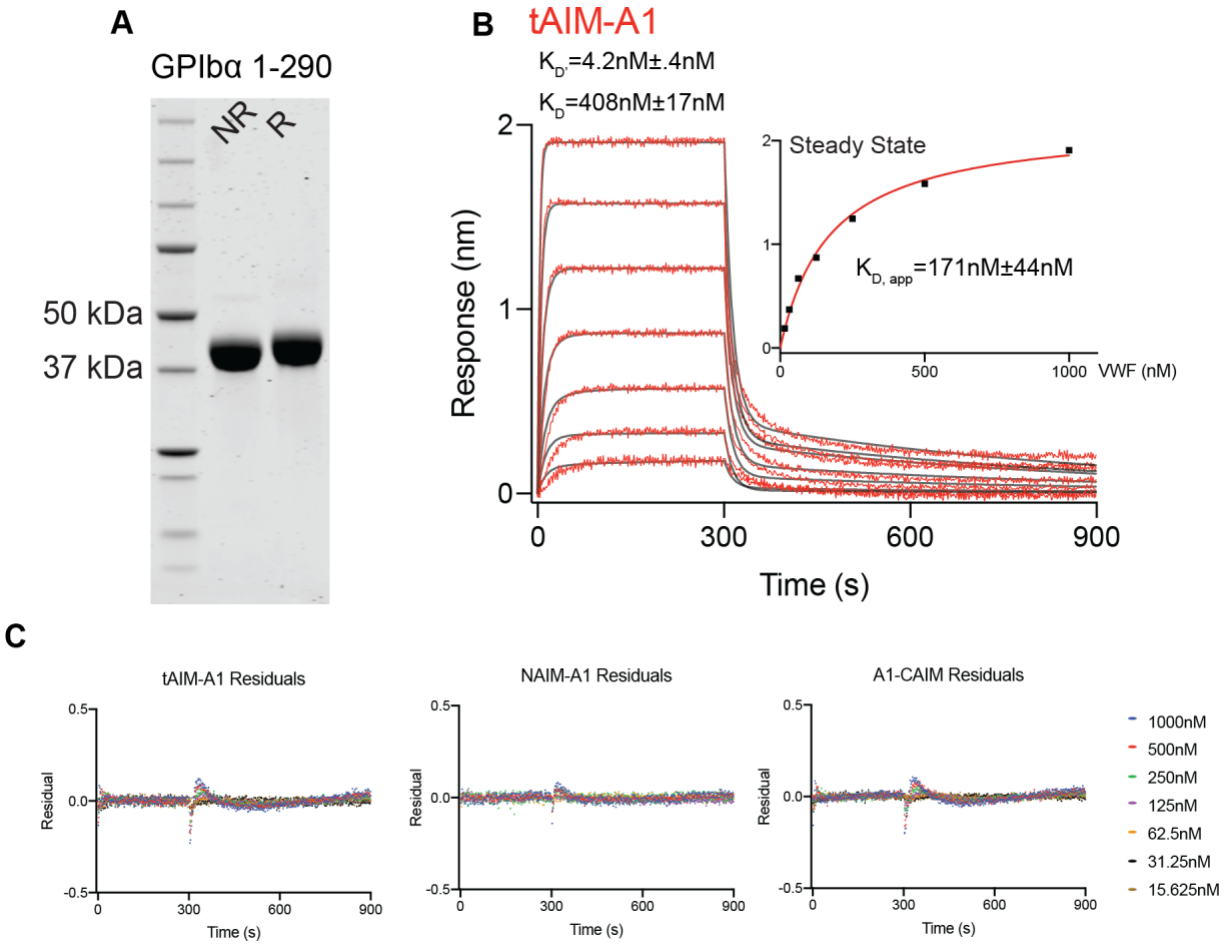

Supplementary Figure 2.6. Truncation of the AIM yields a highly active A1 fragment towards GPIbα.

(A) Coomassie blue stained gel of recombinant GPIbα LBD under non-reducing and reducing conditions. Lane 1 are molecular weight markers with 37 kDa and 50 kDa indicated. The gel shows one of the two batches of equally purified recombinant GPIbα LBD. (B) Sensorgram of rVWF 1261-1472 (tAIM-A1) binding to immobilized GPIbα. Fitting traces are underlaid in black. Inset is steady state fit to a hyperbola. K_D and $K_{D'}$ are presented as mean ± standard devation of individual fits while $K_{D,app}$ is shown as mean ± 95% confidence interval. (C) Residual plot versus time for the fittings subtracted from observed sensorgrams for GPIbα to tAIM-A1, NAIM-A1 and A1-CAIM.

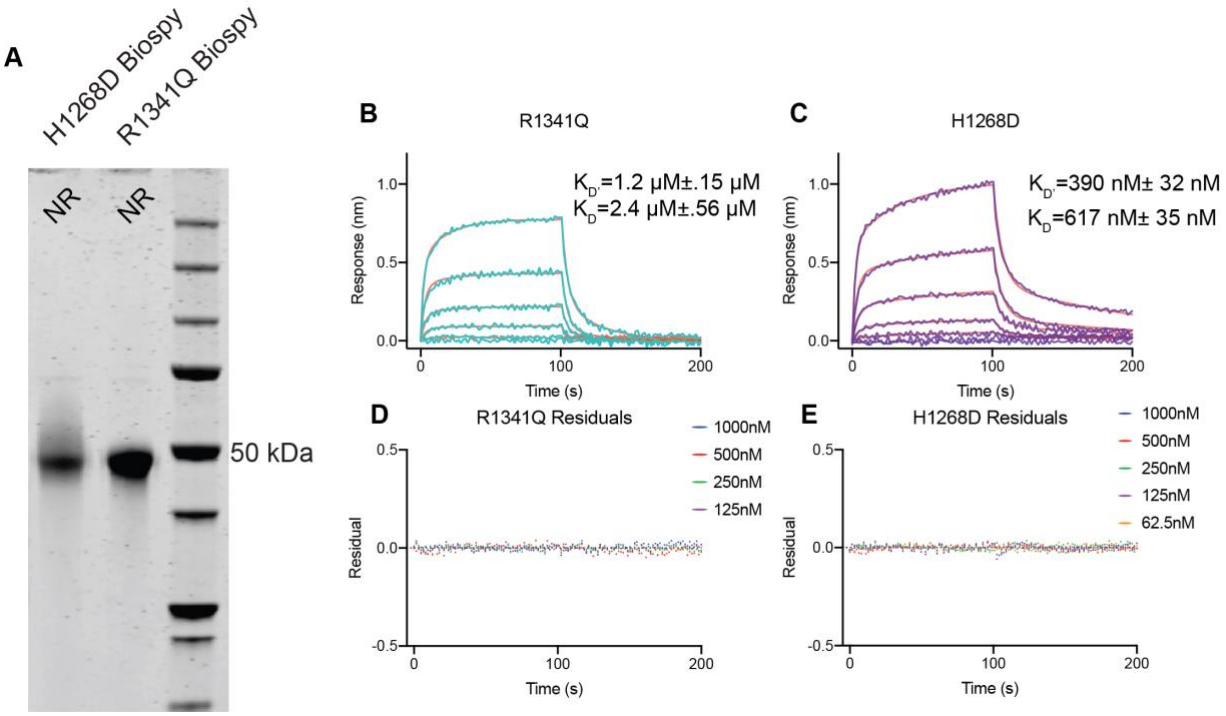

Supplementary Figure 2.7. Expression and binding of Type 2B VWD AIM-A1 mutants.

(A) Coomassie stained gel of H1268D and R1341Q Biospy mutants under non-reducing conditions. The lane on the right shows molecular weight markers with that of 50 kDa marked. The gel shows the result after two successful purification runs of H1268D and 3 runs of R1341Q. (B, C) Sensorgrams of a dilution series from 1 μM to 15.6 nM H1268D and R1341Q binding to immobilized GPIbα. Fitting overlaid in red is a heterogenous ligand binding model, K_D and $K_{D'}$ are presented as mean ± standard deviation of global fits for concentrations showing observable binding responses. (D, E) Fitting residual plots versus time for observed sensorgrams.

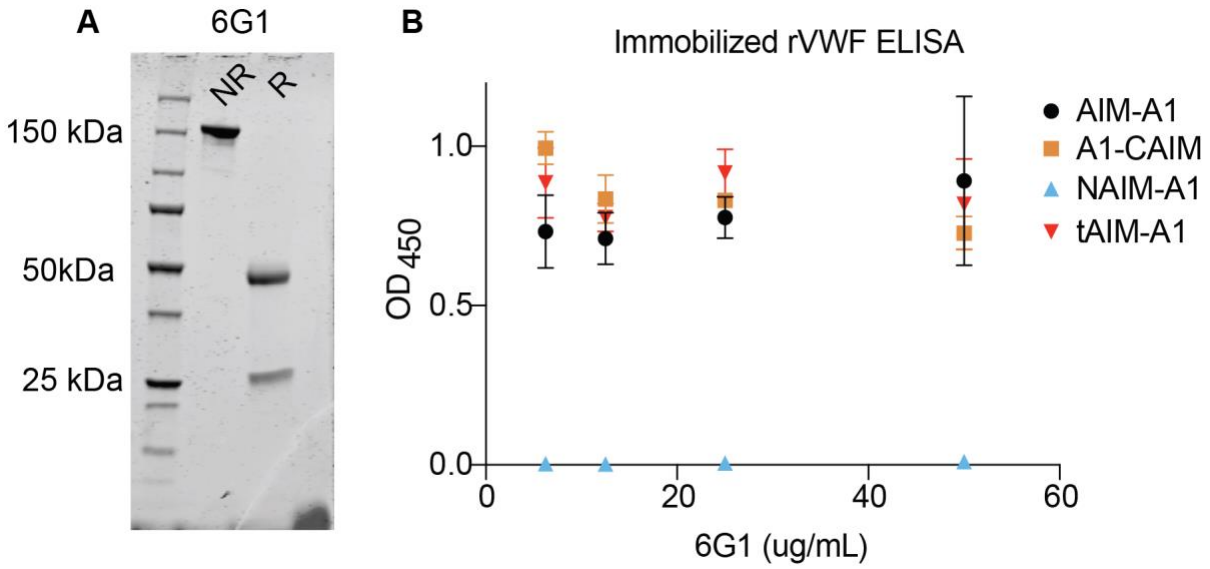

Supplementary Figure 2.8. Expression and binding site verification of monoclonal antibody 6G1.

(A) Coomassie stained gel of purified 6G1. Molecular weight markers are run in lane 1, with 150, 50 and 25 kDa highlighted. This gel is the result of 1 successful protein purification run that produced 4 mg of 6G1. (B) rVWF fragments were coated to an ELISA plate, and a dilution series of 6G1 binding was detected with anti-mouse secondary antibody. Data shown are means ± standard deviation, where each condition is done in triplicate (n=3). 6G1 binds to all recombinant fragments, except 1238-1461, confirming the binding site to previous works.

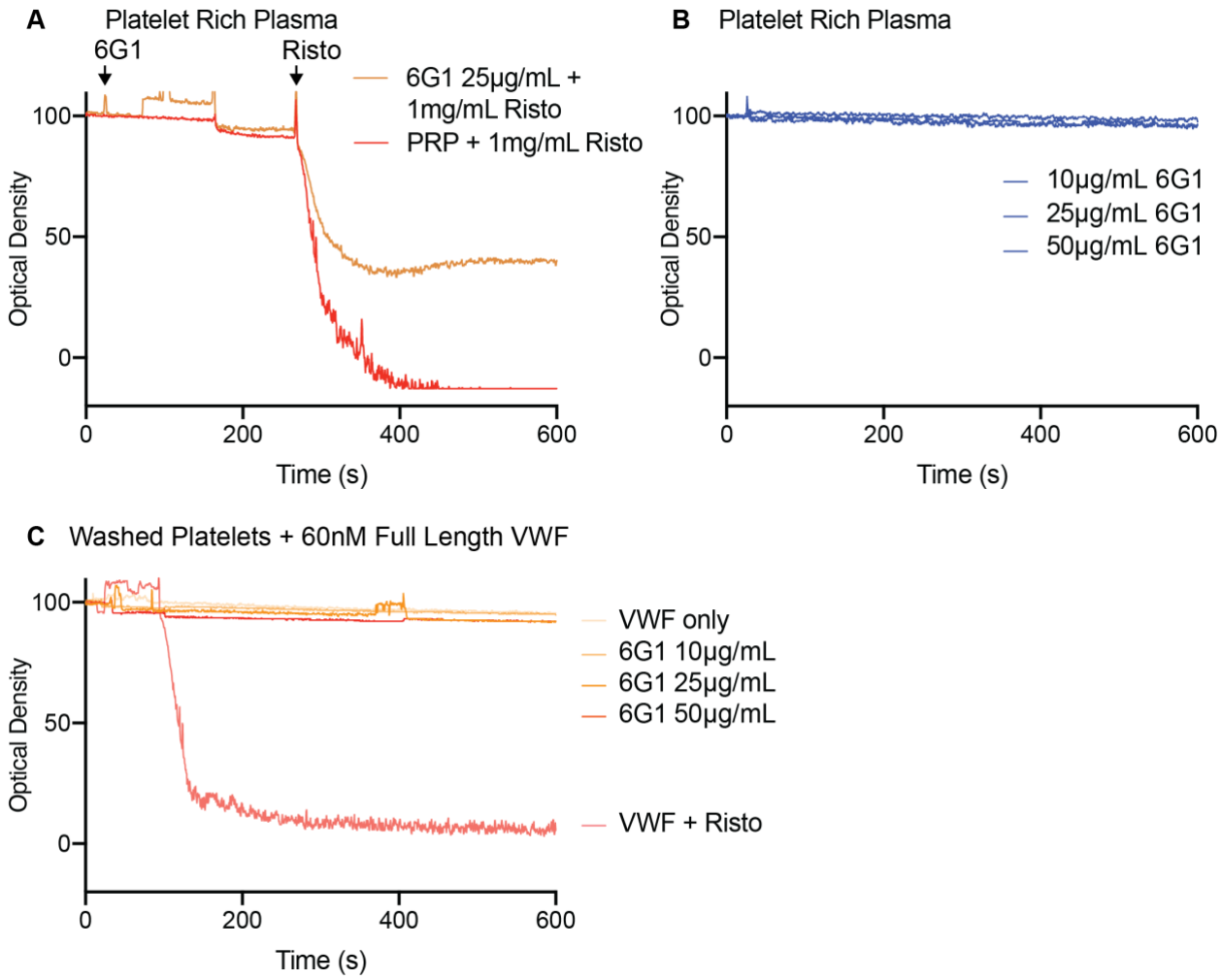

Supplementary Figure 2.9. The effects of 6G1 on platelet aggregation in the presence of full-length VWF.

Aggregometry traces of 6G1 in PRP (A), the effect of 6G1 on ristocetin induced platelet aggregation (B) and aggregometry of washed platelets with 60 nM full length VWF with 6G1 or ristocetin (C). 6G1 is able to reduce ristocetin induced platelet aggregation in platelet-rich plasma. 6G1 is unable to induce aggregation of full length VWF in washed platelets or in platelet-rich plasma.

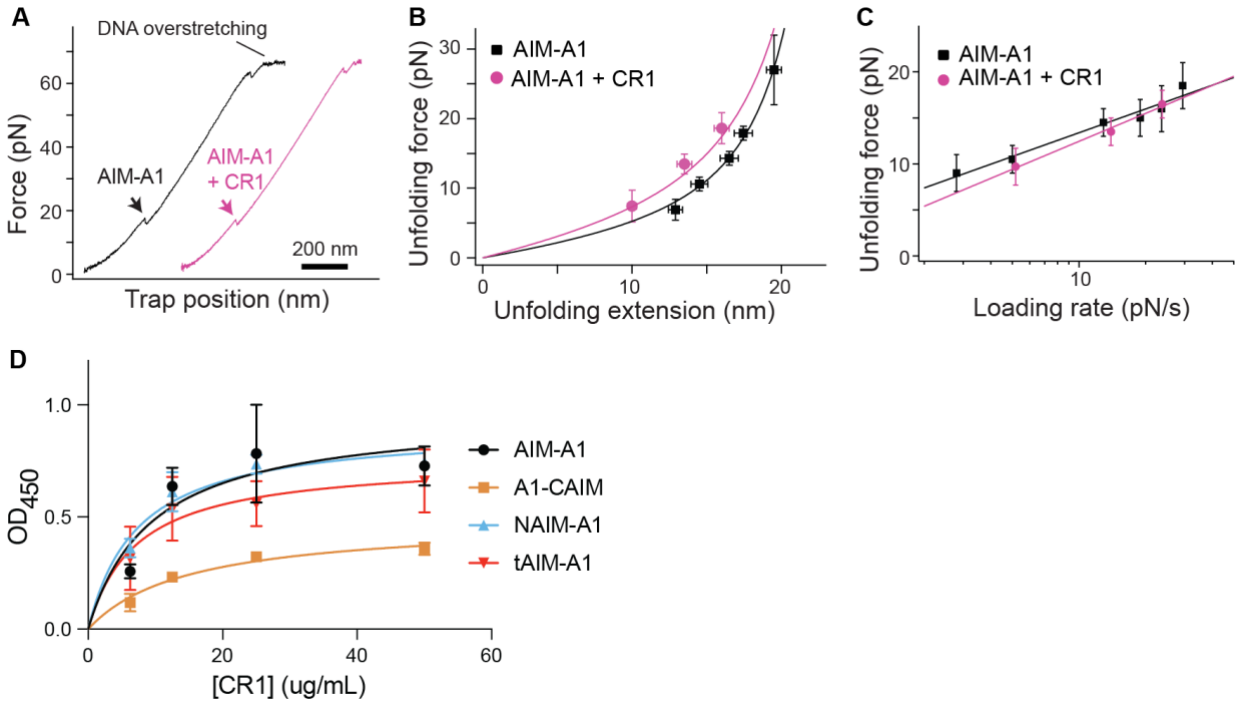

Supplementary Figure 2.10. Single-molecule characterization of AIM-A1 unfolding in the presence of monoclonal antibody CR1.

(A) Force-extension unfolding traces of AIM-A1 in the presence of CR1. The extension event in each trace is marked by an arrowhead. (B) Superimposed plots of unfolding force versus unfolding extension data and their fits to the worm-like chain model. Force data are presented as mean values ± standard deviation., and extension data are presented as the peak of the Gaussian fit ± the FWHM of Gaussian fit divided by the square root of counts. The data was obtained from n=52 and 28 biologically independent single-molecule tethers for AIM-A1 and CR1, respectively. (C) Regression of most probable unfolding forces fit to the Bell-Evans model. Unfolding force data are presented as the center of the tallest bin of the histogram . Error bars are one-half of the bin width for unfolding force. The data was obtained from n=52 and 28 biologically independent single-molecule tethers for AIM-A1 and CR1, respectively. (D) ELISA of immobilized VWF fragments to a dilution series of CR1. Data shown are means ± standard

deviation, where each condition is done in triplicate (n=3). Data are fit to a hyperbola. CR1 binds to all VWF fragments tested.

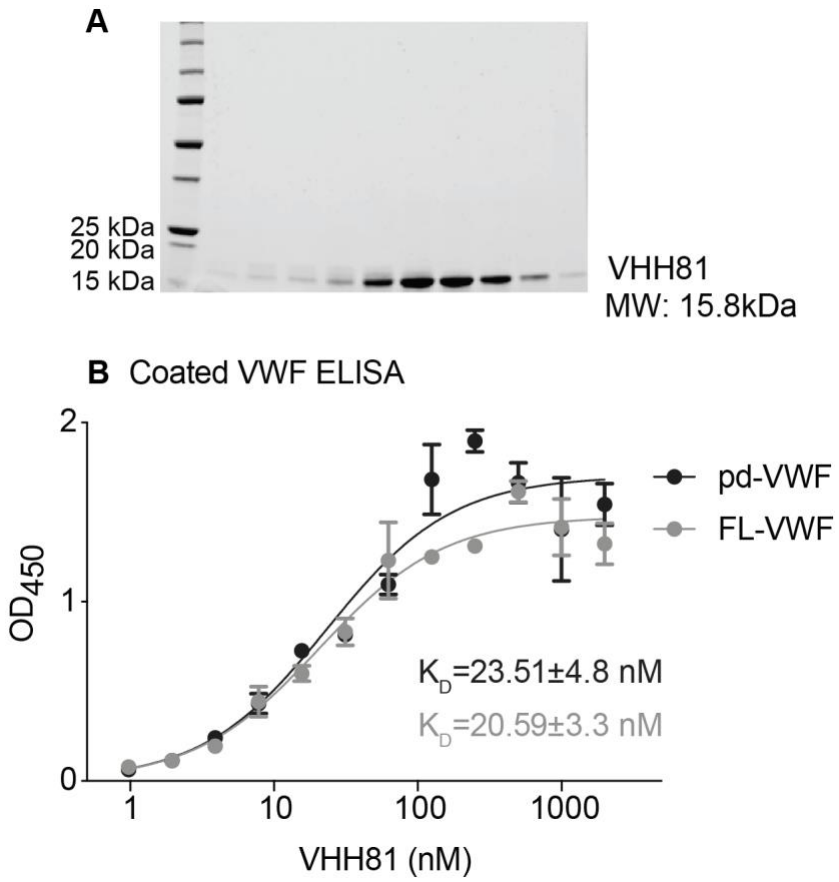

Supplementary Figure 2.11. Expression and binding of VHH81 to multimeric VWF.

(A) Representative Coomassie stained gel of size exclusion fractions of VHH81. Expected MW is 15.8 kDa. Molecular weight markers are in lane 1 with weights of 25, 20, and 15 kDa explicitly labelled. The gel shows one of the 5 batches of equally purified VHH81. (B) Binding isotherms of VHH81 to immobilized purified VWF (grey) and plasma derived VWF in Humate-P (black). Data shown are means ± standard deviation, where each condition is done in quadruplicate. K_D is presented as mean ± standard deviation from hyperbolic fitting.

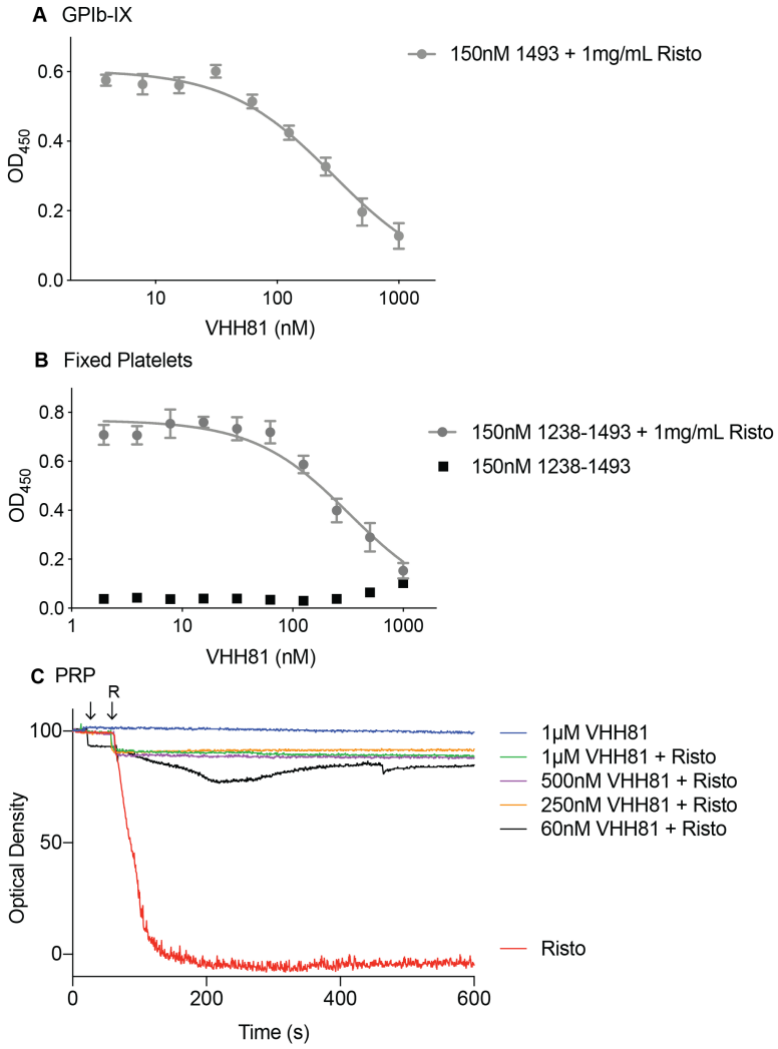

Supplementary Figure 2.12. VHH81 inhibition of VWF binding to GPIbα.

(A) 150 nM AIM-A1 + 1 mg/mL ristocetin was incubated with a titration of VHH81 to inhibit binding to purified GPIb-IX complex. Data shown are means ± standard deviation, where each condition is done in triplicate. (B) 150 nM AIM-A1 + 1 mg/mL ristocetin was incubated with a titration with VHH81 (grey) and without (black) to inhibit binding to fixed platelets. Data shown are means ± standard deviation, where each condition is done in triplicate. (C) Aggregation traces of platelet-rich plasma with various amounts of VHH81 in response to 1 mg/mL ristocetin. Arrows indicate the addition of VHH81 followed by the addition of 1 mg/mL ristocetin.

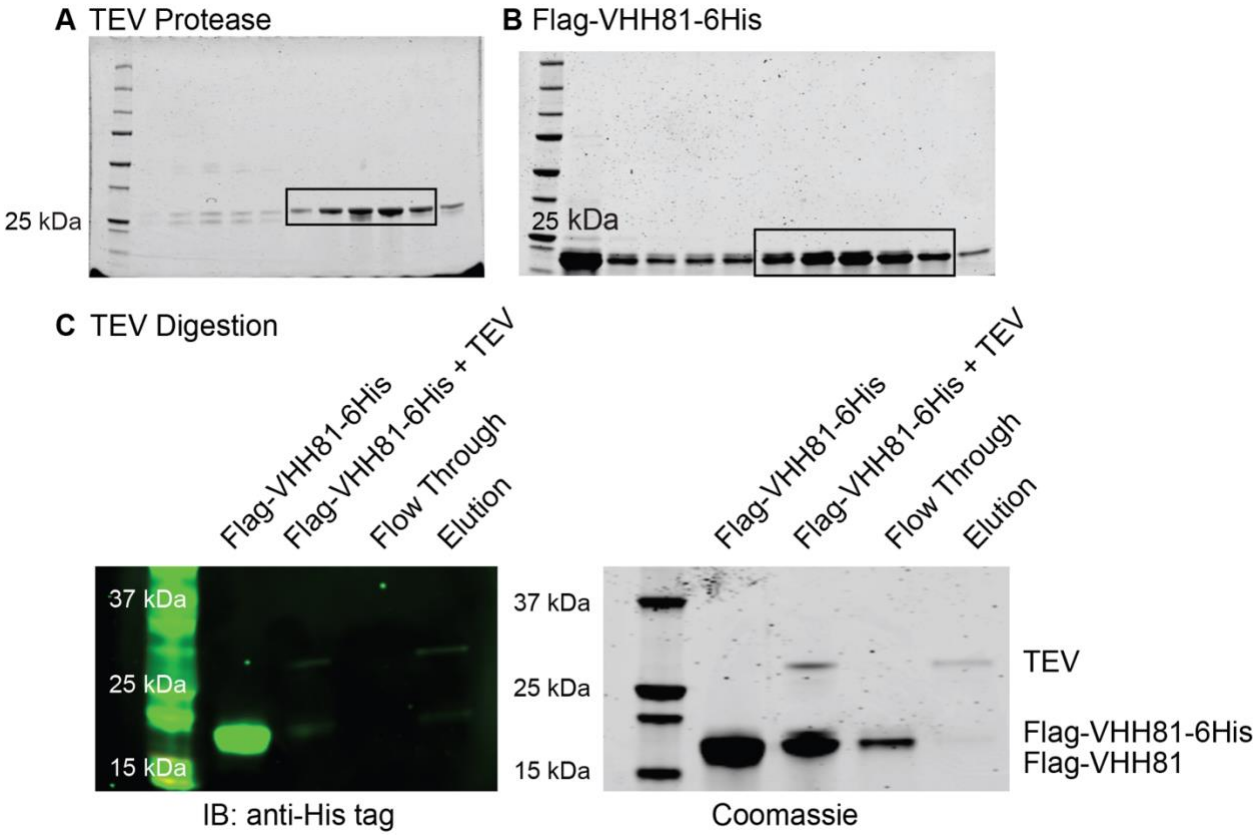

Supplementary Figure 2.13. Expression and purification of Flag-VHH81-6His.

(A) Size exclusion fractions of recombinant TEV protease. (B) Size exclusion fractions of Flag-VHH81-6xHis, bearing an N-terminal FLAG tag and C terminal TEV cleavable 6xHis Tag. Molecular weight markers are in the first lanes, with 25 kDa highlighted. (C) Immunoblot verification of Histag removal of in flow through of a Ni-sepharose column. TEV treatment of the protein removes identification of the protein by western blot through anti-His tag antibody. TEV-protease contains a His tag that was caught in the Ni-column. These gels demonstrate the quality of Flag-VHH81-6His from 2 successful purification runs, which followed 4 cycles of condition optimization.

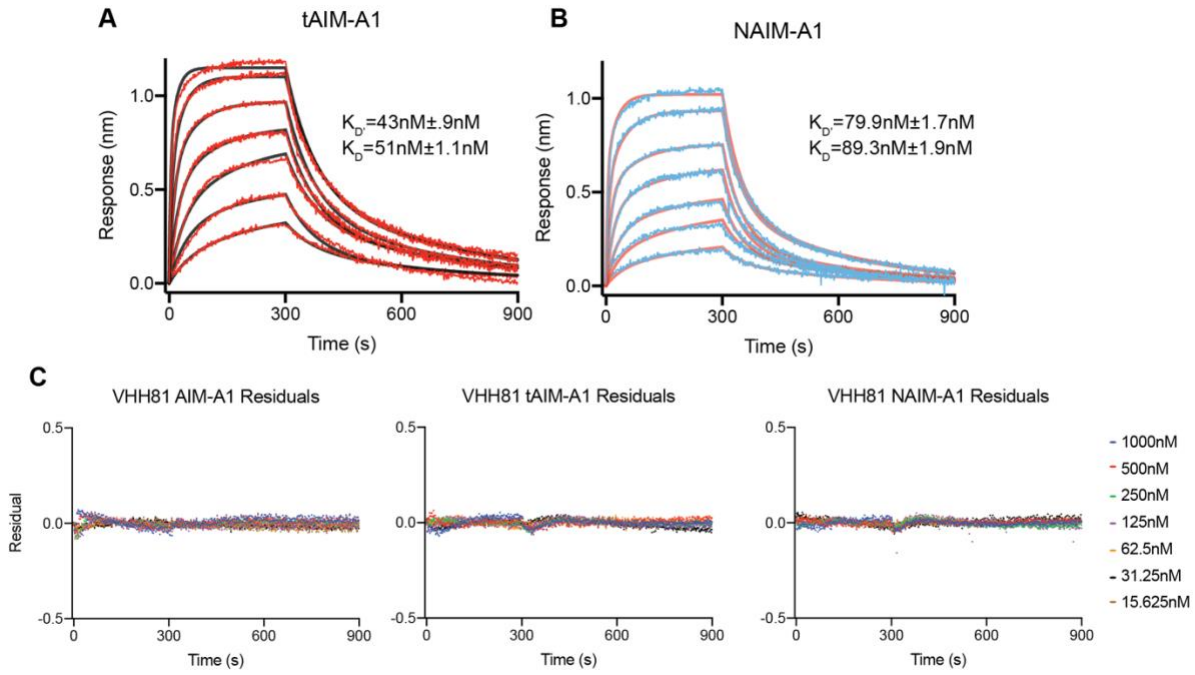

Supplementary Figure 2.14. Binding of Flag-VHH81 to rVWF fragments containing parts of the NAIM measured by BLI.

(A, B) Binding sensorgrams of tAIM-A1 (red) and NAIM-A1 (cyan) to Flag-VHH81. Global fit is overlaid in black in A, and red in B. K_D and $K_{D'}$ are presented as mean ± standard deviation of global fits. (C) Residual plot versus time for the fittings subtracted from observed sensorgrams.

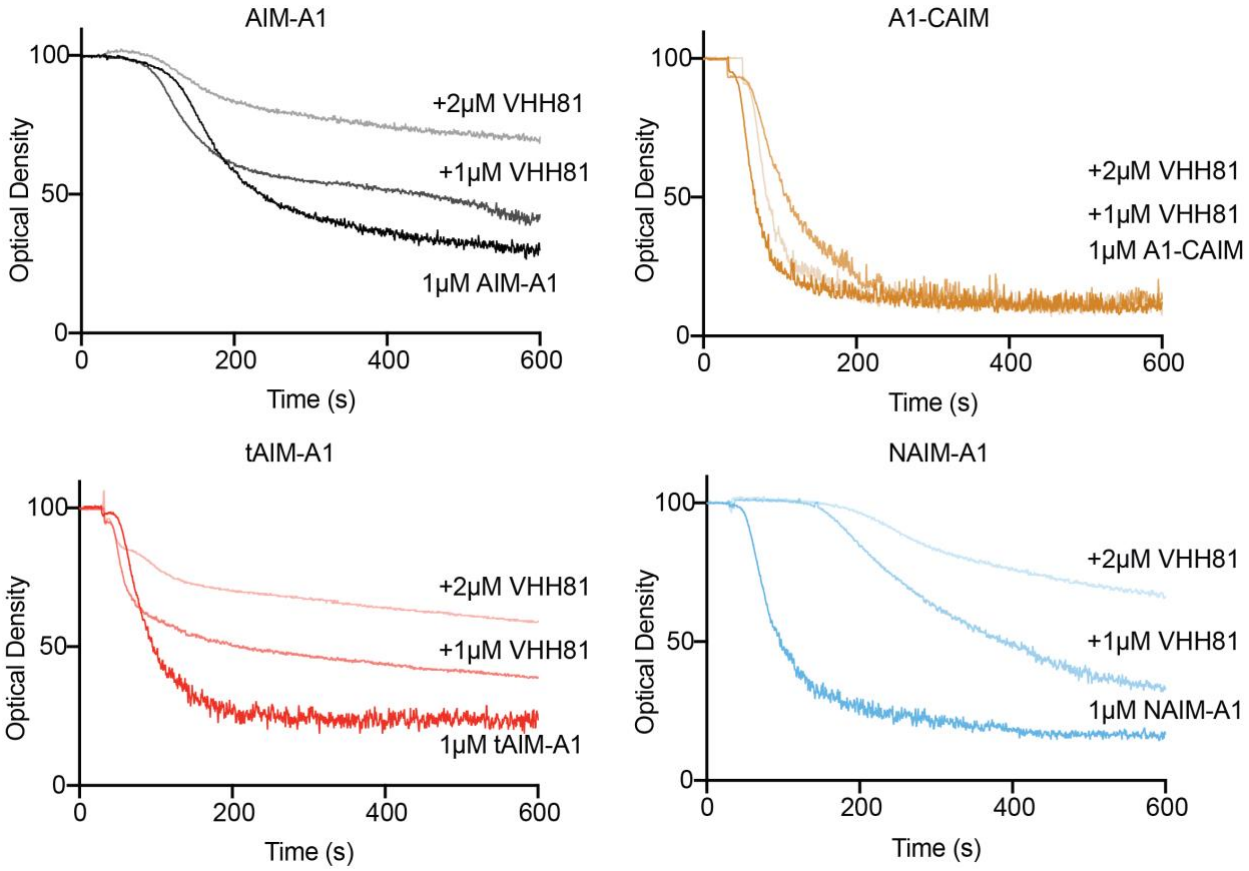

Supplementary Figure 2.15. VHH81 inhibition of rVWF fragment induced washed platelet aggregation.

Representative washed platelet aggregometry inhibition by 0,1, or 2 μM VHH81 of various AIM-A1 proteins (1μM).

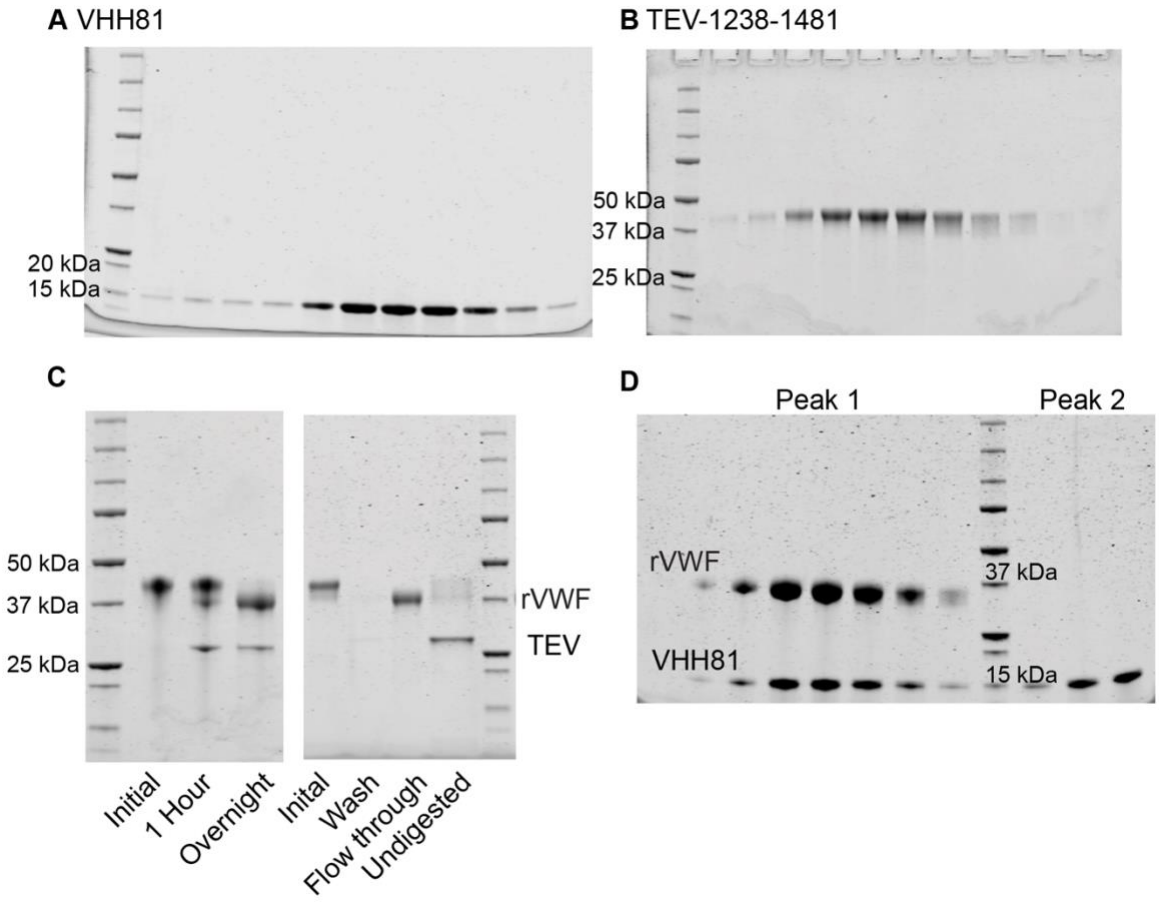

Supplementary Figure 2.16. Expression and purification of rVWF-VHH81 complex used for crystallization.

Size exclusion fractions of VHH81 (A) and TEV-1238-1481 (B). (C) Cleavage of TEV-1238-1481. (D) Coomassie stained SDS-PAGE gel of size exclusion fractions of the formed complex. Peak 1 was used for crystallization trials. These gels demonstrate the quality of the protein following a protein purification run that produced ~20 mg of purified protein complex. Similar results were obtained during 3 successive cycles of condition optimization.

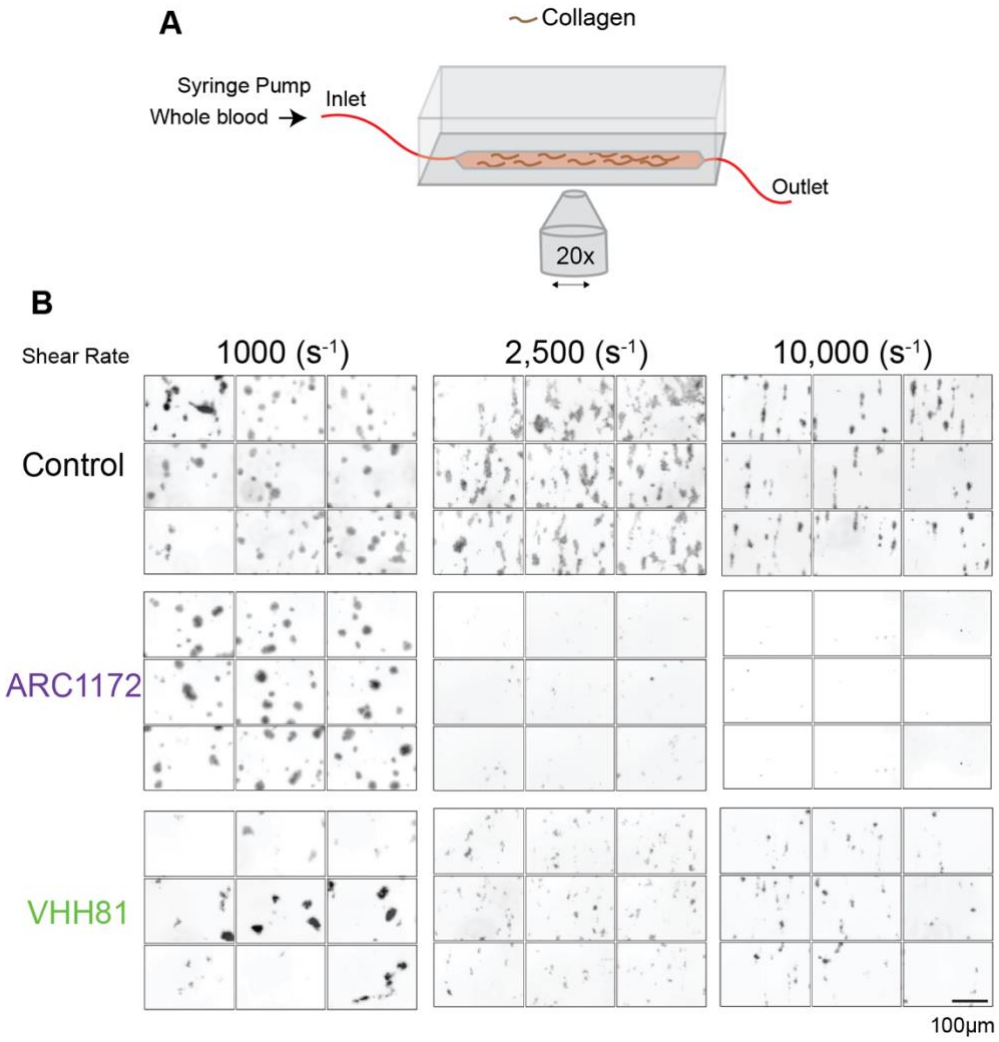

Supplementary Figure 2.17. Parallel-plate flow chamber set up and representative images of whole blood platelet adhesion to a collagen substrate in the presence of VHH81 or ARC1172.

(A) Cartoon of the flow chamber set-up. Labelled whole blood is perfused into the chamber at desired shear rates and imaged immediately after 4 minutes of perfusion followed by 2 minutes of washing with modified Tyrode's buffer for 2 minutes. (B) Representative flow chamber images of platelet adhesion on collagen coated substrate. Images were collected on the FITC channel as platelets were labelled with DIOC-6, and a greyscale LUT as applied in FIJI. Scale bar, 100 µm.

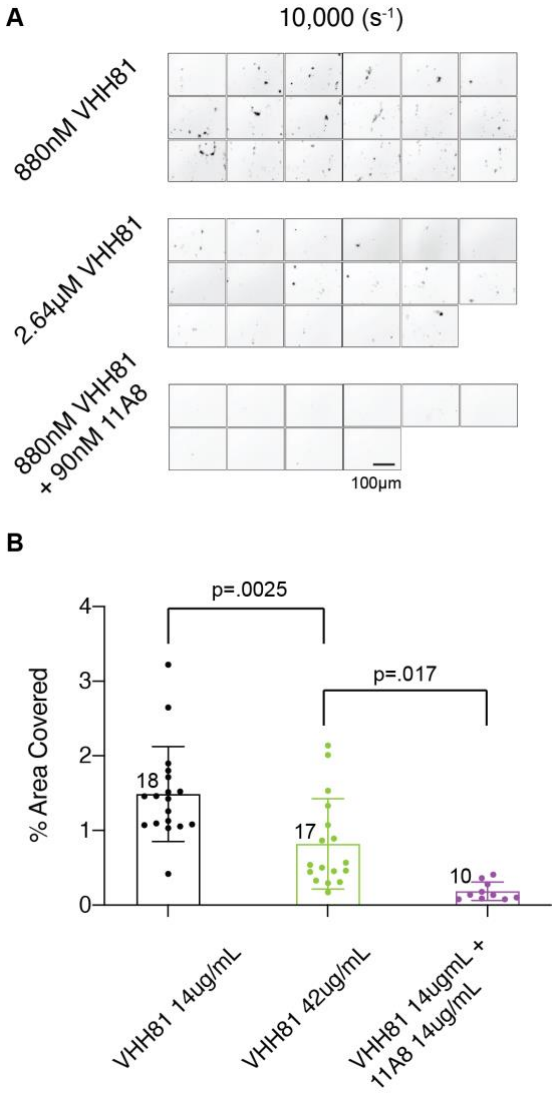

Supplementary Figure 2.18. Additional parallel-plate flow chamber experiments with VHH81 and the effects of direct inhibition of GPIbα by the anti-GPIbα monoclonal antibody 11A8.

(A) Representative flow chamber images of platelet adhesion on collagen coated substrate with additional VHH81 or anti GPIbα LBD antibody 11A8. Scale bar is 100 μm. (B) Data presented in histogram is mean ± standard deviation. Number of images used for analysis is denoted next

to the histogram. Comparison between area covered was analyzed with a 1-way ANOVA with Tukey's multiple comparison correction, $F(2, 42) = 18.57$. P-values are denoted above the comparison bars.

Chapter 3

Conservation and species-specific adaptation of force-dependent activation of von Willebrand factor

Nicholas A. Arce, Yi Liu, Wenchun Chen, X. Frank Zhang, Renhao Li

N.A.A., Y.L., W.C. performed research. N.A.A., Y.L., and X.F.Z. analyzed data. N.A.A and R.L. designed research and wrote the paper

3.1 Abstract

Von Willebrand factor (VWF) is a multimeric plasma protein that bridges the gap between vessel injury and platelet capture especially at high shear rates. Under high shear or tension, VWF can become activated upon unfolding of its autoinhibitory module (AIM). AIM unfolding exposes the A1 domain, allowing for binding to platelet glycoprotein (GP)Ibα to initiate primary hemostasis. Recombinant A1 fragments of human VWF containing or lacking the AIM can mimic autoinhibited or activated full-length VWF, respectively. Here, we show that recombinant mouse AIM-A1 is more active than the human counterpart in terms of binding to GPIbα. Recombinant mouse proteins lacking part of the AIM show further increases in activity, suggesting the mouse AIM still does protect A1. Activated A1 fragments lacking the AIM can effectively agglutinate platelets across the species barrier. The mouse AIM appears to be comprised of less residues than the human AIM yet unfolds at the same force as the human AIM. Additionally, the human AIM paired with mouse A1 largely recapitulates the behavior of human AIM-A1. Our results suggest that the regulation of VWF-GPIbα binding has been specifically tuned to work optimally in different rheological architectures. Furthermore, conservation of the AIM should be considered for cross-reaction between human and mouse VWF and GPIbα.

3.2 Introduction

Von Willebrand factor (VWF) is an ultra-large, multimeric, and multi-purpose plasma glycoprotein that initiates primary hemostasis (149). Circulating in an inactive state, VWF can respond to a vascular injury through immobilization and exposure to high shear stress or elongational flows (37). This process relieves VWF of its autoinhibited state, exposing the A1 domain that then binds to the VWF receptor on platelets, glycoprotein (GP)Ibα (97).

The organization of the domains that constitute VWF is conserved in mammals, while VWA and VWD domains can found in vertebrates as old as agnathans (200). We therefore postulated that the shear dependence of VWF activation is also conserved. Since VWF activity is critical to hemostasis and tightly regulated, it would be naive to expect the biophysical parameters that underlie VWF activation are the same between all mammals given their diversity in physical sizes, vessel diameters, and threat from predation. The comparison of humans and mice is a great juxtaposition of the difference in rheological parameters of mammals. Beating at a faster rate than a human heart, the mouse heart pumps blood through vessels at relatively higher shear rates to the human equivalent (201). Mouse platelet count in the same volume also greatly outnumbers humans, while also being significantly smaller in size (202). Regardless of these vast physical differences, mice and humans still achieve a similar hemostatic balance, as a mouse model of VWF deficiency largely replicates the bleeding symptoms observed in humans devoid of VWF (Type 3 VWD) (40; 203).

The generation of a transgenic mouse bearing the human GPIbα subunit (hTg) was the first test of species specificity between human GPIbα and mouse VWF (204). These mice can sustain hemostasis, and both wild-type and hTg platelets can bind to human VWF in the presence of botrocetin, a snake venom that has profound procoagulant activity in dozens of species (156;

205; 206). Human VWF activated with ristocetin, a commonly used glycopeptide activator of VWF, showed reduced binding to mouse platelets, but showed normal binding and aggregation with hTg platelets (204). Despite the orthology between human and mouse GPIbα, it was then demonstrated that mouse platelets do not bind human VWF under flow as well as they do mouse VWF (207). Further investigation into the species specificity has yielded disparate results (86; 208), but generally conclude that human VWF is not sufficient for hemostasis in mice, yet human GPIbα and mouse VWF can support hemostasis (209; 210).

The direct interaction between GPIbα and VWF, or more specifically between the ligand-binding domain (LBD) of GPIbα and the A1 domain of VWF, has been studied using purified recombinant fragments, with apparent affinities reported to range from nanomolar to micromolar (80; 83; 211). Such heterogeneity in reported binding affinities may likely reflect the variety in the detection method, the source of recombinant proteins, and the chosen N and C termini of the VWF fragment. It is also confounded by the existence of multiple conformational states of the A1 domain. Recent studies suggest that residues flanking the A1 domain modulate the A1 binding activity (88; 100; 101). However, the length of the flanking residues in recombinant A1 proteins in these studies varied greatly, and the activation state of these proteins was often not clearly characterized or verified.

We recently demonstrated that the mechanism of VWF activation, and exposure of the A1 domain, is dependent on the force-resistive nature of the autoinhibitory module (AIM) of VWF (88; 212). This module comprises discontinuous sequences flanking the A1 domain that is delimited by the 1272-1458 disulfide bond (89). The AIM will unfold when sufficient tensile force is applied across the VWF multimer, creating a barrier for activation that could be overcome only under specific conditions. With the recent discovery and characterization of the

AIM, a more accurate representation of autoinhibited VWF (include all residues of the AIM) or activated VWF (truncated AIM) can be used to probe the differences in human and mouse VWF and GPIbα. In this paper, we sought to investigate the biophysical differences between the species' VWF A1 domains, their AIMs, and how they interact with GPIbα.

3.3 Methods

Materials and reagents

Expi293F cells, DMEM/F12, Freestyle F17, GlutaMAX, penicillin/streptomycin, bovine serum albumin fraction V, hygromycin, and D-biotin were purchased from ThermoFisher Scientific. Ristocetin was purchased from MP Biomedicals and reconstituted to 25 mg/mL stocks in phosphate buffered saline (PBS). Mono/Dibasic sodium phosphate, sodium chloride, and imidazole was purchased from Sigma.

Protein Alignment

Protein sequences were obtained from NCBI VWF Orthologs database (Gene ID: 7450). Individual sequences were extracted to contain the AIM and the A1 domain by selecting all residues after the highly conserved, last cysteine residue of the D3 domain, extending through to the start of the A2 domain, usually marked by the motif GPKRN/K. Selected sequences were imported into DNASTAR MegAlign Pro (v 17.2.1) and aligned with the MUSCLE algorithm (213). Phylogenetic tree construction was computed using neighbor joining and rooted on *Danio rerio* (Zebrafish, Supplemental Figure 1). Alignment files are available from the authors upon reasonable request.

Construction and expression of VWF fragments

Recombinant human VWF fragments have been described and characterized previously (212). All mouse VWF sequence numbering is based on NCBI protein accession NP_035838.3. Listed sequences of mouse VWF fragments are listed in supplemental Table 1. Gene sequences encoding mouse VWF fragments were codon optimized for expression in mammalian cells, then synthesized and cloned into pcDNA3.1 Hygro(+) by Genscript (Piscataway, NJ). All sequences in expression plasmids were verified by Sanger sequencing (Genewiz). Complete amino acid sequences of mouse VWF fragments can be found in Supplemental Table 1.

Stable expressing cell lines were established by transfection of adherent Expi293F or Expi293F-BirA with Lipofectamine 3000 followed by selection in DMEM/F12 with 10% FBS and 250 μg/mL hygromycin. Individual colonies were selected, screened for high expression, and adapted to suspension culture in Freestyle F17 media supplemented with 2x GlutaMAX and .1 g/L Pluronic F68 (BASF). Cell lines expressing proteins with BirA for in-vivo biotinylation were cultured in media containing 2 μM D-biotin.

Mouse tAIM-A1 (containing VWF residues 1261-1472) was produced via transient transfection of suspension Expi293F in Freestyle F17 media with Mirus Trans-It Pro according to manufacturer's directions. Cultures were harvested 6 days after transfection.

Suspension media was clarified by centrifugation at 8000 x g for 30 minutes and loaded to equilibrated (20 mM phosphate buffer, 500 mM NaCl, pH 7.4) Nickel-Sepharose Excel resin (Cytiva). The column was washed with the above buffer supplemented with 20 mM imidazole until a flat A_{280} baseline was achieved. Bound proteins were eluted with equilibration buffer plus 500 mM imidazole at pH 7.4. The elution was concentrated to ~2-5 mL and further purified by size exclusion chromatography using a Superdex 75 or 200 pg 16/600 column equilibrated with phosphate buffered saline (PBS), pH 7.4. Proteins eluted at expected retention times given their

molecular weights with symmetrical peaks suggestive of a monomeric, monodisperse protein. Proteins were purified to homogeneity as assessed by SDS-PAGE and Coomassie stain (Supplemental Figure 2), with sizes indicative of added glycosylation consistent with the expectation of 8 O-linked glycans on the AIM-A1 protein, or 2 in the tAIM-A1 protein. All proteins were concentrated to ~1 mg/mL using Amicon Ultra 15mL, 3kDa MWCO centrifugal filters (Millipore), aliquoted, and frozen at -80°C. Protein concentrations were calculated based on their extinction coefficients at 280 nm. Protein aliquots were used within a day of thawing and were never subjected to freeze-thaw more than once.

Construction of mouse GPIbα LBD and human GPIbα W230L

Human GPIbα LBD (mature protein residues 1-290) W230L was generated by site-directed mutagenesis of a previously described vector(212) using primers W230L_F and W230L_R (Supplemental Table 2). The gene fragment encoding mouse GPIbα LBD (mLBD, residues 1-290) was generated by overlap extension PCR using the mouse GPIbα cDNA as the template (Unpublished, Renhao Li) and primers mLBD_F and mLBD_R to append a biotinylation sequence and FLAG-tag at its C-terminus. The DNA fragment was cloned into the same expression vector as for the human GPIbα LBD constructs. Stably expressing cell lines and protein was produced and purified as described above. The purity of purified LBD proteins was verified by SDS-PAGE (Supplemental Figure 2).

Bio-layer Interferometry (BLI)

BLI experiments were performed using an Octet QK^{e} instrument with data acquired at 0.3 Hz with 1000 rpm shaking during all steps. Samples were diluted in kinetics buffer

(ForteBio/Sartorius), comprised of PBS, 0.1% BSA, and 0.02% Tween-20. Equilibrated streptavidin (SA) sensors were loaded with ~10 μg/mL GPIbα-LBD from either species until hitting a set threshold for 2 nm of binding. Sensors were then washed briefly and set to association in various VWF fragments for 100 seconds and dissociate for 500 seconds. Loaded sensors were washed with 1 M NaCl to remove any remaining bound VWF and equilibrated again for the next samples. BLI experiments were repeated at least twice for each binding interaction. Sensorgrams presented are representative samples. Data was fit to a heterogenous ligand binding model using two rate equations. Kinetic parameters can be found in Supplemental Table 3. To obtain equilibrium response (ΣR_{eq} K_D) values for each binding reaction, Req1 and Req2 were summed for each concentration and fitted to a hyperbola assuming a 1:1 stoichiometric binding ratio.

Platelet Aggregometry

Human fresh whole blood was obtained from healthy donors via venipuncture into Vacutainer 3.2% sodium citrate tubes (BD). Written informed consent was obtained from participants before their inclusion in studies, and all procedures using donor-derived human blood and platelets were approved by the Institutional Review Board at Emory University. C57BL/6J mice were purchased from The Jackson Laboratory. Preparation of mouse platelets used in the study was approved by the IACUC of Emory University. Human and mouse platelet-rich plasma and washed platelets were obtained as described (167; 214). Platelet aggregation studies were performed as previously described (212). Briefly, platelets were resuspended to 200,000/μL in either modified Tyrode's buffer or pooled normal plasma from humans (George-

King Biomedical) or mice. After 30 seconds, VWF fragments or ristocetin were added to the suspension and aggregation was followed for up to 10 minutes.

Single-molecule force spectroscopy

Single-molecule force measurement was performed largely as described.(212) Briefly, the biotinylated VWF fragment was immobilized on a streptavidin bead held by a fixed micropipette. SpyCatcher003-S49C (215) was produced by expression in SHuffle T7 express cells (NEB) according to standard procedures. Bacterial pellets were lysed with BugBugster (Millipore) and clarified supernatant containing SpyCatcher was purified on Ni-Sepharose 6 FF (Cytiva). The eluate was incubated with 5 mM DTT and 5 mM EDTA for 30 minutes and isolated by size exclusion chromatography in PBS on a Superdex 75 16/600 pg column. SpyCatcher was coupled to a biotin-DNA handle of 802 bp, and then coupled to streptavidin beads of 2.0-μm diameter (Spherotech, Lake Forest, IL). For pulling experiments, the SpyCatcher-DNA handle bead, trapped and controlled by the optical tweezer, was brought to interact with the VWF fragment bead. The force measurement was performed at force-ramp mode with varying pulling speeds (50, 100, 200, 400, and 500 nm/s) in Tris-buffered saline (20 mM Tris, 150 mM NaCl, pH 7.5). The force-extension data were fitted to the worm-like chain (WLC) model (174). Unfolding extension is defined as the increase in end-to-end distance between the point of unfolding and the point at which the force at unfolding is re-established. To find the most probable extension at various forces, the force-extension data was first binned by force. Unfolding was also analyzed according to the Bell-Evans model to determine most probable unfolding force of the protein (46; 169; 170).

3.4 Results

Multiple sequence alignment of mammalian autoinhibitory modules

Multiple sequence alignments were performed for all available mammalian, some avian, and some reptile VWF coding sequences between the last cysteine at the end of the D3 assembly and the start of the A2 domain. We define the A1 domain as all residues inside the 1272-1458 disulfide bond, the N-AIM as residues between D3 and A1, and the C-AIM as residues between A1 and A2 (Figure 3.1A). Mammalian AIMs appear to largely retain an overall acidic nature, enriched with proline, serine, and threonine (Supplemental File 3.1). Human and mouse AIM-A1 share 84.3% identical amino acids from 255 residues and are 89.4% similar. The AIMs specifically share 74% identity and are 83% similar (Figure 3.1A). There are a number of differences in the AIM itself such as a charge switch at residue 1269 that could explain why caplacizumab does not bind mouse VWF (182). In addition, several differences are present in residues 1460-1472 of CAIM that contains the ristocetin-binding site (88), which may explain why ristocetin is unable to activate full-length mouse VWF. There are no differences with the known interfacial residues between AIM and A1 such as His1268 or Glu1264. We thus speculated that mouse VWF likely retains elements of autoinhibition through its AIM, but given the changes in the primary sequence, it might have different properties compared to the human AIM.

The mouse AIM provides reduced protection to mouse A1

We have previously demonstrated that the protein containing residues 1238-1493 of human VWF (hAIM-A1) largely recapitulates the activity of full-length VWF, as the protein shows little detectable affinity for the LBD of human GPIbα (hLBD) (89; 212). Recombinant proteins lacking significant portions of the AIM, such as 1261-1472 (htAIM-A1), can

Figure 3.1.

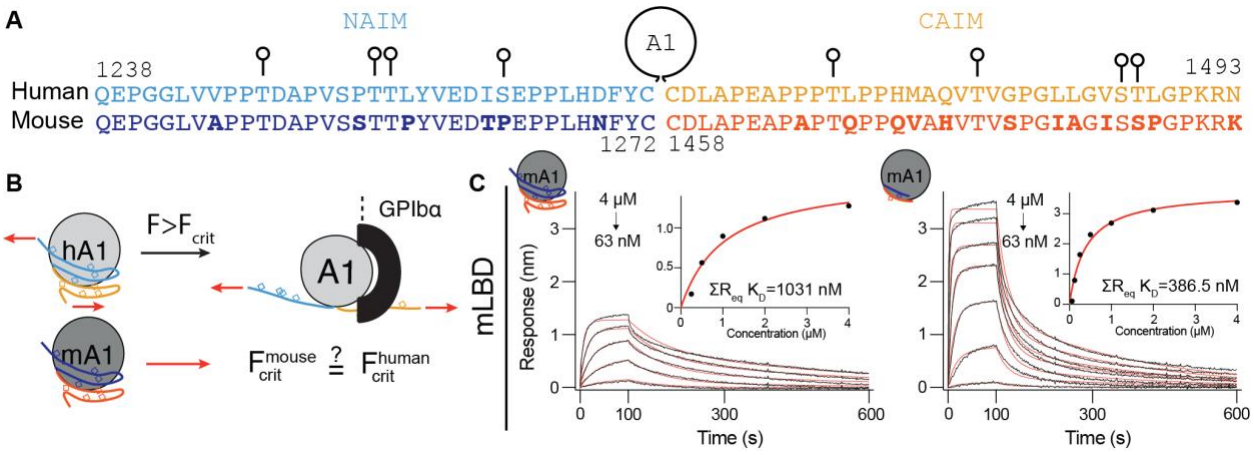

Figure 3.1. Protection of mouse VWF A1 binding by flanking AIM sequences.

(A) Alignment of human and mouse NAIM (blue) and CAIM (orange) sequences that flank the A1 domain (shown as a circle, delimited by the 1272-1458 disulfide bond) was performed using MUSCLE. Non-identical residues are shown in bold. Alignment of complete AIM-A1 sequences from various organisms can be found in Supplemental File 1. (B) Illustration of human AIM-A1 protein and its activation when the tension exceeds the critical threshold (F_{crit}) and disrupts the AIM. In the inactive form, the A1 domain (gray circle) is masked by the AIM (blue and orange lines). It is not clear if mouse AIM (purple and red lines) confers similar protection to the mouse A1 domain (dark gray circle) and affects its activity. (C) Binding BLI sensorgrams of mouse VWF AIM-A1 (left panel) and tAIM-A1 (dark gray circle with short purple and red lines, right panel), in serial dilution from 4 μM, to mouse GPIbα LBD. Association at each concentration was performed for 100 seconds followed by dissociation into kinetics buffer for an additional 500 seconds. A global fit of heterogenous ligand binding for all concentrations (red traces) is performed. The sum of equilibrium responses from two-state equations for each concentration were fit to a hyperbola and K_D was derived as half-maximal binding (insets). Sensorgrams are reflective of two technical replicates.

spontaneously bind to hLBD with high affinity (K_D 332 nM, Figure 3.3C, D) and dissociate with a two-phase decay as has been observed for activated A1 or gain-of-function GPIbα binding sensorgrams (88; 89). Thus, AIM-deleted A1 proteins mimic force-dependent disruption of the AIM. Furthermore, htAIM-A1 can be used as a constitutively active form of VWF as it can activate platelets using light-transmission platelet aggregometry (212). We hypothesized that the AIM would serve a similar role in mouse VWF, whereby inclusion of the AIM would inhibit binding to mouse platelets or mouse LBD (Figure 3.1B).

In SDS gels, the recombinantly expressed mouse AIM-A1 protein (mAIM-A1, VWF residues 1238-1493) migrated at a much higher molecular weight than is expected based on the primary sequence. This protein likely contains several O-linked (S or T) glycosylation sites similar to hAIM-A1, which would explain the apparent molecular weight of ~40 kDa (Supplemental Figure 3.2). We analyzed the activity of this protein towards mLBD using bio-layer interferometry. mAIM-A1 showed moderate affinity (~1 μM) towards mLBD (Figure 3.1C). In comparison, a recombinant protein containing a truncated form of the mouse AIM, mtAIM-A1 (residues 1261-1472), bound to mLBD with higher affinity at 386 nM (Figure 3.1C). The difference in mLBD-binding affinity between mAIM-A1 and mtAIM-A1 (1 μM vs. 386 nM), albeit relatively small when compared to that between human VWF fragments, suggests that the mouse AIM provides some protection for the A1 domain.

Mouse VWF A1 fragments can activate platelets and respond to ristocetin

We previously showed that washed human platelets can be dose-dependently activated by recombinant A1 fragments (212). Furthermore, htAIM-A1 can induce apparent aggregation of these platelets at low concentrations (60 nM), while micromolar concentrations of hAIM-A1 are necessary for full aggregation (212). Here we tested the activity of mouse A1 fragments towards

mouse platelets. As shown in Figure 3.2, addition of mAIM-A1 dose-dependently induced apparent aggregation of washed mouse platelets, similar to the responses observed for the human pair. At the physiological circulating VWF level (60 nM), mAIM-A1 was unable to cause platelet aggregation. However, addition of recombinant proteins approaching micromolar concentrations induced a robust aggregation response (Figure 3.2A). mtAIM-A1 is a more potent agonist of platelet activation, showing near complete aggregation at 250 nM (Figure 3.2B). Furthermore, the aggregation of platelets via AIM-A1 fragments was not dependent on intraplatelet stores of full-length VWF, as $VWF^{-/-}$ mouse platelets were still aggregated following the addition of mAIM-A1 (Supplemental Figure 3.3).

Ristocetin is a glycopeptide antibiotic that has been used for decades to activate human VWF in a manner similar to shear-dependent activation (216). We recently reported evidence that ristocetin induces exposure of the A1 domain for LBD association by binding to the C-AIM of human VWF and disrupting the AIM conformation (88; 212). However, earlier studies reported that ristocetin was unable to induce aggregation in mouse platelet-rich plasma (209; 216). Thus, to our surprise, 1.5 mg/ml ristocetin was able to induce apparent aggregation of washed mouse platelets in the presence of murine A1 fragments (Figure 3.2A, B), even though the primary sequence at the presumed ristocetin-binding site is not identical (Human-APEAPPPTLPPDM, Mouse-APEAPAPTQPPQV). This result suggests that either ristocetin exhibits a lower affinity for full-length mouse VWF, or that the disruptive nature of ristocetin on the mouse AIM is less effective in the context of full-length VWF.

As the mouse A1 domain is orthologous to human A1, we tested if the mAIM-A1 could activate human platelets. Indeed, mAIM-A1 dose-dependently induced apparent aggregation of

Figure 3.2.

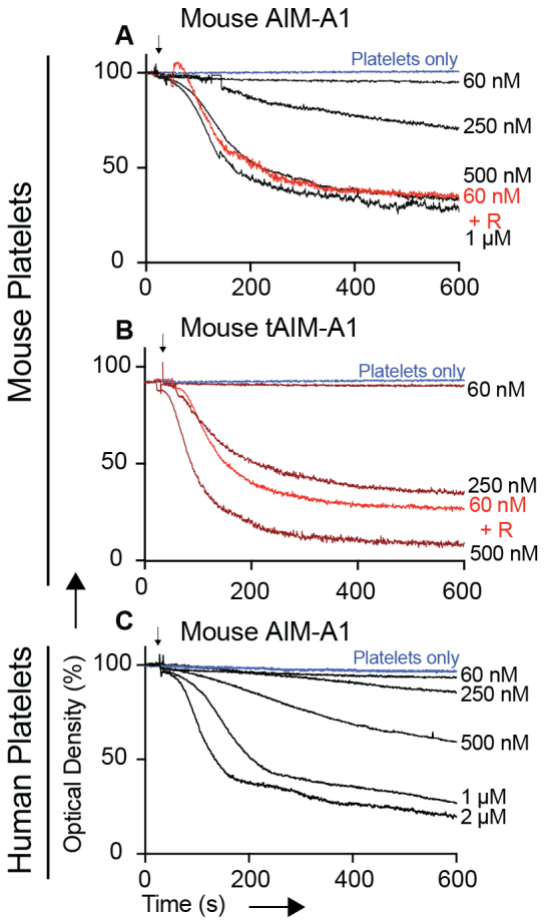

Figure 3.2. Platelet aggregation traces showing the activation of mouse and human platelets by supraphysiological concentrations of mouse AIM-A1 proteins.

Mouse (A,B) or human (C) washed platelets were resuspended in modified Tyrode's buffer and gently stirred. Reagents were added at 30 seconds following establishment of a stable baseline (arrows). Aggregation is seen as a decrease in the optical density as the platelets agglutinate and clump together. When needed, ristocetin was added to a final concentration of 1.5 mg/mL. Mouse AIM-A1 or tAIM-A1 protein was added to the denoted final concentrations.

washed human platelets (Figure 3.2C). Based on these results, we conclude that mouse VWF contains similar, although apparently less protective, autoinhibitory properties as human VWF.

Cross reactivity of mouse and human VWF with GPIbα

We next probed the ability of the AIM-A1 fragments to bind the LBD of either species. It should be noted that both A1 fragments and LBD are monomeric proteins, and all detectable binding was fitted to global, heterogenous ligand binding model given a pronounced two-phase decay in the sensorgrams. Similar to the binding behavior of human A1 fragments to hLBD (88; 89; 212), hAIM-A1 showed little binding to mLBD at up to 2 μM, and htAIM-A1 bound to mLBD with a moderate affinity of 2.4 μM, although the slow phase dissociation of htAIM-A1 is less pronounced (Figure 3.3A, B). In comparison, mAIM-A1 bound to hLBD with an affinity of 515 nM, and the presumably more active mtAIM-A1 shows a lower affinity of around 1 μM although this behavior likely due to a fast off-rate (Figure 3.3E, F).

The human AIM confers strong protection to the A1 domain, irrespective of species

As a whole, it appears the mouse fragments are much more active in their native capacity to bind to the LBD. The AIM largely controls the autoinhibition of A1 in human fragments. As the mouse fragments appear to be more active, we sought to test if the human AIM confers a stronger protective effect compared to the mouse AIM. To this end, a chimera AIM-A1 protein, in which the human AIM sequence flanks the mouse A1 (hAIM-mA1, Figure 3.4A), was generated. In a dose dependent manner, hAIM-mA1 was able to aggregate platelets from either species, as well as respond to ristocetin, consistent with the ability of ristocetin to recognize the human AIM (Figure 3.4B, C).

Figure 3.3.

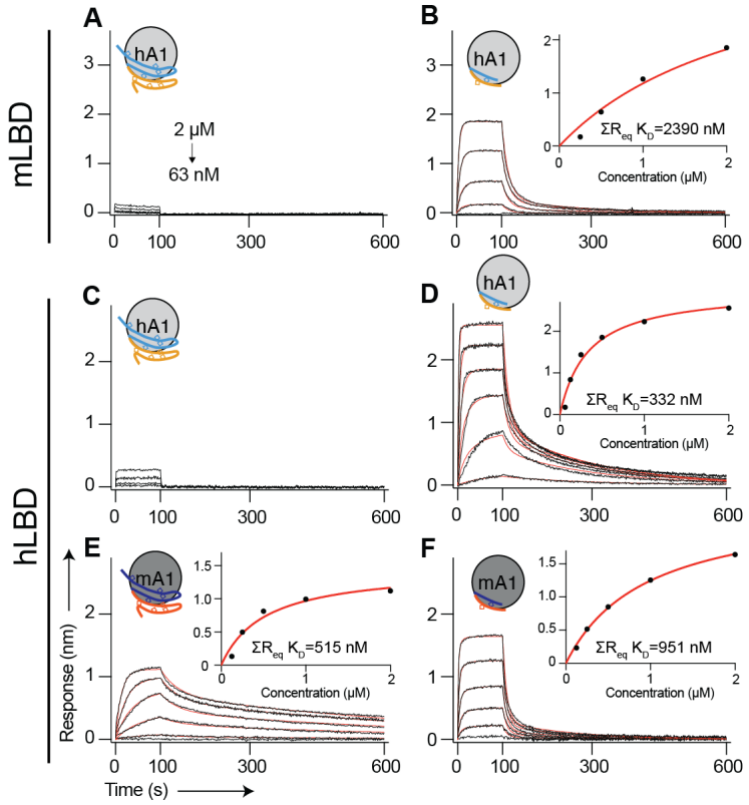

Figure 3.3. Binding of autoinhibited and activated AIM-A1 proteins to GPIbα LBD across human and mouse species.

AIM-A1 proteins, depicted at the top of each panel following the same format as in Figure 1, were assessed for binding to immobilized LBD by BLI using a dilution series from 2 μM to 63 nM. Association into each protein concentration was performed for 100 seconds followed by dissociation into kinetics buffer for an additional 500 seconds. Global fitting (red traces) was performed as in Figure 1. The sum of equilibrium responses from two-state equations for each concentration were fit to a hyperbola and K_D was derived as half-maximal binding (inset). Sensorgrams are reflective of two to three technical replicates.

Figure 3.4.

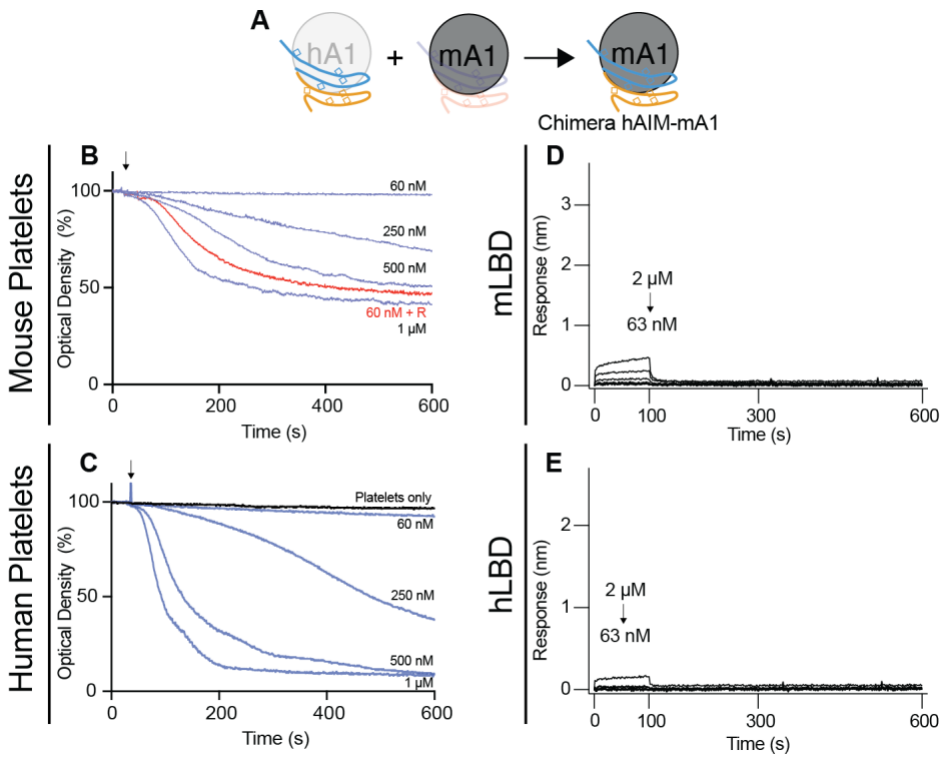

Figure 3.4. Chimeric human AIM-mouse A1 shows similar autoinhibition as observed in hAIM-A1.

(A) The human AIM was fused to the mouse A1 domain to yield a chimeric hAIM-mA1 protein. (B,C) Aggregation traces of mouse (B) and human (C) platelets induced by hAIM-mA1 at noted concentrations. 1.5 mg/ml ristocetin (R, red trace) could induce apparent aggregation in the presence of 60 nM hAIM-mA1. (D, E) Binding BLI sensorgrams of hAIM-mA1, in serial dilution from 2 μM to 63 nM, to mouse (D) and human (E) LBD. In either case, the affinity could not be determined as little binding responses were observed.

We next tested the ability of the chimera to bind to the LBD from either species. The human AIM appears to indeed confer enhanced protection to the mouse A1 as the binding response is barely detectable up to 2 μM. Biding to hLBD and mLBD results in binding sensorgrams similar to those seen with hAIM-A1 (Figures 3.4D, E;3.3B, C).

While it is apparent that various AIM-A1 constructs can bind to platelets and activate them, we wanted to ensure that the lack of binding to the LBD is due to the presence of AIM, and not the inability of A1 to bind to the LBD. To ensure the A1 still retains all the elements to bind to the LBD, we used a gain-of-function hLBD bearing a platelet-type (PT) VWD, W230L mutation (64; 217). This mutation increases the affinity of the LBD to VWF by increasing the binding affinity to the primary binding site on A1. This mutated PT-LBD can overcome some of the protection provided by the AIM. hAIM-A1, mAIM-A1, and the chimera all show increased binding responses to the PT-LBD compared to the wild-type LBD (Figure S3.4). From these sensorgrams, the A1 domain contained in these constructs can still bind to the LBD.

The mouse AIM is weaker than the human AIM by single-molecule force spectroscopy

The function of the AIM in plasma VWF is to provide a force-resistive switch to turn on the ability of VWF to strongly bind to the LBD. We previously demonstrated that the human AIM is unfolded by piconewton forces in single-molecule force spectroscopy (212) We sought to define the unfolding parameters of the mouse AIM by the same means. Using optical tweezers to exert forces on the most distal ends of the protein, we can detect unfolding events below 60 pN (Figure 3.5A). Representative DNA unfolding traces with accompanying protein unfolding events are shown in Figure 5B. Unfolding events are fitted to the worm-like chain model to obtain the unfolding force with a corresponding extension of the unfolding (Figure 3.5C). The

Figure 3.5.

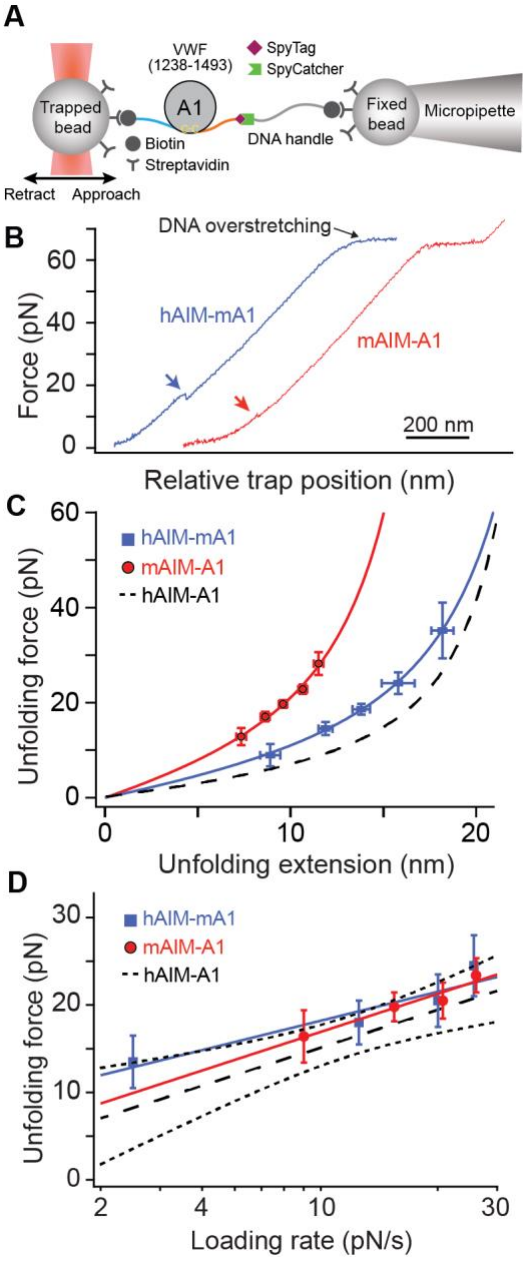

Figure 3.5. Single-molecule force spectroscopy reveals unfolding parameters of the mouse AIM

(A) Schematic of single-molecule optical tweezer apparatus in this study. An N-terminal biotinylated tag and C-terminal SpyTag003 were used to conjugate the AIM-A1 protein to a streptavidin bead and SpyCatcher DNA handle, respectively. (B) Representative force-extension

traces of mouse AIM-A1 (red) and chimera hAIM-mA1 (blue). The extension event in each trace is marked by an arrowhead. (C) Plots of unfolding force versus unfolding extension for noted AIM-A1 fragments and fits to the worm-like chain model. The human AIM-A1 unfolding data has been published previously and is overlaid here as a black dashed line for comparison. Force data are presented as mean values ± standard deviation, and extension data are presented as the peak of the Gaussian fit ± the full width at half maximum (FWHM) of Gaussian fit divided by the square root of counts. (D) Plots of unfolding force versus loading rate for noted AIM-A1 fragments and fits to the Bell-Evans model. Unfolding force data are presented as the center of the tallest bin of the histogram ± one-half of the bin width. Previous data from hAIM-A1 are shown in black dashed line with 99 % confidence interval predictions of the upper and lower limits based on the error shown as fine dashed lines.

mouse AIM-A1 construct shows a single unfolding event, with a contour length, L_C, of 21.8 ± 1.2 nm, which is shorter than the contour length of the human AIM at 26.6 ± 0.5 nm (Table 3.1). As the unfolding force is a function of the loading rate, these two parameters can be used to fit to the Bell-Evans model to yield unfolding force parameters. When compared to human AIM-A1, the mouse AIM-A1 unfolding force is similar to the human unfolding force, although it appears to be slightly diminished (Figure 3.5D). A reduced contour length indicates that the mouse AIM is composed of less residues than the human AIM yet unfolds at similar forces. Substitution of the human AIM onto mouse A1 in the chimeric protein does slightly raise the unfolding force but more drastically increases the contour length considerably to 29.0 ± 0.4 nm. The increase in contour length suggests the AIM may help to obscure the binding site of GPIbα without substantially increasing the contacts between the AIM and A1. Alternatively, there may be residues in the mouse AIM that increase the stability of the AIM that are closer to the disulfide compared to the human AIM.

3.5 Discussion

Our investigation into the binding between both mouse and human GPIbα and VWF demonstrates the presence of A1-specific autoinhibition in mouse VWF, albeit with less protection compared to human VWF. Like its human counterpart, mouse AIM-A1 could dose dependently activate platelets from both humans and mice, although at supraphysiological concentrations. The removal of part of the AIM in the tAIM-A1 construct created a more potent agonist for platelet activation, although mouse AIM-A1 itself is more active than human AIM-A1. A more active VWF fragment may be more promiscuous in binding to non-optimized binding partners, as observed in mouse VWF binding to human GPIbα. We therefore

Table 3.1. Single-molecule force spectroscopy parameters associated with unfolding events of various constructs and additives

Construct	Contour length L_C (nm)[a]	Persistence length L_p (nm)[a]	Unstressed unfolding rate $\boldsymbol{k_u^0}$ (s^{-1})[b]	Barrier position $\boldsymbol{\gamma_u}$ (nm)[b]
Mouse AIM	21.8 ± 1.2	0.21 ± 0.02	0.074 ± 0.035	0.75 ± 0.13
Chimera AIM – one unfolding	29.0 ± 0.4	0.25 ± 0.01	0.027 ± 0.056	0.99 ± 0.24
Chimera AIM – two unfolding – lower force	28.0 ± 1.0	0.20 ± 0.01		

[a] Contour length and persistence length are fitted worm-like chain model parameters. Uncertainties are the standard error of the fits.
[b] Unstressed unfolding rate and barrier position are fitted Bell-Evans model parameters. Uncertainties are the standard error of the fits.

hypothesized that the mouse AIM is either less resistant to force, or physically shields less of the A1 domain from GPIbα. The contour length of the mouse AIM is considerably shorter than the human AIM, implicating that there are less folded residues that constitute the mouse AIM. As the unfolding forces of the human AIM and mouse AIM are not significantly different from each other, there must be more distal residues in the human AIM providing protection to A1 compared to the mouse AIM.

A reductionist, single-domain approach must be used as binding studies with full-length VWF would be impossible to delineate affinities to GPIbα without an equally efficacious agonist to both species VWF tested. Furthermore, binding would be dependent on the extent of multimerization of the VWF tested due to avidity effects. Studying the AIM unfolding alone is not fully representative of VWF unfolding and elongation as other domains might be involved in autoinhibiting VWF (118). However, the AIM constitutes most of the force-resistance as our force data agrees with the estimated local transition for GPIbα binding using full-length VWF under flow (97).

The translation of single domain-domain interactions to shear-dependent multivalent platelet-VWF interactions is difficult to scale. However, our studies can recapitulate and explain many previously reported VWF-platelet interactions, or lack thereof. For instance, the weak binding of human tAIM-A1 to mouse GPIbα coupled with a fast off rate could explain the inability of human VWF to initiate adhesion of mouse platelets and thus the bleeding tendency in mice expressing human VWF (208; 209). Previous studies have demonstrated that this combination is insufficient for hemostasis, as demonstrated by *ex-vivo* perfusion studies on collagen (218), *in-vivo* hydrodynamic injection (208), and genetic replacement (209). Human VWF has also been previously demonstrated to be a poor binder to pig platelets (219). The

converse species mis-match also presents an interesting view. Human GPIbα can bind with higher affinity to the autoinhibited mouse AIM-A1. Based on previous reports, human platelets appear to readily agglutinate with plasma of pig, cow, sheep, and goat (220), indicating that human GPIbα enables enhanced binding, necessitating a stronger AIM in human VWF. In agreement with this, both hTg mice and mice expressing human GPIbα and human VWF A1 show no drastic defects in the cessation of bleeding (204; 209). However, human GPIbα expressing mice can form ferric chloride induced vascular occlusions regardless of the type of VWF in circulation whereas WT mice cannot (209), implicating human GPIbα as potentially pro-thrombotic if not paired with a strong AIM.

It was reported in a previous study that mutation of residue 1326 in mouse VWF from arginine to histidine could allow for human platelet binding (218). It was further reported that this mutation inhibited mouse VWF binding to mouse platelets (86). However, this mutation is not necessary for mouse VWF to bind human GPIbα and maintain hemostasis in hTg mice and another similar strain (204; 209). Efforts from Navarrete et al. were unable to demonstrate this mutation to the mouse residue within human VWF corrects hemostasis (208). Replacement of key binding interfaces within human VWF to mouse specific sequences (1326-1333; 1370-1385) was unable to correct bleeding in mice, further suggesting the human AIM confers strong protection (208). Evidence for a weaker mouse AIM can be supported by a recent investigation into ancestral reconstruction of VWF (109). Compared to human VWF, full-length variant An88 derived from a lineage of rodents shows increased GPIbα-dependent activity, whereas An101 from a lineage of primates shows decreased activity, which the authors attributed to sequence differences within the AIM, not A1 (109).

Previous binding assays between human and mouse GPIbα and VWF used multivalent ligands and analytes (dimeric GPIbα-LBD and dimeric A1), resulting in single digit nanomolar interactions which we know do not occur *in-vivo* (209). This spontaneous binding is not representative of plasma VWF, as plasma VWF does not bind to platelets at nanomolar, or even micromolar concentrations, without the help of an activating agonist (216).

The binding of VWF to platelets must occur under high shear conditions, and under force, the human LBD-A1 interaction is strengthened, *i.e.* a catch-bond is formed (90). This catch-bond behavior is essential to slow platelets down during elongational flows that occur during vessel injury as a result of vasoconstriction. Elimination of the slip-to-catch bond to pure slip by mutations in either GPIbα or VWF results in a bleeding diathesis (96; 221). The disappearance of the slow phase decay in activated, tAIM-A1 constructs to the opposite species LBD suggests that the conformational change associated with catch-bond behavior could be impaired. From these results, it is clear that the LBD can sample the primary binding site of A1, regardless of species, but the reinforcement of this interaction by the secondary binding site of A1 is altered. Specific residues within the leucine rich repeats of GPIbα have previously been identified as important mediators of the catch bond and may not be conserved between species (95).

The A domains of VWF all serve essential purposes for hemostasis. The A3 domain binds to collagen to facilitate localization of VWF to vessel injury (222). This function is somewhat redundant as the A1 domain can also bind to collagen (223). It was speculated that the A3 domain likely arose after the A1 domain for higher force circulatory systems, perhaps as a direct response to increased shear that A1 alone was incapable of arresting VWF (200). This

specialized function of the A3 domain would have created the need for the exposure of the A1 domain to be carefully controlled, to avoid platelet accumulation in the absence of injury. This suggestion is supported by the primary sequence of N and C flanking regions around A1 of *Myxine glutinosa* do not resemble the sequence of mammalian AIMs (200). Furthermore, zebrafish, birds, reptiles, and the platypus have remarkably different sequences to that of humans.

The force resistive nature of the AIM therefore should be suitable adapted to different organisms, allowing for VWF activation to different shear stresses experienced in different vessel architectures. The human coagulation system as a whole is largely not optimized for clotting compared to other animals, as evidenced by the low enzymatic activity of human coagulation factors VIII and IX compared to other species (224; 225). This may help to explain why the mouse A1 appears to be more active than human A1 in its ability to bind to GPIbα in the context of the AIM.

The function of a balanced hemostatic system is essential to the survival of mice and humans alike. While there are unique features between human and mouse platelets, as well as their VWF multimers, the regulation of their interaction is key to maintain vessel integrity without excessive thrombus generation. The autoinhibitory module is only one of several regulatory mechanisms within hemostasis. Careful control over the initial events preceding platelet activation and coagulation have given rise to an elusive, yet elegant mechanism that has adapted to an ever-changing environment.

3.6 Acknowledgements

This work was supported by the National Institutes of Health research grants HL082808, HL143794, and HL153986 and an infrastructure grant from Hemophilia of Georgia Center for Bleeding & Clotting Disorders of Emory. N.A.A. was supported in part by National Institutes of Health fellowship HL154656.

3.7 Supplemental Information

Supplemental Table 3.1. Amino acid sequences of mouse VWF and mouse GPIbα used in this study. (/) indicates predicted cleavage of the signal peptide. The site of the W230L mutation in human GPIbα is highlighted in yellow. Dark grey shading indicates mouse residues 1238-1493. Light grey residues indicate human AIM residues swapped in place of mouse AIM residues.

Construct	ORF
IL2ss-mouseVWF 1238-1493 His	MYRMQLLSCIALSLALVTNS/QEPGGLVAPPTDAPVSSTTPYVEDTPEPPLH NFYCSKLLDLVFLLDGSSMLSEAEFEVLKAFVVGMMERLHISQKRIRVAVV EYHDGSRAYLELKARKRPSELRRITSQIKYTGSQVASTSEVLKYTLFQIFGKI DRPEASHITLLLTASQEPPRMARNLVRYVQGLKKKKVIVIPVGIGPHASLKQ IRLIEKQAPENKAFLLSGVDELEQRRDEIVSYLCDLAPEAPAPTQPPQVAHV TVSPGIAGISSPGPKRKHHHHHHHHHH
IL2ss-mouseVWF 1261-1472 His	MYRMQLLSCIALSLALVTNS/DTPEPPLHNFYCSKLLDLVFLLDGSSMLSEA EFEVLKAFVVGMMERLHISQKRIRVAVVEYHDGSRAYLELKARKRPSELRR ITSQIKYTGSQVASTSEVLKYTLFQIFGKIDRPEASHITLLLTASQEPPRMARN LVRYVQGLKKKKVIVIPVGIGPHASLKQIRLIEKQAPENKAFLLSGVDELEQ RRDEIVSYLCDLAPEAPAPTQPPQHHHHHHHHHH
IL2ss-Biotag mouse 1238-1493 His SpyTag003	MYRMQLLSCIALSLALVTNS/LNDIFEAQKIEWHTSQEPGGLVAPPTDAPVS STTPYVEDTPEPPLHNFYCSKLLDLVFLLDGSSMLSEAEFEVLKAFVVGMM ERLHISQKRIRVAVVEYHDGSRAYLELKARKRPSELRRITSQIKYTGSQVAS TSEVLKYTLFQIFGKIDRPEASHITLLLTASQEPPRMARNLVRYVQGLKKKK VIVIPVGIGPHASLKQIRLIEKQAPENKAFLLSGVDELEQRRDEIVSYLCDLA PEAPAPTQPPQVAHVTVSPGIAGISSPGPKRKHHHHHHHHHHRGVPHIVMV DAYKRYK
IL2ss-Biotag Human AIM Mouse A1 His SpyTag003	MYRMQLLSCIALSLALVTNS/LNDIFEAQKIEWHTSQEPGGLVVPPTDAPVS PTTLYVEDISEPPLHDFYCSKLLDLVFLLDGSSMLSEAEFEVLKAFVVGMME RLHISQKRIRVAVVEYHDGSRAYLELKARKRPSELRRITSQIKYTGSQVAST SEVLKYTLFQIFGKIDRPEASHITLLLTASQEPPRMARNLVRYVQGLKKKKV IVIPVGIGPHASLKQIRLIEKQAPENKAFLLSGVDELEQRRDEIVSYLCDLAPE APPPTLPPHMAQVTVGPGLLGVSTLGPKRNHHHHHHHHHHRGVPHIVMVD AYKRYK
α1ATss-His-TEV-Biotag-human GPIbα1-290 2xFLAG	MPSSVSWGILLLAGLCCLVPVSLA/ERHHHHHHHHHHENLYFQGSGLNDIF EAQKIEWHEHPICEVSKVASHLEVNCDKRNLTALPPDLPKDTTILHLSENLL YTFSLATLMPYTRLTQLNLDRCELTKLQVDGTLPVLGTLDLSHNQLQSLPL LGQTLPALTVLDVSFNRLTSLPLGALRGLGELQELYLKGNELKTLPPGLLTP TPKLEKLSLANNNLTELPAGLLNGLENLDTLLLQENSLYTIPKGFFGSHLLPF AFLHGNPWLCNCEILYFRRWLQDNAENVYVWKQGVDVKAMTSNVASVQ CDNSDKFPVYKYPGKGCPTLGDEGDTDLYDYYPEEDTEGDKVRDYKDDD DKDYKDDDDK
α1ATss-His-TEV-Biotag-mouse GPIbα1-290 FLAG	MPSSVSWGILLLAGLCCLVPVSLA/ERHHHHHHHHHHENLYFQGSGLNDIF EAQKIEWHEHPQHTCSISKVTSLLEVNCENKKLTALPADLPADTGILHLGEN QLGTFSTASLVHFTHLTYLYLDRCELTSLQTNGKLIKLENLDLSHNNLKSLP SLGWALPALTTLDVSFNKLGSLSPGVLDGLSQLQELYLQNNDLKSLPPGLL LPTTKLKKLNLANNKLRELPSGLLDGLEDLDTLYLQRNWLRTIPKGFFGTL LLPFVFLHANSWYCDCEILYFRHWLQENANNVYLWKQGVDVKDTTPNVA SVRCANLDNAPVYSYPGKGCPTSSGDTDYDDYDDIPDVPATRTEVKDYKD DDDK

Supplemental Table 3.2. Primers used in this study

Primer	Sequence 5'-3'
W230L_F	GACGTCCACACCTTGCTTCAGTACGTAGACATTTTCAGCA
W230L_R	TGCTGAAAATGTCTACGTACTGAAGCAAGGTGTGGACGTC
mLBD_F	ACTGGATCCGGCCTGAACGACATCTTCGAGGCTCAGAAAA TCGAATGGCACGAACACCCCCAGCACACTTGTAGTATCTCCA
mLBD_R	TAGACTCGAGTCATTTGTCATCATCATCCTTATAGTC CTTGACCTCAGTTCTTGTGG

Supplemental Table 3.3. Kinetic fitting parameters of BLI interactions

VWF-GPIbα	K_{D1} (M)	K_{D2} (M)	K_{D1} error (M)	K_{D2} error (M)	K_D Req (nM)
Mouse 1493-Mouse LBD	3.45E-08	7.41E-07	2.27E-09	5.28E-08	1031
Mouse 1261-Mouse LBD	2.75E-08	2.26E-07	1.66E-09	9.86E-09	386.5
Human 1261-Mouse LBD	6.06E-08	9.51E-07	1.01E-08	5.36E-08	2390
Mouse 1493 – Human LBD	4.31E-08	8.62E-07	2.75E-09	1.44E-07	514.7
Mouse 1261-Human LBD	8.77E-08	4.71E-07	6.39E-09	1.56E-08	951.3
Human 1261-Human LBD	2.88E-08	3.82E-07	1.35E-09	2.31E-08	331.9
Human 1493-PT LBD	1.14E-09	7.20E-07	3.85E-10	4.12E-08	909.1
Mouse 1493-PT LBD	8.56E-08	7.86E-08	2.61E-09	1.12E-08	569.5
Chimera-PT LBD	1.32E-07	3.52E-07	1.11E-08	1.94E-08	1243

Kinetic parameters were fitted using a global 2:1 heterogenous ligand binding model fitting of 5-7 serial dilutions depending on the magnitude of observable response. Interactions such as hAIM-A1 to hLBD are not listed as the affinity of the interaction could not be determined using the concentrations tested.

Supplemental Figure 3.1. Phylogenetic tree construction of AIM-A1 proteins

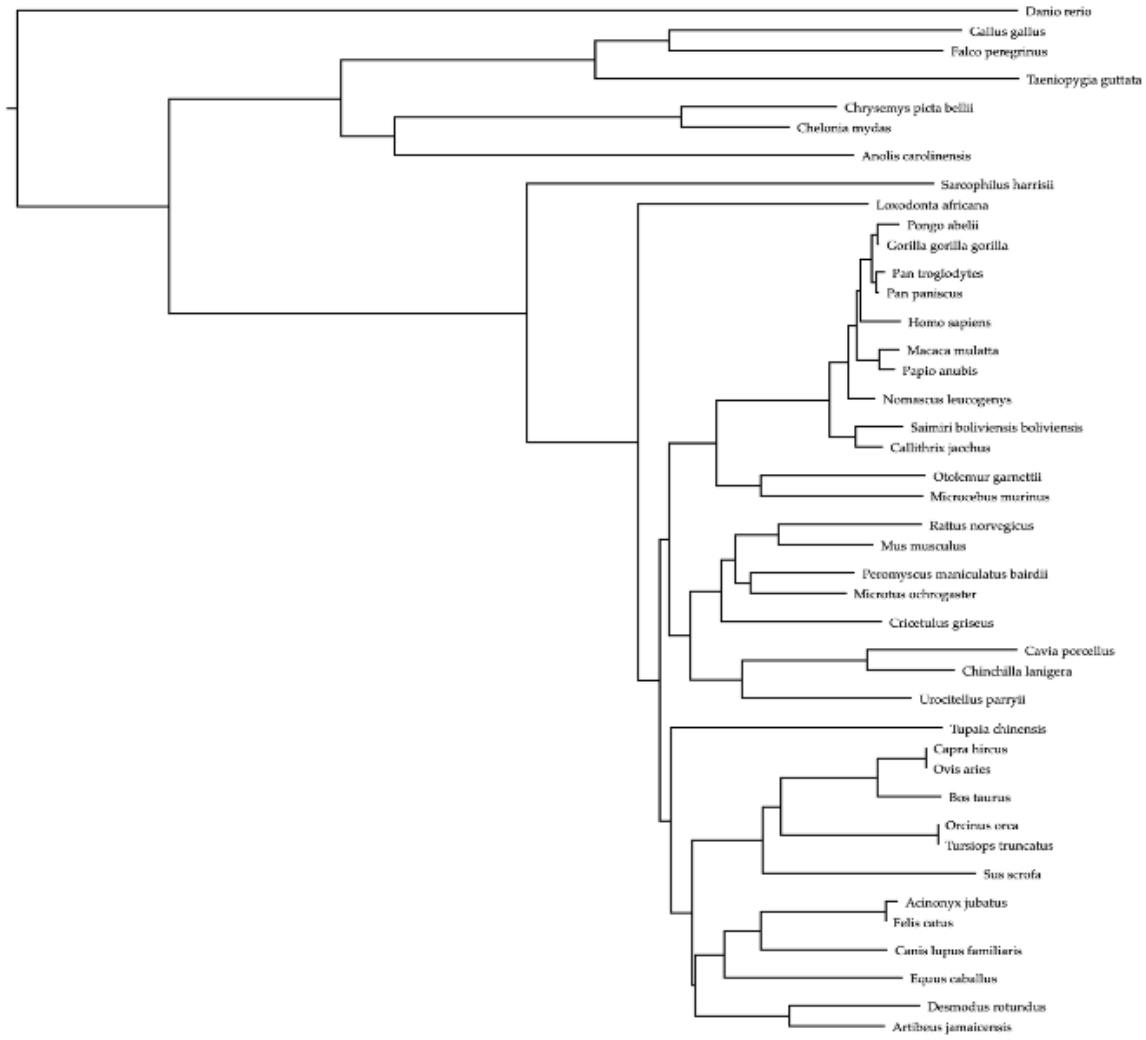

Supplemental Figure 3.2. Coomassie stained SDS-PAGE gels of novel proteins produced and used in this study.

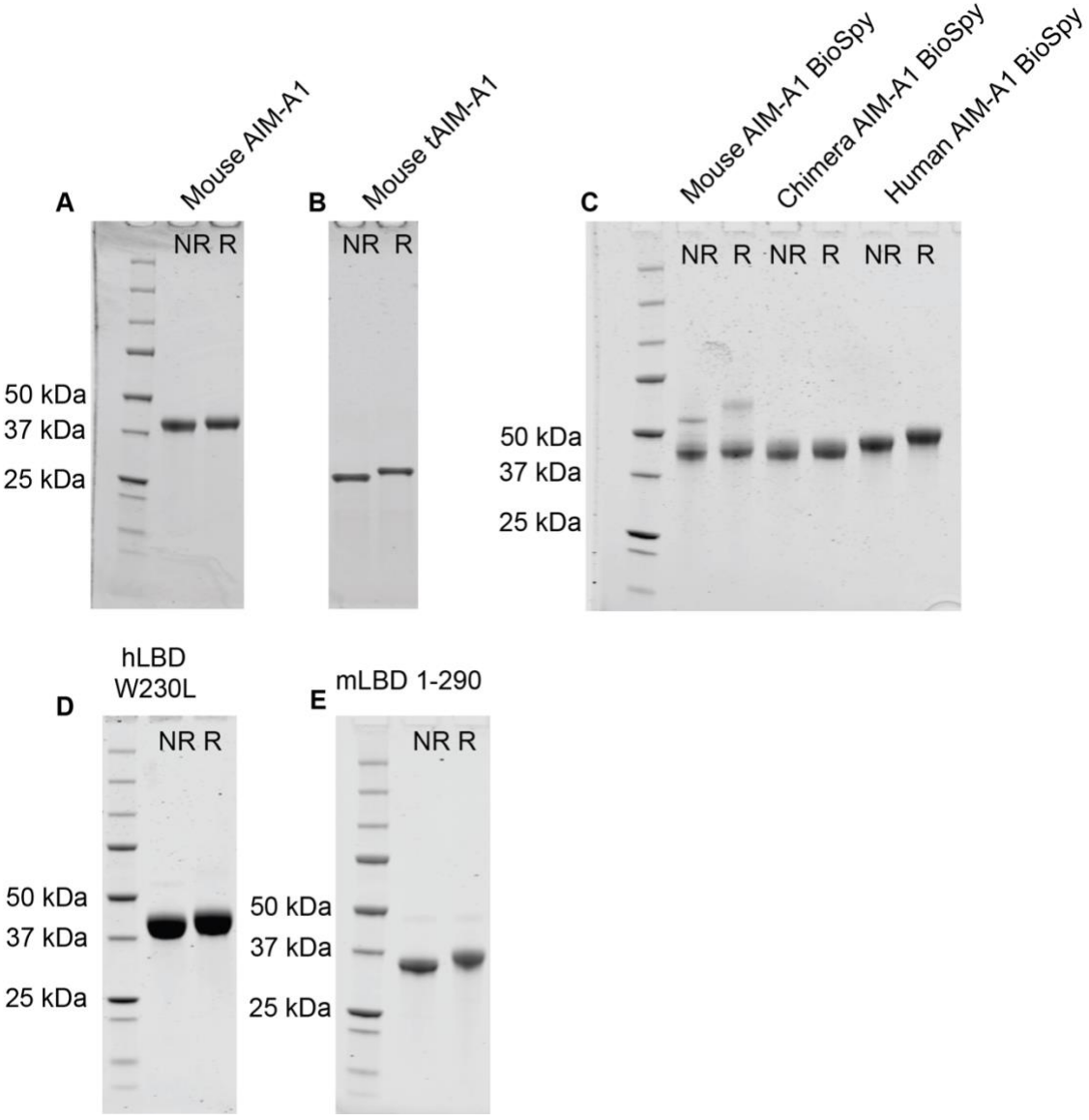

Supplemental Figure 3.3. Dose-dependent aggregation of VWF deficient mouse platelets upon addition of AIM-A1 or AIM-A1 with ristocetin.

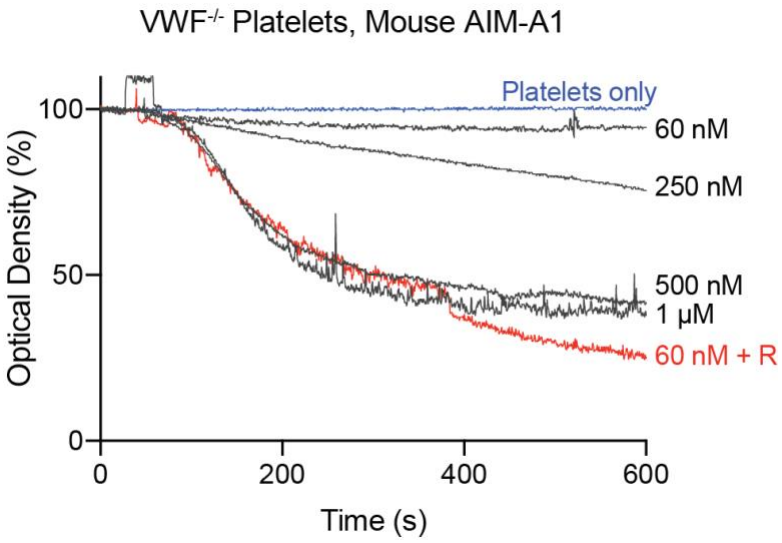

Supplemental Figure 3.4. Platelet Type GPIbα LBD binding sensorgrams to AIM-A1 VWF fragments

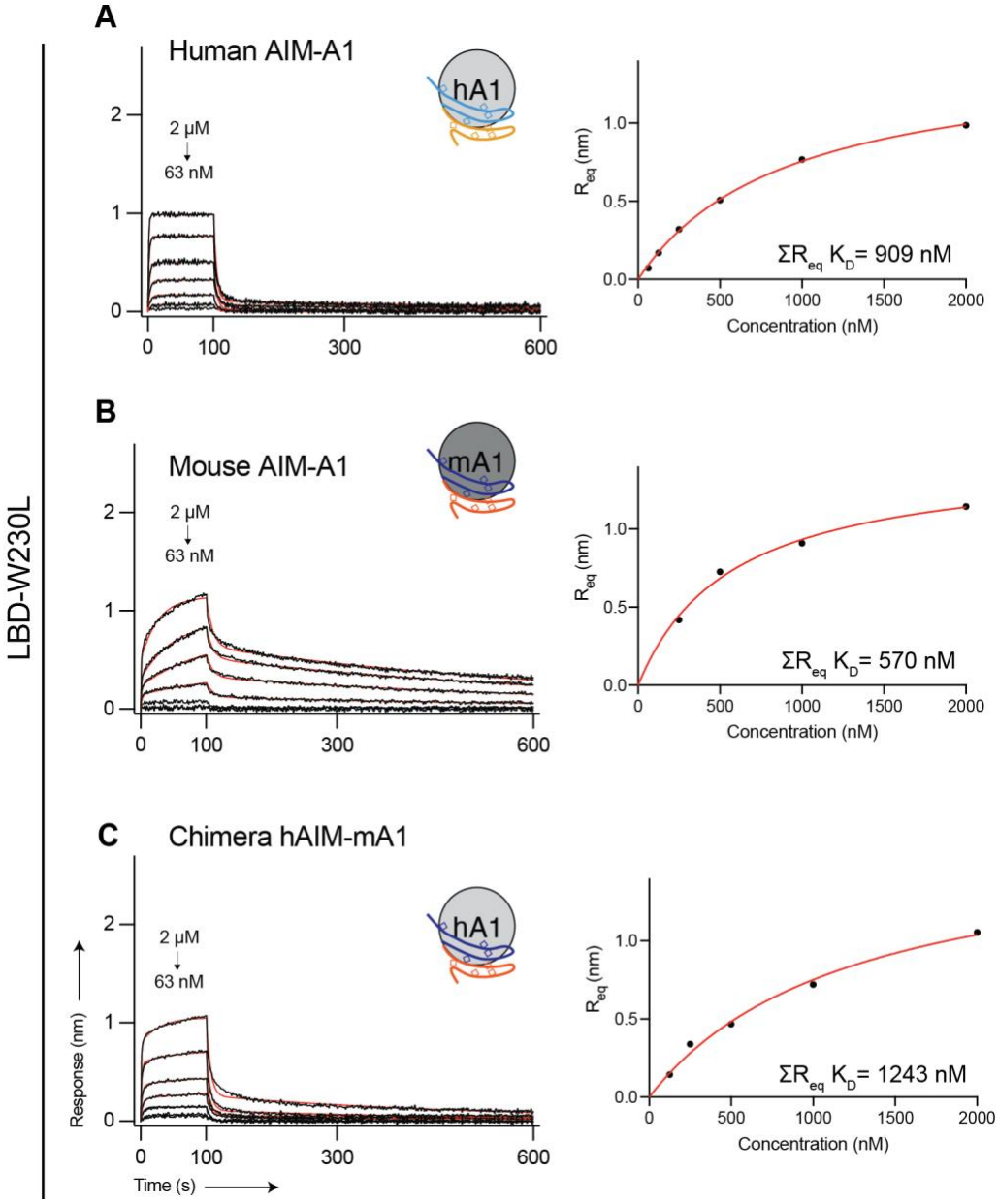

Chapter 4

Nanobody activation of von Willebrand factor by disrupting the inhibition of the N-terminal autoinhibitory module

Nicholas A. Arce, Ally J. Su, Moriah S. Wilson, Robert Sidonio, Jorge Di Paola, Renhao Li

N.A.A., A.J.S., M.S.W. performed research. N.A.A. analyzed data. R.S. and J.D.P. contributed critical reagents. N.A.A and R.L. designed research and wrote the paper.

4.1 Abstract

Activation of von Willebrand factor is a tightly controlled mechanosensory process governed by local elements around the A1 domain. The O-glycosylated sequences flanking the A1 domain constitute a force-sensitive autoinhibitory module (AIM) that can unfold to expose A1 for binding to platelet GPIbα. We have previously shown that this module can be stabilized by caplacizumab, and we speculate that the AIM is likely destabilized by ristocetin. Here, we describe a family of nanobodies isolated from an immunized yeast display library that bind to the distal portions of the N-terminal AIM and induce activation of VWF. Further characterization of three nanobodies demonstrated their epitope is dependent on both primary sequence and the presence of O-linked glycosylation. They bind a conformationally insensitive, linear epitope around residues 1253 to 1266. Purified monomeric solutions of nanobodies can induce robust, VWF-dependent aggregation in platelet-rich plasma at nanomolar EC_{50} values. Furthermore, the activating function of these nanobodies is unaffected by common CAIM polymorphisms, such as D1472H. These nanobodies can be used in place of ristocetin to assess VWF activity in plasma and can distinguish the subtypes of von Willebrand's disease in an ELISA format. These nanobodies demonstrate the importance of the distal portion of the AIM on preserving the autoinhibited state of VWF.

4.2 Introduction

Von Willebrand Factor (VWF) is an essential plasma glycoprotein responsible for the initiation of primary hemostasis (149). By sensing and responding to specific forces, VWF captures platelets at loci where drastic changes in blood flow occur, such as the extraluminal area surrounding vascular insult (37). VWF is only capable of binding to platelets after force-dependent activation, which complicates traditional biochemical measurements and makes the clinical definition of VWF activity difficult to conceptualize. Recent advances in studying the mechanosensation of VWF have helped to elucidate what VWF activation is and is not. As plasma VWF is a multimer of disulfide-linked concatemers spanning from dimers to 40-mers or more, it was reasonable to assume that the global transition of a 'coiled' multimer into an elongated polymer might be responsible for VWF activation (226). However, it was recently shown that 1) multimeric VWF in solution does not adopt a globular shape (38) and 2) global extension of a multimer is not sufficient for platelet capture (97). We have recently demonstrated that activation of VWF is controlled by local elements that respond to physiologically relevant forces (Chapter 2) (212). In brief, two discontinuous, mucin-like polypeptides that surround the A1 domain of VWF form a quasi-stable structure with A1 that prevents A1 from binding to platelet glycoprotein (GP)Ibα (88; 89). Upon application of sufficient tensile force, this autoinhibitory module (AIM) unfolds to expose the GPIbα binding site on the A1 domain of VWF. With this knowledge, the AIM is a clear target for activation of VWF under static conditions.

Ristocetin is a glycopeptide antibiotic derived from the bacteria *Amycolatopsis lurida* that was used to treat staphylococcal infections in the 1950s and 60s. Its bactericidal activity coincided with thrombocytopenia after administration (227). It was then noted that while patients with von Willebrand Disease (VWD) can respond to typical platelet agonists such as ADP or collagen, their

platelet-rich plasma would show a variety of responses to ristocetin (228; 229). This antibiotic soon yielded differentiation of VWF activity from coagulation factor VIII activity (230) and lead to the development of a ristocetin-based clinical test of VWF activity to aid in the diagnosis of the VWD and its subtypes.

Despite the immense research into ristocetin, no crystal structure of ristocetin-bound VWF has been obtained despite documented attempts (81), and there is still debate into the exact binding site on VWF, although the binding site must include several residues within the AIM (160; 216). Furthermore, the precise mechanism of action of ristocetin has not been elucidated. However, it is widely accepted that ristocetin exhibits fundamentally different effects on VWF and platelets compared to that of botrocetin, a snake derived heterodimer that induces platelet-VWF complexes (108). To this effect, ristocetin appears to mimic shear-dependent activation of VWF (147).

Despite being used today for basic research and clinical diagnostics, there are several downsides of ristocetin based VWF activation owing to its relatively low affinity for VWF. Commercial preparations of ristocetin A cannot be easily purified to homogeneity and will be contaminated with the B stereoisomer (180). Furthermore, there is a common polymorphism in VWF that occurs around the ristocetin binding site at residue 1472. This polymorphism is present in around 50% of African Americans, and up to 20% of Caucasians (110). Patients with this polymorphism show a falsely low VWF activity, which can lead to the misdiagnosis of VWD. While a new, non-ristocetin based assay of VWF activity has been developed, it is not widely available for researchers or clinicians in the United States (231). The ristocetin-cofactor assay therefore is still widely used in clinics around the world.

We have previously suggested that ristocetin can surreptitiously activate VWF by destabilizing the AIM. We have shown that ristocetin induces exposure of the secondary binding

site for GPIbα on A1 by hydrogen-deuterium exchange mass spectrometry (88). In our studies of AIM unfolding (Chapter 2), we attempted to test if ristocetin could lower the unfolding force of the AIM. However, ristocetin in the optical trap induced strange behavior in the DNA tethers, making interpretation of the traces impossible. We used a monoclonal antibody, 6G1, that competitively inhibits ristocetin and can activate isolated A1 domain, in its place. While we did observe that 6G1 disrupts the AIM, we cannot definitively say that ristocetin acts in the same manner.

After our investigation of 6G1, we hypothesized that antibody-based targeting of the AIM may yield novel VWF activators. 6G1 is unable to agglutinate platelets in platelet-rich plasma, perhaps due to its binding site paradoxically partially occluding GPIbα binding. Furthermore, both 6G1 and ristocetin bind to the C(terminal)AIM, even though we have shown that the CAIM provides less protection to A1 compared to the N(terminal)AIM. Targeting the NAIM therefore may yield more potent activators of VWF. Here, we describe 3 monoclonal, monomeric nanobodies that bind to the NAIM and activate VWF in a mechanism reminiscent of ristocetin, but with orders of magnitude higher affinity, a clearly defined epitope, and are unaffected by common VWF polymorphisms.

4.3 Methods

Recombinant VWF protein expression and purification

VWF fragments 10His-TEV-1238-1481, Biotag-1238-1493-SpyTag, Biotag-1268-1493-SpyTag, and Biotag-1238-1461-SpyTag have been described previously (212). The construct containing Biotag-1261-1472-SpyTag003 was generated as a gBlock from Integrated DNA Technologies (IDT) and cloned between the NheI and XhoI sites in pcDNA3.1 Hygro (+). Constructs with a

biotag (AviTag) were expressed from Expi293F BirA cells for in-vivo biotinylation. 10His-TEV-1238-1481 was expressed from Expi293F cells. Stable cell lines were generated by transfection with Lipofectamine 3000 (Invitrogen) and selection with 250 μg/mL hygromycin (Invitrogen) for around 2 weeks. Highest expressing clones were selected for propagation and adaptation to Freestyle F17 media (Gibco) supplemented with 2x GlutaMAX (Gibco), 0.1 g/L Pluronic F68 (BASF), and 1 μM biotin (Thermo Scientific) when desired. Glycosylation was temporarily missing from expressed protein during serum-free adaptation and was restored after 7 days. Media containing secreted VWF proteins was clarified by centrifugation and filtration followed by loading to Ni-Sepharose Excel media (Cytiva). After washing with 20 mM phosphate buffer, 500 mM NaCl, 20 mM imidazole pH 7.4, protein was eluted with 500 mM imidazole in the same buffer. The eluate was then concentrated using a 3 kDa MWCO Amicon Ultra centrifugal filter (Millipore). Proteins were further purified by size-exclusion chromatography on a Superdex 16/600 200pg or 75pg (Cytiva) with phosphate buffered saline pH 7.4.

For 10His-TEV-1238-1481, the tag and additional amino acids were removed by digestion with TEV protease overnight at 4ºC at 1:10 W/W protease to VWF. The reaction was passed through a Ni-Sepharose excel column, and the tag-less VWF fragment was collected in the flow through. The flow through was concentrated and subjected to size exclusion chromatography as the final purification step. Protein concentrations were determined using their extinction coefficients at 280 nm (232).

To produce unglycosylated AIM-A1, a bacterial codon optimized fragment of 1238-1481-6xHis (IDT) was subcloned in pDEST14 in between the NdeI and XhoI sites. The construct was transformed into Shuffle T7 express cells (New England Biolabs). A starter culture of 10 mL LB with 100 μg/mL carbenicillin (Research Products International, RPI) was inoculated with a single

colony and grown overnight with agitation at 37º C. 5mL of the saturated culture was pelleted and used to inoculate 500 mL of Terrific Broth with carbenicillin. The culture was grown at 37º C for around 4 hours until an OD_{600} of 0.8 was achieved at which point 0.4 mM IPTG (RPI) was added to the culture to induce protein expression. The temperature was lowered to 30º C for expression. Cell pellets were collected after 5 hours and lysed after a freeze thaw at -80ºC with Bugbuster (Millipore) containing 20 mM imidazole, 50 mM NaCl, and benzonase. After lysis, the suspension was clarified by centrifugation at 16,000 xg for 20 minutes at 4º C. The supernatant was loaded to Ni-Sepharose 6 FF resin (Cytiva), washed with 30 mM imidazole, and eluted with 500 mM imidazole. The elution was concentrated by ultrafiltration and further purified by size exclusion chromatography on a Superdex 75pg 16/600 column. The fractions containing the VWF fragment were slightly contaminated by a 20 kDa species. The presence of the AIM-A1 fragment (~29 kDa) was confirmed by western blot with anti-CAIM mAb 6G1, a gift from Michael Berndt (160).

Recombinant GPIbα Ligand-binding domain (LBD)

The recombinant GPIbα-LBD and LBD-W230L have been described in depth before (212). Briefly, residues 1-290 of GPIbα (mature protein residues) with a N-teminal Bio-tag, 10x His tag and C terminal FLAG tag are produced from Expi293F BirA cells and purified to homogeneity by Ni-Sepharose Excel chromatography and size exclusion chromatography (SEC) as described above. The resulting protein is a monomer as based on retention times on SEC and molecular weight by SDS-PAGE.

NAIM peptide generation

Various NAIM peptides were generated with a N-terminal biotin by Genscript (Table S2). For the NAIM peptides to be O-glycosylated, they would need to be produced in mammalian cells. To this end, a gBlock was synthesized of an α1 antitrypsin leader sequence, either NAIM (1238-1271) or residues 1253-1266, a TEV cleavage site followed by eight histidine residues connected to a human IgG1 Fc fragment. This fragment was then cloned into pcDNA 3.1 Hygro (+) for expression. Protein was produced by transient transfection of suspension Expi293F cells in Freestyle F17 media using ExpiFectamine (Gibco) following manufacturer's instructions with reduced cell density (2E6/mL) at the start of transfection. Media was collected at day 6 post transfection and purified on a rProtein A FF column (Cytiva). Protein was eluted with 100 mM sodium citrate pH 3 and fractions were neutralized with 1 M Tris-HCl pH 9. The resulting fractions were pooled, and the protein was further purified by size exclusion on a Superdex 200 Increase 10/300 GL column (Cytiva). The protein was subject to removal of sialic acids by digestion with 1 U neuraminidase (from *Arthrobacter ureafaciens*, Roche) per 100 uL of protein at 0.5 mg/mL when desired.

Immunized yeast display library

One adult *Lama glama* was immunized with approximately 600 μg total of tagless AIM-A1 over a period of 77 days by Abbiotec (San Diego, CA). A 50 mL production bleed was performed at day 84 where PBMC RNA was isolated, and cDNA was generated from 10 μg of RNA extract by oligo dT reverse transcription. VHH specific genes were amplified from the cDNA library by polymerase chain reaction using Q5 high fidelity DNA polymerase (NEB) with primers VHHgenFv2_50, VHHgenL7v2_50, and VHHgenL8v2_50 (Table S1) annealing to the CH1 and hinge regions of IgG2b and IgG3b respectively (134). The primers contained 50 base pair

overhangs homologous to the backbone vector pYDNB, a derivative of pCTcon2 (139). pYDNB was constructed by digesting pCTcon2 with EcoRI and BglII and insertion of a gBlock containing the improved secretory leader sequence αppS4 (233), a NdeI-SalI-XhoI insertion site, and a C-terminal aga2p fusion protein as occlusion at the N-terminus of nanobodies may interfere with antigen recognition. When cloned in frame, yeast display of aga2p surface expression can be validated with either anti-FLAG or anti-c-Myc antibodies. Approximately 120 μg of purified PCR products were mixed with 40 μg triple digested (NdeI-SalI-XhoI) pYDNB for electroporation reactions. Electrocompetent EBY100 *Saccharomyces cerevisiae* (ATCC MYA-4941) were prepared as described (20130105). 11 electroporation reactions were conducted at 2.5 kV, 175 Ω, and 25 μF. Time constants ranged between 3 and 4.7 seconds. A total library size of around 1.4E8 transformants was obtained from colony counts of serial dilutions of transformants. The transformed cells were grown in SD-CAA media pH 4.5 with 1% penicillin/streptomycin for 2 days at 30º C.

Library sorting to obtain NAIM-specific clones

Approximately 1.5E9 yeast were induced with SG-CAA media for 20 hours at 30º C for nanobody expression. Magnetic sorting was performed largely as described (139). The library size was reduced to around 2.2E7 by magnetic activated cell sorting (MACS) using LS columns (Miltenyi) and streptavidin magnetic beads. Yeasts were incubated with 1 μM biotinylated AIM-A1 for one hour at 25º C with agitation. After pelleting of the yeasts the cells were incubated with streptavidin-magnetic beads (Miltenyi) on ice for 15 minutes. Yeasts were washed with ice-cold PBS containing 1% BSA (PBS-F), resuspended and loaded to equilibrated LS columns. A 10-fold excess of diversity was preserved for the following flow sorting steps. Cell sorting was performed

on a BD FACS Aria II. Induced cells were incubated with 500 nM biotinylated AIM-A1, washed, then labelled with Alexa Fluor 488 anti-DYKDDDDK Tag antibody (1:100, Biolegend 637318) and Streptavidin-APC (1:100, Invitrogen 21629) in PBS-F for 30 minutes on ice, washed, nylon-filtered and sorted for all double positive events. The library size was estimated to include 1.4E6 colonies. We then sought depletion instead of further enrichment of AIM-A1 (Biospy 1238-1493) to preserve diversity. The mostly AIM-A1 enriched library was then depleted against biotinylated-A1-CAIM using MACS as described above using around 3E7 cells as the input. Nanobodies that bound to the A1 domain or CAIM would adhere to the column while non binders and NAIM-specific nanobodies would flow through. The yeast in the flow through were then re-grown, induced and sorted for AIM-A1 binding as above by FACS. The resulting library resulted in roughly 15,000 colonies. Individual clones were selected for sequencing by yeast miniprep (Zymo Research) followed by PCR with primers Gal1F and T7. The PCR products were sequenced by Genewiz using primer pYDNBseqF which anneals ~100 base pairs before the start of the nanobody gene. Primer sequences can be found in Supplemental Table 4.1.

Flow cytometery

For the GPIbα binding induction assay, 1E7 of each clone were induced overnight at 30º C in SG-CAA. A suspension of 1E7 induced cells in PBSF was made by dilution of the saturated culture usually around 1:20 v/v. After washing in PBSF, around 1E6 cells were incubated with biotinylated-GPIbα LBD, non-biotinylated AIM-A1, or a mixture of both for one hour at room temperature. The cells were then washed in PBSF and labelled with 1:250 Streptavidin-Phycoerythrin (BD 554061) for 15 minutes on ice. The cells were then washed and resuspended in PBSF. Data was obtained on a Beckman Coulter Cytoflex. 10,000 events were captured for each

condition, and yeasts were gated by FSC and SSC area then singlets were obtained by SSC area and height. Data was analyzed in FlowJo v10.8 (BD).

Nanobody subcloning, expression, and purification

Nanobody PCR products from the yeast display plasmid were digested with NdeI and XhoI and were ligated into pDEST14 digested with the same enzymes which resulted in the addition of a 6xHis to the c-terminus of the reading frame. Expression plasmids were transformed into Shuffle T7 Express *E. coli* (NEB). For protein expression, bacteria were grown and induced as described for bacterial AIM-A1 with the modification of 1 mM IPTG to induce protein expression. Purification was performed as described above for bacterial AIM-A1, with an increased 40 mM imidazole in the wash buffer for nickel affinity chromatography, and size exclusion chromatography performed on a Superdex 200 Increase 10/300 GL column in PBS.

Biolayer interferometry (BLI)

BLI experiments were performed on an Octet QK^{e} instrument using the Data Acquisition software v11.1.1.19 (ForteBio, Fremont, CA). Data was acquired at 0.3 Hz at 25^{o} C. We have noticed that quite low loading amounts to the bio-sensors results in greatly improved kinetic fittings and reduced non-specific binding at the higher concentrations tested for different analytes. For streptavidin sensors loaded with VWF fragments we found 0.3 nm of ligand was sufficient. The optimal level for human Fc-conjugates loaded to protein A sensors was 0.5 nm. For biotinylated full-length VWF, 1 nm was loaded to streptavidin sensors to obtain sufficient signal given the discrepancy between molecular weight of a VWF monomer (280 kDa) to a nanobody (15 kDa). Full-length VWF was biotinylated as described previously (97) and collected in the void volume

of a Superdex 200 10/300 Increase column. Streptavidin sensors were washed with 1 M NaCl at the end of the dissociation step and Protein A sensors were regenerated with 10mM glycine pH 1.7. In all cases proteins were diluted to the desired concentration with Kinetics buffer (Sartorious) diluted in PBS pH 7.4. All data was corrected by an analyte deficient, loaded reference to account for instrument drift and ligand dissociation. All binding sensorgrams are all fitted to a 1:1 global binding model for the included concentrations.

ELISA

For the detection of nanobody 6D12 and antibody 6G1 binding to AIM-A1, a high-binding microtiter plate (Corning) was coated overnight at 4º C with 5 μg/mL AIM-A1 in PBS from bacteria or Expi293F cells. The plate was blocked with 1% BSA in PBS-T for two hours at room temperature and washed 3x with PBS-T. Protein dilutions were then applied to the plate for one hour. After washing, rabbit anti-VHH antibody (Genscript, A01860) was added at 1:2000 to detect 6D12 or 1:4000 goat anti-Mouse HRP polyclonal antibodies (Jackson ImmunoResearch, 115-035-003) to detect 6G1. After one hour, the plate was washed and One-step Ultra TMB (Thermo Scientific) was added. The TMB-HRP reaction was quenched with H_2SO_4 and then read at 450 nm with subtraction at 620 nm.

For the GPIbM:Nb (LBD-W230L, plasma incubated with activating nanobodies) assay, 10 μg/mL of streptavidin (Agilent) in carbonate coating buffer pH 9.6 was coated overnight at 4º C. The plate was blocked with 1% BSA in PBS-T for one hour at room temperature. The plate was washed 3 times between all steps with HBS-T. Site-specifically biotinylated GPIbα W230L residues 1-290 was then added at 10 μg/mL for one hour. An equal volume of normal human plasma (George

King Biomedical), or patient plasma samples, diluted 1:15 in .1% BSA in PBS-T was mixed with various dilutions of each nanobody at the specified concentrations. The plate was gently agitated for one hour at room temperature. Anti-VWF polyclonal antibodies (Agilent/Dako, A0082) at 1 μg/mL were added for 30 minutes followed by goat anti-rabbit polyclonal antibodies conjugated with HRP (Jackson ImmunoResearch, 111-035-144) at 1:2000 dilution in 1% BSA PBS-T for 30 minutes. One-step ultra TMB was added, and the reaction was quenched with 2M sulfuric acid. The plate was then read at 450 nm with subtraction at 620 nm.

VWF antigen level (VWF:Ag) was determined by coating a high binding microtiter plate with 5 μg/mL rabbit anti-VWF antibodies (Agilent/Dako, A0082) in carbonate coating buffer pH 9.6 overnight at 4º C. The plate was blocked with 1% BSA in PBS-T for one hour at room temperature. VWF samples were added at dilutions of 1:26 and 1:130 and detected with HRP-conjugated polyclonal rabbit anti-VWF at 1:2000 dilution in blocking buffer. Substrate and quenching were performed as described above. VWF antigen was determined from the standard curve of the VWF calibrators by averaging the two dilutions (Diapharma).

SDS-PAGE, western blotting, and dot blotting

Samples were diluted with Laemmli sample buffer with or without β-mercaptoethanol as a reducing agent. SDS-PAGE gels (4-20%, Genscript) were stained with One-step blue (Biotium) for Coomassie staining. After protein transfer to a nitrocellulose membrane, the membrane was blocked with 1% BSA in PBS-T, and around 5 μg/mL nanobody or antibody was added overnight at 4º C with agitation. The membranes were washed with TBS-T, and then incubated with either biotinylated or non-biotinylated rabbit anti VHH (96A3F5, Genscript) at 1:4000. The membranes

were then blotted with Licor IRdye 680 goat anti-Rabbit and Licor IRdye 800 goat anti-mouse at 1:4000. For dot blots, 1 μg of VWF fragment or 0.01 μg of peptide were blotted to a nitrocellulose strip. Gels and membranes were scanned on a Licor Odyssey CLx.

Platelet aggregation

Written informed consent was obtained from participants before their inclusion in studies, and all procedures using donor-derived human blood and platelets were approved by the Institutional Review Board at Emory University. Human blood obtained by venipuncture into sodium citrate tubes (BD) was centrifuged at 240 xg with no brake for 12 minutes. PRP was gently aspirated away from RBCs and platelet counts corrected to 200,000/μL in freshly thawed pooled normal plasma (George-King Biomedical). Nanobodies or ristocetin (MP Biomedicals) were added to the stirred suspension at 30 seconds. When ARC1172 or mAb 11A8 were used, they were added at 30 seconds with 500 nM nanobodies added at 60 seconds. Platelet aggregation was recorded in AGGRO/LINK software (Chrono-log, Havertown, PA), exported, and normalized to initial optical densities of 100 manually. The extent of aggregation was measured as the optical density at 300 seconds. Each concentration and condition were performed in triplicate. Dose response curves to obtain EC_{50} and hill slope were generated by non-linear regression using a 4-parameter variable slope dose-response in GraphPad Prism 9.

4.4 Results

The conformation of the AIM determines the potential for VWF activation. When the AIM has been disrupted, and A1 is exposed, VWF is in an activated state capable of binding to platelets. Proteins or small molecules that bind to the AIM have the potential to disturb the autoinhibition it

confers to A1 (Fig. 4.1A). We sought to generate nanobodies to the AIM by immunization of a llama with recombinant, glycosylated, human AIM-A1 (1238-1481) followed by nanobody yeast display. A yeast display library of 1.4E8 transformants was sorted for AIM-A1 specific binding by antigen coupled magnetic bead sorting to reduce the library size, followed by rounds of fluorescence-activated cell sorting. After the library size had been reduced to around 1E6 colonies, nanobodies that bound to A1-CAIM were removed by magnetic depletion. The library was then resorted for AIM-A1 binding (Fig. 4.1B). From this population, several thousand colonies emerged, with one dominant clone found in over 75% of sequenced nanobodies. This nanobody, CAIM-depleted (Cd) Round **6** Clone 1**C4**, henceforth referred to as 6C4, showed high-affinity binding to AIM-A1 by flow cytometry (Fig. S4.1A). Two related clones, 6C11 and 6D12, bound with even higher affinity (Fig. S4.1A).

Using the tag-less immunogen and a biotinylated LBD, we tested the ability of the nanobodies to induce LBD binding to AIM-A1. It should be noted that wild type GPIbα will not bind to AIM-A1 in the absence of force or activating reagent at nanomolar concentrations. Yeast cells only stained positive for GPIbα in the presence of AIM-A1 (Fig. 4.1C, D). In essence, the yeast displayed nanobodies could bind to AIM-A1 and facilitate a conformational change within AIM-A1 to induce binding to GPIbα.

Monomeric nanobodies were produced in *E. coli* and purified to determine their binding affinity to various VWF fragments (Fig. S4.1B, C). Despite the overwhelming presence of 6C4 in the screen, it bound with the lowest affinity to AIM-A1 of the three clones tested by BLI with an equilibrium dissociation constant of around 120 nM (Fig. 4.2A, D). 6C11 (K_D ~10 nM) and 6D12 (K_D ~30 nM) are likely products of *in-vivo* somatic hypermutation as there are subtle differences in CDRs 1 and 3 (Fig 4.2B, C, D). When added to stirred platelet-rich plasma at high enough

Figure 4.1. Isolation of NAIM binding nanobodies by yeast surface display.

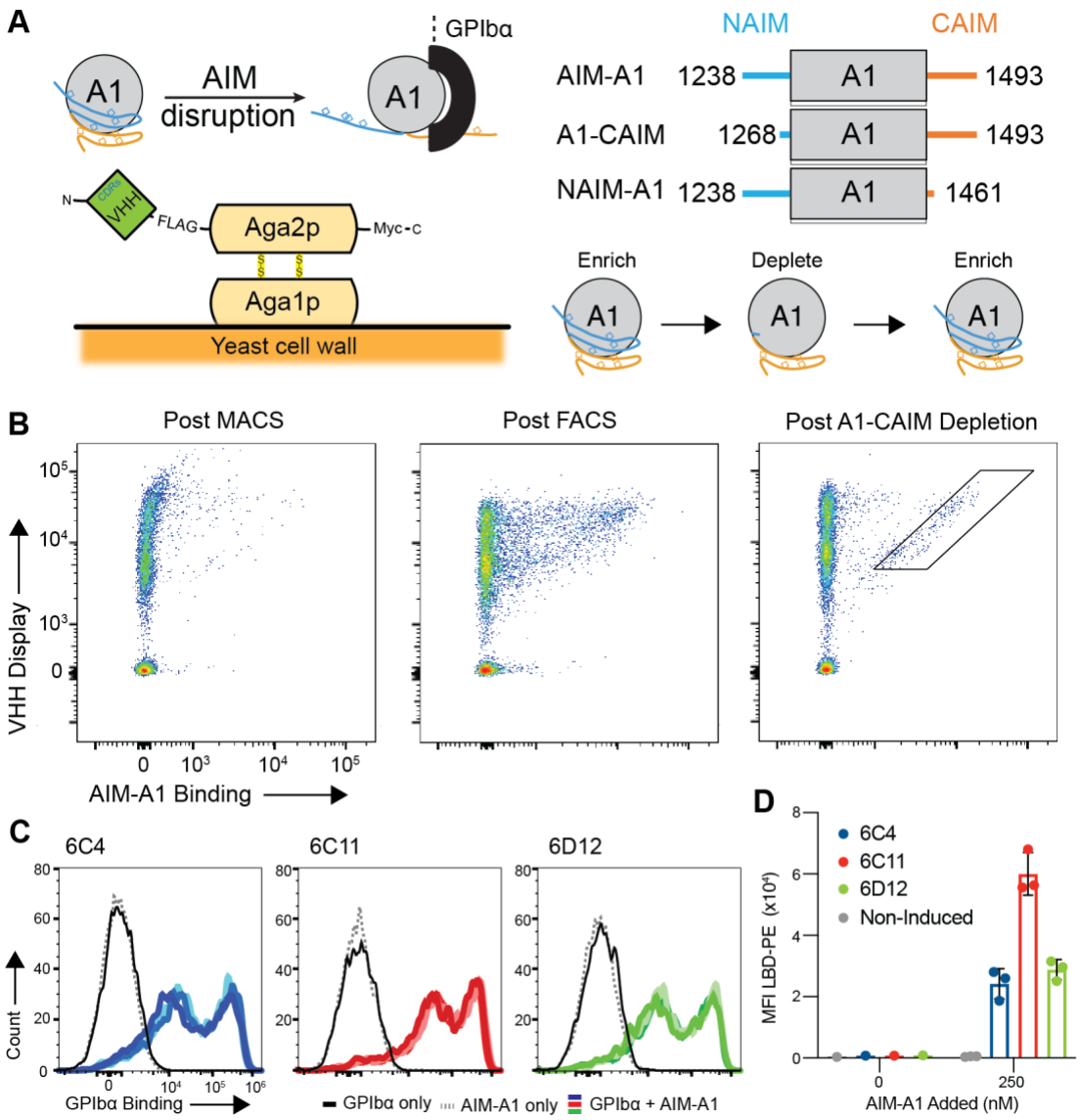

(A, top) Schematic of AIM disruption leading to VWF activation and GPIbα binding and various AIM containing or lacking proteins. VHH genes were fused to Aga2-p subunit and displayed on the surface of yeast. Yeast were sorted for AIM-A1 binding, depleted with A1-CAIM, and resorted for AIM-A1 to obtain NAIM specific binders (A, bottom). (B) Dot-plots of a subset of each sorting step. AIM-A1 specific binders were first isolated by MACS to reduce the library size and FACS was performed to quantitative select double positive events. VHH display from the FLAG-epitope displayed on the Aga2p fusion is shown on the y-axis, and AIM-A1 binding is

shown on the x-axis. NAIM-specific binders were isolated from the approximate sort gate on the third panel. (C) Individual colonies of yeast induced to display 6C4, 6C11, and 6D12 were incubated with either AIM-A1 (250 nM), GPIbα-LBD (1 μM), or both AIM-A1 and GPIbα-LBD. The amount of biotinylated-LBD binding was determined using streptavidin-PE. (D) The median fluorescence intensity of LBD binding was determined in the presence or absence of 250 nM AIM-A1 using each clone in triplicate. Non-induced yeast cells show no binding to GPIbα in the presence of AIM-A1.

Figure 4.2. Isolated nanobodies bind with nanomolar affinity to AIM-A1.

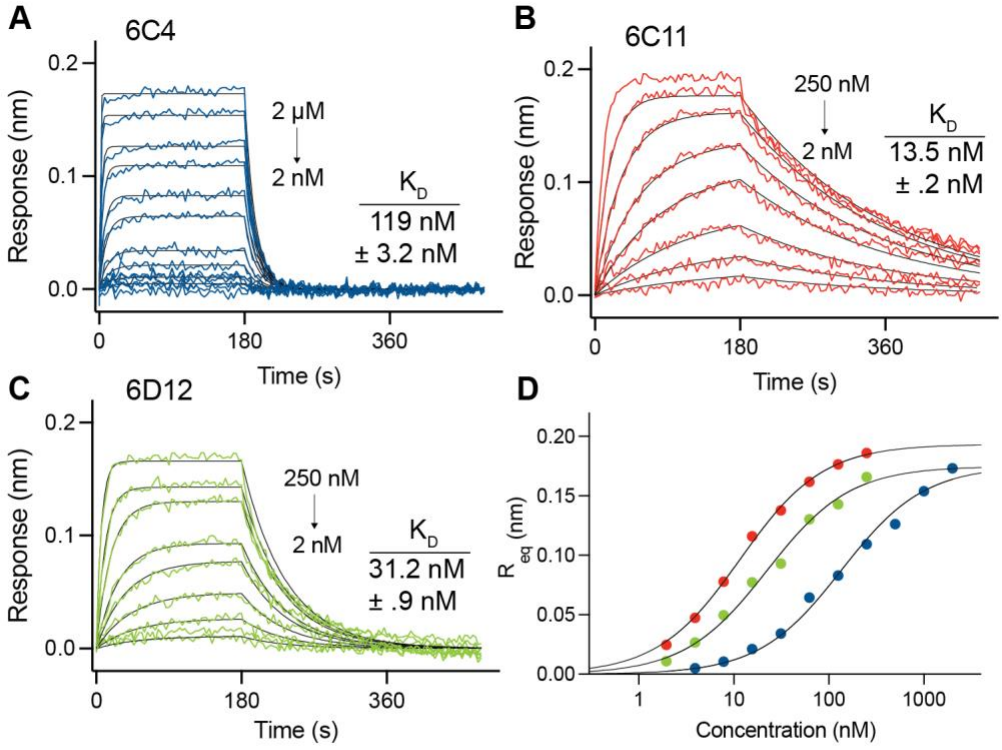

E

VHH	K_D (M)	K_D error	k_a (1/Ms)	k_a error	k_d (1/s)	k_d error	$K_{D,eq}$	$K_{D,eq}$ error
6C4	1.19E-07	3.18E-09	6.48E+05	1.56E+04	7.73E-02	8.90E-04	135.7 nM	34 nM
6C11	1.35E-08	2.13E-10	4.11E+05	6.14E+03	5.55E-03	2.79E-05	11.65 nM	1.40 nM
6D12	3.12E-08	8.82E-10	5.93E+05	1.60E+04	1.85E-02	1.56E-04	22.45 nM	7.30 nM

Representative bio-layer interferometry sensorgrams of site-specifically immobilized AIM-A1 binding to a serial dilution of purified 6C4 (A), 6C11 (B), or 6D12 (C). Concentrations in the serial dilution are shown in each panel alongside the calculated affinity for each nanobody. Affinities and standard deviation of the measurement was determined through 1:1 global kinetic fitting to each trace with observable binding. The theoretical sensorgram based on the global fit for each concentration is shown in black. (D) Equilibrium binding isotherms for each nanobody plotted as the log of concentration used. Calculated equilibrium binding responses (R_{eq}) from the global 1:1 fitting for the concentrations in the serial dilution for each nanobody were fit to a

hyperbola (black). Half-maximal binding was obtained from the fit to hyperbola and the equilibrium K_D along with kinetic fitting parameters are shown in panel (E).

concentrations, all nanobodies induced ristocetin-like aggregation traces (Fig. 4.3). Despite having the highest affinity, 6C11 is less potent than 6D12 at inducing VWF-dependent platelet aggregation. EC_{50} values were ordered 6C4>6C11>6D12 with values of 167, 100 and 57 nM respectively (Fig. 4.3D). The hill slope of the dose-response was 7-8 for each nanobody, although we are unsure what this translates to physiologically. To verify that the aggregation was VWF-and GPIbα-dependent, we used two inhibitors to block either A1 (ARC1172) (161) or GPIbα-LBD (mAb 11A8) (88). Both inhibitors completely blocked the nanobody-induced aggregation, confirming that the activation of platelets in this case is induced by VWF binding to GPIbα (Fig. S4.2).

Using our AIM-deleted constructs we were able to further identify the binding epitope of these nanobodies within the AIM. As expected, the nanobodies showed no binding to A1-CAIM (Fig. 4.4A) and bound to NAIM-A1 (Fig. 4.4B, S4.3A) with comparable affinities to AIM-A1. Unexpectedly, the nanobodies showed no binding to tAIM-A1 (1261-1472, Fig. 4.4C, S4.3B). The primary sequence of the NAIM preceding residue 1261 is presumably largely unstructured as it is rich in prolines and contains 3 O-glycans. Furthermore, this epitope is strange as nanobodies are particularly known for their ability to bind to pockets and cavities due to the length of their third CDR loop (129). We tested the ability of the nanobody family to bind to the immunogen by western blot. All nanobodies were able to blot AIM-A1, regardless of reducing or non-reducing conditions, which indicates that the nanobodies recognize a linear epitope in the NAIM (Fig. S4.4A).

15mer overlapping peptides within the NAIM were generated by chemical synthesis. By dot blot, none of the nanobodies showed any binding to the peptides, but clearly bound to the immobilized AIM-A1 on the same blotting membrane, suggesting that the nanobodies may bind to glycans located on the NAIM (Fig. S4.4B). The 4 O-linked glycans on the NAIM are nearly

Figure 4.3. Addition of the nanobodies to PRP induces ristocetin-like platelet aggregation.

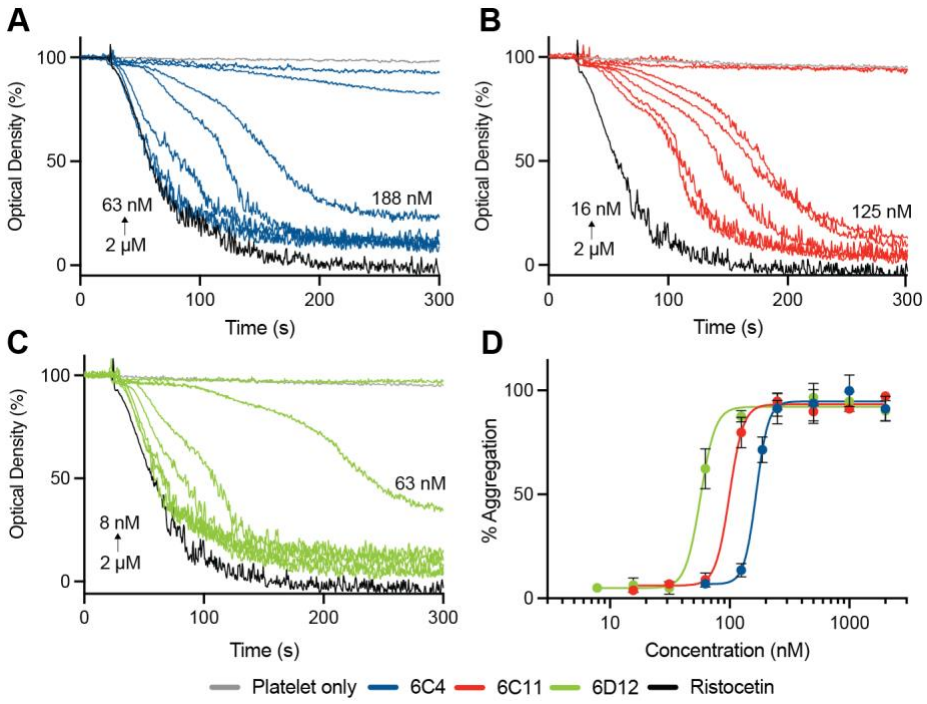

Human platelet-rich plasma was gently stirred, and aggregation was followed in a light transmission aggregometer. At 30 seconds 6C4 (A), 6C11 (B), or 6D12 (C) was added at various concentrations spanning tens of nanomolar to 2 micromolar depending on the nanobody being tested. Each concentration was tested in triplicate. Ristocetin was added in separate runs to 1.5 mg/mL, shown in black. Platelets stirred without addition of an agonist is shown in grey. (D) Dose-aggregation curves were plotted for each concentration of each nanobody and fit to a 4-parameter dose-response curve. Percentage aggregation is the inverse of optical densities seen in panels A-C. Error bars are the standard deviation of the measurements.

Figure 4.4. Binding specificity to the NAIM is mediated by both primary sequence and O-glycan sugars

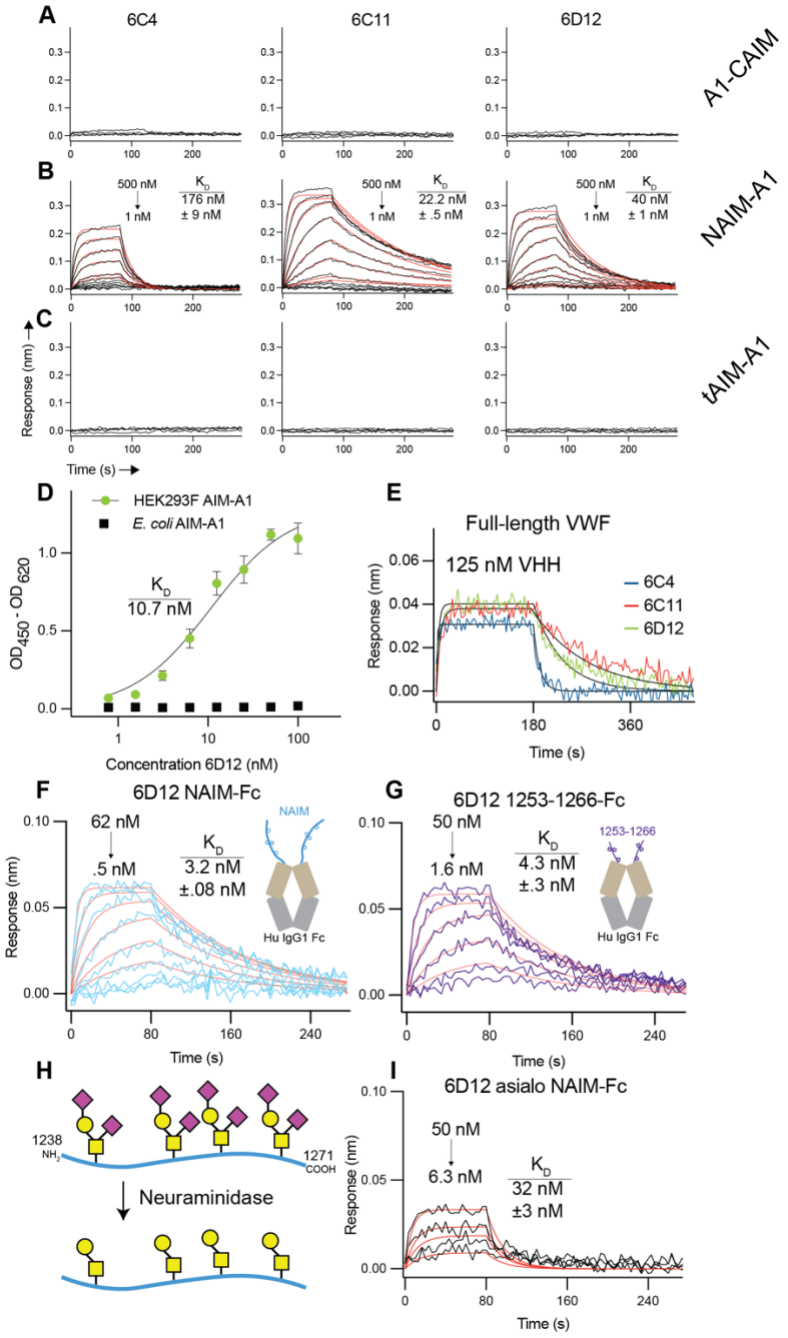

Dilutions of each nanobody were tested for binding by bio-layer interferometry to A1-CAIM (A), NAIM-A1 (B), and tAIM-A1 (C). Observable binding was only seen for NAIM-A1. Global 1:1 kinetic fitting was applied to the dilutions tested and theoretical curves are shown in red.

Kinetic K_D and standard deviation of the kinetic fitting is shown to the right of the sensorgrams. Steady state fittings are shown in Figure S3A. (D) ELISA binding isotherms of 6D12 to immobilized AIM-A1 purified from mammalian cells (green circles) or *E. coli* (black squares). Error bars are the standard deviation of triplicate measurements. Responses were fit to a hyperbola and K_D derived from half-maximal binding. (E) BLI traces of 125 nM of each nanobody binding to immobilized full-length VWF. BLI traces of a dilution series of 6D12 binding to immobilized NAIM-Fc (F) or 1253-1266-Fc (G). 1:1 global kinetic fitting is shown in red and kinetic K_D and standard deviation of the kinetic fitting is shown to the right of the sensorgrams. (H) The NAIM is occupied with four core 1 O-linked glycans bearing sialic acids (purple squares). Treatment with neuraminidase removes the sialic acids leaving only core 1 structures. Reduction of apparent molecular weight after treatment is shown in Figure S8. (I) BLI traces of 6D12 binding to neuraminidase treated NAIM-Fc. 1:1 global kinetic fitting is shown in red and kinetic K_D and standard deviation of the kinetic fitting is shown to the right of the sensorgrams.

always of core 1 structure and the sugars are further decorated with sialic acids, and sometimes are disialyated (99; 117). We produced unglycosylated AIM-A1 from *E. coli* (Fig. S4.5A,B). By ELISA, 6D12 did not show any binding to bacterial AIM-A1, but bound with nanomolar affinity to the immobilized, mammalian AIM-A1 (Fig. 4.4D). There was no difference in binding of mAb 6G1 to the *E. coli* derived AIM-A1 or mammalian AIM-A1, which recognizes a linear sequence in the CAIM (Fig. S4.5C) (160). We also confirmed that the nanobodies bind to full-length, plasma derived VWF by BLI (Fig. 4.4E, S4.5D).

To further validate that the glycan-containing NAIM was responsible for the epitope, we fused either the NAIM or a section of the NAIM containing 3 glycans (1253-1266) to a human IgG1-Fc fragment and expressed the protein in human, Expi293F cells (Fig. S4.6A). Both the NAIM-Fc and 1253-1266-Fc proteins were able to support binding of 6D12 by western blot (Fig. S4.6B) and bio-layer interferometry (Fig. 4.4F, G, S4.7). Interestingly, the nanobodies bound these peptide-Fc proteins with higher affinity than AIM-A1, suggesting that the epitope is partially protected in the inactive state of VWF.

The importance of sialylation to VWF activity has been known for several decades (234). Recently, we demonstrated that desialylation of the AIM can partially destabilize the AIM (117). We subjected the NAIM-Fc protein to digestion with α2-3,6,8 neuraminidase, a bacterial glycohydrolase that will cleave sialic acids off of glycans, in order to determine if sialic acids contributed to 6D12 binding (Fig. 4.4H). The protein was slightly reduced in apparent size by SDS-PAGE (Fig. S4.8) indicative of the removal of a few kilodaltons worth of sialic acids consistent with our previous investigation of asialo AIM-A1 (117). Surprisingly, the relative binding response and apparent affinity of 6D12 to NAIM-Fc was reduced after α2-3,6,8 neuraminidase treatment (Fig. 4.4I). Overall, these results suggest that the nanobodies recognize

both primary amino acid sequence and core 1, sialylated, O-glycans as none of the nanobodies bind to A1-CAIM, which also contains four core 1, sialylated, O-linked glycans (99; 235).

While the nanobody family may serve as a useful set of research reagents in the future, we wanted to evaluate the performance of the nanobodies in a ristocetin cofactor-like ELISA assay for clinical diagnosis of VWD. Normally, ristocetin is mixed with plasma and binding to recombinant GPIbα or fixed platelets is evaluated (VWF:Rco) in comparison to total VWF levels, VWF antigen (VWF:Ag). Patients with type 2 VWD will have a skewed Rco/Ag ratio, while patents with only low levels of VWF will have a low activity corresponding with a low antigen, such as in Type 1 VWD. There have been several documented cases of patients with mutations in the CAIM where ristocetin may bind, such as residues 1460, 1461, 1462, 1464, 1467, 1472, 1475 (111; 236). D1472H is a common polymorphism that can confound ristocetin based measurements of VWF activity. These mutations will yield a falsely low VWF activity, confounding further diagnosis.

We designed an ELISA using a recombinant LBD bearing a W230L mutation, a platelet-type (PT) VWD mutation, that has the highest known affinity of any PT mutation in combination with the nanobodies (64). We first used a titration of each nanobody to determine the EC50 of each in this ELISA format, GPIbM:Nb. Each nanobody could dose dependently induce plasma VWF binding to LBD-W230L, with 6D12 showing the highest potency for activation (Fig. 4.5A), in agreement with our aggregation studies (Fig. 4.3). Based on these curves, using hundreds of nanomolar 6D12 mixed with plasma dilutions would yield maximum activation.

The most apparent usage of this GPIbM:Nb assay would be to confirm type 2B VWD. Confirmed type 2B VWD patient samples bearing a V1316M or P1266L plus D1472H polymorphism were tested using this assay. Additionally, a type 1 VWD sample was tested with a

Figure 4.5. A gain-of-function GPIbα fragment used with activating nanobodies can discriminate between subtypes of von Willebrand's Disease.

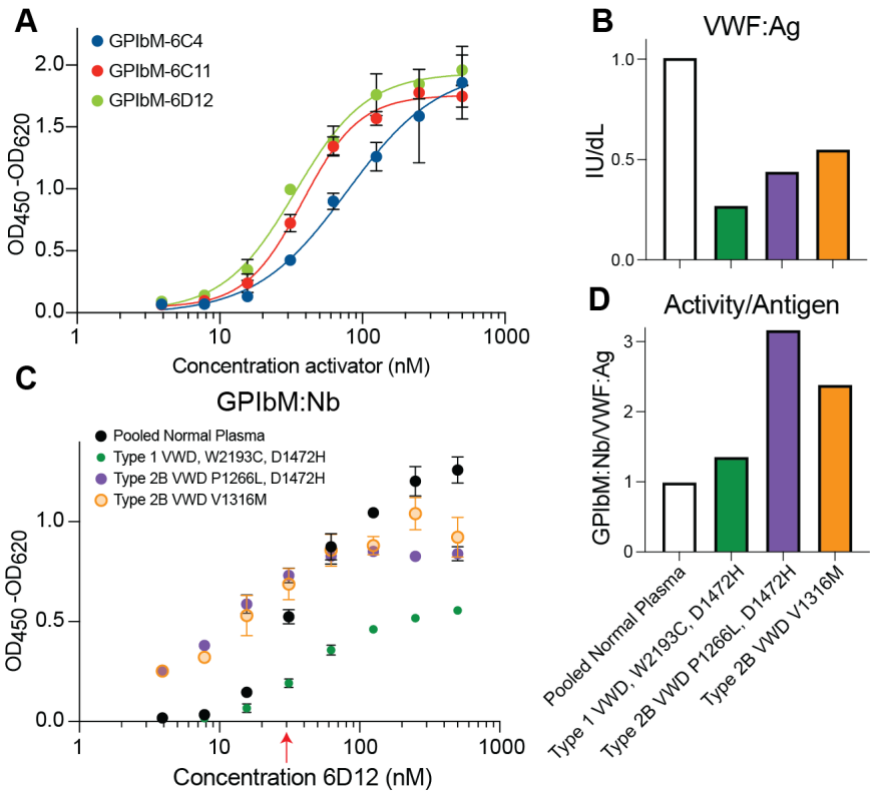

(A) Binding isotherms of a constant dilution of pooled normal human plasma to immobilized GPIbM (W230L-LBD) with a dilution series of the activating nanobodies. Error bars are the standard deviation of triplicate measurements. Binding curves were fit to a hyperbola. (B) VWF antigen levels were measured in pooled normal plasma, a type 1 VWD sample bearing a W2193C mutation and D1472H polymorphism (green), a type 2B VWD sample bearing a P1266L mutation and D1472H polymorphism (purple), and a type 2B VWD sample bearing a V1216M sample. Measurements are determined by averaging the values obtained from triplicate measurements of 1:26 and 1:130 dilutions of sample compared to commercial VWF antigen standards. (C) Binding isotherms of a constant dilution of plasma samples to immobilized GPIbM (W230L-LBD) with a dilution series of 6D12. Error bars are the standard deviation of

triplicate measurements. (D) Activity/antigen ratios for each of the samples. The activity of VWF for each sample was determined by dividing the response at 32 nM 6D12 (red arrow) of each sample in panel C compared to pooled normal plasma. That activity value was divided by the antigen value in panel B to yield the activity ratio.

heterozygous mutation of W2193C, also with the D1472H polymorphism. Consistent with the diagnosis, both type 1 and 2B samples show reduced VWF levels (Fig. 4.5B). Using a titration of 6D12, we are able to observe that the activity of the 2B samples is increased at the lower concentrations of 6D12 used compared to pooled normal plasma, despite the decreased amount of VWF present in the plasma (Fig. 4.5C). Type 2B mutations increase the affinity of VWF for GPIb, which is reflected in this assay. The type 1 sample shows a decreased binding signal compared to pooled normal plasma at all concentrations. The resulting ratio of activity to antigen levels using 32 nM 6D12 is 1 for pooled normal plasma, 1.35 for this type 1 sample, 3.17 for the P1266L mutation, and 2.39 for the V1316M mutation (Fig. 4.5D). Based on the results from these initial samples, the difference in activity between type 2B, type 1, and a normal sample would be easily distinguishable.

4.5 Discussion

We sought to use nanobody discovery to further our understanding of the AIM and how it regulates VWF activation. Generation of an immunized nanobody library yielded three nanobody clones that activate VWF through binding to the NAIM. We localized the binding epitope of these nanobodies to a distal, structurally unresolved section of the AIM – residues 1253-1266. The binding epitope 6D12 was further dependent on the presence of O-linked glycosylation, as we demonstrated lack of binding to unglycosylated AIM-A1 produced in bacteria. O-linked glycans can be highly branched, and for VWF are nearly always decorated with sialic acids, a negatively charged alpha-keto sugar that has demonstrable importance in VWF clearance and activity. The activating function of these nanobodies can be used to induce rapid agglutination of human platelet-rich plasma. Furthermore, a GPIb:RCo-like ELISA assay utilizing these

nanobodies can easily discriminate type 2B VWD from normal or type 1 VWF when using activity to antigen ratios and are unaffected by the presence of common polymorphisms found at 1472.

Despite attempts to crystallize proteins containing the AIM and A1, we and others were unable to resolve any electron density before residues 1262 or past residues 1466. However, previous studies have demonstrated that the unresolved residues do participate in the autoinhibition of VWF, as a construct from 1262 to 1466 will show ~200 nM affinity for GPIbα (75). The demonstration that the epitope of these nanobodies must contain residues 1253-1266 suggests that the conformation of the distal AIM (residues unresolved in the crystal structures of AIM-A1) is indispensable for AIM-based protection of A1. The difference in binding affinity of the nanobodies to the NAIM-Fc versus AIM-A1 suggests that the binding epitope is partially obscured in the presence of A1. To this end, the nanobodies may act as a decoy for the NAIM, pulling it away from interacting with the A1 domain, thereby activating VWF.

The precise mechanism of ristocetin-based activation of VWF is still unsolved. It is known that recognition of a specific sequence is necessary, as ristocetin has reduced effects on mouse VWF or samples with polymorphisms in the A1-proximal CAIM (111; 204). The mechanism of ristocetin is also unusual given its low affinity to VWF and its apparent oligomerization in solution (180). Furthermore, despite the NAIM constituting the majority of the force resistance of the AIM, ristocetin uses the CAIM to activate VWF (160). The binding of these nanobodies with nanomolar affinities to a well-defined epitope on the NAIM is an interesting juxtaposition to ristocetin.

Other activating agents for the GPIbα-VWF interaction have been developed, although none as well defined, mechanistically, as our nanobodies. The mAb 1C1E7 binds to the D'D3

assembly on VWF and can increase the susceptibility of VWF for activation using ristocetin (118). The precise epitope, and mechanism of action of this antibody await elucidation. The snake venom protein botrocetin is an interesting molecule, as its activation is dependent on GPIbα and VWF. Botrocetin also binds near the primary binding site of VWF A1, aiding the formation of the beta sheet across the thumb of the LBD and overpowering the protection of the AIM (108). In an attempt to develop a small molecule inhibitor of VWF-GPIbα, a small molecule called G6 was screened for its binding to GPIbα and inhibitory properties. Unexpectedly, G6 could enhance the binding of platelets to VWF under shear (237).

We cannot currently explain the differential efficacy for activation of VWF between the individual nanobody clones. While 6C11 is clearly the higher affinity clone, 6D12 is superior in terms of its activating qualities, despite binding to the same epitope. Future structural studies may help to elucidate the precise binding epitope, including sugars, as well as shed light on the molecular basis of this increased efficacy. Affinity is not always the only determinant of receptor activation, as the unknown intrinsic efficacy of a compound must be considered (238).

4.6 Acknowledgments

The authors would like to thank Lisa Bixby and Aaron Rae of the Emory Pediatric/Winship Flow Cytometry Core for their assistance with FACS sorting of yeasts. This work was supported in part by NIH research grants HL082808 and HL143794 and an infrastructure grant from Hemophilia of Georgia Center for Bleeding & Clotting Disorders of Emory. N.A.A. was supported in part by NIH fellowship HL154656.

4.7 Supplemental Information

Supplemental Table 4.1. Primers used in this study, 5' to 3'

VHHgenFv2_50	*AGCATTGCTGCTAAAGAAGAAGGGGTACAATTAGATAAAAGAGAGG CCCATATG*CAGGTGCAGCTGGTGGAGTCTGGRG
VHHgenL7v2_50	*CCTCCTCCACCCCAATGGTGGGACCCTTTGTCATCATCATCCTTAT AGTCCTCGAG*GGGGTCTTCGCTGTGGTGCG
VHHgenL8v2_50	*CCTCCTCCACCCCAATGGTGGGACCCTTTGTCATCATCATCCTTAT AGTCCTCGAG*TGGTTGTGGTTTTGGTGTCTTGGGTT
pYDNBseqF	CCTTGCCATTATCCGATAGC
Gal1F	ATTTTCGGTTTGTATTACTTC
T7	TAATACGACTCACTATAGGG

Italics denote homologous regions for *in-vivo* recombination

Supplemental Table 4.2. NAIM-peptides used in this study N-C

1238-1257	QEPGGLVVPPTDAPVSPTTL
1243-1262	LVVPPTDAPVSPTTLYVEDI
1248-1267	TDAPVSPTTLYVEDISEPPL
1252-1271	VSPTTLYVEDISEPPLHDFY

Supplemental Information 4.1. DNA insert of improved secretory leader sequence and C-terminal Aga2p fusion

EcoRI

GAATTCATGAGATTTCCTTCAATTTTTACTGCAGTTGTCTTCGCAGCATCCTCCGCATTAGCTG
CTCCAGCAAACACTACAGCTGAAGATGAAACGGCACAAATTCCAGCTGAAGCTGTCATCGGTTA
CTTAGGTTTAGAAGGGGATAGCGATGTTGCTGCCTTGCCATTATCCGATAGCACAAATAACGGG
TCATTGTCCACAAATACTACTATTGCCAGCATTGCTGCTAAAGAAGAAGGGGTACAATTAGATA
AAAGAGAGGCCCATATGGAGGTTCAAGTCGACGTGTCATCCCTCGAGGACTATAAGGATGATGA
TGACAAAGGGTCCCACCATTGGGGTGGAGGAGGCTCTGGTGGAGGCGGTAGCGGAGGCGGAGGG
TCGCAGGAACTGACAACTATATGCGAGCAAATCCCCTCACCAACTTTAGAATCGACGCCGTACT
CTTTGTCAACGACTACTATTTTGGCCAACGGGAAGGCAATGCAAGGAGTTTTTGAATATTACAA
ATCAGTAACGTTTGTCAGTAATTGCGGTTCTCACCCCTCAACAACTAGCAAAGGCAGCCCCATA
AACACACAGTATGTTTTTGAACAAAAGCTTATTTCTGAAGAGGACTTGTGA**AGATCT**

BglII

Supplemental Figure 4.1. Binding and purification of 6C4, 6C11, and 6D12.

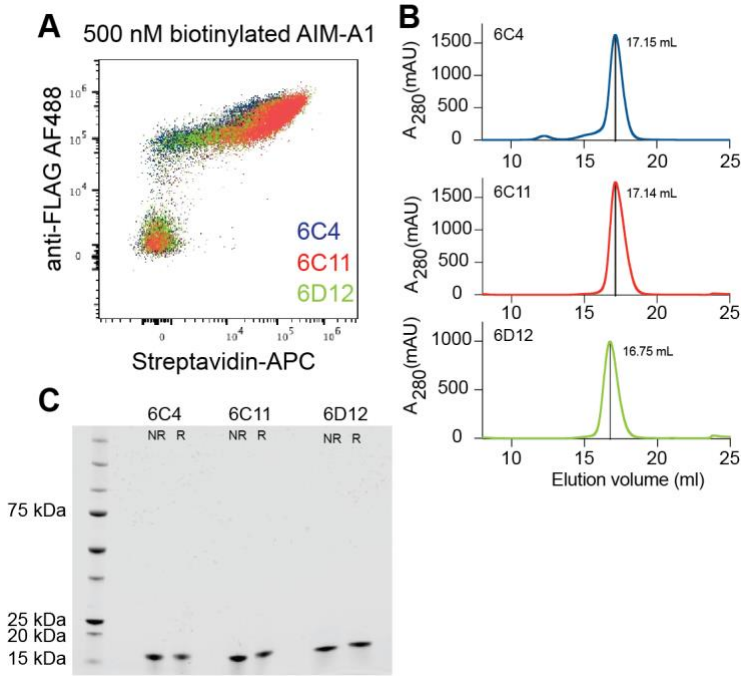

(A) Representative dot plots demonstrating 6C4, 6C11, and 6D12 nanobody display on the surface of yeast (y-axis) and binding to 500 nM AIM-A1 (x-axis) by flow cytometry. (B) Size exclusion chromatograms of each nanobody after elution from Ni-Sepharose 6FF on a Superdex 200 13/100 column in PBS. Retention times are similar for each nanobody. (C) Coomassie stained SDS-PAGE gels of pooled fractions of gel filtered nanobody preparations under non-reducing and reducing conditions.

Supplemental Figure 4.2. Nanobody induced aggregation is dependent on VWF A1 and GPIbα

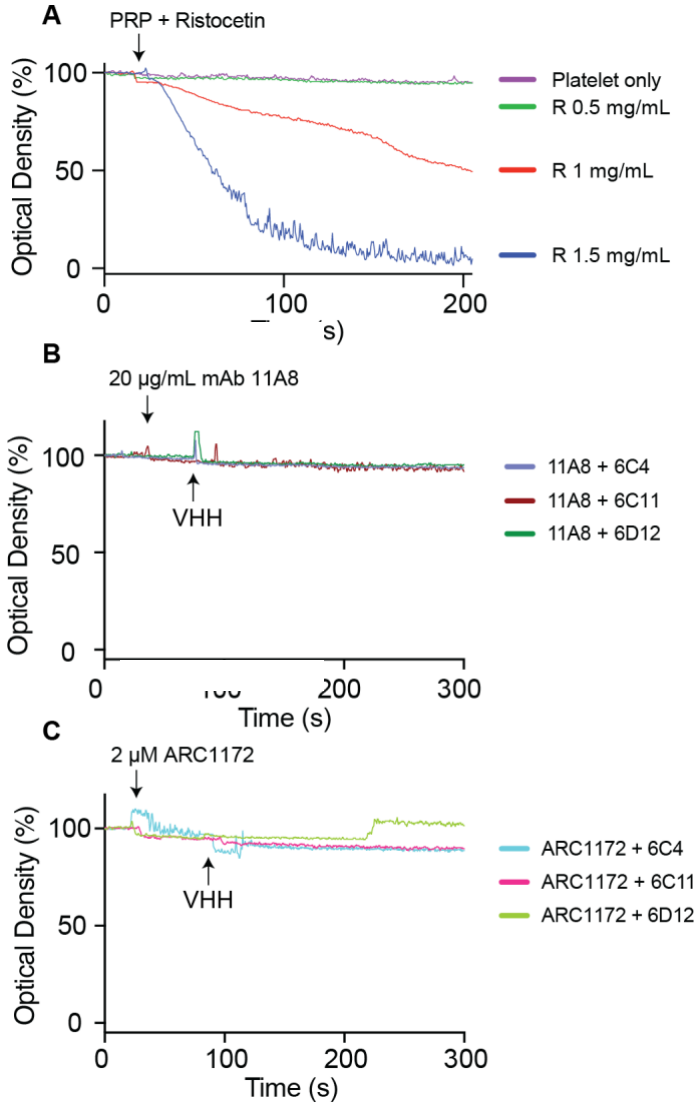

(A) Platelet-rich plasma aggregation responses to different amounts of ristocetin. Ristocetin was added at 30 seconds (arrow) to the platelet suspension. (B) PRP incubated with 20 µg/mL anti-LBD antibody 11A8 which blocks the interaction with VWF does not activate in response to the nanobodies. Antibody was added at 30 seconds (first arrow), nanobody was added at 90 seconds (second arrow). (C) PRP incubated with A1 function blocking aptamer ARC1172 does not activate in response to the nanobodies. The aptamer was added at 30 seconds (first arrow), nanobody was added at 90 seconds (second arrow).

Supplemental Figure 4.3. Steady state binding of nanobodies to NAIM-A1

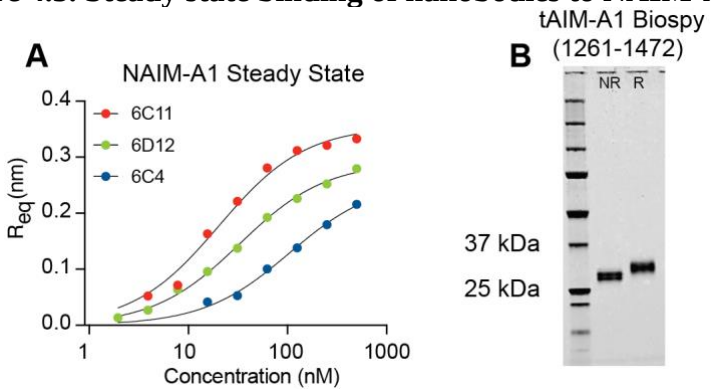

(A) Steady state binding isotherms of each nanobody to NAIM-A1. Binding was fit to a hyperbola (black). (B) Coomassie stained SDS-page gel of purified tAIM-A1 Biospy, residues 1261-1472 under non-reducing and reducing conditions.

Supplemental Figure 4.4. Nanobodies recognize a linear, glycosylated epitope.

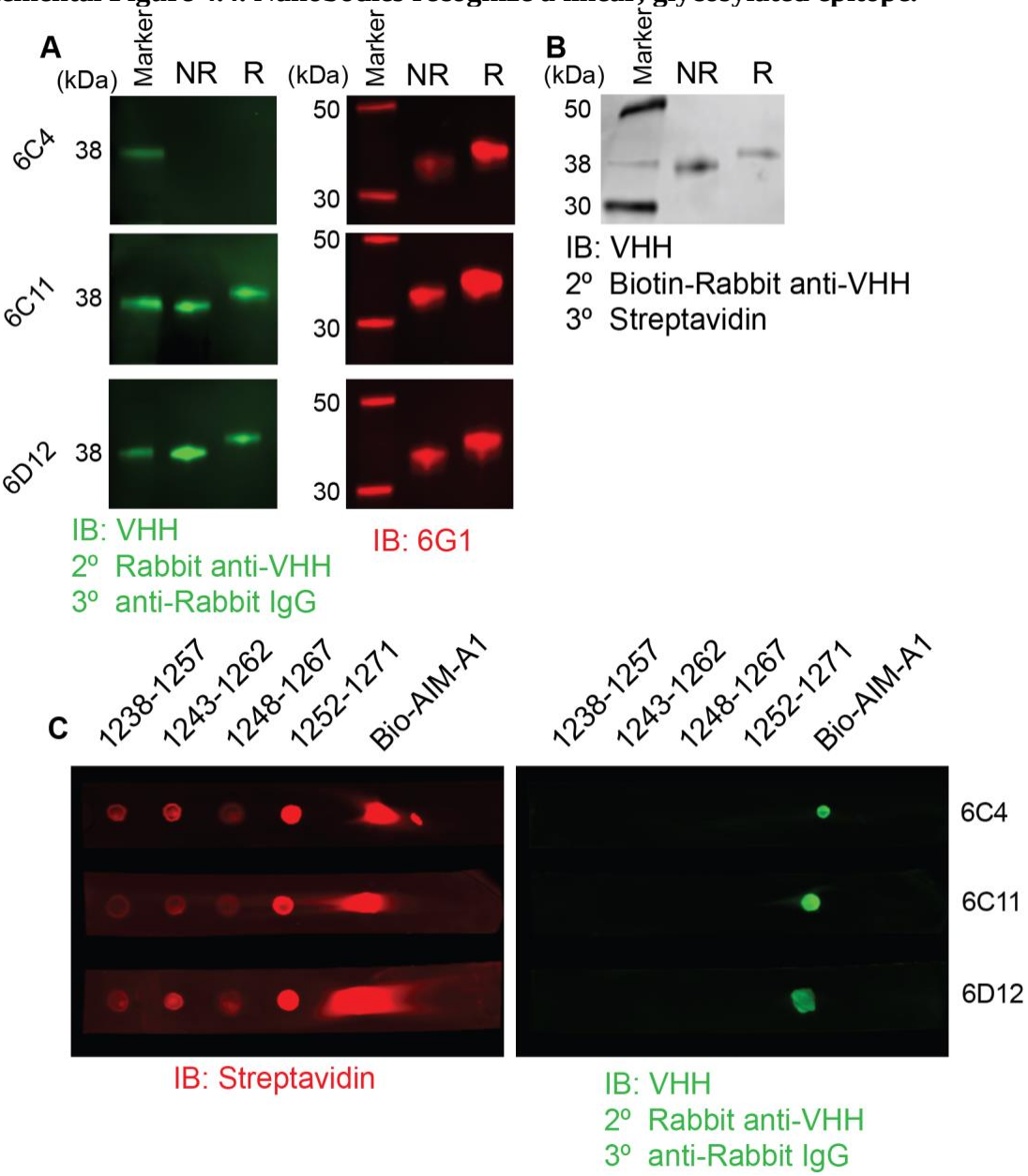

(A) Western blots of reduced AIM-A1 or non-reduced AIM-A1 stained with each nanobody and 6G1. 6G1 is a CAIM-specific antibody that binds to a linear epitope. 6C4 showed no apparent binding, likely due to its low affinity and need to use three detection reagents. Usage of a biotinylated anti-VHH antibody and streptavidin was able to increase the signal to observe binding of 6C4 to AIM-A1 (far right). The nanobodies bound equally well to reduced or non-reduced samples. (B) Dot blots of immobilized biotinylated NAIM peptides (0.01 μg per spot).

The individual strips were blotted with each nanobody separately and detected with an anti-VHH antibody or streptavidin to detect the adsorbed peptides. On the same strip 1 μg of biotinylated AIM-A1 was adsorbed to the strip. No binding of the nanobody to any peptide was observed (green), although there was binding to the AIM-A1 immobilized on the same strip.

Supplemental Figure 4.5. Bacterial derived A1 and purified full-length VWF

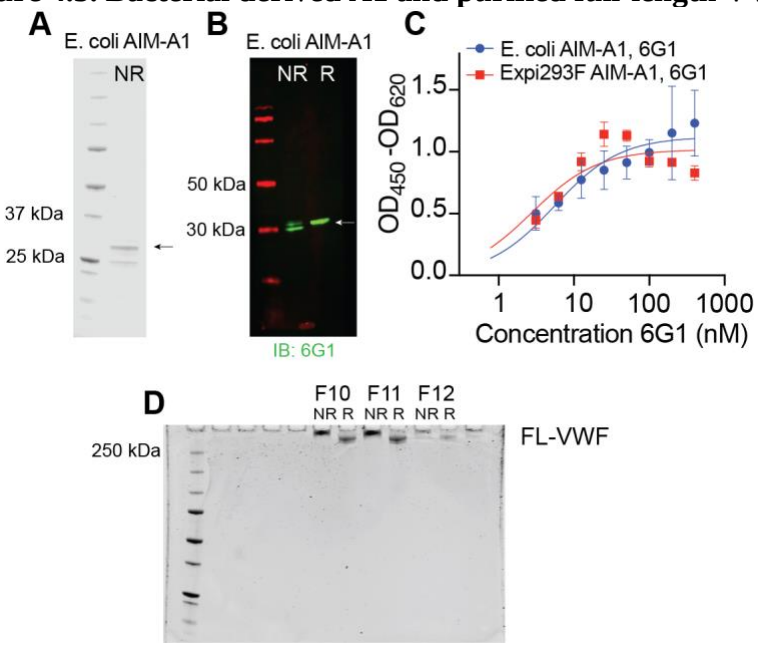

(A) Coomassie stained SDS-PAGE gel of semi-purified bacterial derived AIM-A1 (~28 kDa). The preparation is slightly contaminated with a lower, 20 kDa species. The species at 28 kDa was confirmed to be AIM-A1 as a western blot with 6G1 under non-reducing and reducing conditions showed a band around 30 kDa (B). (C) ELISA of 6G1 binding to coated AIM-A1 from bacteria (blue) or Expi293F cells (red) demonstrating that 6G1 binding is unaffected with the presence of glycans. Error bars are the standard deviation of triplicate measurements. Measurements were fit to a hyperbola. (D) Coomassie stained SDS-PAGE gel of biotinylated full-length VWF fractions from size-exclusion with a Superdex 200 13/100 column in PBS. Fractions 10-12 were run under reducing and non-reducing conditions, demonstrating that the VWF is multimerized and can be reduced to a single species above 250 kDa.

Supplemental Figure 4.6. Purification and reactivity of NAIM-Fc and 1253-1266-Fc to 6D12

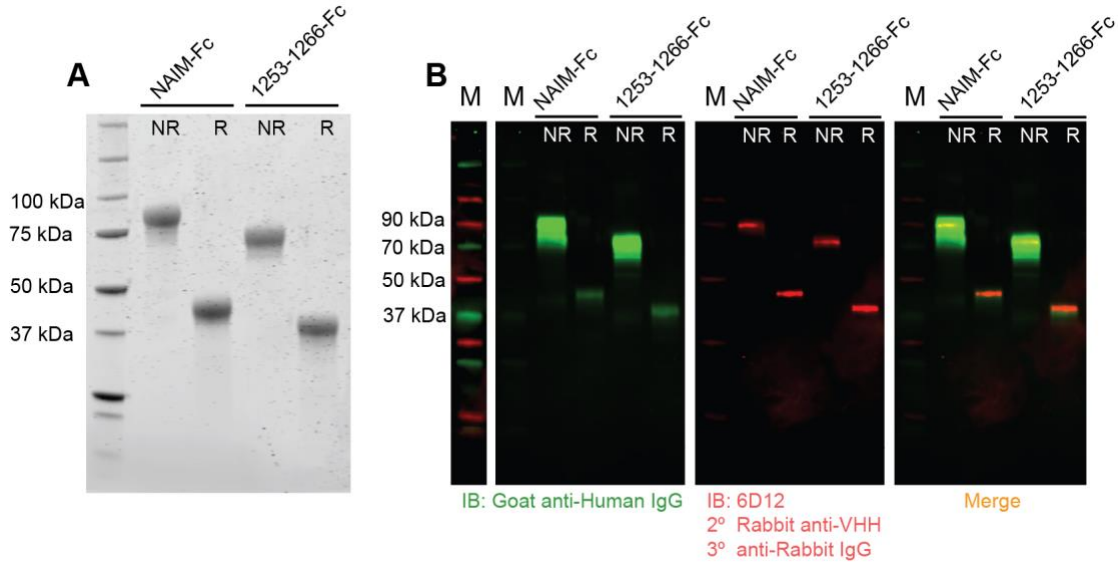

(A) Coomassie stained SDS-PAGE gel of purified NAIM-Fc and 1253-1266-Fc under non-reducing and reducing conditions. Formation of a disulfide linked dimer results in the reduction of the dimer to a monomer. Human IgG1-Fc alone results in a molecular weight of around 25 kDa under reducing conditions. (B) Western blots of NAIM-Fc and 1253-1266-Fc under non-reducing and reducing conditions. Membranes were stained with anti-Human IgG polyclonal antibodies to detect the Fc portion. Staining is weaker for the reduced protein. Staining with VHH 6D12 and detection using anti-VHH and then anti-rabbit results in staining of the non-reduced and reduced proteins.

Supplemental Figure 4.7. BLI traces of the nanobodies binding to NAIM-Fc and NAIM 1253-1266-Fc

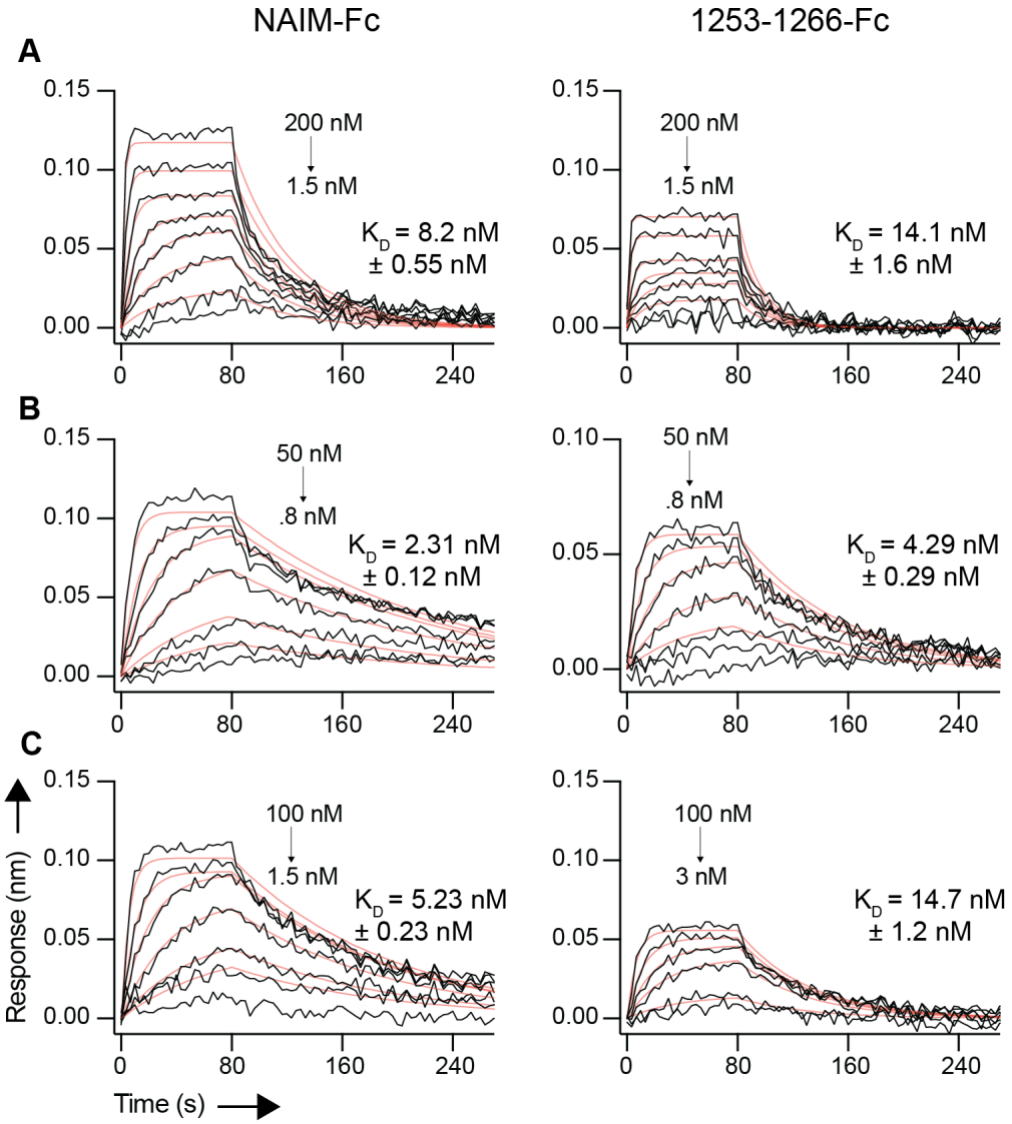

(A) Representative bio-layer interferometry sensorgrams of NAIM-Fc or 1253-1266-FC immobilized on Protein A sensors binding to a serial dilution of 6C4, 6C11, or 6D12. Concentrations in the serial dilution are shown in each panel alongside the calculated affinity for each nanobody. Affinities and standard deviation of the measurement was determined through 1:1 global kinetic fitting to each trace with observable binding. The theoretical sensorgram based on the global fit for each concentration is shown in red.

Supplemental Figure 4.8. Digestion of NAIM-Fc with neuraminidase removes sialic acid content.

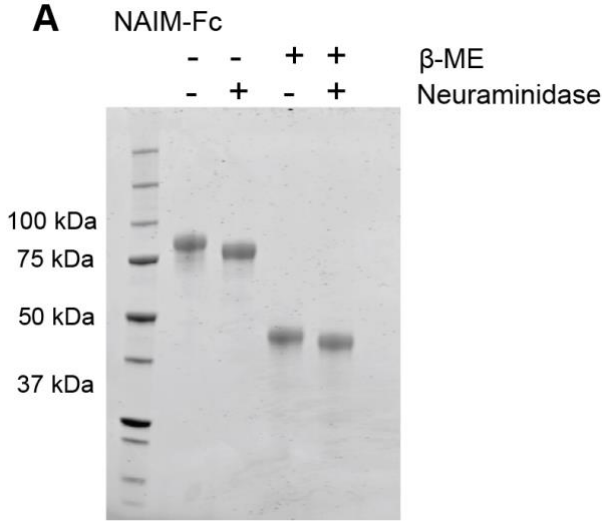

(A) Coomassie stained SDS-PAGE gel of purified NAIM-Fc under non-reducing and reducing (β-ME) conditions after digestion with neuraminidase. There is a slight reduction in molecular weight of the proteins after digestion. Removal of around 16 sialic acids (two NAIMs, two sialic acids per 4 glycans per NAIM) with a molecular weight of around 300 Da per sialic acid would remove 4.8 kDa on the dimer and 2.4 kDa on the reduced monomer.

Chapter 5

Mechanism-directed selection of allosteric inhibitors of a mechanosensory protein

Nicholas A. Arce, Wenchun Chen, Pete Lollar, Renhao Li

N.A.A., W.C., and P.L. performed research. N.A.A. and P.L. analyzed data. N.A.A and R.L. designed research and wrote the paper.

5.1 Abstract

Von Willebrand factor (VWF) is an essential plasma glycoprotein that mediates the capture of platelets to the site of vascular insult, especially at high shear. Pharmacological inhibition of VWF's platelet binding ability is an attractive alternative to platelet-based inhibitors, especially in VWF-linked thrombosis like that seen in thrombotic thrombocytopenic purpura. However, direct antagonism of platelet-VWF interactions can lead to bleeding. The activation of VWF is controlled by an autoinhibitory module (AIM) that unfolds under force to expose the A1 domain of VWF to permit binding to platelets. We hypothesized that targeting the AIM to inhibit A1 exposure though allosteric stabilization may yield an inhibitor with reduced bleeding effects. To this end, we developed two nanobodies from a yeast display library, Nd4 and Nd6, that target the C-terminal AIM (CAIM) and inhibit VWF activation under flow in human blood. Paradoxically, these nanobodies target the ristocetin binding site of VWF, a reagent that is commonly used to activate VWF. By stabilizing, as opposed to disrupting the CAIM like ristocetin, these nanobodies can allosterically inhibit platelet-VWF interactions. Furthermore, we demonstrate that Nd6 can cross react with mouse VWF and can inhibit VWF-dependent platelet adhesion in mouse blood. These results demonstrate that the CAIM can be specifically targeted for allosteric inhibition of VWF activation.

5.2 Introduction

Hemostasis is a complex mechanism that has evolved to arrest bleeding in vertebrates. While the enzymatic process mediated by coagulation factors is imperative to seal a wound, the initial capture of platelets to support coagulation is an equally important factor. Blood flowing through a system of ever-changing vessel architecture creates the need for overlapping, sometimes redundant mechanisms to localize platelets to the site of vessel injury. Platelet receptors such as glycoprotein (GP)VI, CLEC-2, and certain integrins can bind to exposed subendothelial components that are exposed following vessel rupture (239; 240). However, as the vessel responds to injury through vasoconstriction and blood velocity increases, these receptors cannot always sustain binding to their ligands. Von Willebrand factor (VWF) has specifically evolved to bridge the gap between subendothelial matrix and platelets at high flow velocities and shear rates (15). Some VWF domains and modules are mechanosensitive and can change conformation when exposed to sufficient tensile force (46; 190; 212). VWF can respond to forces through its long shape, a concatemerized polymer, spanning dozens of 280 kDa disulfide-linked multimers (37). VWF's polymeric properties lend it to stretching under elongational flows and lead to at least two specific, force-dependent events. First, the A2 domain regulates VWF size by shear dependent ADAMTS13 proteolysis. Under sufficient force, the A2 domain will unfold and expose itself to cleavage by ADAMTS13 to reduce the size of a VWF multimer (45; 46). Second, an autoinhibitory module (AIM) that surrounds the A1 domain undergoes a similar folded to unfolded transition under force to expose the A1 domain (212). The exposed A1 domain binds to GPIbα, which can form incredibly strong bonds, reinforced under shear (90; 96; 221), that can bind, activate, and slow down platelets long enough for other adhesive receptors to activate such as integrin αIIbβ3 and GPVI. VWF can greatly influence the hemostatic balance between bleeding and clotting. VWF

multimers of insufficient size, as seen in von Willebrand Disease type 2A, are insufficient for platelet capture and lead to bleeding (40). VWF multimers that are too long due to lack of or inhibited ADAMTS13 will lead to thrombosis (72).

Inhibition of platelet-VWF complexes has shown promise treating thrombotic thrombocytopenic purpura (183; 241), reperfusion injury (242), and certain thromboinflammatory diseases (243; 244). Complete inhibition of the platelet-VWF binding may tip the scale of hemostasis too far towards a bleeding tendency. Furthermore, targeting certain epitopes on the A1 domain may yield undesired effects, such as reduced VWF clearance leading to enhanced coagulation factor VIII levels and an elevated risk for thrombosis (245). VWF based thrombosis is related to enhanced activation in non-hemostatic situations, *e.g.* ultra-large VWF activating at low forces. Preservation of VWF function at hemostatic shear rates and inhibition of VWF under non-hemostatic conditions would yield a functional inhibitor with reduced risk of bleeding complications without needing an antidote for correction. Serendipitously, caplacizumab targets the VWF AIM, and we have shown that it exhibits its anti-thrombotic effects through increasing the unfolding force of the AIM (212). At higher forces and higher shear rates, the inhibition by caplacizumab can be overcome and VWF function can proceed. However, there are increasing reports of severe bleeding events during treatment with caplacizumab, perhaps owing to its incredible apparent affinity in the picomolar range as a dimer (246). With our knowledge of the AIM and its function, we sought to design a strategy to generate allosteric inhibitors of the A1-GPIbα interaction by specifically targeting the AIM. With this approach, our inhibitors target the AIM and incompletely inhibit A1 activity. By preserving necessary VWF function while inhibiting thrombotic VWF function, hemostasis may be minimally affected.

5.3 Methods

Materials and reagents

Expi293F cells, DMEM/F12, Freestyle F17, GlutaMAX, penicillin/streptomycin, bovine serum albumin fraction V, hygromycin, and D-biotin were purchased from ThermoFisher Scientific. Ristocetin was purchased from MP Biomedicals and reconstituted to 25 mg/mL stocks in phosphate buffered saline (PBS). Mono/Dibasic sodium phosphate, sodium chloride, and imidazole was purchased from Sigma. 6G1, CR1, and ARC1172 have been described previously (160; 161).

VWF fragment expression and purification

Biotinylated AIM-A1 (VWF residues 1238-1493), NAIM-A1 (1238-1461), A1-CAIM (1268-1493), tAIM-A1 (1261-1472), mouse AIM-A1 (mouse VWF residues 1238-1493), chimeric hAIM-mA1, and tagless-AIM-A1 have been described in detail previously (212). Briefly, supernatant from Expi293F cells expressing each construct was collected and purified on Ni-Sepharose excel resin (Cytiva) and subjected to size-exclusion chromatography on a Superdex 200 pg 16/600 column (Cytiva) in PBS. Peaks containing the desired protein were concentrated with Vivaspin centrifugal filters (Millipore).

Immunized yeast display library

Described in Chapter 4.

Library sorting to obtain CAIM-specific clones

Described in Chapter 4. Substitute NAIM-A1 protein for A1-CAIM during depletion steps.

Nanobody subcloning, expression, and purification

Described in Chapter 4.

Biolayer interferometry (BLI)

BLI experiments were performed on an Octet QK^e instrument using the Data Acquisition software v11.1.1.19 (ForteBio, Fremont, CA). Data was acquired at .3 Hz at 25º C. VWF fragments we loaded to .3 nm on streptavidin sensors, and dipped into a dilution series of each nanobody. Streptavidin sensors were washed with 1 M NaCl at the end of the dissociation step. For epitope binning, 5 μg/mL nanobody was loaded to Ni-Penta sensors until saturation, and then loaded with 10 μg/mL tagless AIM-A1 for 180 seconds. The loaded sensors were then dipped into mAb solutions of 1 μM for 60 seconds followed by dissociation into kinetics buffer. In all cases protein analytes were diluted to the desired concentration with Kinetics buffer (Sartorious) diluted in PBS pH 7.4. All data was corrected by an analyte deficient, loaded reference to account for instrument drift and ligand dissociation. All binding sensorgrams are all fitted to a 1:1 global binding model for the included concentrations, and steady state fits to a hyperbola are shown as either predicted equilibria (R_{eq}) or response if the sensorgrams reached equilibria.

Production of AIM-A1/nanobody complexes and AUC

The protein construct of 10xHis-TEV-1238-1481 has been used previously for crystallization trials (212). Briefly, a stable cell line expressing this construct in Expi293F cells was grown in suspension with Freestyle F17, 2x Glutamax, and .1g/L Pluronic F68. Saturated cultures were clarified by centrifugation and filtration and purified using a Ni-Sepharose excel column followed by gel filtration. TEV protease was produced in BL21 pRIL cells. Protein expression was

performed as described.(162) Frozen pellets were lysed by Dounce homogenization in 25 mM HEPES, 250 mM NaCl, 5 % glycerol, .5 % Triton-X100 and 20 mM imidazole pH 7.4 with added benzonase. The lysate was clarified by ultracentrifugation at 20,000 xg and purified in the same manner as the nanobodies with gel filtration performed on a Superdex 75 pg 16/600 column. In two separate preparations, 4 milligrams of TEV protease was added to 20 milligrams of AIM-A1 with 5 % glycerol overnight at 4ºC in a volume of around 15 mL total. After around 16 hours the reaction was loaded through a Ni-Sepharose excel column, and washed with 20 mM phosphate, 500 mM NaCl, pH 7.4 to collect the tag-less protein. The flow through was then concentrated with a 10 kDa MWCO Sartorius Vivaspin centrifugal filter and then excess molar amounts of either Nd4 or Nd6 were added. The complexes were allowed to form at room temperature with gentle agitation and then injected onto a Superdex 200 pg 16/600 column equilibrated with 10 mM HEPES, 100 mM NaCl, pH 7.4. Fractions containing the desired complex were then concentrated further with the above centrifugal filter at 4º C until the volume was below 1 mL. Sedimentation velocity experiments were performed at 20°C in a Beckman Coulter XLI analytical ultracentrifuge using standard procedures and has been described previously.(117)

Parallel plate flow chamber

Bovine collagen fibrils (Type I, Chrono-log Corporation) were diluted to 250 ug/mL in 5% glucose, pH 2.7. 20uL of the suspension was loaded into a tissue culture treated Ibidi µ-Slide VI 0.1 overnight at 37 °C, flushed with modified Tyrode's buffer, blocked with 1% bovine serum albumin (Fraction V, Fisher Scientific) in PBS for 1 hour, and then washed with mTyrodes. Citrated whole blood was mixed with 2 µg/mL DIOC-6 (Invitrogen), 2 mM $CaCl_2$ and various antagonists for 30 minutes. Blood was then loaded to a 3 mL Luer lock syringe (BD), connected

via Tygon tubing and elbow connectors (Ibidi) to the chamber slides. Blood was perfused under the control of a Harvard Apparatus Pump 11 Elite. Desired shear rates, γ in s^{-1}, were obtained as γ=10.7* Q where Q is flow rate in μL/min and 10.7 is a constant based on the geometry of the chamber. Human blood was perfused for 2 minutes, while mouse blood was perfused for 6 minutes, and 3-4 images were captured along the center of the chamber at desired time points. Nikon NIS-Elements Advanced Research v4.6 controlled a Nikon Ti-Eclipse microscope with a Photometics CoolSnap HQ2 CCD camera. Images were obtained in the FITC channel with a 10x objective with 1 second exposure times set to auto contrast during acquisition. An automated macro obtained platelet coverage parameters by setting an auto-threshold and field measurements in NIS-Elements. For low platelet coverage seen with ARC1172, the low threshold was set manually for each image (~400). Each experiment was performed in two separate flow channels at randomly non-consecutive shear rates.

Dot blots

1 μg of reduced (100 mM β-ME) or non-reduced AIM-A1 was adsorbed to a nitrocellulose membrane and blocked with 1% BSA in PBS-T for 2 hours. Around 5 μg/mL nanobody or antibody was added overnight at 4º C with agitation. The membranes were washed with PBS-T, and then incubated with rabbit anti-VHH (96A3F5, Genscript) at 1:2000 dilution. The membranes were then blotted with Licor IRdye 680 goat anti-rabbit and Licor IRdye 800 goat anti-mouse (for 6G1 and CR1) at 1:4000. Membranes were scanned on a Licor Odyssey CLx.

Platelet Aggregation

Written informed consent was obtained from participants before their inclusion in studies, and all procedures using donor-derived human blood and platelets were approved by the Institutional Review Board at Emory University. Human blood obtained by venipuncture into sodium citrate tubes (BD) was centrifuged at 240 xg with no brake for 12 minutes. PRP was gently aspirated away from RBCs and platelet counts corrected to 200,000/μL in freshly thawed pooled normal plasma (George-King Biomedical). Nanobodies were added to the suspension at 30 seconds at 1 μM followed by 1.2 mg/mL ristocetin (MP Biomedicals) at 60 seconds. Platelet aggregation was recorded in AGGRO/LINK software (Chrono-log, Havertown, PA), exported, and normalized to initial optical densities of 100 manually.

ELISA

Human AIM-A1, mouse AIM-A1, or chimeric human AIM mouse A1 were coated to high binding, half area microtiter plates at 10 μg/mL in PBS overnight at 4ºC. The plate was blocked with 1% BSA in PBS-T for one hour at room temperature. The plate was washed 3 times between all steps with HBS-T. A dilution series of Nd6 was dispensed into the wells and incubated for 1 hour. The nanobody was detected with HRP-conjugated rabbit anti-VHH (96A3F5, Genscript) at 1:2000 dilution in 1% BSA in PBS-T. One-step ultra TMB was added, and the reaction was quenched with 2 M sulfuric acid. The plate was then read at 450 nm with subtraction at 620 nm.

5.4 Results

We previously have generated an immunized nanobody yeast display library from a llama immunized with a recombinant AIM-A1 protein (Chapter 4, Fig. 5.1A). While it would be feasible

to screen for nanobodies that inhibit the GPIbα-A1 interaction by flow cytometry, this strategy would likely identify direct, primary binding site inhibitors near the β3 strand. Instead, we opted to find AIM-specific nanobodies first and assess their function second. Using various AIM-deleted proteins, we are able to deplete the library of binders to the A1 domain and to either the N(terminal)AIM or C(terminal)AIM. The library was first enriched for AIM-A1 by magnetic sorting and fluorescence-activated cell sorting. After depletion of the library using NAIM-A1 coupled magnetic streptavidin beads, the library was resorted for AIM-A1 to identify CAIM specific binders (Fig. 5.1B). We identified 4 unique clones from this NAIM depleted (Nd) library. Two clones, Nd4 and Nd6, showed specific binding to AIM-A1 on yeast and in monomeric protein form. These nanobodies were chosen for further investigation (Fig. S5.1A).

Nd4 and Nd6 bound to AIM-A1 with drastically different affinities. Nd4 binds with a K_D of 18.6 nM, while Nd6 binds with a K_D of 604 nM by bio-layer interferometry (Fig. 5.1C). The binding specificity of the nanobodies to the CAIM was confirmed as neither nanobody showed any binding to NAIM-A1, the protein that was used for depleting the library (Fig. 5.1D). The binding epitope was then demonstrated to include residues 1459 to 1472, as the nanobodies bound with similar affinity to a VWF fragment from 1261 to 1472 (Fig. 5.1E). Interestingly, Nd4 showed reduced binding to A1-CAIM, suggesting that this nanobody binds to residues in the NAIM (Fig. 5.1F). Steady state binding isotherms to the AIM-A1 fragments are shown in Figure S5.1B.

We further confirmed the binding epitope of these nanobodies using two monoclonal antibodies, CR1 and 6G1. 6G1 binds to a linear stretch of residues from 1461 to 1472 while CR1 has a conformationally sensitive epitope, yet both can inhibit ristocetin induced platelet aggregation (160). 6G1 and CR1 share a binding epitope, as 6G1 and CR1 cannot bind to the CAIM concurrently (160). By immobilizing the nanobodies with their his-tag, we then loaded

Figure 5.1. Isolation of CAIM-binding nanobodies by yeast display

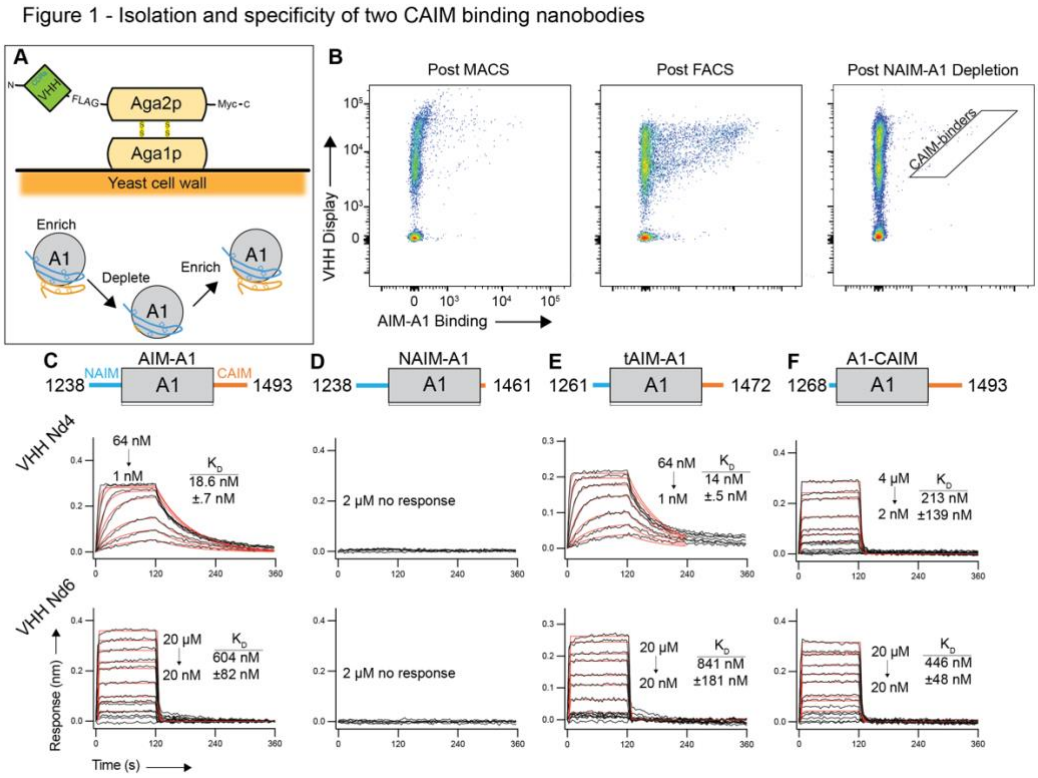

(A) VHH genes were fused to Aga2p subunit and displayed on the surface of yeast. Yeast were sorted for AIM-A1 binding, depleted with NAIM-A1, and resorted for AIM-A1 to obtain CAIM specific binders. (B) Dot-plots of a subset of each sorting step. AIM-A1 specific binders were first isolated by MACS to reduce the library size and FACS was performed to quantitative select double positive events. VHH display from the FLAG-epitope displayed on the Aga2p fusion is shown on the y-axis, and AIM-A1 binding is shown on the x-axis. CAIM-specific binders were isolated from the approximate sort gate on the third panel. Dilutions of each nanobody were tested for binding by bio-layer interferometry to AIM-A1 (C), NAIM-A1 (D), tAIM-A1 (E), and A1-CAIM (F). Global 1:1 kinetic fitting was applied to the dilutions tested and theoretical curves are shown in red. Kinetic K_D and standard deviation of the kinetic fitting is shown to the right of the sensorgrams. Steady state fittings are shown in Figure S5.1B.

AIM-A1 lacking a his-tag to the nanobodies and assessed the ability of the mAbs to bind to AIM-A1 while bound to Nd4 or Nd6. Nd4 was able to inhibit both 6G1 and CR1 binding to AIM-A1 (Fig. S5.2A), while Nd6 only blocked 6G1 binding (Fig. S5.2B). The precise epitope of CR1 is unknown, but we would suggest that it must be near the disulfide bond between residues 1272 and 1458. Nd4 and Nd6 appear to have conformationally specific epitopes, as neither could dot blot AIM-A1(Fig. S5.2C). 6G1 showed high binding to both reduced and non-reduced AIM-A1, while CR1 showed limited binding as previously observed for these antibodies (Fig. S5.2C) (160).

Both nanobodies were able to inhibit ristocetin-induced platelet aggregation in platelet-rich plasma (Fig. S5.3A). As ristocetin binds to residues 1459-1472 to activate VWF, we are unable to differentiate if the inhibition of ristocetin-induced aggregation is due to competitive inhibition of ristocetin binding, allosteric stabilization of the AIM, or both.

To elucidate the epitope of both nanobodies, we have generated large amounts of AIM-A1/Nd4 and AIM-A1/Nd6 for crystallization trials. AIM-A1 was produced in mammalian cells bearing O-linked glycosylation with purification tags removed by TEV protease (Fig S5.4). Approximately 20 milligrams of AIM-A1 was complexed with excess nanobody and purified by gel filtration (Fig. S5.5A, B). Both complexes eluted earlier than AIM-A1 alone by size exclusion chromatography, and SDS-PAGE demonstrated the presence of both proteins in the complex peak (Fig. S5.5A, B). Characterization of these complexes by sedimentation velocity analytical ultracentrifugation showed a nearly monodisperse sample with an apparent molecular weight of 47.3 kDa and 45.0 for AIM-A1/Nd4 and AIM-A1/Nd6, respectively, confirming the formation of both complexes (Fig. S5.5C, D).

As the importance of VWF function scales with increasing shear forces in the blood, we sought to investigate the adhesion of platelets to a collagen coated surface at different shear rates after incubation with various VWF inhibitors (Fig. 5.2A, B). ARC1172, a nucleic acid aptamer, directly inhibits the A1-LBD interaction by inhibiting the formation of a beta sheet between the β3 of A1 and the β-switch of the LBD (161). mCaplacizumab is a monomer of the nanobody homodimer caplacizumab (182). At a shear rate of 300/s, platelet adhesion is mediated by several surface receptors and can occur in the absence of VWF (247). All inhibitors did not change platelet surface coverage at this shear rate. At a higher, arterial shear rate of 1000/s, VWF function impacts platelet adhesion as seen by the increase in platelet coverage compared to the lower shear rate. As previously observed, ARC1172 inhibited platelet capture and drastically reduced platelet coverage compared to normal blood. Nd4, Nd6, and mCaplacizumab were able to reduce platelet coverage compared to normal blood, but platelet capture and adhesion were not reduced to nearly the same level as ARC1172. Further increasing the shear rate to 3000/s emphasizes the importance of VWF to hemostasis. ARC1172 treated blood was nearly devoid of any platelet adhesion, which suggests that *in-vivo* at these shear rates, platelet capture is unlikely. Nd4 and Nd6 reduced platelet adhesion compared to normal blood, but the reduction of adhesion was less than that induced by mCaplacizumab. ARC1172 and mCaplacizumab are better inhibitors of VWF compared to Nd4 and Nd6. Yet, in this case, increased intrinsic efficacy is not necessarily a desirable feature, especially at the highest shear rates, as this effect could lead to bleeding.

We then investigated if either Nd4 or Nd6 could bind to mouse VWF (Fig. 5.3A, B). Nd4 showed no binding to mouse AIM-A1 by BLI. Nd6 exhibited reduced affinity (K_D of 1.43 μM) for mouse AIM-A1 compared with human AIM-A1 (K_D of 604 nM). We further tested the binding of Nd6 to various fragments by ELISA. We previously generated a recombinant

Figure 5.2. Nd4 and Nd6 reduce VWF-dependent platelet adhesion *in-vitro* similar to caplacizumab.

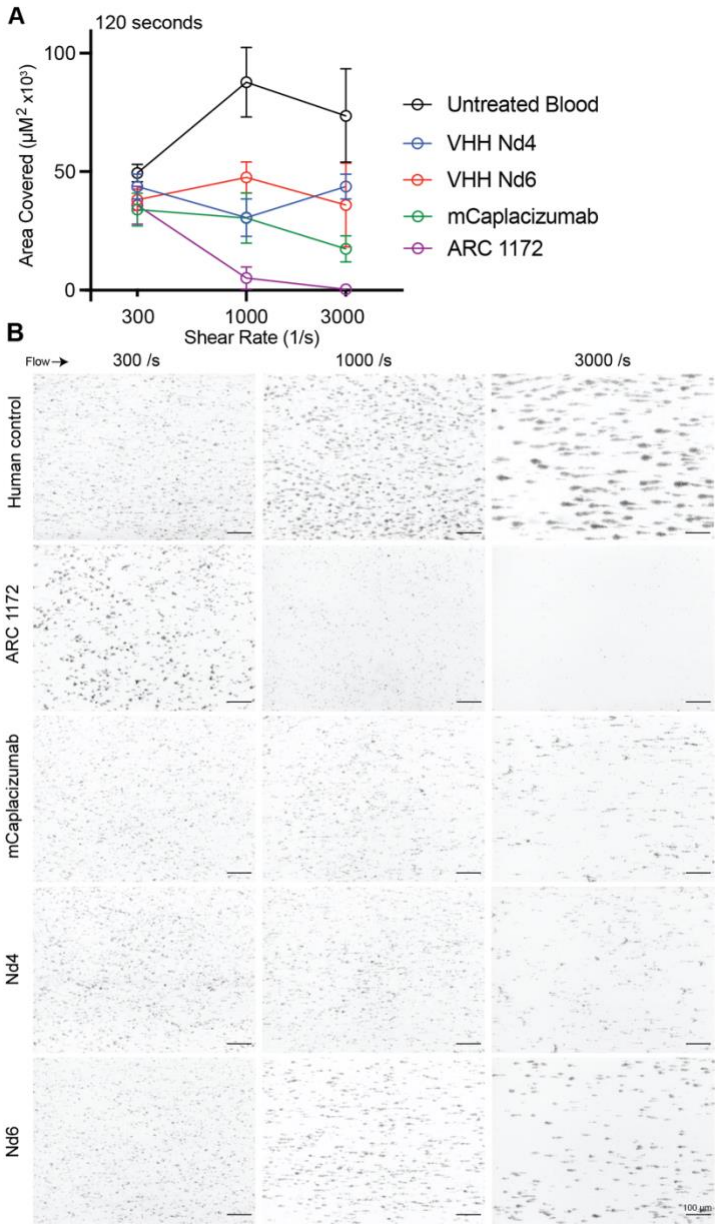

(A) Comparison of platelet adhesion onto collagen as a function of shear rate. Inhibitors were added to whole blood at 1 μM and platelet were fluorescently labelled (pseudo-colored in black). Each condition was performed in three separate flow channels and 3-5 images were taken along the length of each channel. Platelet coverage was measured after 2 minutes of perfusion. (B)

Representative images of each condition after 2 minutes. Scale bar is 100 μm. Blood is perfused from right to left in all images. Platelet coverage is nearly undetectable at 3000/s using ARC1172.

Figure 5.3. Nd6 cross reacts with mouse VWF.

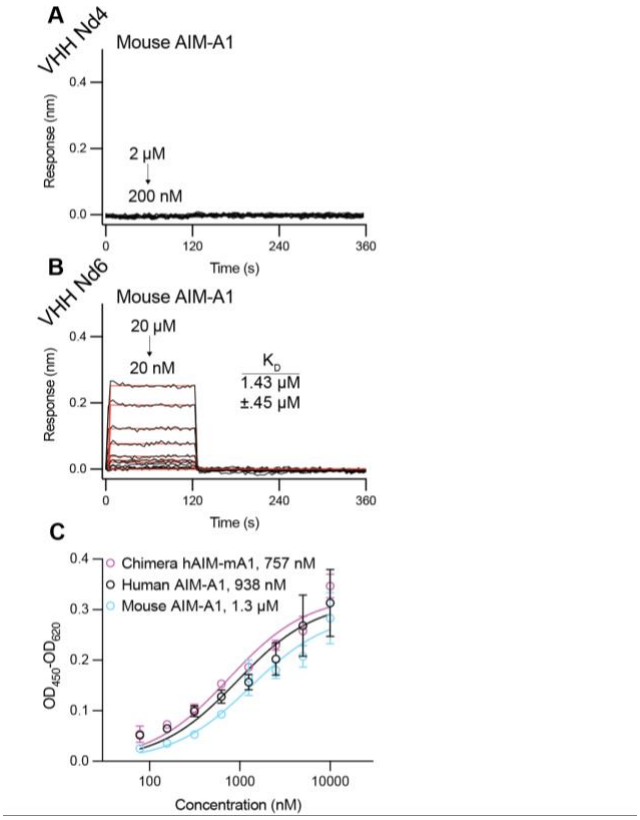

Representative bio-layer interferometry sensorgrams of site-specifically immobilized mouse AIM-A1 binding to a serial dilution either Nd4 (A) or Nd6 (B). Concentrations in the serial dilution are shown in each panel alongside the calculated affinity for each nanobody. Affinities and standard deviation of the measurement was determined through 1:1 global kinetic fitting to each trace with observable binding. The theoretical sensorgram based on the global fit for each concentration is shown in red. No binding was detected for Nd4. (C) ELISA of immobilized mouse AIM-A1, human AIM-A1 or hAIM-mA1 was incubated with a dilution series of Nd6 to assess equilibrium binding. Each concentration was tested in triplicate. Dose response was fitted to a hyperbola and K_D determined as half maximal binding.

chimeric hAIM-mA1 construct (Chapter 3). Nd6 bound to all fragments tested by ELISA, binding with the highest affinity to the chimera, followed by human AIM-A1 and then mouse AIM-A1 with equilibrium dissociation constants in agreement with those obtained by kinetic and steady state fitting with BLI (Fig. 5.3C).

Despite the lowered affinity compared to human, we sought to test if Nd6 could modulate the activity of mouse VWF *in-vitro*. Mouse whole blood takes considerably longer to form thrombi on collagen compared to human blood, and thus images were acquired at several durations up to 6 minutes to monitor thrombus growth (248). 3 μM Nd6 was added to mouse blood to account for the decreased affinity, and the blood was perfused at shear rates of 100, 300, 600, 1000, and 1500/s. Treated, and untreated blood showed no appreciable differences of adhesion at the earliest time points of 2 and 4 minutes (Fig. 5.4A, B). However, at 600 and 1000/s, the amount of platelet coverage was decreased in the Nd6 treated blood at 6 minutes (Fig. 5.4C, D). At 1500/s the platelet adhesion is quite similar between Nd6 treated and untreated blood, suggesting that Nd6 exhibits differential effects on mouse VWF compared to human VWF. It is also possible that in this system, human and mouse blood behave differently given the decreased size of mouse platelets and longer time to form appreciable thrombi. Regardless, it would appear that Nd6 has a narrow force window of VWF inhibition in this assay.

5.5 Discussion

In this work, we have investigated two nanobodies that bind specifically to the CAIM and exert inhibitory effects on the A1-GPIbα interaction. Using a yeast display library from an immunized llama and specific library enrichment and depletion steps, we are able to specifically eliminate binders to the A1 domain inside the 1272-1458 disulfide bond. Enrichment for only A1-

Figure 5.4. Nd6 shows a shear-specific reduction in platelet adhesion in mouse whole blood.

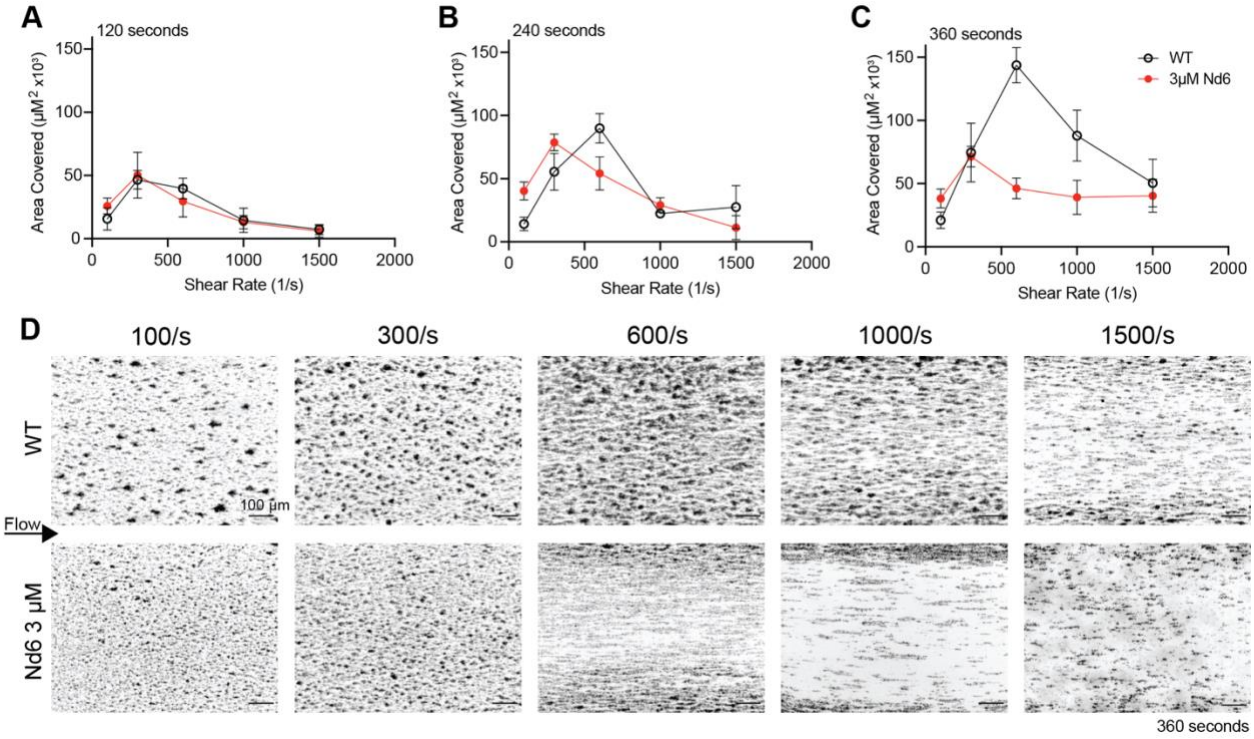

Recalcified mouse whole blood was left untreated or dosed with 3 μM Nd6 before perfusion over collagen in a parallel-plate flow chamber. Platelet adhesion was tracked for up to 6 minutes per run. Calculated coverage for 4 images per chamber for two minutes (A), four minutes (B), or 6 minutes (C) are shown. Error is the standard deviation of the 4 measurements. (D) Representative images of total platelet adhesion (black) at 6 minutes for each shear rate are shown. Scale bar is 100 μm. Blood is perfused from right to left in all images.

binders would yield nanobodies with diverse epitopes that could bind to undesired locations that may have no effect on A1-GPIbα or directly inhibit their interaction similar to NMC-4 (249) or ARC1172 (161). Therefore, selective depletion of NAIM-A1 binders would most likely yield binders to the CAIM.

Nd4 and Nd6 bind to a similar epitope on the CAIM yet have drastically different affinities towards AIM-A1. While both are able to inhibit the most common method to activate VWF, the inhibition of ristocetin-induced platelet aggregation is likely due to competitive inhibition given ristocetin could not out compete either of the nanobodies due to its low affinity. Structural elucidation of their precise epitopes will hopefully yield an explanation for their different affinities, as well as species specificity.

Caplacizumab binds to the NAIM and is able to inhibit VWF in a similar manner (212). It is surprising that targeting an epitope that is known to activate VWF, the CAIM, has instead yielded inhibitors of A1-GPIbα. Ristocetin as well as 6G1 can bind to the CAIM and are able to activate VWF (160; 212), yet these nanobodies can inhibit VWF activation. This reinforces that the conformation of the AIM is crucial to determining the activation potential of A1, and that perturbation or stabilization is possible for both the NAIM or CAIM.

Nd4 and Nd6 were able to inhibit platelet adhesion onto collagen at higher shear rates. Above a shear rate of around 1000/s, VWF and GPIbα are indispensable for platelet capture (250). Direct inhibition of A1 with ARC1172 shows nearly complete inhibition at 1000/s in support of previous findings (Fig. 5.3). Nd4, Nd6, and mCaplacizumab can inhibit platelet adhesion at this shear rate, as well as at 3000/s, but not to the same extent as ARC1172. This result suggests that the VWF can still act to capture platelets, but its ability to do so has been reduced. This incomplete

inhibition is not due to incomplete occupancy, as the concentrations of nanobodies and aptamer used are well above the K_D of the compounds tested.

Allosteric inhibition of the A1-GPIbα interaction by caplacizumab has been the only clinical success at targeting VWF. Despite compounds being developed to block VWF-collagen (251), VWF-integrin (208), and several direct inhibitors of A1-GPIbα (249; 252; 253), only caplacizumab has passed through clinical trials. Allosteric inhibition of VWF via binding to the AIM may present as the right balance between inhibition of VWF without inducing bleeding. Nd4 and Nd6 show similar inhibitory effects as caplacizumab *in-vitro*, and further studies *in-vivo* will elucidate if their inhibition is sufficient to block A1-GPIbα without causing bleeding.

5.6 Acknowledgements

The authors would like to thank Lisa Bixby and Aaron Rae of the Emory Pediatric/Winship Flow Cytometry Core for their assistance with flow-sorting of yeasts. This work was supported in part by NIH research grants HL082808 and HL143794 and an infrastructure grant from Hemophilia of Georgia Center for Bleeding & Clotting Disorders of Emory. N.A.A. was supported in part by NIH fellowship HL154656.

5.7 Supplemental Information

Supplemental Figure 5.1. Binding of Nd4 and Nd6 on yeast to AIM-A1 and steady state BLI plots.

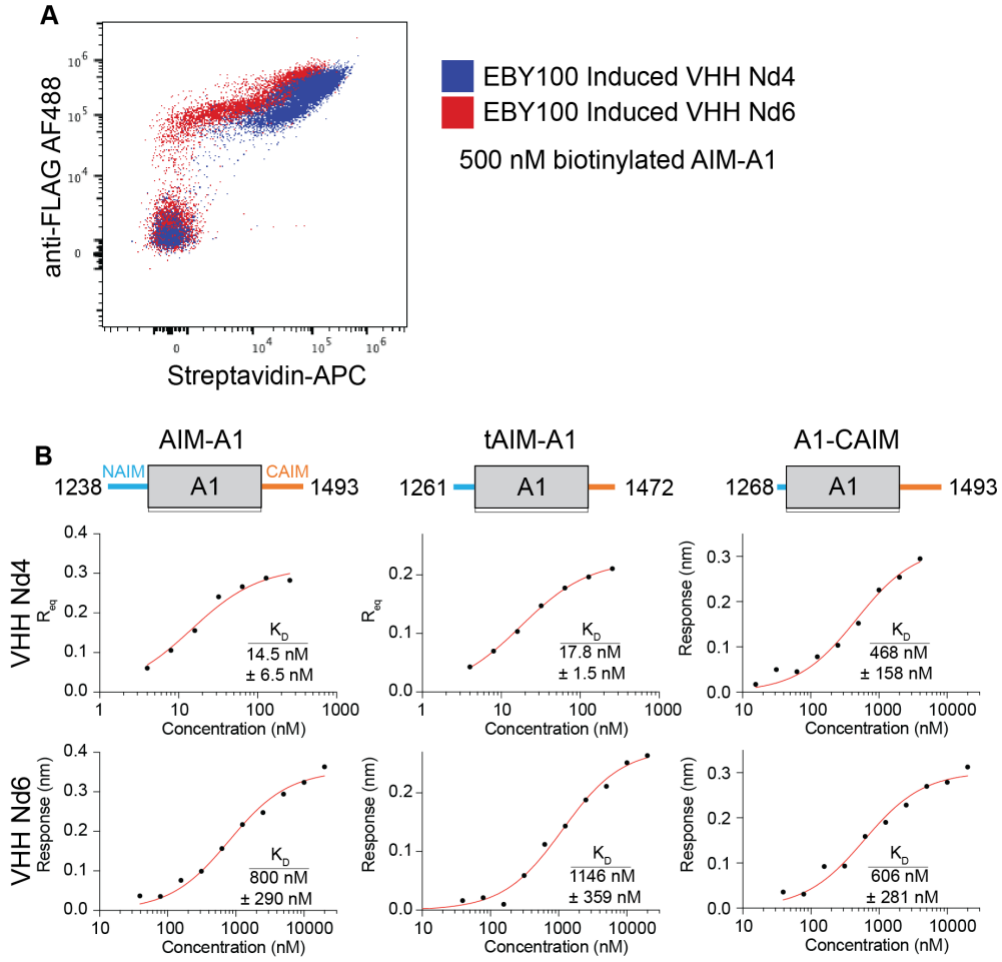

(A) Representative dot plots demonstrating Nd4 and Nd6 nanobody display on the surface of yeast (y-axis) and binding to 500 nM AIM-A1 (x-axis) by flow cytometry. (B) Steady state binding isotherms of each nanobody to AIM-A1, tAIM-A1 or A1-CAIM from BLI traces in Figure 1. Binding was fit to a hyperbola (black). Half-maximal binding was obtained from the fit to determine the steady state K_D. Error is 95% confidence interval of the fit.

Supplemental Figure 5.2. Epitope binning experiments with Nd4 and Nd6 using CR1 and 6G1.

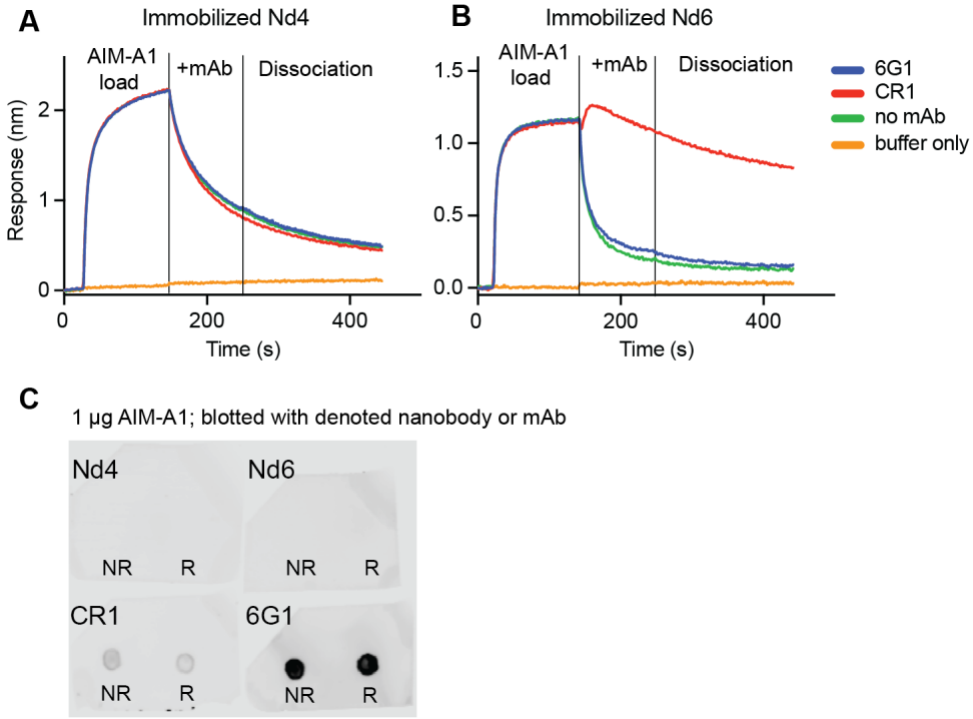

Epitope binning experiments of CR1 and 6G1 binding to AIM-A1 that has been immobilized by Nd4 (A) or Nd6 (B). The first section of the experiment is the loading of AIM-A1 to Nd4 or Nd6 on the sensor. The second section is the association of either 6G1 (blue) or CR1 (red) to AIM-A1. The last section is total dissociation. A reference buffer is shown in green, which is only the association/dissociation of AIM-A1 from Nd4 or Nd6. (C) Dot blots of immobilized AIM-A1 demonstrate the conformational dependence of Nd4 and Nd6. 6G1, which recognizes a linear epitope show high reactivity. CR1 is partially conformationally dependent. NR is non reducing, and R indicates a reduced sample with 100 mM β-ME.

Supplemental Figure 5.3. Nd4 and Nd6 inhibit ristocetin-induced platelet aggregation.

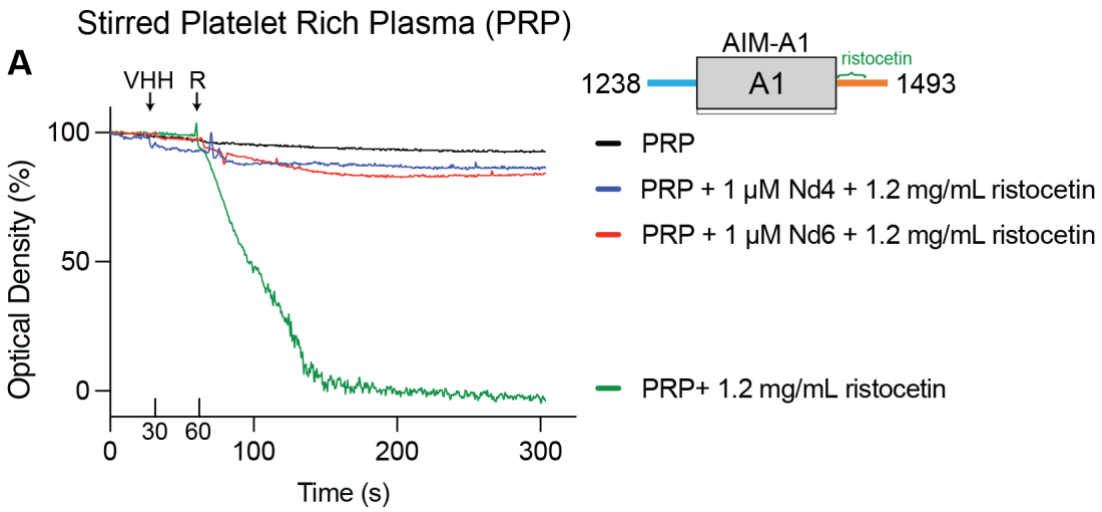

(A) Ristocetin-induced platelet aggregation is inhibited by the addition of 1 μM Nd4 (blue) or Nd6 (red) in human platelet-rich plasma. Resting PRP is shown in black, while full aggregation with ristocetin is shown in green. The ristocetin binding site is shown below a green bracket in AIM-A1. Curves are representative of three separate donors.

Supplemental Figure 5.4. Preparation of tag-less AIM-A1

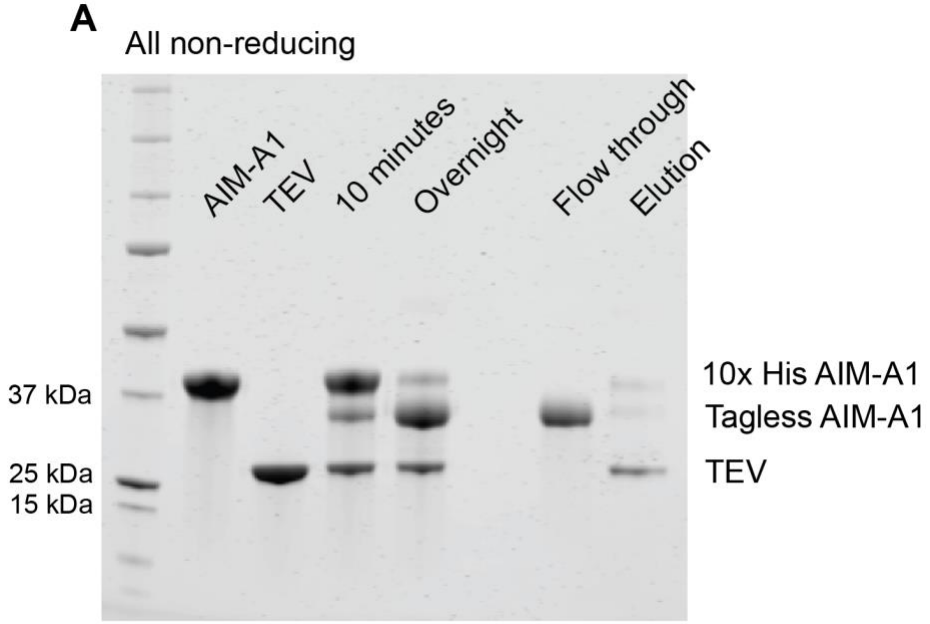

(A) Coomassie stained SDS-PAGE gel showing purified AIM-A1, TEV protease, and the process of cleaving the His-tag off of AIM-A1. An overnight reaction leads to a nearly complete digestion of AIM-A1, and after passing the sample through a nickel-column the AIM-A1, tag removed protein is still pure. His-tagged TEV and the undigested substrate remained bound to the column, as indicated by their removal during the elution step with 500 mM imidazole.

Supplemental Figure 5.5. Complex formation and analysis of AIM-A1/Nd4 and AIM-A1/Nd6

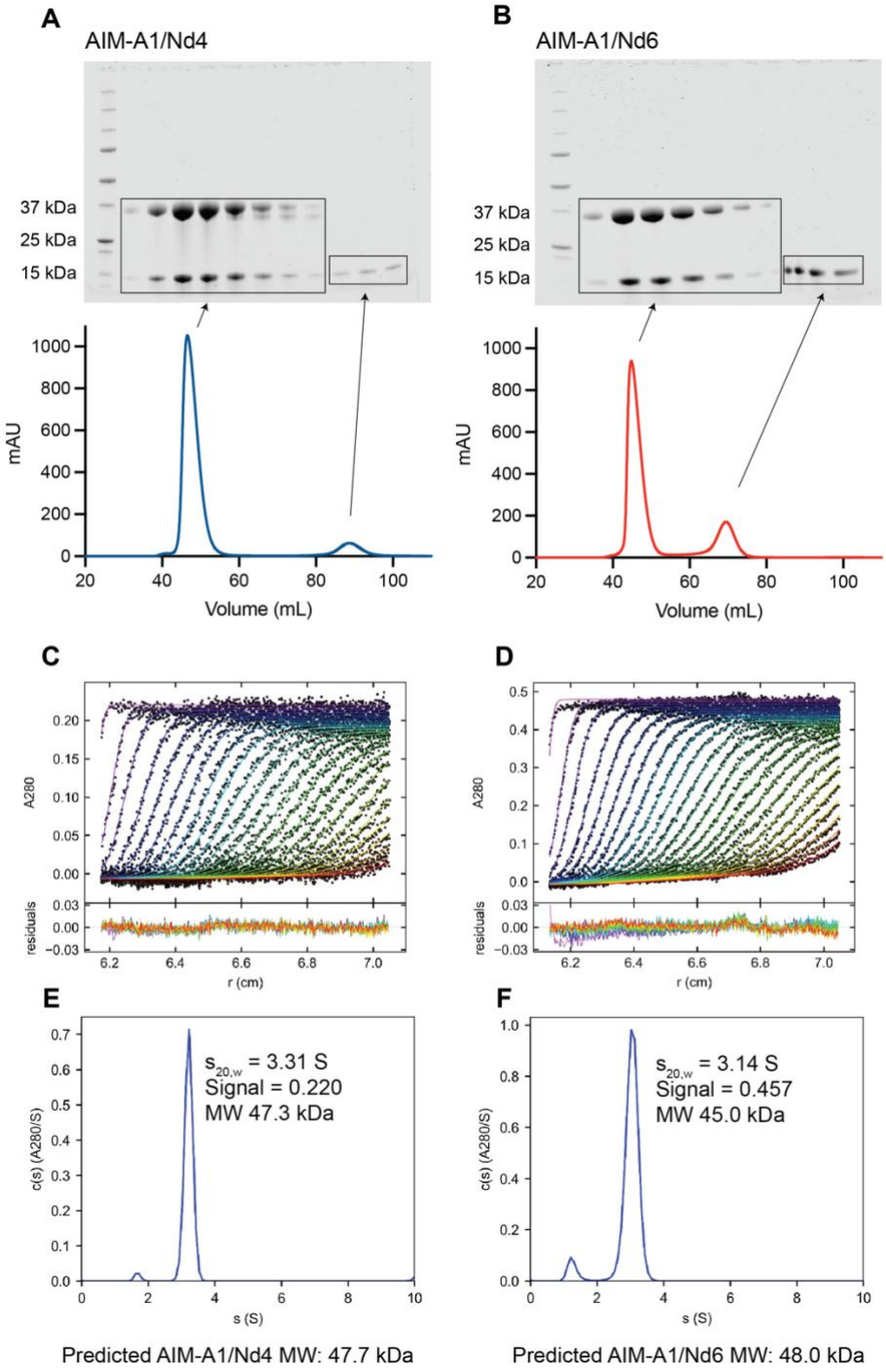

Nd4 (A) or Nd6 (B) was added in molar excess to tag-less AIM-A1 and subjected to size exclusion chromatography to isolate the AIM-A1/nanobody complex. Coomassie stained SDS-PAGE gels indicate the presence of equivalent amounts of AIM-A1 to nanobody as indicated by

their densities in the peak fractions. Excess nanobody can be seen in the adjacent peaks. Chromatograms are displayed below the gels. The complexes were subjected to analytical ultra-centrifugation to determine their molecular weight and relative purity. Analysis of the A_{280} scans (C, D) as the protein sedimented revealed the presence of a slight low molecular weight contaminant, as well a strong signal that represents the formation of the complex (E, F). AIM-A1/Nd4 is shown in the left column and AIM-A1/Nd6 shown in the right column. Predicted molecular weights for each complex are shown below (E) for AIM-A1/Nd4 and (F) for AIM-A1/Nd6.

Chapter 6

General Discussion

6.1 Summary of Results and General Discussion

Allosteric changes in protein structure govern the abilities of proteins to change shape in response to a stimulus (254). Despite being inherently difficult to visualize, conformational changes due to ligand binding are responsible for nearly all cell surface receptor signaling events (255). Allostery induced by force is being discovered in many proteins and receptors. MHC-TCR interactions (256), integrin activation (257), NOTCH signaling (258), and the Piezo receptors (259) have all been captured responding to force. Soluble proteins flowing in the blood stream have a different route to feel the force, as they are not tethered to a mass several thousand times larger than itself *i.e.*, a cell.

Activation of VWF has been known to be dependent on force but no single molecular mechanism could adequately explain the activation of VWF in response to both force and all of the known activating reagents. It had been observed for several decades that flowing blood fast enough over thrombogenic surfaces enables platelet capture by VWF (260), and even recently it was shown that individual GPIbα molecules bind to VWF after VWF has been exposed to enormous shear force (97). Investigations into the shear-dependent unfolding of VWF have also been unsatisfactory as VWF activation may not be dependent on the global extension of a multimer (97). Earlier results from our lab suggested that local elements within VWF must be responsible for responding to force, to work in concert with the global extension of a multimer.

We surmised that these local elements would be the flanking regions around the A1 domain, although others have dismissed their potential role, as these flanking regions appear to be dissociated from A1 in EM and AFM images (35). In Chapter 2, we sought to definitively determine what the role of the complete flanking regions, or autoinhibitory module as we call it, (1238-1271, 1459-1493) play in both VWF activation and response to force. By using single-

molecule force spectroscopy with isolated AIM-A1 fragments, we were able to detect the presence of an unfolding event that could not be attributed to the unfolding of the A1 domain, based on the deviation from a pure DNA unfolding signal in the optical trap. This event showed an unfolding signal that corresponds to the liberation of approximately 67 residues from adopting secondary structure. The combination of residues within the whole AIM is 66 residues. The force applied to induce this conformational change was similar to the amount of force to unfold the A2 domain, a well characterized shear sensor directly adjacent to the CAIM. To confirm that this event was attributable to the AIM and not to other sections of the protein, we produced fragments lacking either the NAIM or CAIM. The unfolding events observed using these AIM-truncated fragments were of lower force and of lower extension, indicating that the NAIM and CAIM are unfolded cooperatively in AIM-A1. Only proteins containing the whole AIM were also able to impede binding to GPIbα, and truncation of either AIM resulted in high affinity binding to GPIbα. Through this work, we have unambiguously demonstrated that the residues that surround the A1 domain that comprise the AIM are 1) force-resistive and 2) required for complete autoinhibition of human VWF. Furthermore, we have shown that the N- and C-terminal AIMs are *both* required to retain A1 autoinhibition. The cooperative unfolding of this module is another unique feature that reinforces that the NAIM and CAIM are adjoined to make one structural unit, otherwise they would unfold in two separate events. This is the first investigation that has demonstrated a force-dependent, conformational change of local elements within VWF that can explain VWF activation and VWF autoinhibition.

Given that human VWF contains a force resistant autoinhibitory module, we wanted to investigate if this module was present in mouse VWF (Chapter 3). Mice have some interesting hemostatic parameters compared to humans such that they do not readily form atherosclerotic

plaques without genetic manipulation (261), although this may be confounded by the shorter lifespan of small animals. The rheological parameters that define blood flow in mice is also different than humans, without mention of the differences in platelet size and vessel radius. In Chapter 3, we could detect an unfolding event within a mouse VWF fragment from residues 1238-1493. The unfolding of the presumed mouse AIM was much smaller than the human AIM, corresponding to 50 or so residues. Despite containing less residues, the force required to induce this event was comparable, if not slightly higher compared to the human AIM. Mouse AIM-A1 did not show the same behavior as human AIM-A1 towards its GPIbα either. Mouse AIM-A1 did show binding to the mouse LBD marked by a very slow off-rate. Mouse VWF fragments containing a truncated AIM did show higher affinity binding, suggesting the mouse AIM is an autoinhibitory module, it just is not as effective as the human AIM at shielding A1. This statement is supported by the binding of mouse A1 coupled with the human AIM resembling human AIM-A1. This chimeric protein showed no binding towards any species GPIbα LBD up to 2 μM. Furthermore, this chimeric protein has an increased contour length compared to mouse AIM-A1, demonstrating the human AIM has some intrinsic property to create a longer, more stable module compared to the mouse AIM.

If the AIM controls the exposure of the A1 domain, then modulation of the AIM should alter the properties of VWF activation. In Chapter 2, we tested the hypothesis that the AIM can be stabilized, and we generated the antigen binding portion of the FDA-approved drug caplacizumab. We tested the ability of this nanobody to bind to different VWF fragments and assessed its effects on AIM unfolding. We confirmed that the binding site of caplacizumab is mostly to the NAIM through both direct binding assays as well as crystallography. In our efforts to crystallize this complex, we hoped to elucidate more of the structure of the AIM. While our

structure has revealed two novel AIM to A1 electrostatic interactions, as well as resolved the most residues to date, there are still 40 or so residues that are unresolved in the AIM. We next demonstrated that caplacizumab can increase the unfolding force of the AIM, and in doing so, can inhibit VWF-based platelet capture at certain shear rates. Interestingly, at the highest shear rates tested, 10,000/s, platelets could still be captured, albeit at lower rates than untreated blood. In comparison, completely blocked A1 through ARC1172 could not capture any platelets at such shear rate. These results present a new direction for VWF targeting drugs. If such an antagonist can bind to VWF and inhibit its activation only at low shear rates, the hemostatic capabilities of VWF could be preserved at high shear rates.

We next sought to develop AIM-specific modulators to further probe the structure and function of the AIM. Using an immunized yeast display nanobody library against AIM-A1, we isolated several clones that were able to specifically bind to either the NAIM or CAIM. We discovered a family of nanobodies that bind to the NAIM and induce instantaneous VWF-dependent platelet agglutination, similar to the effects seen with ristocetin (Chapter 4). Further investigation into these nanobodies demonstrated that they bind to a distal portion of the NAIM, around the vicinal O-glycans of residues 1255 and 1256. These nanobodies could only bind to AIM-A1 bearing O-glycans and could not bind to AIM-A1 produced in bacteria, or NAIM-derived peptides, despite their ability to immunoblot mammalian expressed AIM-A1. These activating nanobodies were then demonstrated to be useful in a VWF activity assay as a means to discriminate between the subtypes of VWD. Determination of the sugar-dependent binding interface may yield insights into how sugars can stabilize the AIM or elucidate how a nanobody is able to recognize a specific proteoglycan interface.

We also discovered two nanobodies that showed nanomolar binding affinity to the CAIM (Chapter 5). These nanobodies differ greatly in their antigen-binding loops, and likely target different epitopes, although likely bind in a similar region. These nanobodies block ristocetin-induced platelet aggregation, likely due to direct antagonism of the binding site. These CAIM-binders were able to reduce platelet adhesion to collagen at high shear rates, yet at low, venous shear rates, the platelet binding was unaffected. These nanobodies did not reduce platelet capture to same extent as either ARC1172, a direct inhibitor of A1, or caplacizumab, suggesting that while their ability to reduce VWF-platelet interactions is inferior to caplacizumab, they may have limited bleeding side effects compared to caplacizumab. One of the nanobodies, Nd6, can cross react with murine VWF, and shows a modest reduction in platelet adhesion in mouse blood. These inhibitors suggest that allosteric modulation of VWF, or other mechanosensitive proteins, may yield more favorable effects, especially if complete blockade of a protein or receptor would be deleterious to a complex interactome. Future work will define the structures of these inhibitors in complex with AIM-A1, hopefully elucidating their inhibitory properties, how they use the CAIM to inhibit GPIbα binding, and may shed light on the conformation of the distal CAIM.

It is an important distinction that we have uncovered an activator that binds to the to the NAIM, yet caplacizumab binds to the NAIM but is inhibitory towards A1 activation. Similarly, we have demonstrated that the CAIM can be used for inhibition, while ristocetin and 6G1 use the CAIM for activation. This approach has demonstrated that both the NAIM and CAIM can be modulated to exhibit differential effects on VWF function.

There is some debate as to existence of the AIM, despite our immense efforts to demonstrate its function from several orthogonal approaches. The desire to define a protein

domain or the assignment of particular residues as a cohesive unit is a construct of human design. It is common to designate a domain of a protein based on homology or by what residues can be observed in a crystal structure. In most instances, a domain is a well folded, defined structural unit that may be adjoined to neighboring domains by short, 5 to 10 residue linkers. The fact that the linking residues between the last cysteine of the D3 domain and first cysteine of the A1 domain span nearly 40 residues make exact domain assignment complicated. Similarly, there is roughly 30 residues between the last cysteine of A1 and the motif that begins the A2 domain in all mammals. Dr. Tim Springer has ambiguously defined the A1 domain to start at the first resolved residue in most crystals, around residue 1263. Similarly, the end of the domain has been roughly assigned to residue 1466. However, a VWF fragment from 1263-1466 will be highly active towards GPIbα. High affinity binding to GPIbα is not a feature of full-length VWF, and therefore this definition of the A1 domain is flawed without recognition of the AIM. Our argument in this case is that the A1 domain, based on homology with other VWA domains, should only be encompassed by the cysteines at residues 1272 and 1458. Other VWA domains do not contain such long linkers between neighboring domains, such as those in integrin subunits. The length of the AIM is indeed highly conserved in mammals, suggesting that this length is imperative to the function of VWF.

We have further defined that the NAIM and CAIM are both required to reconstitute the behavior of full-length VWF. Previous works have shown that the NAIM appeared to be highly important to the inhibition of A1 (146), which we can agree with, as the NAIM constitutes most of the unfolding force of the AIM itself (Chapter 2). However, the unfolding of the CAIM cannot be ignored. Even in constructs containing the NAIM and CAIM we can observe, although rare, two separate unfolding events. The overwhelming majority of unfolding events are one long

unfolding, indicating that the NAIM and CAIM unfold together. Deletion of the CAIM also yields a highly active VWF fragment, suggesting that clearly the CAIM is indispensable for A1 protection. The suggestion that the AIM acts through non-specific steric-hinderance to inhibit GPIbα binding is also flawed (85). We can clearly demonstrate that addition of an antibody or nanobody to the AIM does not further block GPIbα, but in fact can facilitate binding (Chapters 2, 4)! Similarly, inhibition of the AIM acts not through steric-hinderance, but rather allosteric stabilization of the off-state. We hope to end the debate with our work on the activating nanobodies, as they clearly demonstrate that unresolved residues before 1261 are clearly involved in protection of A1, as these nanobodies target an epitope from 1255 to 1263. We concede that the distal portion of the CAIM such as residues between 1481 and 1493 are either unstructured or bind to the A2 domain. We have seen little difference in binding to GPIbα using VWF fragments from 1238-1472, 1238-1481, and 1238-1493, although there are subtle differences between ending the 1472 and 1493 in respects to ristocetin-induced binding – suggesting these residues play a minor role in the protection of A1. We are hopeful that the Nd4/AIM-A1 or Nd6/AIM-A1 crystal structures will help elucidate the structure of the distal CAIM to residue 1481.

6.2 Limitations and Future Directions

All studies on VWF are limited if not studying the entire multimer. Studying full-length VWF is inherently difficult, as preparations of VWF will contain different compositions of multimers. The avidity of the multimers makes biochemical measurements of binding more difficult to interpret as well. An important, and still outstanding question is the role of the AIM in full-length VWF. Unfolding of the AIM was also recently observed in a fragment containing

the D'D3 to A2 domains (190), however specific isolation of AIM unfolding in dimeric or monomeric full-length VWF has yet to be explicitly demonstrated. It would be an important step to generate recombinant full-length VWF with point mutations to limit multimerization. The CK domain is difficult to stop from dimerizing VWF without disrupting the network of disulfide bonds, while mutations in D'D3 to stop dimerization have been shown to yield homogenous protein (158). Using a homogenous dimer in an optical trap is not ideal, as two different reaction chemistries need to be used on each end of each monomer. For this, protein should be generated by bicistronic expression of two proteins, one with a SpyTag at the N-terminus and one with an Avitag or 3xFLAG tag at the other N-teminus. Due to chance, 50% of the expressed dimeric protein will have unique tags at each N-terminal, facilitating capture in the optical trap by unique beads. Deconvolution of A2 unfolding versus the AIM unfolding should now be possible as we know the contour lengths of these steps.

The epitopes targeted by the single domain antibodies in these studies are not all inclusive of all possible binding epitopes to the AIM. It is quite likely that inhibitors of AIM unfolding could be found in the library that bind to the NAIM, and that activators could be found that bind to the CAIM. It is also likely that using nanobodies may present different possible binding epitopes compared to nucleic-acid aptamers or traditional antibodies. Future work to specifically isolate AIM-A1 stabilizers is feasible with two-chained antibodies, as they can physically bind a larger surface area than a nanobody. Specific isolation of antibodies than can span such a discontinuous epitope such that it bound the NAIM and A1, the CAIM and A1, or the NAIM and CAIM, would likely require a sufficiently large library and rounds of mutagenesis and/or protein engineering. Such isolation of antibodies spanning complex or even dimer interfaces has been demonstrated to be feasible (262). *A priori* predictions about where the

immune response is mounted in relation to an immunogen are difficult to make. Considering VWF is expressed in all animals that would be used for immunization, a careful consideration of where in the AIM and A1 each animal is orthologous to human may inform where the immune response is directed. The activating nanobodies in Chapter 4 bind to an epitope on the human NAIM that does not resemble the sequence of the llama NAIM, perhaps suggesting that primary sequence divergence could result in targeting specific epitopes.

The invention and commercialization of fluorescence-coupled optical tweezers is changing the way force-sensitive proteins are studied. Observation of the LBD binding to unfolded VWF precisely controlled by optical tweezers will definitively demonstrate the molecular mechanism of activation of VWF. Interaction of fluorescent ADAMTS13 may also be feasible using such an instrument and should be able to define the order of operations in terms of AIM unfolding, A2 unfolding, GPIbα binding, and ADAMTS13 binding/cleavage.

The structure, or lack thereof, of the AIM is difficult to stabilize in order to visualize by crystallography. The presence of the O-linked sugars only enables more disorder in this region, yet paradoxically these sugars are important to the fold of the AIM. Other domains may further stabilize the AIM. To fully elucidate the structure of the AIM, a large VWF fragment should be used. An atomic level structure of D'D3-A1-A2-A3 solved by single particle cryo-EM is the proper construct to get the best chance to observe the AIM. Additionally, this could reveal if D'D3 or A2 plays a role in stabilizing the AIM and if A2 or A3 makes contact with A1. It remains to be seen if generation of this protein at high enough levels and homogeneity is possible. Further stabilization of this fragment using a combination of caplacizumab, Nd4, or Nd6 may yield more favorable results. Immobilization of the A1 domain onto plastics is

demonstrably destructive to the AIM (unpublished observations) and a solution-based structure is the only way to obtain information on the conformation of the AIM.

6.3 Conclusion

In this dissertation, I have studied the properties of a quasi-stable module that forms a complex with the A1 domain of VWF to shield it from GPIbα. This module is unfolded under physiologically relevant forces. This module appears to exist in other mammals, although its properties are likely distinct from the properties of the human AIM. The AIM can be both stabilized and destabilized. Disruption of the AIM leads to VWF activation, while stabilization of the AIM can increase the force resistance of VWF. My study not only describes and characterizes the function of VWF but provides a map to study other mechanosensory proteins using single domain antibodies.

References

1. Von Willebrand EA. 1999. Hereditary pseudohaemophilia. *Haemophilia : the official journal of the World Federation of Hemophilia* 5:223-31; discussion 2
2. Zimmerman TS, Ratnoff OD, Powell AE. 1971. Immunologic differentiation of classic hemophilia (factor 8 deficiency) and von Willebrand's dissase, with observations on combined deficiencies of antihemophilic factor and proaccelerin (factor V) and on an acquired circulating anticoagulant against antihemophilic factor. *The Journal of clinical investigation* 50:244-54
3. Weiss HJ, Rogers J, Brand H. 1973. Defective ristocetin-induced platelet aggregation in von Willebrand's disease and its correction by factor VIII. *The Journal of clinical investigation* 52:2697-707
4. Bouma BN, Wiegerinck Y, Sixma JJ, Van Mourik JA, Mochtar IA. 1972. Immunological characterization of purified anti-haemophilic factor A (factor VIII) which corrects abnormal platelet retention in Von Willebrand's disease. *Nat New Biol* 236:104-6
5. Sporn LA, Chavin SI, Marder VJ, Wagner DD. 1985. Biosynthesis of von Willebrand protein by human megakaryocytes. *The Journal of clinical investigation* 76:1102-6
6. Jaffe EA, Hoyer LW, Nachman RL. 1974. Synthesis of von Willebrand factor by cultured human endothelial cells. *Proceedings of the National Academy of Sciences of the United States of America* 71:1906-9
7. Nachman R, Levine R, Jaffe EA. 1977. Synthesis of factor VIII antigen by cultured guinea pig megakaryocytes. *The Journal of clinical investigation* 60:914-21
8. Lynch DC, Zimmerman TS, Collins CJ, Brown M, Morin MJ, et al. 1985. Molecular cloning of cDNA for human von Willebrand factor: authentication by a new method. *Cell* 41:49-56
9. Ginsburg D, Handin RI, Bonthron DT, Donlon TA, Bruns GA, et al. 1985. Human von Willebrand factor (vWF): isolation of complementary DNA (cDNA) clones and chromosomal localization. *Science (New York, N.Y.)* 228:1401-6
10. Verweij CL, de Vries CJ, Distel B, van Zonneveld AJ, van Kessel AG, et al. 1985. Construction of cDNA coding for human von Willebrand factor using antibody probes for colony-screening and mapping of the chromosomal gene. *Nucleic Acids Res* 13:4699-717
11. Sadler JE, Shelton-Inloes BB, Sorace JM, Harlan JM, Titani K, Davie EW. 1985. Cloning and characterization of two cDNAs coding for human von Willebrand factor. *Proceedings of the National Academy of Sciences of the United States of America* 82:6394-8
12. Shelton-Inloes BB, Titani K, Sadler JE. 1986. cDNA sequences for human von Willebrand factor reveal five types of repeated domains and five possible protein sequence polymorphisms. *Biochemistry* 25:3164-71
13. Zhou YF, Eng ET, Zhu J, Lu C, Walz T, Springer TA. 2012. Sequence and structure relationships within von Willebrand factor. *Blood* 120:449-58
14. Turitto VT, Weiss HJ, Baumgartner HR. 1983. Decreased platelet adhesion on vessel segments in von Willebrand's disease: a defect in initial platelet attachment. *J Lab Clin Med* 102:551-64
15. Savage B, Saldivar E, Ruggeri ZM. 1996. Initiation of platelet adhesion by arrest onto fibrinogen or translocation on von Willebrand factor. *Cell* 84:289-97

16. Sakariassen KS, Nievelstein PF, Coller BS, Sixma JJ. 1986. The role of platelet membrane glycoproteins Ib and IIb-IIIa in platelet adherence to human artery subendothelium. *Br J Haematol* 63:681-91
17. Savage B, Almus-Jacobs F, Ruggeri ZM. 1998. Specific synergy of multiple substrate-receptor interactions in platelet thrombus formation under flow. *Cell* 94:657-66
18. Bernard J, Soulier JP. 1948. Sur une nouvelle variété de dystrophie thrombocytaire-hémorragipare congénitale. *Sem Hop* 24:3217-23
19. Jenkins CS, Phillips DR, Clemetson KJ, Meyer D, Larrieu MJ, Luscher EF. 1976. Platelet membrane glycoproteins implicated in ristocetin-induced aggregation. Studies of the proteins on platelets from patients with Bernard-Soulier syndrome and von Willebrand's disease. *Journal of Clinical Investigation* 57:112-24
20. Clemetson KJ, McGregor JL, James E, Dechavanne M, Luscher EF. 1982. Characterization of the platelet membrane glycoprotein abnormalities in Bernard-Soulier syndrome and comparison with normal by surface-labeling techniques and high-resolution two-dimensional gel electrophoresis. *The Journal of clinical investigation* 70:304-11
21. Nurden AT, Caen JP. 1975. Specific roles for platelet surface glycoproteins in platelet function. *Nature* 255:720-2
22. Du X, Beutler L, Ruan C, Castaldi PA, Berndt MC. 1987. Glycoprotein Ib and glycoprotein IX are fully complexed in the intact platelet membrane. *Blood* 69:1524-7
23. Modderman PW, Admiraal LG, Sonnenberg A, von dem Borne AE. 1992. Glycoproteins V and Ib-IX form a noncovalent complex in the platelet membrane. *J Biol Chem* 267:364-9
24. Luo SZ, Mo X, Afshar-Kharghan V, Srinivasan S, Lopez JA, Li R. 2007. Glycoprotein Ibalpha forms disulfide bonds with 2 glycoprotein Ibbeta subunits in the resting platelet. *Blood* 109:603-9
25. Luo SZ, Li R. 2008. Specific heteromeric association of four transmembrane peptides derived from platelet glycoprotein Ib-IX complex. *J Mol Biol* 382:448-57
26. Mo X, Luo S-Z, López JA, Li R. 2008. Juxtamembrane basic residues in glycoprotein Ibβ cytoplasmic domain are required for assembly and surface expression of glycoprotein Ib-IX complex. *FEBS Lett* 582:3270-4
27. Tao Y, Gan C, Zhang X, Liu L, Zakas PM, et al. 2020. Unaccompanied mechanosensory domain mediates low expression of glycoprotein Ibalpha: implications for Bernard-Soulier syndrome. *J Thromb Haemost* 18:510-7
28. Griggs TR, Cooper HA, Webster WP, Wagner RH, Brinkhous KM. 1973. Plasma aggregating factor (bovine) for human platelets: a marker for study of antihemophilic and von Willebrand Factors. *Proceedings of the National Academy of Sciences of the United States of America* 70:2814-8
29. Weiss HJ, Tschopp TB, Baumgartner HR, Sussman, II, Johnson MM, Egan JJ. 1974. Decreased adhesion of giant (Bernard-Soulier) platelets to subendothelium. Further implications on the role of the von Willebrand factor in hemostasis. *Am J Med* 57:920-5
30. Quach ME, Li R. 2020. Structure-function of platelet glycoprotein Ib-IX. *J Thromb Haemost* 18:3131-41
31. Kahn ML, Diacovo TG, Bainton DF, Lanza F, Trejo J, Coughlin SR. 1999. Glycoprotein V-deficient platelets have undiminished thrombin responsiveness and do not exhibit a Bernard-Soulier phenotype. *Blood* 94:4112-21

32. Quach ME, Chen W, Wang Y, Deckmyn H, Lanza F, et al. 2021. Differential regulation of the platelet GPIb-IX complex by anti-GPIbβ antibodies. *J Thromb Haemost* 19:2044-55
33. Katsumi A, Tuley EA, Bodó I, Sadler JE. 2000. Localization of disulfide bonds in the cystine knot domain of human von Willebrand factor. *The Journal of biological chemistry* 275:25585-94
34. Huang RH, Wang Y, Roth R, Yu X, Purvis AR, et al. 2008. Assembly of Weibel-Palade body-like tubules from N-terminal domains of von Willebrand factor. *Proceedings of the National Academy of Sciences of the United States of America* 105:482-7
35. Zhou YF, Eng ET, Nishida N, Lu C, Walz T, Springer TA. 2011. A pH-regulated dimeric bouquet in the structure of von Willebrand factor. *EMBO J* 30:4098-111
36. Berriman JA, Li S, Hewlett LJ, Wasilewski S, Kiskin FN, et al. 2009. Structural organization of Weibel-Palade bodies revealed by cryo-EM of vitrified endothelial cells. *Proceedings of the National Academy of Sciences of the United States of America* 106:17407-12
37. Springer TA. 2014. von Willebrand factor, Jedi knight of the bloodstream. *Blood* 124:1412-25
38. Parker ET, Lollar P. 2021. Conformation of the von Willebrand factor/factor VIII complex in quasi-static flow. *The Journal of biological chemistry* 296:100420
39. Fischer K, Pendu R, van Schooten CJ, van Dijk K, Denis CV, et al. 2009. Models for prediction of factor VIII half-life in severe haemophiliacs: distinct approaches for blood group O and non-O patients. *PloS one* 4:e6745
40. Leebeek FW, Eikenboom JC. 2016. Von Willebrand's Disease. *N Engl J Med* 375:2067-80
41. Hill-Eubanks DC, Parker CG, Lollar P. 1989. Differential proteolytic activation of factor VIII-von Willebrand factor complex by thrombin. *Proceedings of the National Academy of Sciences of the United States of America* 86:6508-12
42. Whittaker CA, Hynes RO. 2002. Distribution and evolution of von Willebrand/integrin A domains: widely dispersed domains with roles in cell adhesion and elsewhere. *Mol Biol Cell* 13:3369-87
43. Fujimura Y, Titani K, Holland LZ, Russell SR, Roberts JR, et al. 1986. von Willebrand factor. A reduced and alkylated 52/48-kDa fragment beginning at amino acid residue 449 contains the domain interacting with platelet glycoprotein Ib. *The Journal of biological chemistry* 261:381-5
44. Andrews RK, Gorman JJ, Booth WJ, Corino GL, Castaldi PA, Berndt MC. 1989. Cross-linking of a monomeric 39/34-kDa dispase fragment of von Willebrand factor (Leu-480/Val-481-Gly-718) to the N-terminal region of the alpha-chain of membrane glycoprotein Ib on intact platelets with bis(sulfosuccinimidyl) suberate. *Biochemistry* 28:8326-36
45. Ying J, Ling Y, Westfield LA, Sadler JE, Shao JY. 2010. Unfolding the A2 domain of von Willebrand factor with the optical trap. *Biophys J* 98:1685-93
46. Zhang X, Halvorsen K, Zhang CZ, Wong WP, Springer TA. 2009. Mechanoenzymatic cleavage of the ultralarge vascular protein von Willebrand factor. *Science* 324:1330-4
47. Tsai HM. 2004. A journey from sickle cell anemia to ADAMTS13. *J Thromb Haemost* 2:1510-4

48. Cruz MA, Yuan H, Lee JR, Wise RJ, Handin RI. 1995. Interaction of the von Willebrand factor (vWF) with collagen. Localization of the primary collagen-binding site by analysis of recombinant vWF a domain polypeptides. *Journal of biological chemistry* 270:10822-7
49. Flood VH, Schlauderaff AC, Haberichter SL, Slobodianuk TL, Jacobi PM, et al. 2015. Crucial role for the VWF A1 domain in binding to type IV collagen. *Blood* 125:2297-304
50. Crawley JTB, de Groot R, Xiang Y, Luken BM, Lane DA. 2011. Unraveling the scissile bond: how ADAMTS13 recognizes and cleaves von Willebrand factor. *Blood* 118:3212-21
51. Wu YP, Vink T, Schiphorst M, van Zanten GH, MJ IJ, et al. 2000. Platelet thrombus formation on collagen at high shear rates is mediated by von Willebrand factor-glycoprotein Ib interaction and inhibited by von Willebrand factor-glycoprotein IIb/IIIa interaction. *Arteriosclerosis, thrombosis, and vascular biology* 20:1661-7
52. Sánchez-Cortés J, Mrksich M. 2009. The platelet integrin alphaIIbbeta3 binds to the RGD and AGD motifs in fibrinogen. *Chem Biol* 16:990-1000
53. Farrell DH, Thiagarajan P, Chung DW, Davie EW. 1992. Role of fibrinogen alpha and gamma chain sites in platelet aggregation. *Proceedings of the National Academy of Sciences of the United States of America* 89:10729-32
54. Muia J, Zhu J, Gupta G, Haberichter SL, Friedman KD, et al. 2014. Allosteric activation of ADAMTS13 by von Willebrand factor. *Proc Natl Acad Sci U S A* 111:18584-9
55. Peake I, Goodeve A. 2007. Type 1 von Willebrand disease. *Journal of thrombosis and haemostasis : JTH* 5 Suppl 1:7-11
56. Flood VH, Garcia J, Haberichter SL. 2019. The role of genetics in the pathogenesis and diagnosis of type 1 Von Willebrand disease. *Curr Opin Hematol* 26:331-5
57. Jacobi PM, Gill JC, Flood VH, Jakab DA, Friedman KD, Haberichter SL. 2012. Intersection of mechanisms of type 2A VWD through defects in VWF multimerization, secretion, ADAMTS-13 susceptibility, and regulated storage. *Blood* 119:4543-53
58. Woods AI, Sanchez-Luceros A, Kempfer AC, Powazniak Y, Calderazzo Pereyra JC, et al. 2012. C1272F: a novel type 2A von Willebrand's disease mutation in A1 domain; its clinical significance. *Haemophilia : the official journal of the World Federation of Hemophilia* 18:112-6
59. Lankhof H, Damas C, Schiphorst ME, MJ IJ, Bracke M, et al. 1997. Functional studies on platelet adhesion with recombinant von Willebrand factor type 2B mutants R543Q and R543W under conditions of flow. *Blood* 89:2766-72
60. Casari C, Du V, Wu YP, Kauskot A, de Groot PG, et al. 2013. Accelerated uptake of VWF/platelet complexes in macrophages contributes to VWD type 2B-associated thrombocytopenia. *Blood* 122:2893-902
61. Nishio K, Anderson PJ, Zheng XL, Sadler JE. 2004. Binding of platelet glycoprotein Ibalpha to von Willebrand factor domain A1 stimulates the cleavage of the adjacent domain A2 by ADAMTS13. *Proceedings of the National Academy of Sciences of the United States of America* 101:10578-83
62. Doggett TA, Girdhar G, Lawshe A, Miller JL, Laurenzi IJ, et al. 2003. Alterations in the intrinsic properties of the GPIbalpha-VWF tether bond define the kinetics of the platelet-type von Willebrand disease mutation, Gly233Val. *Blood* 102:152-60

63. Othman M, Kaur H, Emsley J. 2013. Platelet-type von Willebrand disease: new insights into the molecular pathophysiology of a unique platelet defect. *Semin Thromb Hemost* 39:663-73
64. Tischer A, Machha VR, Moon-Tasson L, Auton M. 2019. Platelet-type von Willebrand disease: Local disorder of the platelet GPIbalpha beta-switch drives high-affinity binding to von Willebrand factor. *Journal of thrombosis and haemostasis : JTH* 17:2022-34
65. Bury L, Malara A, Momi S, Petito E, Balduini A, Gresele P. 2019. Mechanisms of thrombocytopenia in platelet-type von Willebrand disease. *Haematologica* 104:1473-81
66. Doruelo AL, Haberichter SL, Christopherson PA, Boggio LN, Gupta S, et al. 2017. Clinical and laboratory phenotype variability in type 2M von Willebrand disease. *Journal of thrombosis and haemostasis : JTH* 15:1559-66
67. Seidizadeh O, Peyvandi F, Mannucci PM. 2021. Von Willebrand disease type 2N: An update. *Journal of thrombosis and haemostasis : JTH* 19:909-16
68. Federici AB, James P. 2012. Current management of patients with severe von Willebrand disease type 3: a 2012 update. *Acta Haematol* 128:88-99
69. Perkins TT, Smith DE, Chu S. 1997. Single polymer dynamics in an elongational flow. *Science (New York, N.Y.)* 276:2016-21
70. Smith DE, Babcock HP, Chu S. 1999. Single-polymer dynamics in steady shear flow. *Science (New York, N.Y.)* 283:1724-7
71. Feys HB, Roodt J, Vandeputte N, Pareyn I, Lamprecht S, et al. 2010. Thrombotic thrombocytopenic purpura directly linked with ADAMTS13 inhibition in the baboon (Papio ursinus). *Blood* 116:2005-10
72. Zheng XL. 2015. ADAMTS13 and von Willebrand factor in thrombotic thrombocytopenic purpura. *Annu Rev Med* 66:211-25
73. Uff S, Clemetson JM, Harrison T, Clemetson KJ, Emsley J. 2002. Crystal structure of the platelet glycoprotein Iba N-terminal domain reveals an unmasking mechanism for receptor activation. *J Biol Chem* 277:35657-63
74. Emsley J, Cruz M, Handin R, Liddington R. 1998. Crystal structure of the von Willebrand Factor A1 domain and implications for the binding of platelet glycoprotein Ib. *J Biol Chem* 273:10396-401
75. Huizinga EG, Tsuji S, Romijn RA, Schiphorst ME, de Groot PG, et al. 2002. Structures of glycoprotein Iba and its complex with von Willebrand factor A1 domain. *Science* 297:1176-9
76. Dumas JJ, Kumar R, McDonagh T, Sullivan F, Stahl ML, et al. 2004. Crystal structure of the wild-type von Willebrand factor A1-glycoprotein Iba complex reveals conformation differences with a complex bearing von Willebrand disease mutations. *J Biol Chem* 279:23327-34
77. Federici AB, Mannucci PM, Castaman G, Baronciani L, Bucciarelli P, et al. 2009. Clinical and molecular predictors of thrombocytopenia and risk of bleeding in patients with von Willebrand disease type 2B: a cohort study of 67 patients. *Blood* 113:526-34
78. Cruz MA, Handin RI, Wise RJ. 1993. The interaction of the von Willebrand factor-A1 domain with platelet glycoprotein Ib/IX. The role of glycosylation and disulfide bonding in a monomeric recombinant A1 domain protein. *Journal of biological chemistry* 268:21238-45

79. Miyata S, Goto S, Federici AB, Ware J, Ruggeri ZM. 1996. Conformational changes in the A1 domain of von Willebrand factor modulating the interaction with platelet glycoprotein Ibalpha. *J Biol Chem* 271:9046-53
80. Miura S, Li CQ, Cao Z, Wang H, Wardell MR, Sadler JE. 2000. Interaction of von Willebrand factor domain A1 with platelet glycoprotein Ibα-(1-289). Slow intrinsic binding kinetics mediate rapid platelet adhesion. *Journal of biological chemistry* 275:7539-46
81. Blenner MA, Dong X, Springer TA. 2014. Structural basis of regulation of von Willebrand factor binding to glycoprotein Ib. *J Biol Chem* 289:5565-79
82. Sadler JE. 1991. von Willebrand factor. *J Biol Chem* 266:22777-80
83. Huizinga EG, Tsuji S, Romijn RA, Schiphorst ME, de Groot PG, et al. 2002. Structures of glycoprotein Ibalpha and its complex with von Willebrand factor A1 domain. *Science* 297:1176-9
84. Schneider SW, Nuschele S, Wixforth A, Gorzelanny C, Alexander-Katz A, et al. 2007. Shear-induced unfolding triggers adhesion of von Willebrand factor fibers. *Proc Natl Acad Sci U S A* 104:7899-903
85. Tischer A, Machha VR, Moon-Tasson L, Benson LM, Auton M. 2020. Glycosylation sterically inhibits platelet adhesion to von Willebrand factor without altering intrinsic conformational dynamics. *J Thromb Haemost* 18:79-90
86. Chen J, Zhou H, Diacovo A, Zheng XL, Emsley J, Diacovo TG. 2014. Exploiting the kinetic interplay between GPIbalpha-VWF binding interfaces to regulate hemostasis and thrombosis. *Blood* 124:3799-807
87. Tischer A, Madde P, Moon-Tasson L, Auton M. 2014. Misfolding of vWF to pathologically disordered conformations impacts the severity of von Willebrand disease. *Biophys J* 107:1185-95
88. Deng W, Wang Y, Druzak SA, Healey JF, Syed AK, et al. 2017. A discontinuous autoinhibitory module masks the A1 domain of von Willebrand factor. *J Thromb Haemost* 15:1867-77
89. Deng W, Voos KM, Colucci JK, Legan ER, Ortlund EA, et al. 2018. Delimiting the autoinhibitory module of von Willebrand factor. *J Thromb Haemost* 16:2097-105
90. Kim J, Zhang CZ, Zhang X, Springer TA. 2010. A mechanically stabilized receptor-ligand flex-bond important in the vasculature. *Nature* 466:992-5
91. Zhang W, Deng W, Zhou L, Xu Y, Yang W, et al. 2015. Identification of a juxtamembrane mechanosensitive domain in the platelet mechanosensor glycoprotein Ib-IX complex. *Blood* 125:562-9
92. Deng W, Xu Y, Chen W, Paul DS, Syed AK, et al. 2016. Platelet clearance via shear-induced unfolding of a membrane mechanoreceptor. *Nat Commun* 7:12863
93. Ju L, Chen Y, Xue L, Du X, Zhu C. 2016. Cooperative unfolding of distinctive mechanoreceptor domains transduces force into signals. *Elife* 5:e15447
94. Ju L, Lou J, Chen Y, Li Z, Zhu C. 2015. Force-Induced Unfolding of Leucine-Rich Repeats of Glycoprotein Ibalpha Strengthens Ligand Interaction. *Biophys J* 109:1781-4
95. Shen Y, Cranmer SL, Aprico A, Whisstock JC, Jackson SP, et al. 2006. Leucine-rich repeats 2-4 (Leu60-Glu128) of platelet glycoprotein Ibalpha regulate shear-dependent cell adhesion to von Willebrand factor. *J Biol Chem* 281:26419-23

96. Kim J, Hudson NE, Springer TA. 2015. Force-induced on-rate switching and modulation by mutations in gain-of-function von Willebrand diseases. *Proc Natl Acad Sci U S A* 112:4648-53
97. Fu H, Jiang Y, Yang D, Scheiflinger F, Wong WP, Springer TA. 2017. Flow-induced elongation of von Willebrand factor precedes tension-dependent activation. *Nat Commun* 8:324
98. Matsushita T, Meyer D, Sadler JE. 2000. Localization of von willebrand factor-binding sites for platelet glycoprotein Ib and botrocetin by charged-to-alanine scanning mutagenesis. *J Biol Chem* 275:11044-9
99. Solecka BA, Weise C, Laffan MA, Kannicht C. 2016. Site-specific analysis of von Willebrand factor O-glycosylation. *J Thromb Haemost* 14:733-46
100. Nakayama T, Matsushita T, Dong Z, Sadler JE, Jorieux S, et al. 2002. Identification of the regulatory elements of the human von Willebrand factor for binding to platelet GPIb. Importance of structural integrity of the regions flanked by the CYS1272-CYS1458 disulfide bond. *J Biol Chem* 277:22063-72
101. Tischer A, Cruz MA, Auton M. 2013. The linker between the D3 and A1 domains of vWF suppresses A1-GPIbalpha catch bonds by site-specific binding to the A1 domain. *Protein Sci* 22:1049-59
102. Interlandi G, Yakovenko O, Tu AY, Harris J, Le J, et al. 2017. Specific electrostatic interactions between charged amino acid residues regulate binding of von Willebrand factor to blood platelets. *J Biol Chem* 292:18608-17
103. Zhang C, Kelkar A, Nasirikenari M, Lau JTY, Sveinsson M, et al. 2018. The physical spacing between the von Willebrand factor D'D3 and A1 domains regulates platelet adhesion in vitro and in vivo. *J Thromb Haemost* 16:571-82
104. Auton M, Sowa KE, Behymer M, Cruz MA. 2012. N-terminal flanking region of A1 domain in von Willebrand factor stabilizes structure of A1A2A3 complex and modulates platelet activation under shear stress. *J Biol Chem* 287:14579-85
105. Ju L, Dong JF, Cruz MA, Zhu C. 2013. The N-terminal flanking region of the A1 domain regulates the force-dependent binding of von Willebrand factor to platelet glycoprotein Ibalpha. *J Biol Chem* 288:32289-301
106. Ju L, Chen Y, Zhou F, Lu H, Cruz MA, Zhu C. 2015. Von Willebrand factor-A1 domain binds platelet glycoprotein Ibalpha in multiple states with distinctive force-dependent dissociation kinetics. *Thromb Res* 136:606-12
107. Girma JP, Takahashi Y, Yoshioka A, Diaz J, Meyer D. 1990. Ristocetin and botrocetin involve two distinct domains of von Willebrand factor for binding to platelet membrane glycoprotein Ib. *Thromb Haemost* 64:326-32
108. Fukuda K, Doggett T, Laurenzi IJ, Liddington RC, Diacovo TG. 2005. The snake venom protein botrocetin acts as a biological brace to promote dysfunctional platelet aggregation. *Nat Struct Mol Biol* 12:152-9
109. Zakas PM, Coyle CW, Brehm A, Bayer M, Solecka-Witulska B, et al. 2021. Molecular coevolution of coagulation factor VIII and von Willebrand factor. *Blood Adv* 5:812-22
110. Flood VH, Gill JC, Morateck PA, Christopherson PA, Friedman KD, et al. 2010. Common VWF exon 28 polymorphisms in African Americans affecting the VWF activity assay by ristocetin cofactor. *Blood* 116:280-6

111. Flood VH, Friedman KD, Gill JC, Morateck PA, Wren JS, et al. 2009. Limitations of the ristocetin cofactor assay in measurement of von Willebrand factor function. *J Thromb Haemost* 7:1832-9
112. Gill JC, Endres-Brooks J, Bauer PJ, Marks WJ, Jr., Montgomery RR. 1987. The effect of ABO blood group on the diagnosis of von Willebrand disease. *Blood* 69:1691-5
113. Ward S, O'Sullivan JM, O'Donnell JS. 2019. von Willebrand factor sialylation-A critical regulator of biological function. *J Thromb Haemost* 17:1018-29
114. Grainick HR, Williams SB, Coller BS. 1985. Asialo von Willebrand factor interactions with platelets. Interdependence of glycoproteins Ib and IIb/IIIa for binding and aggregation. *J Clin Invest* 75:19-25
115. Nowak AA, Canis K, Riddell A, Laffan MA, McKinnon TA. 2012. O-linked glycosylation of von Willebrand factor modulates the interaction with platelet receptor glycoprotein Ib under static and shear stress conditions. *Blood* 120:214-22
116. Badirou I, Kurdi M, Legendre P, Rayes J, Bryckaert M, et al. 2012. In vivo analysis of the role of O-glycosylations of von Willebrand factor. *PloS one* 7:e37508
117. Voos KM, Cao W, Arce NA, Legan ER, Wang Y, et al. 2021. Desialylation of O-glycans activates von Willebrand factor by destabilizing its autoinhibitory module. *J Thromb Haemost* Online ahead of print
118. Ulrichts H, Udvardy M, Lenting PJ, Pareyn I, Vandeputte N, et al. 2006. Shielding of the A1 domain by the D'D3 domains of von Willebrand factor modulates its interaction with platelet glycoprotein Ib-IX-V. *J Biol Chem* 281:4699-707
119. Shibata M, Shima M, Fujimura Y, Takahashi Y, Nakai H, et al. 1999. Identification of the binding site for an alloantibody to von Willebrand factor which inhibits binding to glycoprotein Ib within the amino-terminal region flanking the A1 domain. *Thromb Haemost* 81:793-8
120. Madabhushi SR, Zhang C, Kelkar A, Dayananda KM, Neelamegham S. 2014. Platelet GpIba binding to von Willebrand Factor under fluid shear:contributions of the D'D3-domain, A1-domain flanking peptide and O-linked glycans. *Journal of the American Heart Association* 3:e001420
121. Martin C, Morales LD, Cruz MA. 2007. Purified A2 domain of von Willebrand factor binds to the active conformation of von Willebrand factor and blocks the interaction with platelet glycoprotein Ibalpha. *J Thromb Haemost* 5:1363-70
122. Aponte-Santamaria C, Huck V, Posch S, Bronowska AK, Grassle S, et al. 2015. Force-sensitive autoinhibition of the von Willebrand factor is mediated by interdomain interactions. *Biophys J* 108:2312-21
123. Butera D, Passam F, Ju L, Cook KM, Woon H, et al. 2018. Autoregulation of von Willebrand factor function by a disulfide bond switch. *Science advances* 4:eaaq1477
124. Kroll MH, Hellums JD, McIntire LV, Schafer AI, Moake JL. 1996. Platelets and shear stress. *Blood* 88:1525-41
125. Kulkarni S, Dopheide SM, Yap CL, Ravanat C, Freund M, et al. 2000. A revised model of platelet aggregation. *J Clin Invest* 105:783-91
126. Varga-Szabo D, Pleines I, Nieswandt B. 2008. Cell adhesion mechanisms in platelets. *Arterioscler Thromb Vasc Biol* 28:403-12
127. Hamers-Casterman C, Atarhouch T, Muyldermans S, Robinson G, Hamers C, et al. 1993. Naturally occurring antibodies devoid of light chains. *Nature* 363:446-8

128. Muyldermans S. 2013. Nanobodies: natural single-domain antibodies. *Annual review of biochemistry* 82:775-97
129. De Genst E, Silence K, Decanniere K, Conrath K, Loris R, et al. 2006. Molecular basis for the preferential cleft recognition by dromedary heavy-chain antibodies. *Proc Natl Acad Sci U S A* 103:4586-91
130. Arbabi Ghahroudi M, Desmyter A, Wyns L, Hamers R, Muyldermans S. 1997. Selection and identification of single domain antibody fragments from camel heavy-chain antibodies. *FEBS Lett* 414:521-6
131. Hussack G, Hirama T, Ding W, Mackenzie R, Tanha J. 2011. Engineered single-domain antibodies with high protease resistance and thermal stability. *PloS one* 6:e28218
132. Messer A, Butler DC. 2020. Optimizing intracellular antibodies (intrabodies/nanobodies) to treat neurodegenerative disorders. *Neurobiol Dis* 134:104619
133. Lobstein J, Emrich CA, Jeans C, Faulkner M, Riggs P, Berkmen M. 2012. SHuffle, a novel Escherichia coli protein expression strain capable of correctly folding disulfide bonded proteins in its cytoplasm. *Microb Cell Fact* 11:56
134. Roth L, Krah S, Klemm J, Günther R, Toleikis L, et al. 2020. Isolation of Antigen-Specific VHH Single-Domain Antibodies by Combining Animal Immunization with Yeast Surface Display. *Methods in molecular biology (Clifton, N.J.)* 2070:173-89
135. Pardon E, Laeremans T, Triest S, Rasmussen SG, Wohlkönig A, et al. 2014. A general protocol for the generation of Nanobodies for structural biology. *Nat Protoc* 9:674-93
136. van der Linden R, de Geus B, Stok W, Bos W, van Wassenaar D, et al. 2000. Induction of immune responses and molecular cloning of the heavy chain antibody repertoire of Lama glama. *J Immunol Methods* 240:185-95
137. Uchański T, Zögg T, Yin J, Yuan D, Wohlkönig A, et al. 2019. An improved yeast surface display platform for the screening of nanobody immune libraries. *Sci Rep* 9:382
138. McMahon C, Baier AS, Pascolutti R, Wegrecki M, Zheng S, et al. 2018. Yeast surface display platform for rapid discovery of conformationally selective nanobodies. *Nat Struct Mol Biol* 25:289-96
139. Chao G, Lau WL, Hackel BJ, Sazinsky SL, Lippow SM, Wittrup KD. 2006. Isolating and engineering human antibodies using yeast surface display. *Nat Protoc* 1:755-68
140. Boder ET, Wittrup KD. 1997. Yeast surface display for screening combinatorial polypeptide libraries. *Nat Biotechnol* 15:553-7
141. Wellner A, McMahon C, Gilman MSA, Clements JR, Clark S, et al. 2021. Rapid generation of potent antibodies by autonomous hypermutation in yeast. *Nat Chem Biol* 17:1057-64
142. Wang J, Kang G, Yuan H, Cao X, Huang H, de Marco A. 2021. Research Progress and Applications of Multivalent, Multispecific and Modified Nanobodies for Disease Treatment. *Front Immunol* 12:838082
143. Peyvandi F, Scully M, Kremer Hovinga JA, Cataland S, Knobl P, et al. 2016. Caplacizumab for Acquired Thrombotic Thrombocytopenic Purpura. *N Engl J Med* 374:511-22
144. Vincke C, Loris R, Saerens D, Martinez-Rodriguez S, Muyldermans S, Conrath K. 2009. General strategy to humanize a camelid single-domain antibody and identification of a universal humanized nanobody scaffold. *The Journal of biological chemistry* 284:3273-84

145. Jailkhani N, Ingram JR, Rashidian M, Rickelt S, Tian C, et al. 2019. Noninvasive imaging of tumor progression, metastasis, and fibrosis using a nanobody targeting the extracellular matrix. *Proceedings of the National Academy of Sciences of the United States of America* 116:14181-90
146. Tischer A, Cruz MA, Auton M. 2013. The linker between the D3 and A1 domains of vWF suppresses A1-GPIbalpha catch bonds by site-specific binding to the A1 domain. *Protein Science* 22:1049-59
147. Dong J-F, Berndt MC, Schade A, McIntire LV, Andrews RK, López JA. 2001. Ristocetin-dependent, but not botrocetin-dependent, binding of von Willebrand factor to the platelet glycoprotein Ib-IX-V complex correlates with shear-dependent interactions. 97:162-8
148. Wagner DD. 1990. Cell biology of von Willebrand factor. *Annu Rev Cell Biol* 6:217-46
149. Sadler JE. 1998. Biochemistry and genetics of von Willebrand factor. *Annual review of biochemistry* 67:395-424
150. Mannucci PM. 1998. von Willebrand factor: a marker of endothelial damage? *Arterioscler Thromb Vasc Biol* 18:1359-62
151. Li F, Li CQ, Moake JL, Lopez JA, McIntire LV. 2004. Shear stress-induced binding of large and unusually large von Willebrand factor to human platelet glycoprotein Ibalpha. *Ann Biomed Eng* 32:961-9
152. Chow TW, Hellums JD, Moake JL, Kroll MH. 1992. Shear stress-induced von Willebrand factor binding to platelet glycoprotein Ib initiates calcium influx associated with aggregation. *Blood* 80:113-20
153. Du X. 2007. Signaling and regulation of the platelet glycoprotein Ib-IX-V complex. *Curr Opin Hematol* 14:262-9
154. Kremer Hovinga JA, Coppo P, Lammle B, Moake JL, Miyata T, Vanhoorelbeke K. 2017. Thrombotic thrombocytopenic purpura. *Nat Rev Dis Primers* 3:17020
155. Howard MA, Firkin BG. 1971. Ristocetin--a new tool in the investigation of platelet aggregation. *Thromb Diath Haemorrh* 26:362-9
156. Read MS, Shermer RW, Brinkhous KM. 1978. Venom coagglutinin: an activator of platelet aggregation dependent on von Willebrand factor. *Proc Natl Acad Sci U S A* 75:4514-8
157. Zhang Q, Zhou YF, Zhang CZ, Zhang X, Lu C, Springer TA. 2009. Structural specializations of A2, a force-sensing domain in the ultralarge vascular protein von Willebrand factor. *Proc Natl Acad Sci U S A* 106:9226-31
158. Dong X, Leksa NC, Chhabra ES, Arndt JW, Lu Q, et al. 2019. The von Willebrand factor D'D3 assembly and structural principles for factor VIII binding and concatemer biogenesis. *Blood* 133:1523-33
159. Tischer A, Campbell JC, Machha VR, Moon-Tasson L, Benson LM, et al. 2016. Mutational Constraints on Local Unfolding Inhibit the Rheological Adaptation of von Willebrand Factor. *J Biol Chem* 291:3848-59
160. De Luca M, Facey DA, Favaloro EJ, Hertzberg MS, Whisstock JC, et al. 2000. Structure and function of the von Willebrand factor A1 domain: analysis with monoclonal antibodies reveals distinct binding sites involved in recognition of the platelet membrane glycoprotein Ib-IX-V complex and ristocetin-dependent activation. *Blood* 95:164-72

161. Huang RH, Fremont DH, Diener JL, Schaub RG, Sadler JE. 2009. A structural explanation for the antithrombotic activity of ARC1172, a DNA aptamer that binds von Willebrand factor domain A1. *Structure* 17:1476-84
162. Raran-Kurussi S, Cherry S, Zhang D, Waugh DS. 2017. Removal of Affinity Tags with TEV Protease. *Methods Mol Biol* 1586:221-30
163. Yan R, Mo X, Paredes AM, Dai K, Lanza F, et al. 2011. Reconstitution of platelet glycoprotein Ib-IX complex in phospholipid bilayer nanodiscs. *Biochemistry* 50:10598-606
164. Zakeri B, Fierer JO, Celik E, Chittock EC, Schwarz-Linek U, et al. 2012. Peptide tag forming a rapid covalent bond to a protein, through engineering a bacterial adhesin. *Proc Natl Acad Sci U S A* 109:E690-7
165. Mize GJ, Harris JE, Takayama TK, Kulman JD. 2008. Regulated expression of active biotinylated G-protein coupled receptors in mammalian cells. *Protein Expr Purif* 57:280-9
166. Mo X, Lu N, Padilla A, López JA, Li R. 2006. The transmembrane domain of glycoprotein Ibβ is critical to efficient expression of glycoprotein Ib-IX complex in the plasma membrane. *J Biol Chem* 281:23050-9
167. Liang X, Russell SR, Estelle S, Jones LH, Cho S, et al. 2013. Specific inhibition of ectodomain shedding of glycoprotein Ibα by targeting its juxtamembrane shedding cleavage site. *J Thromb Haemost* 11:2155-62
168. Zhang XF, Zhang W, Quach ME, Deng W, Li R. 2019. Force-regulated refolding of the mechanosensory domain in the platelet glycoprotein Ib-IX complex. *Biophys J* 116:1960-9
169. Evans E, Ritchie K. 1997. Dynamic strength of molecular adhesion bonds. *Biophys J* 72:1541-55
170. Bell GI. 1978. Models for the specific adhesion of cells to cells. *Science* 200:618-27
171. McCoy AJ, Grosse-Kunstleve RW, Adams PD, Winn MD, Storoni LC, Read RJ. 2007. Phaser crystallographic software. *J Appl Crystallogr* 40:658-74
172. Wiita AP, Ainavarapu SR, Huang HH, Fernandez JM. 2006. Force-dependent chemical kinetics of disulfide bond reduction observed with single-molecule techniques. *Proc Natl Acad Sci U S A* 103:7222-7
173. Ainavarapu SR, Brujic J, Huang HH, Wiita AP, Lu H, et al. 2007. Contour length and refolding rate of a small protein controlled by engineered disulfide bonds. *Biophys J* 92:225-33
174. Bustamante C, Smith SB, Liphardt J, Smith D. 2000. Single-molecule studies of DNA mechanics. *Curr Opin Struct Biol* 10:279-85
175. Sandoval-Perez A, Berger RML, Garaizar A, Farr SE, Brehm MA, et al. 2020. DNA binds to a specific site of the adhesive blood-protein von Willebrand factor guided by electrostatic interactions. *Nucleic Acids Res* 48:7333-44
176. Auton M, Sowa KE, Behymer M, Cruz MA. 2012. N-terminal flanking region of A1 domain in von Willebrand factor stabilizes structure of A1A2A3 complex and modulates platelet activation under shear stress. *Journal of Biological Chemistry* 287:14579-85
177. Auton M, Zhu C, Cruz MA. 2010. The mechanism of VWF-mediated platelet GPIbalpha binding. *Biophys J* 99:1192-201
178. Ozaki Y, Asazuma N, Suzuki-Inoue K, Berndt MC. 2005. Platelet GPIb-IX-V-dependent signaling. *J Thromb Haemost* 3:1745-51

179. Caron C, Hilbert L, Vanhoorelbeke K, Deckmyn H, Goudemand J, Mazurier C. 2006. Measurement of von Willebrand factor binding to a recombinant fragment of glycoprotein Ibalpha in an enzyme-linked immunosorbent assay-based method: performances in patients with type 2B von Willebrand disease. *Br J Haematol* 133:655-63
180. Scott JP, Montgomery RR, Retzinger GS. 1991. Dimeric ristocetin flocculates proteins, binds to platelets, and mediates von Willebrand factor-dependent agglutination of platelets. *J Biol Chem* 266:8149-55
181. Scully M, Cataland SR, Peyvandi F, Coppo P, Knobl P, et al. 2019. Caplacizumab Treatment for Acquired Thrombotic Thrombocytopenic Purpura. *N Engl J Med* 380:335-46
182. Ulrichts H, Silence K, Schoolmeester A, de Jaegere P, Rossenu S, et al. 2011. Antithrombotic drug candidate ALX-0081 shows superior preclinical efficacy and safety compared with currently marketed antiplatelet drugs. *Blood* 118:757-65
183. Callewaert F, Roodt J, Ulrichts H, Stohr T, van Rensburg WJ, et al. 2012. Evaluation of efficacy and safety of the anti-VWF Nanobody ALX-0681 in a preclinical baboon model of acquired thrombotic thrombocytopenic purpura. *Blood* 120:3603-10
184. Maxwell MJ, Westein E, Nesbitt WS, Giuliano S, Dopheide SM, Jackson SP. 2007. Identification of a 2-stage platelet aggregation process mediating shear-dependent thrombus formation. *Blood* 109:566-76
185. Ikeda Y, Handa M, Kawano K, Kamata T, Murata M, et al. 1991. The role of von Willebrand factor and fibrinogen in platelet aggregation under varying shear stress. *J Clin Invest* 87:1234-40
186. Mohri H, Fujimura Y, Shima M, Yoshioka A, Houghten RA, et al. 1988. Structure of the von Willebrand factor domain interacting with glycoprotein Ib. *J Biol Chem* 263:17901-4
187. Miura S, Fujimura Y, Sugimoto M, Kawasaki T, Ikeda Y, et al. 1994. Structural elements influencing von Willebrand factor (vWF) binding affinity for platelet glycoprotein Ib within a dispase-digested vWF fragment. *Blood* 84:1553-8
188. Muller JP, Mielke S, Lof A, Obser T, Beer C, et al. 2016. Force sensing by the vascular protein von Willebrand factor is tuned by a strong intermonomer interaction. *Proc Natl Acad Sci U S A* 113:1208-13
189. Löf A, Walker PU, Sedlak SM, Gruber S, Obser T, et al. 2019. Multiplexed protein force spectroscopy reveals equilibrium protein folding dynamics and the low-force response of von Willebrand factor. *Proc Natl Acad Sci U S A* 116:18798-807
190. Cao W, Cao W, Zhang W, Zheng XL, Zhang XF. 2020. Factor VIII binding affects the mechanical unraveling of the A2 domain of von Willebrand factor. *J Thromb Haemost* 18:2169-76
191. Posch S, Aponte-Santamaria C, Schwarzl R, Karner A, Radtke M, et al. 2017. Mutual A domain interactions in the force sensing protein von Willebrand factor. *J Struct Biol* 197:57-64
192. Gresele P, Momi S. 2012. Inhibitors of the interaction between von Willebrand factor and platelet GPIb/IX/V. *Handb Exp Pharmacol*:287-309
193. Kageyama S, Yamamoto H, Nakazawa H, Matsushita J, Kouyama T, et al. 2002. Pharmacokinetics and pharmacodynamics of AJW200, a humanized monoclonal antibody to von Willebrand factor, in monkeys. *Arterioscler Thromb Vasc Biol* 22:187-92

194. Fontayne A, Meiring M, Lamprecht S, Roodt J, Demarsin E, et al. 2008. The humanized anti-glycoprotein Ib monoclonal antibody h6B4-Fab is a potent and safe antithrombotic in a high shear arterial thrombosis model in baboons. *Thromb Haemost* 100:670-7
195. Gilbert JC, DeFeo-Fraulini T, Hutabarat RM, Horvath CJ, Merlino PG, et al. 2007. First-in-human evaluation of anti von Willebrand factor therapeutic aptamer ARC1779 in healthy volunteers. *Circulation* 116:2678-86
196. Benard SA, Smith TM, Cunningham K, Jacob J, DeSilva T, et al. 2008. Identification of peptide antagonists to glycoprotein Ibalpha that selectively inhibit von Willebrand factor dependent platelet aggregation. *Biochemistry* 47:4674-82
197. Lei X, Reheman A, Hou Y, Zhou H, Wang Y, et al. 2014. Anfibatide, a novel GPIb complex antagonist, inhibits platelet adhesion and thrombus formation in vitro and in vivo in murine models of thrombosis. *Thromb Haemost* 111:279-89
198. Nimjee SM, Dornbos D, 3rd, Pitoc GA, Wheeler DG, Layzer JM, et al. 2019. Preclinical Development of a vWF Aptamer to Limit Thrombosis and Engender Arterial Recanalization of Occluded Vessels. *Mol Ther* 27:1228-41
199. Lopez JA, Andrews RK, Afshar-Kharghan V, Berndt MC. 1998. Bernard-Soulier syndrome. *Blood* 91:4397-418
200. Grant MA, Beeler DL, Spokes KC, Chen J, Dharaneeswaran H, et al. 2017. Identification of extant vertebrate Myxine glutinosa VWF: evolutionary conservation of primary hemostasis. *Blood* 130:2548-58
201. Panteleev MA, Korin N, Reesink KD, Bark DL, Cosemans J, et al. 2021. Wall shear rates in human and mouse arteries: Standardization of hemodynamics for in vitro blood flow assays: Communication from the ISTH SSC subcommittee on biorheology. *J Thromb Haemost* 19:588-95
202. Nakeff A, Ingram M. 1970. Platelet count: volume relationships in four mammalian species. *J Appl Physiol* 28:530-3
203. Denis C, Methia N, Frenette PS, Rayburn H, Ullman-Cullere M, et al. 1998. A mouse model of severe von Willebrand disease: defects in hemostasis and thrombosis. *Proc Natl Acad Sci U S A* 95:9524-9
204. Ware J, Russell SR, Marchese P, Ruggeri ZM. 1993. Expression of human platelet glycoprotein Ib alpha in transgenic mice. *J Biol Chem* 268:8376-82
205. Fujimura Y, Holland LZ, Ruggeri ZM, Zimmerman TS. 1987. The von willebrand factor domain-mediating botrocetin-induced binding to glycoprotein IB lies between Val449 and Lys728. *Blood* 70:985-8
206. Sanders WE, Read MS, Reddick RL, Garris JB, Brinkhous KM. 1988. Thrombotic thrombocytopenia with von Willebrand factor deficiency induced by botrocetin. An animal model. *Lab Invest* 59:443-52
207. Ware J, Russell S, Ruggeri ZM. 1997. Cloning of the murine platelet glycoprotein Ibalpha gene highlighting species-specific platelet adhesion. *Blood Cells Mol Dis* 23:292-301
208. Navarrete AM, Casari C, Legendre P, Marx I, Hu JR, et al. 2012. A murine model to characterize the antithrombotic effect of molecules targeting human von Willebrand factor. *Blood* 120:2723-32
209. Kanaji S, Orje JN, Kanaji T, Kamikubo Y, Morodomi Y, et al. 2018. Humanized GPIbalpha-von Willebrand factor interaction in the mouse. *Blood Adv* 2:2522-32

210. Ware J, Russell S, Ruggeri ZM. 2000. Generation and rescue of a murine model of platelet dysfunction: the Bernard-Soulier syndrome. *Proc Natl Acad Sci U S A* 97:2803-8
211. Gralnick HR, Williams S, McKeown L, Kramer W, Krutzsch H, et al. 1992. A monomeric von Willebrand factor fragment, Leu-504--Lys-728, inhibits von Willebrand factor interaction with glycoprotein Ib-IX [corrected]. *Proc Natl Acad Sci U S A* 89:7880-4
212. Arce NA, Cao W, Brown AK, Legan ER, Wilson MS, et al. 2021. Activation of von Willebrand factor via mechanical unfolding of its discontinuous autoinhibitory module. *Nat Commun* 12:2360
213. Edgar RC. 2004. MUSCLE: multiple sequence alignment with high accuracy and high throughput. *Nucleic Acids Res* 32:1792-7
214. Chen W, Druzak SA, Wang Y, Josephson CD, Hoffmeister KM, et al. 2017. Refrigeration-induced binding of von Willebrand factor facilitates fast clearance of refrigerated platelets. *Arterioscler Thromb Vasc Biol* 37:2271-9
215. Keeble AH, Turkki P, Stokes S, Khairil Anuar INA, Rahikainen R, et al. 2019. Approaching infinite affinity through engineering of peptide-protein interaction. *Proc Natl Acad Sci U S A*
216. Dong JF, Berndt MC, Schade A, McIntire LV, Andrews RK, Lopez JA. 2001. Ristocetin-dependent, but not botrocetin-dependent, binding of von Willebrand factor to the platelet glycoprotein Ib-IX-V complex correlates with shear-dependent interactions. *Blood* 97:162-8
217. Woods AI, Sanchez-Luceros A, Bermejo E, Paiva J, Alberto MF, et al. 2014. Identification of p.W246L as a novel mutation in the GP1BA gene responsible for platelet-type von Willebrand disease. *Semin Thromb Hemost* 40:151-60
218. Chen J, Tan K, Zhou H, Lo HF, Tronik-Le Roux D, et al. 2008. Modifying murine von Willebrand factor A1 domain for in vivo assessment of human platelet therapies. *Nat Biotechnol* 26:114-9
219. Zurbano MJ, Escolar G, Heras M, Ordinas A, Castillo R. 2000. Differential aspects of the glycoprotein Ib-von Willebrand factor axis in human and pig species. *Haematologica* 85:514-9
220. Brinkhous KM, Thomas BD, Ibrahim SA, Read MS. 1977. Plasma levels of platelet aggregating factor/vom Willebrand factor in various species. *Thromb Res* 11:345-55
221. Yago T, Lou J, Wu T, Yang J, Miner JJ, et al. 2008. Platelet glycoprotein Ibalpha forms catch bonds with human WT vWF but not with type 2B von Willebrand disease vWF. *J Clin Invest* 118:3195-207
222. Lankhof H, van Hoeij M, Schiphorst ME, Bracke M, Wu YP, et al. 1996. A3 domain is essential for interaction of von Willebrand factor with collagen type III. *Thrombosis and haemostasis* 75:950-8
223. Posch S, Obser T, König G, Schneppenheim R, Tampé R, Hinterdorfer P. 2018. Interaction of von Willebrand factor domains with collagen investigated by single molecule force spectroscopy. *J Chem Phys* 148:123310
224. Lollar P, Parker ET. 1991. Structural basis for the decreased procoagulant activity of human factor VIII compared to the porcine homolog. *The Journal of biological chemistry* 266:12481-6

225. Simioni P, Tormene D, Tognin G, Gavasso S, Bulato C, et al. 2009. X-linked thrombophilia with a mutant factor IX (factor IX Padua). *The New England journal of medicine* 361:1671-5
226. Siedlecki CA, Lestini BJ, Kottke-Marchant KK, Eppell SJ, Wilson DL, Marchant RE. 1996. Shear-dependent changes in the three-dimensional structure of human von Willebrand factor. *Blood* 88:2939-50
227. Gangarosa EJ, Landerman NS, Rosch PJ, Herndon EG, Jr. 1958. Hematologic complications arising during ristocetin therapy; relation between dose and toxicity. *N Engl J Med* 259:156-61
228. Howard MA, Sawers RJ, Firkin BG. 1973. Ristocetin: a means of differentiating von Willebrand's disease into two groups. *Blood* 41:687-90
229. Meyer D, Jenkins CS, Dreyfus M, Larrieu MJ. 1973. Letter: Experimental model for von Willebrand's disease. *Nature* 243:293-4
230. Weiss HJ, Hoyer IW. 1973. Von Willebrand factor: dissociation from antihemophilic factor procoagulant activity. *Science (New York, N.Y.)* 182:1149-51
231. Flood VH, Gill JC, Morateck PA, Christopherson PA, Friedman KD, et al. 2011. Gain-of-function GPIb ELISA assay for VWF activity in the Zimmerman Program for the Molecular and Clinical Biology of VWD. *Blood* 117:e67-74
232. Wilkins MR, Gasteiger E, Bairoch A, Sanchez JC, Williams KL, et al. 1999. Protein identification and analysis tools in the ExPASy server. *Methods in molecular biology (Clifton, N.J.)* 112:531-52
233. Rakestraw JA, Sazinsky SL, Piatesi A, Antipov E, Wittrup KD. 2009. Directed evolution of a secretory leader for the improved expression of heterologous proteins and full-length antibodies in Saccharomyces cerevisiae. *Biotechnol Bioeng* 103:1192-201
234. De Marco L, Girolami A, Russell S, Ruggeri ZM. 1985. Interaction of asialo von Willebrand factor with glycoprotein Ib induces fibrinogen binding to the glycoprotein IIb/IIIa complex and mediates platelet aggregation. *J Clin Invest* 75:1198-203
235. Canis K, McKinnon TA, Nowak A, Panico M, Morris HR, et al. 2010. The plasma von Willebrand factor O-glycome comprises a surprising variety of structures including ABH antigens and disialosyl motifs. *J Thromb Haemost* 8:137-45
236. McVey JH, Rallapalli PM, Kemball-Cook G, Hampshire DJ, Giansily-Blaizot M, et al. 2020. The European Association for Haemophilia and Allied Disorders (EAHAD) Coagulation Factor Variant Databases: Important resources for haemostasis clinicians and researchers. *Haemophilia : the official journal of the World Federation of Hemophilia* 26:306-13
237. Broos K, Trekels M, Jose RA, Demeulemeester J, Vandenbulcke A, et al. 2012. Identification of a small molecule that modulates platelet glycoprotein Ib-von Willebrand factor interaction. *The Journal of biological chemistry* 287:9461-72
238. Clarke WP, Bond RA. 1998. The elusive nature of intrinsic efficacy. *Trends Pharmacol Sci* 19:270-6
239. Rivera J, Lozano ML, Navarro-Nunez L, Vicente V. 2009. Platelet receptors and signaling in the dynamics of thrombus formation. *Haematologica* 94:700-11
240. May F, Hagedorn I, Pleines I, Bender M, Vogtle T, et al. 2009. CLEC-2 is an essential platelet-activating receptor in hemostasis and thrombosis. *Blood* 114:3464-72

241. Jilma-Stohlawetz P, Gorczyca ME, Jilma B, Siller-Matula J, Gilbert JC, Knobl P. 2011. Inhibition of von Willebrand factor by ARC1779 in patients with acute thrombotic thrombocytopenic purpura. *Thromb Haemost* 105:545-52
242. Momi S, Tantucci M, Van Roy M, Ulrichts H, Ricci G, Gresele P. 2013. Reperfusion of cerebral artery thrombosis by the GPIb-VWF blockade with the Nanobody ALX-0081 reduces brain infarct size in guinea pigs. *Blood* 121:5088-97
243. Ayme G, Adam F, Legendre P, Bazaa A, Proulle V, et al. 2017. A Novel Single-Domain Antibody Against von Willebrand Factor A1 Domain Resolves Leukocyte Recruitment and Vascular Leakage During Inflammation-Brief Report. *Arteriosclerosis, thrombosis, and vascular biology* 37:1736-40
244. Denorme F, Martinod K, Vandenbulcke A, Denis CV, Lenting PJ, et al. 2021. The von Willebrand Factor A1 domain mediates thromboinflammation, aggravating ischemic stroke outcome in mice. *Haematologica* 106:819-28
245. Kovacevic KD, Grafeneder J, Schorgenhofer C, Gelbenegger G, Gager G, et al. 2021. The von Willebrand Factor A-1 domain binding aptamer BT200 elevates plasma levels of VWF and Factor VIII: a first-in-human trial. *Haematologica*
246. Schofield J, Shaw RJ, Lester W, Thomas W, Toh CH, Dutt T. 2021. Intracranial hemorrhage in immune thrombotic thrombocytopenic purpura treated with caplacizumab. *Journal of thrombosis and haemostasis : JTH* 19:1922-5
247. Ruggeri ZM. 2009. Platelet adhesion under flow. *Microcirculation* 16:58-83
248. Banno F, Chauhan AK, Kokame K, Yang J, Miyata S, et al. 2009. The distal carboxyl-terminal domains of ADAMTS13 are required for regulation of in vivo thrombus formation. *Blood* 113:5323-9
249. Celikel R, Varughese KI, Madhusudan, Yoshioka A, Ware J, Ruggeri ZM. 1998. Crystal structure of the von Willebrand factor A1 domain in complex with the function blocking NMC-4 Fab. *Nat Struct Biol* 5:189-94
250. Tsuji S, Sugimoto M, Miyata S, Kuwahara M, Kinoshita S, Yoshioka A. 1999. Real-time analysis of mural thrombus formation in various platelet aggregation disorders: distinct shear-dependent roles of platelet receptors and adhesive proteins under flow. *Blood* 94:968-75
251. Wu D, Vanhoorelbeke K, Cauwenberghs N, Meiring M, Depraetere H, et al. 2002. Inhibition of the von Willebrand (VWF)-collagen interaction by an antihuman VWF monoclonal antibody results in abolition of in vivo arterial platelet thrombus formation in baboons. *Blood* 99:3623-8
252. Knobl P, Jilma B, Gilbert JC, Hutabarat RM, Wagner PG, Jilma-Stohlawetz P. 2009. Anti-von Willebrand factor aptamer ARC1779 for refractory thrombotic thrombocytopenic purpura. *Transfusion* 49:2181-5
253. Zhu S, Gilbert JC, Liang Z, Kang D, Li M, et al. 2020. Potent and rapid reversal of the von Willebrand factor inhibitor aptamer BT200. *Journal of thrombosis and haemostasis : JTH* 18:1695-704
254. Motlagh HN, Wrabl JO, Li J, Hilser VJ. 2014. The ensemble nature of allostery. *Nature* 508:331-9
255. Christopoulos A. 2002. Allosteric binding sites on cell-surface receptors: novel targets for drug discovery. *Nat Rev Drug Discov* 1:198-210
256. Liu B, Chen W, Evavold BD, Zhu C. 2014. Accumulation of dynamic catch bonds between TCR and agonist peptide-MHC triggers T cell signaling. *Cell* 157:357-68

257. Zhu J, Luo BH, Xiao T, Zhang C, Nishida N, Springer TA. 2008. Structure of a complete integrin ectodomain in a physiologic resting state and activation and deactivation by applied forces. *Mol Cell* 32:849-61
258. Mumm JS, Schroeter EH, Saxena MT, Griesemer A, Tian X, et al. 2000. A ligand-induced extracellular cleavage regulates gamma-secretase-like proteolytic activation of Notch1. *Mol Cell* 5:197-206
259. Kefauver JM, Ward AB, Patapoutian A. 2020. Discoveries in structure and physiology of mechanically activated ion channels. *Nature* 587:567-76
260. Alevriadou BR, Moake JL, Turner NA, Ruggeri ZM, Folie BJ, et al. 1993. Real-time analysis of shear-dependent thrombus formation and its blockade by inhibitors of von Willebrand factor binding to platelets. *Blood* 81:1263-76
261. Zadelaar S, Kleemann R, Verschuren L, de Vries-Van der Weij J, van der Hoorn J, et al. 2007. Mouse models for atherosclerosis and pharmaceutical modifiers. *Arteriosclerosis, thrombosis, and vascular biology* 27:1706-21
262. Spangler JB, Moraga I, Jude KM, Savvides CS, Garcia KC. 2019. A strategy for the selection of monovalent antibodies that span protein dimer interfaces. *The Journal of biological chemistry* 294:13876-86